

## **DISCLAIMER**

**This report was prepared as an account of work sponsored by an agency of the United States Government. Neither the United States Government nor any agency thereof, nor any of their employees, makes any warranty, express or implied, or assumes any legal liability or responsibility for the accuracy, completeness, or usefulness of any information, apparatus, product, or process disclosed, or represents that its use would not infringe privately owned rights. Reference herein to any specific commercial product, process, or service by trade name, trademark, manufacturer, or otherwise does not necessarily constitute or imply its endorsement, recommendation, or favoring by the United States Government or any agency thereof. The views and opinions of authors expressed herein do not necessarily state or reflect those of the United States Government or any agency thereof. Reference herein to any social initiative (including but not limited to Diversity, Equity, and Inclusion (DEI); Community Benefits Plans (CBP); Justice 40; etc.) is made by the Author independent of any current requirement by the United States Government and does not constitute or imply endorsement, recommendation, or support by the United States Government or any agency thereof.**

# SANDIA REPORT

Unlimited Release

Printed September 11, 2025



Sandia  
National  
Laboratories

## SIERRA Low Mach Module: Fuego Verification Manual – Version 5.26

SIERRA Thermal/Fluid Development Team

Prepared by  
Sandia National Laboratories  
Albuquerque, New Mexico 87185  
Livermore, California 94550

Issued by Sandia National Laboratories, operated for the United States Department of Energy by National Technology & Engineering Solutions of Sandia, LLC.

**NOTICE:** This report was prepared as an account of work sponsored by an agency of the United States Government. Neither the United States Government, nor any agency thereof, nor any of their employees, nor any of their contractors, subcontractors, or their employees, make any warranty, express or implied, or assume any legal liability or responsibility for the accuracy, completeness, or usefulness of any information, apparatus, product, or process disclosed, or represent that its use would not infringe privately owned rights. Reference herein to any specific commercial product, process, or service by trade name, trademark, manufacturer, or otherwise, does not necessarily constitute or imply its endorsement, recommendation, or favoring by the United States Government, any agency thereof, or any of their contractors or subcontractors. The views and opinions expressed herein do not necessarily state or reflect those of the United States Government, any agency thereof, or any of their contractors.

Printed in the United States of America. This report has been reproduced directly from the best available copy.

Available to DOE and DOE contractors from

U.S. Department of Energy  
Office of Scientific and Technical Information  
P.O. Box 62  
Oak Ridge, TN 37831

Telephone: (865) 576-8401  
Facsimile: (865) 576-5728  
E-Mail: reports@osti.gov  
Online ordering: <http://www.osti.gov/scitech>

Available to the public from

U.S. Department of Commerce  
National Technical Information Service  
5301 Shawnee Road  
Alexandria, VA 22312

Telephone: (800) 553-6847  
Facsimile: (703) 605-6900  
E-Mail: orders@ntis.gov  
Online order: <https://classic.ntis.gov/help/order-methods>



## ABSTRACT

The SIERRA Low Mach Module: Fuego, henceforth referred to as Fuego, is the key element of the ASC fire environment simulation project. The fire environment simulation project is directed at characterizing both open large-scale pool fires and building enclosure fires. Fuego represents the turbulent, buoyantly-driven incompressible flow, heat transfer, mass transfer, combustion, soot, and absorption coefficient model portion of the simulation software. Sierra/PMR handles the participating-media thermal radiation mechanics. This project is an integral part of the SIERRA multi-mechanics software development project. Fuego depends heavily upon the core architecture developments provided by SIERRA for massively parallel computing, solution adaptivity, and mechanics coupling on unstructured grids.

# ACKNOWLEDGMENTS

The following Sandia staff have been involved with the Fuego verification project: Colin Aro, Amalia Black, Fred Blottner, Shawn Burns, Don Chenoweth, Bob Cochran, Stefan Domino, Greg Evans, Bill Houf, Steve Kempka, Chris Kennedy, Mario Martinez, Chris Moen, Vern Nicolette, Don Potter, Warren Tauber, and Tom Voth.

This document is submitted to Ed Boucheron, the Abnormal Thermal Environments project manager under the ASC Applications Program.

# CONTENTS

<b>1. Introduction</b>	<b>19</b>
1.1. Verification Testing Approach .....	20
1.2. Verification Test Suite Structure .....	22
1.3. Verification Test Suite Problems .....	22
1.4. Verification Test Suite Assessment .....	23
<b>2. Species Diffusion</b>	<b>25</b>
2.1. Material Specifications .....	25
2.2. Initial Conditions .....	26
2.3. Boundary Conditions .....	26
2.4. Analytical or Benchmark Solutions .....	26
2.5. Mesh Definition .....	27
2.6. Solution Procedure .....	27
2.7. Results .....	28
<b>3. Laminar, Thermally-Driven Buoyant Plume</b>	<b>31</b>
3.1. Analytic or Benchmark Solution .....	32
3.2. Mesh Definition .....	35
3.3. Material Specifications .....	35
3.4. Initial Conditions .....	36
3.5. Boundary Conditions .....	36
3.6. Solution Procedure .....	36
3.7. Verification Experiments .....	37
<b>4. Laminar, Concentration-Driven Buoyant Plume</b>	<b>49</b>
4.1. Analytic or Benchmark Solution .....	49
4.2. Mesh Definition .....	52
4.3. Material Specifications .....	53
4.4. Initial Conditions .....	53
4.5. Boundary Conditions .....	53
4.6. Solution Procedure .....	54
4.7. Verification Experiments .....	54
<b>5. Pressure-Driven Laminar Duct</b>	<b>61</b>
5.1. Material Specifications .....	61
5.2. Initial Conditions .....	61
5.3. Boundary Conditions .....	62

5.4. Analytic or Benchmark Solution .....	62
5.5. Mesh Definition .....	64
5.6. Solution Procedure .....	64
<b>6. Turbulent Heated Duct</b>	<b>69</b>
6.1. Executive Summary .....	69
6.2. Introduction .....	70
6.3. Problem Description .....	70
6.4. Material Specifications .....	71
6.5. Initial Conditions .....	72
6.6. Boundary Conditions .....	72
6.7. Analytic or Benchmark Solution .....	73
6.8. Mesh Definition .....	73
6.9. Solution Procedure .....	75
6.10. Verification Experiments .....	75
<b>7. EDC Combustion Model</b>	<b>87</b>
7.1. Executive Summary .....	87
7.2. Solution Procedure .....	91
7.3. Sample Output .....	91
<b>8. EDC Soot Model</b>	<b>93</b>
8.1. Material Specifications .....	93
8.2. Initial Conditions .....	93
8.3. Boundary Conditions .....	93
8.4. Analytic or Benchmark Solution .....	93
8.5. Mesh Definition .....	93
8.6. Solution Procedure .....	93
8.7. Verification Experiments .....	93
<b>9. Progress Variable Model for Soot</b>	<b>95</b>
9.1. Initial condition .....	97
9.2. Boundary Conditions .....	97
9.3. Analytic or Benchmark Solution .....	97
9.4. Sample Output .....	97
<b>10. Radiation Properties</b>	<b>99</b>
10.1. Material Specifications .....	99
10.2. Initial Conditions .....	99
10.3. Boundary Conditions .....	99
10.4. Analytic or Benchmark Solution .....	99
10.5. Mesh Definition .....	99
10.6. Solution Procedure .....	99
10.7. Verification Experiments .....	99

<b>11. Turbulent Diffusion Flame</b>	<b>101</b>
11.1. Material Specifications .....	101
11.2. Initial Conditions .....	101
11.3. Boundary Conditions.....	101
11.4. Analytic or Benchmark Solution .....	101
11.5. Mesh Definition .....	101
11.6. Solution Procedure .....	101
11.7. Verification Experiments .....	101
<b>12. Gas Properties</b>	<b>103</b>
12.1. Analytic or Benchmark Solution .....	103
12.2. Mesh Definition .....	104
12.3. Material Specifications .....	104
12.4. Initial Conditions .....	104
12.5. Boundary Conditions.....	104
12.6. Solution Procedure .....	105
12.7. Verification Experiments .....	105
<b>13. Transient Buoyant Flow</b>	<b>109</b>
13.1. Material Specifications .....	109
13.2. Initial Conditions .....	109
13.3. Boundary Conditions.....	109
13.4. Analytic or Benchmark Solution .....	109
13.5. Mesh Definition .....	109
13.6. Solution Procedure .....	109
13.7. Verification Experiments .....	109
<b>14. Buoyant Flow with PMR</b>	<b>111</b>
14.1. Material Specifications .....	111
14.2. Initial Conditions .....	112
14.3. Boundary Conditions.....	112
14.4. Analytic or Benchmark Solution .....	112
14.5. Mesh Definition .....	113
14.6. Solution Procedure .....	113
14.7. Verification Experiments .....	113
<b>15. Five-Meter Pool Fire</b>	<b>117</b>
15.1. Material Specifications .....	117
15.2. Initial Conditions .....	117
15.3. Boundary Conditions.....	117
15.4. Analytic or Benchmark Solution .....	117
15.5. Mesh Definition .....	117
15.6. Solution Procedure .....	117
15.7. Verification Experiments .....	117

<b>16. Manufactured Solution</b>	<b>119</b>
16.1. Analytic or Benchmark Solution .....	120
16.2. Mesh Definition .....	120
16.3. Material Specifications .....	120
16.4. Initial Conditions .....	120
16.5. Boundary Conditions .....	121
16.6. Solution Procedure .....	121
16.7. Verification Experiments .....	121
<b>17. Turbulent Free Jet</b>	<b>127</b>
17.1. Executive Summary .....	127
17.2. Material Specifications .....	128
17.3. Initial Conditions .....	128
17.4. Boundary Conditions .....	129
17.5. Analytic or Benchmark Solution .....	129
17.6. Mesh Definition .....	130
17.7. Solution Procedure .....	131
17.8. Verification Experiments .....	131
<b>18. Surface Transfer Verification</b>	<b>153</b>
18.1. Material Specifications .....	153
18.2. Initial Conditions .....	154
18.3. Boundary Conditions .....	154
18.4. Analytic or Benchmark Solution .....	154
18.5. Mesh Definition .....	154
18.6. Solution Procedure .....	154
18.7. Verification Experiments .....	154
<b>19. Buoyancy Vorticity Generation Model</b>	<b>157</b>
19.1. Executive Summary .....	157
19.2. Material Specifications .....	158
19.3. Initial Conditions .....	158
19.4. Standard Mesh .....	158
19.5. Rotated Mesh .....	159
19.6. Boundary Conditions .....	159
19.7. Analytic or Benchmark Solution .....	159
19.8. Mesh Definition for The SIERRA/Fuego Case Study .....	164
19.9. Solution Procedure .....	164
19.10. Verification Experiments .....	165
19.11. Concluding remarks .....	166
<b>20. Laminar Duct Flow</b>	<b>171</b>
20.1. Material Specifications .....	172
20.2. Initial Conditions .....	172
20.3. Boundary Conditions .....	172

20.4. Richardson Extrapolated Solution .....	172
20.5. Mesh Definition .....	172
20.6. Solution Procedure .....	173
20.7. Results .....	173
<b>21. Laminar Jet</b>	<b>179</b>
21.1. Analytic or Benchmark Solution .....	179
21.2. Mesh Definition .....	181
21.3. Material Specifications .....	181
21.4. Initial Conditions .....	181
21.5. Boundary Conditions .....	181
21.6. Solution Procedure .....	182
21.7. Verification Experiments .....	182
<b>22. Lid-Driven Cavity</b>	<b>185</b>
22.1. Analytic or Benchmark Solution .....	185
22.2. Mesh Definition .....	185
22.3. Material Specifications .....	186
22.4. Initial Conditions .....	186
22.5. Boundary Conditions .....	186
22.6. Solution Procedure .....	187
22.7. Verification Experiments .....	187
<b>23. Turbulent Helium Plume</b>	<b>193</b>
23.1. Material Specifications .....	193
23.2. Initial Conditions .....	193
23.3. Boundary Conditions .....	193
23.4. Analytic or Benchmark Solution .....	193
23.5. Mesh Definition .....	193
23.6. Solution Procedure .....	193
23.7. Verification Experiments .....	193
<b>24. Laminar Shedding from a Sphere</b>	<b>195</b>
24.1. Material Specifications .....	195
24.2. Initial Conditions .....	195
24.3. Boundary Conditions .....	195
24.4. Analytic or Benchmark Solution .....	195
24.5. Mesh Definition .....	196
24.6. Solution Procedure .....	196
24.7. Verification Experiments .....	196
<b>25. Heat Conduction Manufactured Solution</b>	<b>197</b>
25.1. Analytic or Benchmark Solution .....	197
25.2. Mesh Definition .....	198
25.3. Material Specifications .....	198

25.4. Initial Conditions .....	198
25.5. Boundary Conditions .....	198
25.6. Solution Procedure .....	198
25.7. Verification Experiments .....	199
<b>26. Buoyant, Variable Density Manufactured Solution</b>	<b>203</b>
26.1. Analytic or Benchmark Solution .....	207
26.2. Mesh Definition .....	207
26.3. Material Specifications .....	207
26.4. Initial Conditions .....	207
26.5. Boundary Conditions .....	207
26.6. Solution Procedure .....	208
<b>27. K-epsilon Manufactured Solution</b>	<b>209</b>
27.1. Analytic or Benchmark Solution .....	209
27.2. Mesh Definition .....	210
27.3. Material Specifications .....	211
27.4. Initial Conditions .....	211
27.5. Boundary Conditions .....	211
27.6. Solution Procedure .....	211
27.7. Verification Experiments .....	211
<b>28. Conjugate Heat Transfer Manufactured Solution</b>	<b>221</b>
28.1. Analytic or Benchmark Solution .....	221
28.2. Mesh Definition .....	222
28.3. Material Specifications .....	222
28.4. Initial Conditions .....	223
28.5. Boundary Conditions .....	223
28.6. Solution Procedure .....	223
28.7. Verification Experiments .....	223
<b>29. Porous Media</b>	<b>229</b>
29.1. Material Specifications .....	229
29.2. Initial Conditions .....	229
29.3. Boundary Conditions .....	229
29.4. Analytic or Benchmark Solution .....	230
29.5. Mesh Definition .....	231
29.6. Solution Procedure .....	231
<b>Distribution</b>	<b>235</b>

# LIST OF FIGURES

Figure 2.7-1.	Geometry for species diffusion problem with and without mass transfer of species B at the wall .....	28
Figure 2.7-2.	Mass Fraction of O across layer .....	29
Figure 3.1-1.	Coordinate system for laminar buoyant plume similarity solution. ....	32
Figure 3.7-1.	Centerline temperature for the laminar, buoyant plume with hybrid first-order upwinding. Temperature equation with $Pr=2$ , $Re=10$ , $Ra=30500$ . Additional benchmark with cell-centered ANSWER code, $x=0.25$ . ....	39
Figure 3.7-2.	Centerline temperature for the laminar, buoyant plume with hybrid MUSCL upwinding. Temperature equation with $Pr=2$ , $Re=10$ , $Ra=30500$ . ....	40
Figure 3.7-3.	Centerline vertical velocity for the laminar, buoyant plume with hybrid first-order upwinding. Temperature equation with $Pr=2$ , $Re=10$ , $Ra=30500$ . Additional benchmark with cell-centered ANSWER code, $x=0.25$ . ....	41
Figure 3.7-4.	Centerline vertical velocity for the laminar, buoyant plume with hybrid MUSCL upwinding. Temperature equation with $Pr=2$ , $Re=10$ , $Ra=30500$ . ....	41
Figure 3.7-5.	Horizontal velocity for the laminar, buoyant plume with hybrid first-order upwinding. Horizontal cuts at $y=5$ and $y=15$ relative to the inflow plane. Temperature equation with $Pr=2$ , $Re=10$ , $Ra=30500$ . Additional benchmark with cell-centered ANSWER code, $y=4.75$ and $y=14.75$ . ....	42
Figure 3.7-6.	Horizontal velocity for the laminar, buoyant plume with hybrid MUSCL upwinding. Horizontal cuts at $y=5$ and $y=15$ relative to the inflow plane. Temperature equation with $Pr=2$ , $Re=10$ , $Ra=30500$ . ....	42
Figure 3.7-7.	Nonlinear convergence for the $80 \times 80$ mesh, temperature equation. ....	43
Figure 3.7-8.	Horizontal velocity contours for $Pr=2$ , $Re=10$ , $Ra=30500$ , temperature equation. ....	44
Figure 3.7-9.	Horizontal velocity contours with outflow velocity vectors for $Pr=2$ , $Re=10$ , $Ra=30500$ , temperature equation. ....	44
Figure 3.7-10.	Centerline temperature for the laminar, buoyant plume with hybrid first-order upwinding. Enthalpy equation with $Pr=2$ , $Re=10$ , $Ra=30500$ . ....	45
Figure 3.7-11.	Horizontal velocity for the laminar, buoyant plume with hybrid first-order upwinding. Horizontal cut at $y=15$ relative to the inflow plane. Enthalpy equation with $Pr=2$ , $Re=10$ , $Ra=30500$ . ....	45
Figure 3.7-12.	Centerline temperature and velocity for the laminar, buoyant plume. Temperature equation with $Pr=2$ , $Re=16.7$ , $Ra=85000$ . ....	46
Figure 3.7-13.	Lateral profiles of temperature for the laminar, buoyant plume. Temperature equation with $Pr=2$ , $Re=16.7$ , $Ra=85000$ . ....	46
Figure 3.7-14.	Horizontal profiles of vertical velocity for the laminar, buoyant plume. Temperature equation with $Pr=2$ , $Re=16.7$ , $Ra=85000$ . ....	47

Figure 4.7-1.	Centerline H <sub>2</sub> mass fractions. . . . .	55
Figure 4.7-2.	Radial H <sub>2</sub> mass fractions at two axial stations. . . . .	56
Figure 4.7-3.	Radial distribution of radial velocity at two axial stations. . . . .	56
Figure 4.7-4.	Centerline velocity. . . . .	57
Figure 4.7-5.	Order of accuracy contours, x-velocity. . . . .	58
Figure 4.7-6.	Order of accuracy contours, y-velocity. . . . .	59
Figure 4.7-7.	Order of accuracy contours, mass fraction of species 1. . . . .	60
Figure 5.4-1.	L <sub>2</sub> norm of residuals for 20x40x40 mesh. . . . .	64
Figure 5.4-2.	Parabolic velocity profile across x axis at y = 0 m, z = 10 m. . . . .	65
Figure 5.4-3.	Parabolic velocity profile across y axis at x = 0 m, z = 10 m. . . . .	66
Figure 5.4-4.	Centerline pressure in duct showing linear change. . . . .	67
Figure 6.3-1.	Description of the problem (not to scale, L <sub>d</sub> /b = 315). . . . .	71
Figure 6.7-1.	Nusselt numbers: analytic solution and CFX5 benchmark; horizontal coordinate defined in eqn. 6.3. . . . .	74
Figure 6.8-1.	Local heat flux distribution on heated channel wall: CFX results with different mesh spacing. . . . .	75
Figure 6.8-2.	Local heat flux distribution on heated channel wall: CFX results with different mesh spacing and different wall functions. . . . .	76
Figure 6.10-1.	Local Nusselt number distribution on heated channel wall: Fuego, CFX5, and Özişik solutions at Re=50,000. . . . .	78
Figure 6.10-2.	Axial component of velocity profiles across channel half-width upstream and downstream of start of heated channel wall; comparisons between Fuego and CFX5; Re=50,000. . . . .	79
Figure 6.10-3.	Turbulent kinetic energy profiles across channel half-width, upstream and downstream of start of heated channel wall; comparisons between Fuego and CFX5; Re=50,000. . . . .	80
Figure 6.10-4.	Turbulent dissipation rate profiles across channel half-width, upstream and downstream of start of heated channel wall; comparisons between Fuego and CFX5; Re=50,000. . . . .	81
Figure 6.10-5.	Pressure drop along the centerline of the channel; comparison between Fuego and CFX5; Re=50,000. . . . .	82
Figure 6.10-6.	Local Nusselt number distribution on heated channel wall: Fuego results for various thermal wall law parameters; Re=50,000; CFX5 result at Pr <sub>t</sub> =0.9 shown for comparison. . . . .	83
Figure 6.10-7.	Local Nusselt number distribution on heated channel wall: CFX5 results for three values of Pr <sub>t</sub> ; analytical solution for Pr <sub>t</sub> =1.0; Re=50,000. . . . .	84
Figure 6.10-8.	Local Nusselt number distribution on heated channel wall: sensitivity of Fuego results to mesh spacing; Re=50,000; Pr <sub>t</sub> =0.9. . . . .	85
Figure 9.4-1.	Comparison of results (Blue: solution with leaning and a change to the mixture fraction lookup; Orange, no lookup mixture fraction modification; Yellow, no mixture fraction sink or lookup mixture fraction; Fuego, purple circles;) for a short time. Mapping ignores density variation. . . . .	98

Figure 14.7-1. Stream function (left image; colored by velocity vector magnitude) and temperature (right image; colored by temperature) contours for (79x120x20); $Sk = 1.25$ and $Ra_L = 10^4$ .....	114
Figure 14.7-2. Stream function (left image; colored by velocity vector magnitude) and temperature (right image; colored by temperature) contours for (79x120x20); $Sk = 0.125$ and $Ra_L = 10^4$ .....	115
Figure 16.7-1. Convergence performance of the nonlinear equations, $L_2$ norms of the nonlinear residuals. Low Reynolds number test. ....	122
Figure 16.7-2. Velocity solution: error analysis for low Reynolds number test with second order convection and diffusion. Error slopes indicate second order spatial accuracy, as expected. Mesh spacing of 1.0 in this plot corresponds to the $10 \times 10 \times 10$ mesh. ....	124
Figure 16.7-3. Pressure solution: error analysis for low Reynolds number test with second order convection and diffusion. Error slopes indicate less than second order spatial accuracy. Mesh spacing of 1.0 in this plot corresponds to the $10 \times 10 \times 10$ mesh. ....	125
Figure 17.8-1. Scoping study simulation plot of normalized streamwise velocity at three mesh rotations. ....	136
Figure 17.8-2. Scoping study simulation plot of normalized streamwise velocity with varying CFL and relaxation parameters. ....	137
Figure 17.8-3. Scoping study simulation plot of normalized streamwise velocity with varying projection algorithms in use. ....	138
Figure 17.8-4. Scoping study simulation plot of nonlinear residuals with varying projection algorithms in use. ....	139
Figure 17.8-5. Scoping study simulation plot of normalized streamwise velocity as a function of normalized axial distance. Shown are the sensitivities to chosen inflow and outflow boundary conditions. ....	140
Figure 17.8-6. Scoping study simulation plot of normalized streamwise velocity as a function of normalized axial distance. Shown are the sensitivities to chosen projection methods with varying time steps. ....	141
Figure 17.8-7. Scoping study simulation plot of normalized streamwise velocity as a function of normalized axial distance. Shown are the sensitivities to chosen projection methods with varying time steps, close-up of entry region. ....	142
Figure 17.8-8. Scoping study simulation plot of streamwise nonlinear residuals with varying projection algorithms in use; time step and characteristic. ....	143
Figure 17.8-9. $\ L_2\ $ norm as a function of iteration for the 246,013 node turbulent open jet simulation. ....	144
Figure 17.8-10. Normalized streamwise velocity as a function of normalized axial distance for the SIERRA/Fuego mesh refinement study of the turbulent round jet. ....	145
Figure 17.8-11. Normalized turbulent kinetic energy as a function of normalized axial distance for the SIERRA/Fuego mesh refinement study of the turbulent round jet. ....	146
Figure 17.8-12. Normalized turbulence dissipation as a function of normalized axial distance for the SIERRA/Fuego mesh refinement study of the turbulent round jet. ....	147

Figure 17.8-13. Normalized streamwise velocity as a function of normalized radial distance for the 61,251 node mesh comparison study of the turbulent round jet. Shown are profiles $z/d = 20, 40$ , and $60$ .	148
Figure 17.8-14. Radius half-width as a function of normalized axial distance for the 61,251 node mesh comparison study of the turbulent round jet. The slope of this curve represents the “jet spreading rate” and is 0.0975.	149
Figure 17.8-15. Normalized streamwise velocity, turbulent kinetic energy, and turbulence dissipation rate as a function of normalized axial distance for the 61,251 node mesh comparison study of the turbulent round jet.	150
Figure 17.8-16. Normalized streamwise velocity, turbulent kinetic energy, and turbulence dissipation rate as a function of normalized axial distance for the 120,411 node mesh comparison study of the turbulent round jet.	151
Figure 17.8-17. Normalized streamwise velocity, turbulent kinetic energy, and turbulence dissipation rate as a function of normalized axial distance for the 246,013 node mesh comparison study of the turbulent round jet.	152
Figure 18.7-1. Scoping study simulation plot of normalized streamwise velocity at three mesh rotations.	155
Figure 19.10-1. Plot of error vs mesh spacing to demonstrate convergence of the SIERRA/Fuego numerical model to the analytical result.	168
Figure 19.10-2. Plot of error vs mesh spacing to demonstrate convergence of the SIERRA/Fuego numerical model (using a rotated mesh) to the analytical result.	169
Figure 20.7-1. Axial Velocity Contour Plot of Fine Mesh Solution	174
Figure 20.7-2. Order Plot of Axial Velocity	174
Figure 20.7-3. Error Plot of Axial Velocity (Fine Mesh Solution)	175
Figure 20.7-4. Axial Velocity Norms for Coarse, Medium, and Fine Mesh Solutions	175
Figure 20.7-5. Order Plot of Pressure	176
Figure 20.7-6. Error Plot of Pressure (Fine Mesh Solution)	176
Figure 20.7-7. Pressure Norms for Coarse, Medium, and Fine Mesh Solutions	177
Figure 21.7-1. Lateral velocity profiles at axial stations 5 and 15 (relative to the inflow plane) for various boundary condition combinations.	183
Figure 21.7-2. Lateral velocity profiles at axial stations 5 and 15 (relative to the inflow plane). Flux inflow and no viscous stress outflow conditions.	183
Figure 21.7-3. Centerline axial velocity. Flux inflow and no viscous stress outflow conditions.	184
Figure 21.7-4. Convergence history on the 40x40 mesh. Flux inflow and no viscous stress outflow conditions.	184
Figure 22.7-1. Comparison of computed x-velocity with benchmark solution along the vertical centerline, $Re=100$ . The projection method is smoothed with time-step scaling.	188
Figure 22.7-2. Comparison of computed y-velocity with benchmark solution along the horizontal centerline, $Re=100$ . The projection method is smoothed with time-step scaling.	189

Figure 22.7-3.	Convergence history for the driven-cavity problem. $L_2$ norm of the nonlinear residual of the x-momentum equation. The smoothed and unsmoothed projection methods use characteristic scaling with implicit momentum relaxation of 0.5 and explicit pressure relaxation of 0.5. All solutions are run at CFL=10 and all solutions are the same at steady-state. ....	190
Figure 22.7-4.	Convergence history for the driven-cavity problem. $L_2$ norm of the nonlinear residual of the x-momentum equation. The smoothed method with characteristic scaling requires implicit momentum relaxation of 0.5 and explicit pressure relaxation of 0.5. The smoothed method with time step scaling requires no relaxation. All solutions were run at CFL=10. ....	190
Figure 22.7-5.	Pressure profile along the horizontal mid-line. Comparison of different scaling coefficients and time steps for the unsmoothed projection method. ....	191
Figure 22.7-6.	Convergence history for the driven-cavity problem. $L_2$ norm of the nonlinear residual of the x-momentum equation. The unsmoothed method with characteristic scaling requires implicit momentum relaxation of 0.5 and explicit pressure relaxation of 0.5. The unsmoothed method with time step scaling requires no relaxation. ....	191
Figure 25.7-1.	Plot of error vs normalized mesh spacing to demonstrate convergence of the SIERRA/Fuego method of outlined manufactured solution; results shown for the orthogonal study with full CVFEM diffusion operator. ....	199
Figure 25.7-2.	Plot of error vs normalized mesh spacing to demonstrate convergence of the SIERRA/Fuego method of outlined manufactured solution; results shown for the orthogonal study with reduced diffusion operator. ....	200
Figure 25.7-3.	Plot of error vs normalized mesh spacing to demonstrate convergence of the SIERRA/Fuego method of outlined manufactured solution; results shown for the non orthogonal thex study with full CVFEM diffusion operator. ....	201
Figure 25.7-4.	Plot of error vs normalized mesh spacing to demonstrate convergence of the SIERRA/Fuego method of outlined manufactured solution; results shown for the non orthogonal thex study with reduced CVFEM diffusion operator. ....	202
Figure 27.7-1.	Plot of $L_2$ error norms vs normalized mesh spacing for velocity components, $k$ , epsilon, and pressure. Case 1. ....	212
Figure 27.7-2.	Plot of $L_2$ error norms vs normalized mesh spacing for partial derivatives of pressure. Case 1. ....	213
Figure 27.7-3.	Plot of infinity error norms vs normalized mesh spacing for velocity components, $k$ , epsilon, and pressure. Case 1. ....	213
Figure 27.7-4.	Plot of infinity error norms vs normalized mesh spacing for partial derivatives of pressure. Case 1. ....	214
Figure 27.7-5.	Plot of $L_2$ error norms vs normalized mesh spacing for velocity components, $k$ , epsilon, and pressure. Case 2. Projection method = stabilized. ....	216
Figure 27.7-6.	Plot of $L_2$ error norms vs normalized mesh spacing for partial derivatives of pressure. Case 2. Projection method = stabilized. ....	217
Figure 27.7-7.	Plot of infinity error norms vs normalized mesh spacing for velocity components, $k$ , epsilon, and pressure. Case 2. Projection method = stabilized. ....	217

Figure 27.7-8.	Plot of infinity error norms vs normalized mesh spacing for partial derivatives of pressure. Case 2. Projection method = stabilized.	218
Figure 27.7-9.	Plot of L <sub>2</sub> error norms vs normalized mesh spacing for velocity components, k, epsilon, and pressure. Case 2. Projection method = fourth order smoothing with timestep scaling.	218
Figure 27.7-10.	Plot of L <sub>2</sub> error norms vs normalized mesh spacing for partial derivatives of pressure. Case 2. Projection method = fourth order smoothing with timestep scaling.	219
Figure 27.7-11.	Plot of infinity error norms vs normalized mesh spacing for velocity components, k, epsilon, and pressure. Case 2. Projection method = fourth order smoothing with timestep scaling.	219
Figure 27.7-12.	Plot of infinity error norms vs normalized mesh spacing for partial derivatives of pressure. Case 2. Projection method = fourth order smoothing with timestep scaling.	220
Figure 28.7-1.	Plot of error vs. mesh spacing for solution $T_2(x, y, z)$ solved on Mesh 1.	225
Figure 28.7-2.	.....	226
Figure 28.7-3.	.....	227
Figure 28.7-4.	.....	228
Figure 29.4-1.	Centerline pressure in duct showing linear change.	231

# LIST OF TABLES

Table 3.1-1.	Constants in thermal plume similarity solution for two Prandtl numbers (Pr).....	33
Table 3.7-1.	Error norms for Test 1 (temperature equation) with hybrid MUSCL scheme. Errors are relative to the boundary layer solution. ....	38
Table 3.7-2.	Error norms for Test 1 (temperature equation) with hybrid first-order upwind scheme. Errors are relative to the boundary layer solution. ....	43
Table 4.1-1.	Constants in concentration plume similarity solution for two Schmidt numbers (Sc). ....	51
Table 5.4-1.	Function values in similarity solution by Berker .....	63
Table 5.4-2.	Computed Centerline Velocity .....	63
Table 6.1-1.	Asymptotic Nusselt numbers in turbulent channel flow .....	70
Table 6.9-1.	Fuego job parameters .....	77
Table 12.7-1.	Properties for helium/air, cgs units. ....	105
Table 12.7-2.	Properties for methane/air, cgs units. ....	106
Table 12.7-3.	Properties for octane/air, cgs units. ....	106
Table 12.7-4.	Thermodynamic curve fit data for ChemkinIII. Source: CRSIM, University of Utah. ....	107
Table 12.7-5.	Transport property data for ChemkinIII. Source: CRSIM, University of Utah. ....	108
Table 14.1-1.	Physical properties for natural convection/radiation problem for $\text{Ra}_L = 10^4$ . ....	112
Table 14.7-1.	Average inner surface Nusselt number, $\text{Ra}_L = 10^4$ , on different grids (radial $\times$ azimuthal $\times$ axial). ....	114
Table 14.7-2.	Computing resource expenditure for $\text{Sk}=1.25$ . Fraction of time spent in assembling the linear systems and solving the linear systems for the different meshes. ....	114
Table 16.7-1.	Error norms for Test 2 with first order upwind scheme. ....	123
Table 16.7-2.	Error norms for Test 2 with MUSCL scheme. ....	123
Table 17.7-1.	Fuego job parameters from scoping simulation study .....	131
Table 17.7-2.	Fuego job parameters for code comparison simulation study .....	132
Table 22.1-1.	Lid-Driven Cavity: benchmark solution of Ghia and Ghia [1], $\text{Re}=100$ .....	186
Table 22.7-1.	Lid-Driven Cavity: Error Norms for X-Velocity, estimated order of accuracy is 1.5. Smoothed projection method with time-step scaling. ....	187
Table 22.7-2.	Lid-Driven Cavity: Error Norms for Y-Velocity, estimated order of accuracy is 1.9. Smoothed projection method with time-step scaling. ....	187
Table 26.1-1.	Error in velocity, projected pressure gradient, and temperature for the $h$ -based formulation. Uniform mesh. ....	205

Table 26.1-2. Error in velocity, projected pressure gradient, and temperature for the $Z$ -based formulation. Uniform mesh. ....	205
Table 26.1-3. Error in velocity, projected pressure gradient, and temperature for the $h$ -based formulation. THex mesh. ....	206
Table 26.1-4. Error in velocity, projected pressure gradient, and temperature for the $Z$ -based formulation. THex mesh. ....	206
Table 27.7-1. Order of accuracy for pressure solution defined by equation (10) where $dp/dn \neq 0$ at the boundaries ....	215
Table 27.7-2. Order of accuracy for pressure solution defined by equation (13) where $dp/dn = 0$ at the boundaries ....	215
Table 28.7-1. Error norms in fluid region for manufactured solution $T_1(x, y, z)$ . Meshes used are the coarsest meshes in each mesh family. ....	223

# 1. INTRODUCTION

The verification process is intended to demonstrate that a code is solving the governing equations correctly. Verification problems consist of analytical solutions to the mathematical model equations, derived analytical solutions based on an equivalent source term generation procedure (i.e., manufactured solutions), and established numerical bench mark solutions.

The fundamental strategy of verification is the identification and quantification of the numerical error in the computational model and its solution. There are two separate parts to the verification process: code verification and calculation verification as suggested by Blottner and Lopez, 1998. Code verification is concerned with establishing that the computational model produces accurate solutions to the governing equations. This involves ensuring that the numerical scheme is stable and consistent, the algorithm implementation has been performed correctly, and the determination of the discretization error behavior as the mesh is refined (order of numerical scheme). Calculation verification is concerned with determining the numerical error of a solution with a verified code to ensure that the solution has the desired accuracy. Once the code has been verified for a particular application, then it is not necessary to verify a calculation of similar application. It is assumed in the verification process, that the governing equations are well posed mathematically.

Oberkampf, et. al. 1999 suggest that there are six phases in computational modeling and simulation. The process of code verification and calculation verification determine the error in three of these phases: (1) the discretization/algorithm selection activities; (2) the computer programming activities; and (3) the numerical solution activities. Within the discretization/algorithm selection activities, errors result from the discretization of the partial differential equations, boundary conditions, and initial conditions. In addition, given a numerical algorithm, it is necessary to ensure that the numerical solution technique is stable and consistent. That is, the difference equations of a consistent numerical scheme accurately represents the partial differential equations as the mesh spatial sizes go to zero. An example has been pointed out by Turkel 1986, and Turkel, et al., 1986 where the original difference scheme developed by Jameson, et al., 1981, becomes inconsistent on nonuniform meshes. An inconsistent numerical scheme can result in unbounded errors; however, once the numerical scheme is found to be consistent, the errors associated with the discretization/algorithm selection activities can be bounded. Within the computer programming activities, uncertainties result from errors in computer programming (i.e., bugs) and computer compilation/ linkage. Computer bugs can result in unbounded errors and high uncertainties. Within the numerical solution activities, uncertainties result from errors in solution convergence and computer round-off. Solution convergence errors occur when there is insufficient spatial discretization convergence, insufficient temporal discretization convergence, and lack of iterative convergence. These numerical solution errors can be bounded through the use of spatial, temporal, and iterative refinement studies.

In order to determine the uncertainties associated with the three phases of modeling and simulation outlined above, a verification process has been developed that includes two distinct parts: unit testing and verification problem testing. Unit testing is a subroutine level analysis of the software. It is intended to demonstrate that a subroutine or group of subroutines, for which there is an analytical solution, algebraic solution or numerical bench mark solution, returns the correct answer. Unit testing is the responsibility of the software developers and is intended to identify errors associated with the discretization/algorithm selection activities and the computer programming activities. Verification problem testing involves running a set of test problems to demonstrate that the software can solve the math model i.e., either partial differential transport equations or algebraic sub-grid models, correctly. All combinations of math models, boundary conditions, initial conditions, and material properties need to be verified. For each problem, this involves determining the error between the exact and numerical solutions. Verification problem testing is intended to identify errors associated with the discretization/algorithm selection activities and the numerical solution activities. This is needed to build confidence that the code can produce accurate results if used properly.

The current verification process outlines a procedure for determining the code and calculation accuracy and error in order to meet the customer requirements. The validation process will determine the error and uncertainties associated with the math models, including the sub-grid models which are expected to produce the largest errors. As long as the verification errors which can be bounded are small relative to the math model errors, then no further effort needs to be made to drive these errors to zero. However, if errors exist which can not be bounded, such as a computer bug or an inconsistent numerical scheme, then these errors may be comparable to the math model errors. In complex 3-D nonlinear problems, one has to have confidence that the numerical errors are less than the math model errors before the accuracy of the math models can be assessed under the validation activity.

The structure of the verification test suite follows the Sandia ASC V&V Guidelines (Pilch, et al., 2001) in that it uses the three tier approach. Initially, unit testing and testing of individual physics is performed, followed by tests of coupled physics and then by tests of integral physics. By following the tiered testing approach, the majority of the code will be covered. In addition, the PIRT was used to prioritize the verification test problem suite down to the minimum necessary for complete coverage.

## **1.1. VERIFICATION TESTING APPROACH**

The focus of the following sections will be only on verification process. This project will use the following general classes of verification problems to demonstrate correct implementation, quantification of numerical error and order of convergence: 1) Unit Testing, 2) Analytical and Semi-Analytical Solutions of Specific Continuum Mechanics Math Models, 3) Numerical Benchmark Solutions, and 4) Manufactured Solutions.

### **1.1.1. Unit Testing**

Unit testing is a subroutine level analysis of the software. It is intended to demonstrate that a subroutine or group of subroutines returns the correct answer. The correct answer can be either an

analytical, algebraic, or numerical benchmark solution. For example, the analytical solution of the discretization formulae coefficients for each operator in the math models can be used to verify the numerical algorithm. These analytical solutions are usually limited to simple grids. The coefficients of the discretized operator are then extracted from the software implementation at a function level. Documentation of this process is performed and entered into the archive system. There is potentially some overlap across other software projects when common operators are discretized with the same numerical method. This process must be continuously updated as the computer platforms change. Another example of unit testing involves testing specific subroutines of a sub-grid model. The sub-grid models in Fuego are all algebraic models and the output results can be compared to other numerical benchmark solutions. This approach will require specifying input values to the sub-grid model and then comparing the output to the Vulcan code results.

### **1.1.2. Analytical and Semi-Analytical Solutions**

Analytical and semi-analytical solutions of the conservation equations are required. These analytical solutions can be used to verify the various components (convection, diffusion, etc.) in the governing equations. Initially, the governing equations are reduced to a simpler form where only one component appears. Results from the reduced governing equations are compared to the analytical solution with appropriate mesh refinement studies. A series of reduced equations with different components included are evaluated with the appropriate analytical solution to test all components in the governing equations. Typically, simple analytical solutions test only one conservation equation. However, with the exception of the conservation of mass equation, the transport equations of fluid mechanics are of a standard form (Blottner, Lopez Memo) with one dominant dependent variable in each equation. If the coding in the simulation code is in modular (object oriented) form, then testing of the standard form of the conservation equation for any one of the variables can be used to verify a significant part of the solution methodology of the code.

### **1.1.3. Numerical Benchmark Solutions**

Numerical benchmark solutions are based on comparing solutions from different software implementations of identical math models. A variety of these exist in the literature, but care must be taken to assure that the math models are identical. In many cases, these numerical benchmark comparisons have uncertainty due to lack of clarity in what math model was actually solved by each participant. It is hoped that these exercises will become more useful in the future as documentation is improved.

### **1.1.4. Manufactured Solutions**

The method of manufactured solutions is based on the concept that a function is assumed to be the exact solution to the math model. For the Navier-Stokes equations, there will be an analytic function for each dependent variable. Each function is then applied to the math models. Since the functions will not generally satisfy the math models there will be source terms that need to be applied, as well as

changes to initial and boundary conditions. This method provides a basis for verification of math models that have operators and boundary conditions not covered in the previous methods. There is a theoretical issue relative to the numerical method used for the application of the source term and boundary conditions. The numerical method for these terms should be of higher order than the numerical method used. In addition, it must be shown that the discretization is within the convergence region for the method. The success of the manufactured solution method relies on knowledge of the formal order of accuracy of the numerical method. The formal order of accuracy of a numerical method is also a function of the mesh spacing, e.g., uniform or nonuniform. Initial solutions should use a uniform mesh. Then a nonuniform mesh should give the same result as the mesh is refined. A code is determined to be verified if the order of accuracy that is computed by using mesh refinement with the manufactured solution source terms is equivalent to the formal order. Uncertainty in the validity of the verification process is introduced if the formal order of accuracy is unknown.

## 1.2. VERIFICATION TEST SUITE STRUCTURE

Both steady and transient flow problems can be modeled with SIERRA/Fuego. The stages in the verification process will be to add new levels of physics, i.e., new transport equations to test the coupling of the physics. For transient flow, Fuego uses the same procedure to solve the time dependent term for each governing equation. Therefore, it is not necessary to test each equation independently and so a coupled physics problems will be used to test Fuego for transient flows.

In addition to Fuego, the Nalu and Scefir code are being developed separately to solve the participating media radiation equations. For this reason, there are specific test cases being used to verify the SIERRA/Fuego and either Nalu or Scefir MPMD coupling. They are listed at the end of the verification test suite.

The structure of the verification test suite follows the Sandia ASC V&V Guidelines [6] in that it uses the three tier approach. Initially, unit testing and testing of individual physics is performed, followed by tests of coupled physics and then by tests of integral physics. By following the tiered testing approach, the majority of the code will be covered. The verification test suite was structured to align with the PIRT prioritization. The structure of the verification test problems are listed below.

## 1.3. VERIFICATION TEST SUITE PROBLEMS

SIERRA/Fuego, Nalu, and Scefir are a three-dimensional codes; however, it is possible to run two-dimensional verification problems by applying symmetry or periodic boundary conditions in the third coordinate direction. The two-dimensional problem can also rotated 90 degrees to check the equations in the third coordinate direction. Two-dimensional problems are more efficient computationally because they require fewer grid points. This is especially important when a verification problem requires high levels of grid refinement to test the numerical accuracy of the code.

The verification test suite contains a variety of problems each intended to test specific physics which is required for the current application of interest as outlined in the PIRT table. All of the test problems

listed below do exist and references for each are available. In some cases, there are categories, such as the combustion model and soot model cases, where there are no analytical solutions available. For these cases, code to code comparisons will be utilized. Since Fuego is based on the same sub-grid models found in the VULCAN code, unit level testing will be used to test specific subroutines for each sub-grid model.

In addition, verification testing using the manufactured solution approach is also being applied to verify Fuego. It has the potential to provide solutions to complex coupled problems where there are not any analytical or numerical benchmark solutions. Currently, this capability is being used to first test individual physics and then coupled physics problems will follow. There are specific problems (listed below) where the manufactured solution approach will be used.

## 1.4. VERIFICATION TEST SUITE ASSESSMENT

Verification addresses two primary issues in engineering analysis software. First, the implementation of the documented math models in software must be proven correct. Second, the accuracy of the numerical methods used to solve the math models must be determined. As outlined by Salari, et al. 2000, there are four possible acceptance criterion that could be used in verification testing. They are the expert judgement criterion, the percent difference/error criterion, the consistency criterion, and the order of accuracy criterion, with the later being the most rigorous acceptance criterion. In the present verification plan, the error criterion, the consistency criterion, and the order of accuracy criterion will be used as the acceptance tests as discussed below.

For the cases where unit test problems will be used, the error criterion will be the acceptance metric since these cases are mainly algebraic models. Whereas, all three criterion will be used to assess the cases where test problems are used. Since the formal order of accuracy of the numerical algorithm is not known, it may not be possible to use the accuracy criterion as the final acceptance metric but it is the intention to try to attain that level of acceptance with the procedure outlined below.

The generation of a series of colocated, refined meshes with the appropriate variation of mesh cell size is the most important component of the verification procedure. By systematically refining the grid size and time step, the discretization error should asymptotically approach zero. Richardson extrapolation methods for steady and unsteady problems will be used to estimate the discretization error. Point errors across the entire calculation domain will be evaluated as well as the standard error norms. In addition, the importance of mesh refinement studies is more significant than just a procedure to determine solution accuracy. It has been suggested by Blottner and Lopez, 1998, that mesh refinement techniques can be developed to determine consistency of numerical schemes and to determine if governing equations are well posed. Finally, the order of accuracy of the numerical method will be evaluated using the method defined by Roach, 1998. This approach has been used successfully to evaluate the order of accuracy of other codes (Lopez, et al., 1998); however, it requires a working knowledge of its limitations.

In addition, the manufactured solution method is also being used to assess the error and order of accuracy of the numerical method. This approach is being investigated so that its applicability in complex problems can be determined. It is our intention to use both approaches simultaneously.

A computation tool is being developed, VIVID (Potter and Blottner, 2001), to facilitate the process of verification by providing a reliable way to reproduce error and order of accuracy results from numerical solutions. In addition to grid refinement study capabilities, VIVID can utilize a variety of verification problem results, when they are available, to determine the level of error between the numerical solution and the verification results. The VIVID tool is continuously being updated to include more verification problem results.

A documentation plan is in development to define requirements for verification data, simulation, and comparison documentation.

## 2. SPECIES DIFFUSION

<b>Dimension:</b>	3D
<b>Transient/Steady:</b>	steady
<b>Laminar/Turbulent:</b>	laminar
<b>Isothermal/Thermal:</b>	isothermal
<b>Temperature/Enthalpy:</b>	no
<b>Uniform/Nonuniform:</b>	uniform
<b>Combustion:</b>	no
<b>Soot:</b>	no
<b>Coupled Mechanics:</b>	no
<b>Regression Test:</b>	fuego/species_diffusionA fuego/species_diffusionB fuego/species_diffusionC

This problem is used to verify the species conservation equations. The problem consists of the ordinary diffusion of a three-component gas mixture in a stagnant gas layer next to a wall where a steady state has been obtained.

The computational domain is a 1 cm square geometry with a thickness of 0.05 cm in the  $z$ -direction. The 1-D diffusion of species occurs in the  $y$ -direction. Symmetry planes are placed along the boundaries in the  $x$ -direction as well as in the  $z$ -direction.

The turbulence mechanics in Fuego is used for this problem with the turbulence terms set to zero. A constant mass diffusivity is specified and is independent of the turbulent viscosity which is initialized to zero.

The species diffusion problem has shown that the species conservation equations produce the correct answer. In addition, the Fuego solutions were independent of the grid size. Therefore, it was not possible to perform the order of accuracy calculations, given that the Richardson extrapolation method fails when the discretization error is zero. Overall, the Fuego solutions matched the analytical solution exactly.

### 2.1. MATERIAL SPECIFICATIONS

There are three species used in the Fuego simulation, O, O<sub>2</sub> and N<sub>2</sub>. The material properties in Fuego were determined with Chemkin using a reference pressure of 1 atm, a reference temperature of 2000 K, O mass fraction of 0.0, O<sub>2</sub> mass fraction of 0.2, and N<sub>2</sub> mass fraction of 0.8. A constant mass diffusivity of 0.054704 was specified instead of a turbulent Schmidt number.

## 2.2. INITIAL CONDITIONS

The initial conditions used in the Fuego simulation set up a mixture with mass fractions of  $O=0.55$ ,  $O_2=0.30$ , and  $N_2=0.15$ . The turbulence quantities were set to small values,  $1.0e-20$  for turbulent kinetic energy and  $1.0e-10$  for turbulent dissipation, in order to initialize the turbulent viscosity to zero. The flow velocities are zero in this problem.

## 2.3. BOUNDARY CONDITIONS

Along the  $y$ -boundaries, wall boundary conditions are specified with mass fractions of  $O=0.55$ ,  $O_2=0.30$ , and  $N_2=0.15$  at the lower wall and  $O=0.0$ ,  $O_2=0.85$ ,  $N_2=0.15$  at the upper wall. In addition, fixed boundary conditions with zero values of the  $x$ ,  $y$ , and  $z$ -components of velocity are specified at both  $y$ -boundaries. Since Fuego is a 3-D code, symmetry conditions were specified in the  $x$ -direction and in the  $z$ -direction to simulate a 1-D problem.

## 2.4. ANALYTICAL OR BENCHMARK SOLUTIONS

The species diffusion problem is an extension of Example 18.5-5 in Bird, Stewart, and Lightfoot [2]. This problem has an analytical solution with no singularities within the computational domain and has reasonable physical boundary conditions. The problem consists of the ordinary diffusion of a three-component gas mixture in a stagnant gas layer next to the wall where a steady state has been obtained. In Figure 2.7-1, Species A ( $O$  in this case) is diffusing in the  $y$ -direction through a layer of stagnant gas species B ( $N_2$  in this case) to a catalytic wall where species  $A_n$  ( $O_2$  in this case) is formed and diffusing away from the wall. It is assumed that the temperature and pressure are constant in the layer and there are no homogeneous chemical reactions.

The flow solution for this problem was developed in a memo by Blottner and Lopez [3]. A summary of the solution is included in this document. The pressure, temperature, species molecular weight, and density across the layer are as follows:

$$\begin{aligned} p &= p_0 & T &= T_0 & \eta &= y/\delta & 0 \leq \eta \leq 1 \\ \tilde{Y}_A &= -\frac{F_0}{N} + \left( \tilde{Y}_{A0} + \frac{F_0}{N} \right) e^{-\nu N \eta} & Y_B &= Y_{B0} & Y_{A_n} &= 1 - Y_A - Y_B \\ \frac{1}{\tilde{M}} &= \frac{N \tilde{Y}_A + F_0}{\tilde{M}_A} & \rho &= c \tilde{M} & c &= p_0 / (R_u T_0) \end{aligned} \tag{2.1}$$

The parameters in the above species are determined from:

$$\begin{aligned}
N &= 1 - 1/n \\
F_0 &= \left( \frac{\tilde{M}_A}{\tilde{M}_B} - \frac{1}{n} \right) \tilde{Y}_{B0} + \frac{1}{n} \\
\nu &= -\frac{1}{N} \ln \left[ \frac{(F_0/N)}{\tilde{Y}_{A0} + (F_0/N)} \right]
\end{aligned}$$

The mass flux of the species is constant across the layer and the remaining unknowns in the equations are code input quantities.

In addition, the VIVID code was going to be used to calculate the order of accuracy from the Fuego solutions; however, the Fuego solutions were not sensitive to the grid size, even though the solution was of exponential form, and so Richardson extrapolation method is not applicable. Therefore, the results are only compared to the analytical solution for this problem.

## 2.5. MESH DEFINITION

The species diffusion problem was simulated with the Fuego code on three different uniform meshes: coarse (10x10x2) with 100 elements; medium (21x21x2) with 400 elements; and fine (41x41x2) with 1600 elements.

The uniform meshes contained hexagonal elements. Equal spacing was specified in the all coordinate directions. The medium and coarse meshes were created by removing every other grid point such that the meshes contain co-located grid points.

## 2.6. SOLUTION PROCEDURE

Options selected in the Fuego run were: time step = 10.0; projection method = stabilized; upwind method = upw; first order upwind factor = 0.0; underrelaxation factors = 1.0 for turbulent viscosity and 0.0 for all other variables; linear residual tolerances for continuity equation = 1.0e-5, flow and scalar equations = 1.0e-4, and k and  $\epsilon$  equations = 2.0; nonlinear residual tolerances = 1.0e-20 for all equations; and nonlinear iteration = 1.

Each simulation was run until a steady state solution was obtained and all non-linear residuals were reduced below 1.0e-14, except for turbulent dissipation which was on the order of 1.0e-08. The calculations were performed using the turbulence mechanics in Fuego stable version 0.7.0 on a SUN computer platform. The turbulence terms were initialized to zero so that the turbulent viscosity would be zero. Using an underrelaxation value of 1, the turbulent viscosity remained zero for the entire calculation.

## 2.7. RESULTS

Figure 2.7-2 shows the variation of the O species across the gas layer for all three mesh solutions. The analytical solution (i.e., the black line) is also shown on this plot. All three Fuego solutions match the analytical solution exactly. The solutions show no dependence on the grid size, even though the analytical solution is of exponential form. As expected, the other two species matched the analytical solution exactly and are not shown here.

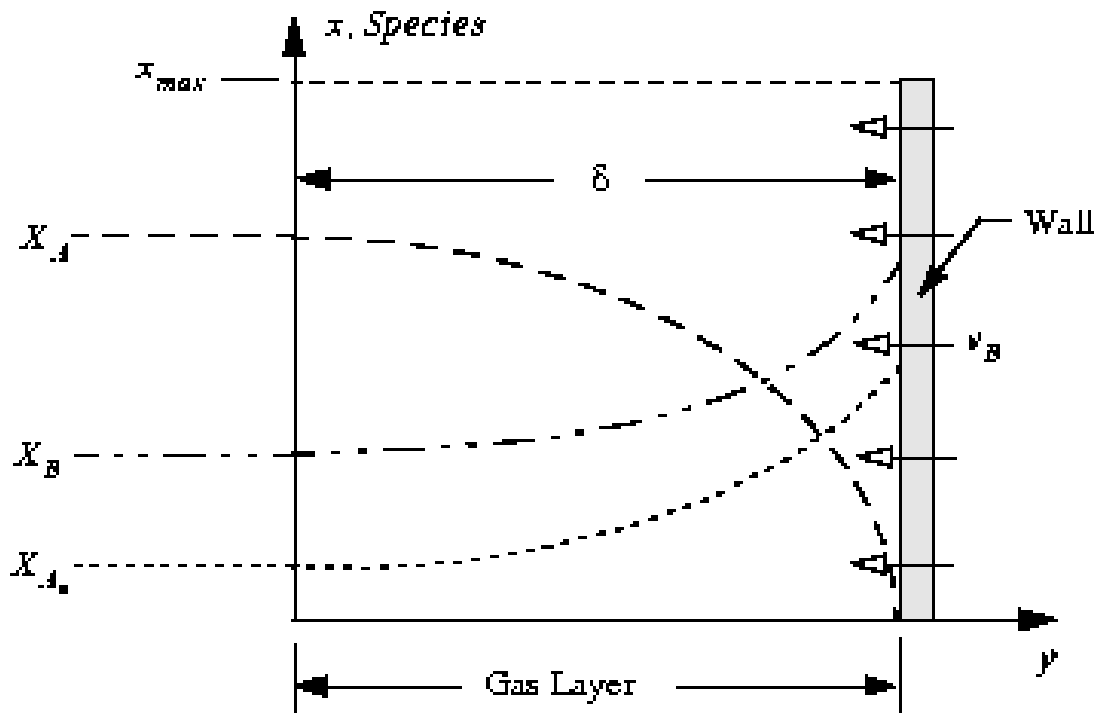


**Figure 2.7-1.. Geometry for species diffusion problem with and without mass transfer of species B at the wall**

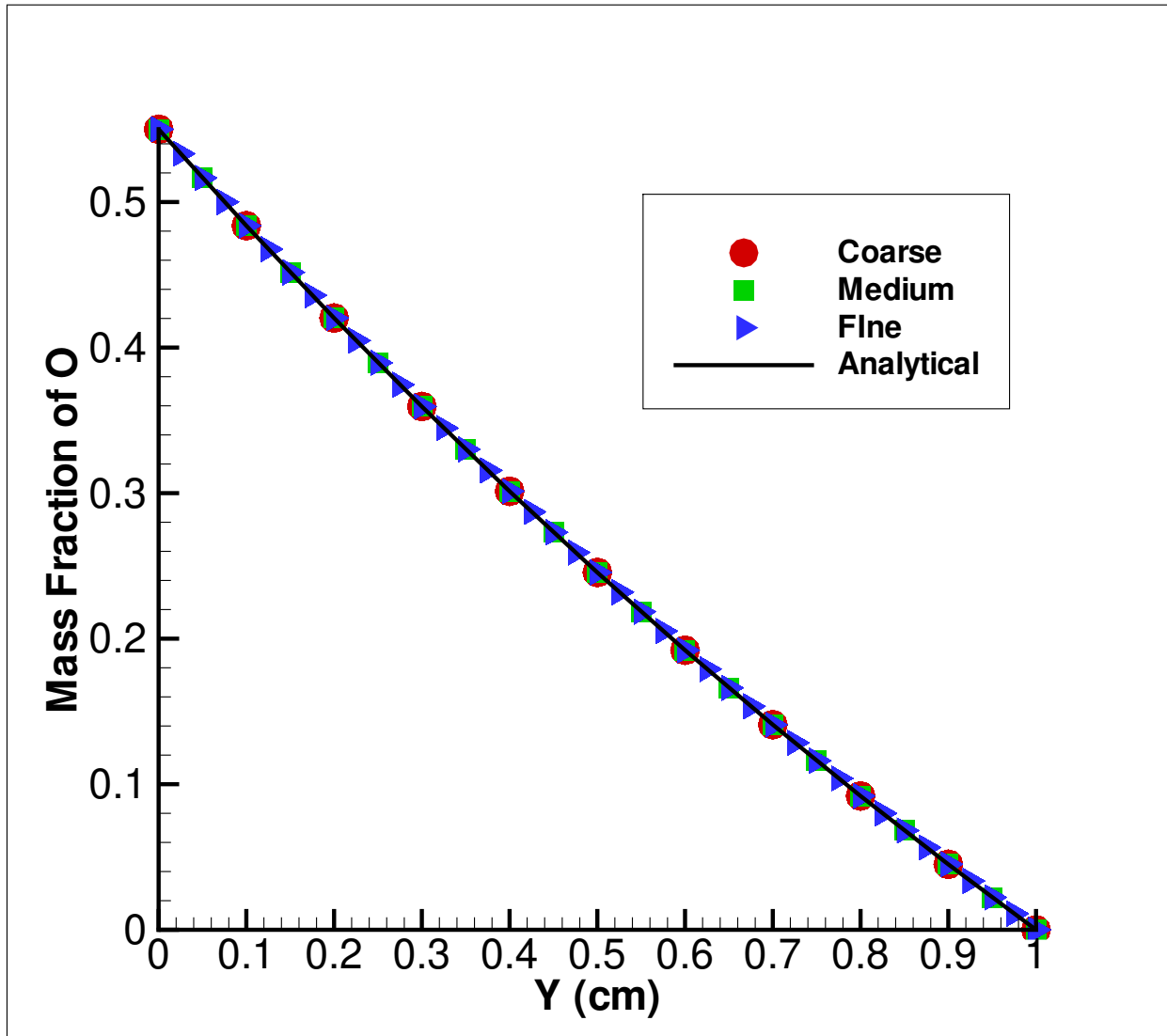


Figure 2.7-2.. Mass Fraction of O across layer

This page intentionally left blank.

### 3. LAMINAR, THERMALLY-DRIVEN BUOYANT PLUME

<b>Dimension:</b>	3D (quasi 2D)
<b>Transient/Steady:</b>	steady
<b>Laminar/Turbulent:</b>	laminar
<b>Isothermal/Thermal:</b>	thermal
<b>Temperature/Enthalpy:</b>	temperature and enthalpy
<b>Uniform/Nonuniform:</b>	uniform mixture
<b>Combustion:</b>	no
<b>Soot:</b>	no
<b>Coupled Mechanics:</b>	no
<b>Regression Test:</b>	fuego/thermal_plumeA_temp fuego/thermal_plumeB_temp fuego/thermal_plumeB_enth fuego/thermal_plumeC_temp fuego/thermal_plumeD_temp

An analytical solution for a thermal plume due to a line source is used as a verification problem. Yih (1977) gave a similarity solution, using boundary layer equations, for the buoyant plume above a line source. Since this solution is not based on the full Navier-Stokes equations, problem parameters have to be specified such that the full flow equations approximate the boundary layer equations. The purpose of this test is to verify energy transport with buoyancy body forces and open boundaries. The most appropriate equation set for this analytic solution is the laminar Navier-Stokes equations with a temperature transport equation. In order to achieve some degree of verification for the terms in the turbulent enthalpy transport equation set, results are included for both laminar enthalpy transport and turbulent enthalpy transport (with zero eddy viscosity).

The velocities and temperatures near the jet core visually converge towards the analytic solution as the mesh is refined. The solution does not converge to the boundary layer solution at the entrainment boundary and there is an additional velocity error at the outflow boundary. Error analysis relative to the exact boundary layer solution are inconclusive.

### 3.1. ANALYTIC OR BENCHMARK SOLUTION

Yih [4] presents similarity solutions for buoyant convection above a point source (Chapter 8, Section 7) and a line source (Chapter 8, Section 8). We consider the latter problem which is two-dimensional and planar. These solutions were first published by Yih [5] in 1952 (corrections in 1953 [6]). Apparently unaware of Yih's work, Brand and Lahey [7] reproduced the same solutions some 15 years later.

Yih found two similarity solutions in closed form for Prandtl numbers of 5/9 and 2. With reference to the coordinate system in Figure 3.1-1, the boundary layer equations are:

$$u \frac{\partial u}{\partial x} + v \frac{\partial u}{\partial y} = \nu \frac{\partial^2 u}{\partial y^2} - g \frac{\Delta \gamma}{\gamma_0}, \quad (3.1)$$

$$u \frac{\partial \Delta \gamma}{\partial x} + v \frac{\partial \Delta \gamma}{\partial y} = \alpha \frac{\partial^2 \Delta \gamma}{\partial y^2}, \quad (3.2)$$

$$\frac{\partial u}{\partial x} + \frac{\partial v}{\partial y} = 0, \quad (3.3)$$

where  $\gamma = \rho g$  is the specific weight. In this problem, it is assumed that the temperature variations are small enough to approximate physical properties as constant. Use of the ideal gas law gives the following relation between specific weight and temperature:

$$\frac{\Delta T}{T_0} = - \frac{\Delta \gamma}{\gamma_0}, \quad (3.4)$$

where  $T_0$  is the ambient temperature,  $\gamma_0$  the corresponding specific weight,  $\Delta T = T - T_0$ , and  $\Delta \gamma = \gamma - \gamma_0$ . The boundary conditions for the problem are:

$$v = \frac{\partial u}{\partial y} = \frac{\partial \Delta \gamma}{\partial y} = 0, \quad \text{for } y = 0, \quad (3.5)$$

$$u = \Delta \gamma = 0, \quad \text{for } y \rightarrow \pm\infty. \quad (3.6)$$

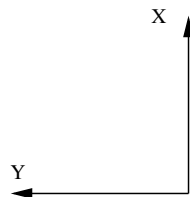


**Figure 3.1-1.. Coordinate system for laminar buoyant plume similarity solution.**

There is an integral quantity which should be independent of  $x$ , namely a measure of the strength of the line source,

$$G = - \int_{-\infty}^{\infty} u \Delta \gamma dy. \quad (3.7)$$

The thermal energy of the source, per unit length, is given in terms of  $G$  as

$$Q = \frac{GC_p T_0}{g}. \quad (3.8)$$

The similarity variable found by Yih is,

$$\xi = \frac{1}{5} \left( \frac{\rho^2 G}{\mu^3 x^2} \right)^{\frac{1}{5}} y, \quad (3.9)$$

and the corresponding similarity solution is sought in terms of the stream function and specific weight

$$\left( \frac{\rho^3}{G \mu^2 x^3} \right)^{\frac{1}{5}} \psi = f(\xi), \quad (3.10)$$

$$\left( \frac{\mu^2 x^3}{G^4 \rho^3} \right)^{\frac{1}{5}} \Delta \gamma = -\frac{1}{125} \theta(\xi), \quad (3.11)$$

which results in the similarity solution

$$f(\xi) = A \tanh(B\xi), \quad (3.12)$$

$$\theta(\xi) = C \operatorname{sech}^n(B\xi). \quad (3.13)$$

The constants are given in Table 3.1-1 for the two values of Prandtl number which admit similarity. The velocity components can be computed from the stream function,  $\psi$ , resulting in

$$5 \left( \frac{\rho \mu}{G^2 x} \right)^{\frac{1}{5}} u = f' = AB \operatorname{sech}^2(B\xi), \quad (3.14)$$

$$5 \left( \frac{\rho^3 x^2}{G \mu^2} \right)^{\frac{1}{5}} v = 2\xi f' - 3f. \quad (3.15)$$

The temperature is given by substituting from Equation 3.4 into Equation 3.11.

**Table 3.1-1.. Constants in thermal plume similarity solution for two Prandtl numbers (Pr).**

Pr	$n$	$A$	$B$	$C$
5/9	2	$(405/8)^{1/5}$	$5A/6$	$50A^4/27$
2	4	$5/(240)^{1/5}$	$3A/2$	$9A^4$

Several assumptions were made at the outset in order to arrive at this analytical solution. In order to use the solution as a benchmark against the full Navier-Stokes equations, the parameters governing the motion must be specified so that the approximations embodied in the analytical solution are closely approximated in the full equations. One of the major assumptions was that the motion can be described by the boundary layer approximation to the full equations.

This requires that the flow Reynolds (Re) and Rayleigh (Ra) numbers be large compared to unity ( $Re \gg 1, Ra \gg 1$ ). There is no intrinsic length scale in the thermal plume problem. However, a (somewhat artificial) length scale can be defined by considering the solution in a region above the source, i.e., by introducing a virtual origin for the line source location at some position beneath the computational region. In this interpretation of Yih's solution for the upper half plane, one considers the solution in a truncated computational domain as a combined thermal/momentum jet in the region above the source. The lower boundary conditions for the computed problem will be specified by the similarity solution values on some plane above the line source. These conditions take the form of a heated jet at the lower boundary of the computational region. This introduces a length scale for the width of the jet. The idea then is to determine values of the virtual origin,  $x_0$ , and the width of the jet,  $2h$ , consistent with the boundary layer equations.

The volume flux through the plume depends on elevation, and can be computed using the expressions for the vertical velocity with the result,

$$U = \int_{-\infty}^{\infty} u dy = 2A \left( \frac{Gx^3 \mu^2}{\rho^3} \right)^{\frac{1}{5}}. \quad (3.16)$$

The Reynolds number at any elevation can then be defined by

$$Re = \frac{\rho U}{2\mu} = A \left( \frac{\rho^2 G x^3}{\mu^3} \right)^{\frac{1}{5}}. \quad (3.17)$$

The definition of the width of the jet is somewhat arbitrary. We define it, for a given elevation, as the lateral dimension where the vertical velocity component is some small fraction,  $\epsilon$ , of the centerline velocity,

$$\epsilon = \frac{f'(\xi(h))}{f'(0)}, \quad (3.18)$$

which leads to

$$h = \frac{5E}{B} \left( \frac{x^2 \mu^3}{\rho^2 G} \right)^{\frac{1}{5}}, \quad (3.19)$$

$$E = \text{acosh}(\epsilon^{-1/2}). \quad (3.20)$$

The Rayleigh number is defined with respect to this length scale and in terms of the source strength,

$$Ra = \frac{GC_p h^3}{\alpha \nu \kappa} = \frac{g \beta Q h^3}{\alpha \nu \kappa}. \quad (3.21)$$

Using the definition of the jet half-width and comparing to the definition of the Reynolds number, we find a definite relationship between the Rayleigh number, Reynolds number and the Prandtl number,

$$\frac{Ra}{(RePr)^2} = \left( \frac{5E}{B} \right)^3 \frac{1}{A^2}. \quad (3.22)$$

Thus, we now have expressions for  $G$  and the virtual origin,  $x_0$ , as functions of the jet half-width,  $h$ , and key dimensionless numbers,

$$G = \rho \left( \frac{\alpha}{h} \right)^3 \text{RaPr}, \quad (3.23)$$

$$x_0 = \rho \left( \frac{G}{\mu^3} \right)^{\frac{1}{2}} \left( \frac{Bh}{5E} \right)^{\frac{5}{2}}. \quad (3.24)$$

These formulae allow us to specify  $\text{Re}$  (and therefore  $\text{Ra}$  via Equation 3.22) and  $h$  and compute the corresponding source strength and virtual origin such that the assumptions made in the similarity solution should be met by the Navier-Stokes solution for these parameters. The Prandtl number is restricted to either  $5/9$  or  $2$  in order to admit a self-similar solution that is analytic rather than numeric.

## 3.2. MESH DEFINITION

There are four three-dimensional meshes with uniform, hexahedral elements. There is only one element in the  $z$ -direction since the  $z$ -planes act as symmetry planes to achieve two-dimensionality. The  $x$  and  $y$ -dimensions are the same in each mesh, 20 units by 20 units. The  $z$ -depth is 0.25 units. (Note that the coordinate system for the mesh is different from the derivation of the boundary layer solution.) Mesh A is  $20 \times 20 \times 1$  elements, mesh B is  $40 \times 40 \times 1$  elements, mesh C is  $80 \times 80 \times 1$  elements, and mesh D is  $160 \times 160 \times 1$  elements. The  $x$  and  $y$ -planes of the mesh each have a side-set defined for a total of four. The element faces of the two  $z$ -planes make up the fifth side-set.

## 3.3. MATERIAL SPECIFICATIONS

The material property specifications are different between the temperature transport set and the enthalpy transport set.

### 3.3.1. Material Specifications for Temperature Transport

The material properties are constant for the temperature transport equation. The units are unimportant as long as they are consistent. The density is 1.0, the viscosity is 1.0, the specific heat is 1.0, and the thermal conductivity is 0.5. The Prandtl number is 2.0. The gravitational acceleration is 1.0. The buoyancy body force is approximated using the Boussinesq approximation and the thermal volumetric expansion parameter is 1.0. The reference temperature is 1.0.

### 3.3.2. Material Specifications for Enthalpy Transport

The enthalpy/temperature relationship is evaluated using the Chemkin libraries when solving the enthalpy transport equation. The units are cgs. The density and viscosity from Chemkin are overwritten with constant values of density=0.001 g/cm<sup>3</sup> and viscosity=0.001 g/cm/s. The thermal conductivity is evaluated from a constant Prandtl number relationship, where the Prandtl number is 2.0 and the specific heat is a function of temperature. The enthalpy and specific heat correspond to nitrogen gas. The thermodynamic reference pressure is 1 atm. The gravitational acceleration is 981. The buoyancy body force is approximated using the Boussinesq approximation and the thermal volumetric expansion parameter is 1/300. The reference temperature is 300 K.

## 3.4. INITIAL CONDITIONS

The velocities and temperature are initialized to the inflow profiles. The inflow profiles are specified as a function of the lateral coordinate. The inflow functions are applied at every node. The pressure is zero.

## 3.5. BOUNDARY CONDITIONS

The boundary conditions are applied over five side-sets. Note that the coordinate system for the mesh is different from the derivation of the boundary layer solution. In the mesh, the vertical direction is along the y-axis and the horizontal is along the x-axis. The analytic solution is derived in a coordinate system rotated by 90 degrees (see Figure 3.1-1). The bottom plane at y=0 is the inflow boundary. The analytic velocities and temperature are enforced at the nodes of the inflow side-set using Dirichlet conditions. The x=0 plane is a symmetry plane since the solution is symmetric about the vertical centerline. The x=xmax plane is the entrainment plane. The pressure is specified as zero and the flow is required to enter the domain normal to the boundary. There is no shear velocity specified since the vertical velocity is negligible that far from the plume. The temperature is entrained at the reference conditions used in the buoyancy model. The y=y<sub>max</sub> plane is the outflow plane. It is applied in the same manner as the entrainment plane. Additionally, the “OMIT DIFFUSION TERMS” command is required at the outflow boundary in order to get a converged steady-state solution. If the diffusion terms are retained on the outflow boundary, the outflow velocities tend to oscillate and the nonlinear residuals hang up. The horizontal velocity will also behave strangely. The z=0 and z=z<sub>max</sub> planes make up the fifth side-set. These boundary conditions are applied as symmetry planes to make the flow quasi-two-dimensional.

## 3.6. SOLUTION PROCEDURE

The equations are time-marched to steady state with an adaptive time step. The time steps adapt to a fixed maximum CFL number of 5.0. The projection method is the “stabilized method” with no under-relaxation.

The linearized continuity equation is solved with the stabilized biconjugate gradient method with two steps of symmetric Gauss-Seidel preconditioning. The linear residuals are reduced by six orders of magnitude at each solve. The linearized momentum equations are solved with the GMRES method with three steps of Jacobi preconditioning. The GMRES method is restarted after 50 iterations. The linear residuals are reduced four orders of magnitude at each solve. Dirichlet boundary conditions are enforced exactly. The linearized temperature equation is solved with the GMRES method with three steps of symmetric Gauss-Seidel preconditioning. The GMRES method is restarted after 50 iterations. The linear residuals are reduced four orders of magnitude at each solve. Dirichlet boundary conditions are enforced exactly. The linearized enthalpy equations are solved in the same manner as the temperature equation.

The temperature equation results are solved using the stable version Fuego-0.07. The enthalpy equation results are solved using the development version Fuego-0.8.0, built on October 30, 2002. The development version was required since changes were required to the material property model in order to achieve the combination: constant density and viscosity, Chemkin for enthalpy and specific heat, and conductivity derived from constant-Prandtl number.

## 3.7. VERIFICATION EXPERIMENTS

Verification tests are performed for both the temperature transport equation and the enthalpy transport equation. Ideally, we would like to use the analytic solution to verify the terms in the turbulent form of the enthalpy equation. A comparison is made between solutions from the laminar enthalpy equation and the turbulent enthalpy equation with zero eddy viscosity. The two equations differ in the form of the conduction term. In all cases, the temperature and enthalpy equation results exhibit similar behavior. Variations of the laminar temperature solutions are tested with rotated meshes since the problem is quasi-two-dimensional.

### 3.7.1. Temperature Transport Equation, Ra=30500

The buoyant plume problem was run with a temperature transport equation for  $Pr=2$ , half-width=5, and  $Re=10$ . This corresponds to  $G=61.03$ ,  $Ra=30512$ ,  $B=2.506$ ,  $E=2.993$ , and  $x_o = 5.011$ . Recall that  $\rho = C_p = \mu = 1$  and  $\alpha = 1/2$ . The centerline temperature, Figures 3.7-1 and 3.7-2, and centerline vertical velocity, Figures 3.7-3 and 3.7-4, track the analytic solution as the mesh is refined. The horizontal profiles of temperature and vertical velocity are nearly indistinguishable for all meshes. The maximum cell Reynolds number is 8 for the coarse 20x20 mesh and 1 for the fine 160x160 mesh.

The horizontal velocity profiles show quite a variation relative to the boundary layer solution. The horizontal velocity profiles are given in Figures 3.7-5 and 3.7-6 at the elevations 5 and 15 relative to the inflow plane (which is 5.011 above the virtual origin). The velocity entrainment is sensitive to stress imbalances at the open boundary.

The solutions are benchmarked against the ANSWER code from ACRI on the 40x40 mesh. The ANSWER code is cell-centered so the line data tends to be shifted from Fuego results by half a cell, 0.25. The centerline temperature and vertical velocity show excellent agreement with the boundary layer

**Table 3.7-1.. Error norms for Test 1 (temperature equation) with hybrid MUSCL scheme. Errors are relative to the boundary layer solution.**

	$\Delta$	U	V	T
$L_\infty$	1.0	5.29380e-01	4.46982e-01	3.52309e-01
	0.5	5.89191e-01	1.73656e-01	1.40779e-01
	0.25	5.72436e-01	1.18592e-01	4.75744e-02
	0.125	5.23681e-01	9.95817e-02	1.95432e-02
$L_1$	1.0	3.19369e-02	2.87470e-02	1.55478e-02
	0.5	2.80297e-02	1.60238e-02	5.78172e-03
	0.25	2.60901e-02	1.26686e-02	2.51902e-03
	0.125	2.48066e-02	1.16534e-02	1.66113e-03
$L_2$	1.0	6.13831e-02	6.68071e-02	5.23133e-02
	0.5	5.35646e-02	3.05998e-02	1.71945e-02
	0.25	4.69177e-02	2.10837e-02	6.51889e-03
	0.125	4.22045e-02	1.84903e-02	3.90933e-03

solution. They look shifted from the Fuego solutions, but the ANSWER solutions are really along the vertical line at  $x=0.25$ . The inflow temperature falls by 0.25 in moving to  $x=0.25$  at the inflow. The horizontal velocities do not match the boundary layer solution, just as Fuego. It is interesting to note that the ANSWER solution is shifted in the opposite direction from the analytic solution relative to Fuego. In this case, the fact that the horizontal lines are 0.25 off from those for Fuego is irrelevant since the solution does not change that fast.

The solutions were converged to nonlinear residual norms ( $L_2$ ) of  $10^{-10}$  or less. A typical convergence history is shown in Figure 3.7-7. If the “OMIT DIFFUSION TERMS” command is not specified for the outflow boundary, then the nonlinear residuals hang at about  $10^{-5}$  and the horizontal velocities slowly oscillate in time.

The error behavior as a function of mesh resolution is shown in Table 3.7-1 for hybrid MUSCL upwinding and Table 3.7-2 for hybrid first-order upwinding. The errors are computed relative to the boundary layer solution. The temperature equation shows a first-order error behavior as the mesh is refined with both the hybrid upwind schemes. The error norm for the horizontal velocity equation shows no convergence. There seems to be an imbalance at the outflow boundary that interacts with the overall entrainment velocity as well as poor entrainment values. The error norm for the vertical velocity does reduce, but it seems to be strongly influenced by the other velocity component. The locations of the maximum nodal residuals for velocity tend to be along the outflow boundary. Color contours of the horizontal velocity are shown in Figure 3.7-8 with superimposed streamlines. There is a horizontal flow reversal near the jet core at the outflow boundary. Velocity vectors for the outflow boundary are shown in Figure 3.7-9. (Further sensitivity studies of the entrainment velocities as a function of boundary condition parameters are given in Chapter 21.)

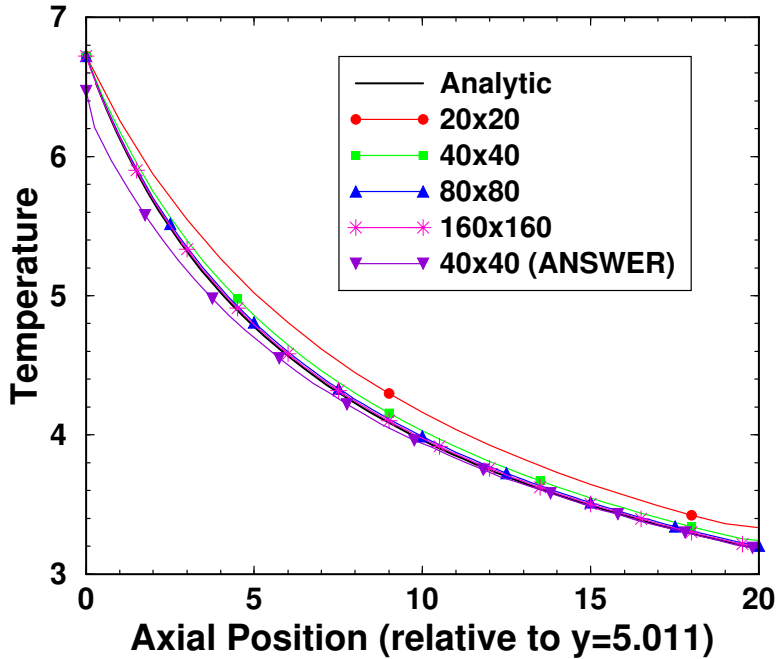


**Figure 3.7-1.. Centerline temperature for the laminar, buoyant plume with hybrid first-order upwinding. Temperature equation with  $\text{Pr}=2$ ,  $\text{Re}=10$ ,  $\text{Ra}=30500$ . Additional benchmark with cell-centered ANSWER code,  $x=0.25$ .**

### 3.7.2. Mesh Rotations

The verification problem is run in three additional coordinate system orientations since it is a quasi-two-dimensional geometry. The first rotated system only involves a 90 degree, counter-clockwise rotation about its x-axis. The vertical direction switches from the y-direction to the z-direction. The second rotated system involves a 90 degree clockwise rotation about the y-axis. The horizontal direction is now in the z-direction. The third rotated system involves two rotations. First, the mesh is rotated 90 degrees in the clockwise direction about its y-axis. The mesh is then rotated 90 degrees counter-clockwise about its z-axis. The vertical direction is now in the negative x-direction and the horizontal direction is in the z-direction. The three problems were run with the  $40 \times 40 \times 1$  mesh,  $\text{Pr}=2$ ,  $\text{Re}=10$ , and  $\text{Ra}=30500$  with the temperature equation. The temperature and velocity components along a horizontal line, 15 units from the inflow, all match the solution on the base mesh to within the accuracy of the rotations (single-precision).

### 3.7.3. Enthalpy Transport Equation, $\text{Ra}=30500$

The buoyant plume problem was run with an enthalpy transport equation for  $\text{Pr}=2$ ,  $\text{half-width}=5$ , and  $\text{Re}=10$ . This corresponds to  $G=0.06103$ ,  $\text{Ra}=30512$ ,  $B=2.506$ ,  $E=2.993$ , and  $x_o = 5.011$ . Additionally, a result is provided for the turbulent transport equations with a zero eddy viscosity. The zero eddy

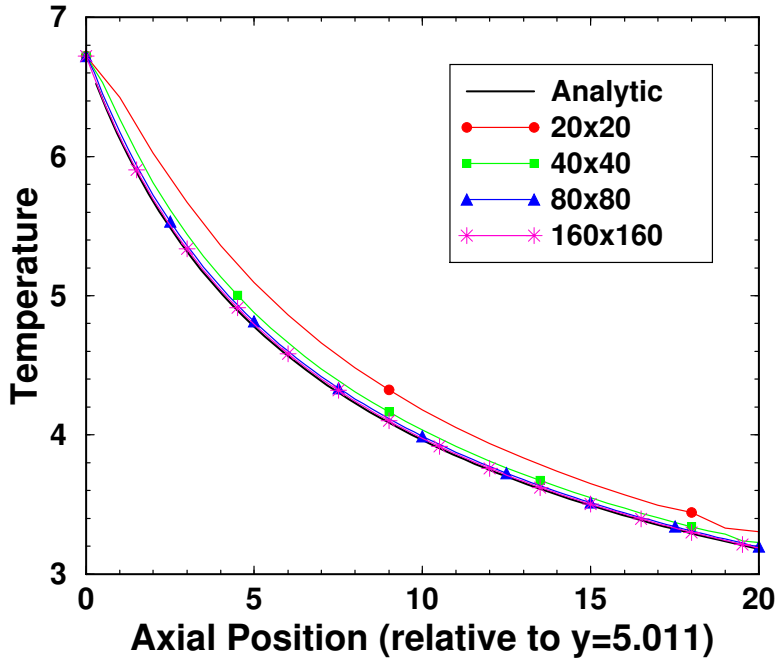


**Figure 3.7-2.. Centerline temperature for the laminar, buoyant plume with hybrid MUSCL upwinding. Temperature equation with  $\text{Pr}=2$ ,  $\text{Re}=10$ ,  $\text{Ra}=30500$ .**

viscosity is achieved by setting initial values of  $k = 10^{-15}$ ,  $\epsilon = 10^{-9}$ ,  $\text{Pr}_t = 10^{12}$ , and an explicit relaxation parameter of 0.0 for the turbulence model equations.

In general, the behavior of the enthalpy transport equation set is similar to the temperature transport equation set. The centerline temperature is shown in Figure 3.7-10 for the laminar enthalpy equation on three meshes as well as the turbulent enthalpy equation on the medium mesh (40x40). The solutions for the laminar and turbulent forms do not agree in temperature because of the difference in the form of the conduction term. The horizontal velocities at 15 cm past the inflow plane are shown in Figure 3.7-11.

### 3.7.4. Temperature Transport Equation, $\text{Ra}=85000$

For the case of  $\text{Pr}=2$ ,  $\text{Re}=16.7$ ,  $\text{Ra}=85000$ , and  $G=61$ , the centerline temperature and velocity are shown in Figure 3.7-12. Horizontal profiles of the temperature at four different vertical stations are shown in Figure 3.7-13. The largest cell Reynolds number value is 3 so the centered convection scheme is predominant and there is negligible difference between the hybrid first-order upwind scheme and a pure second-order scheme. The solution does not change upon refining the mesh. A small non-physical recirculation occurs where the top and entrainment boundaries meet.

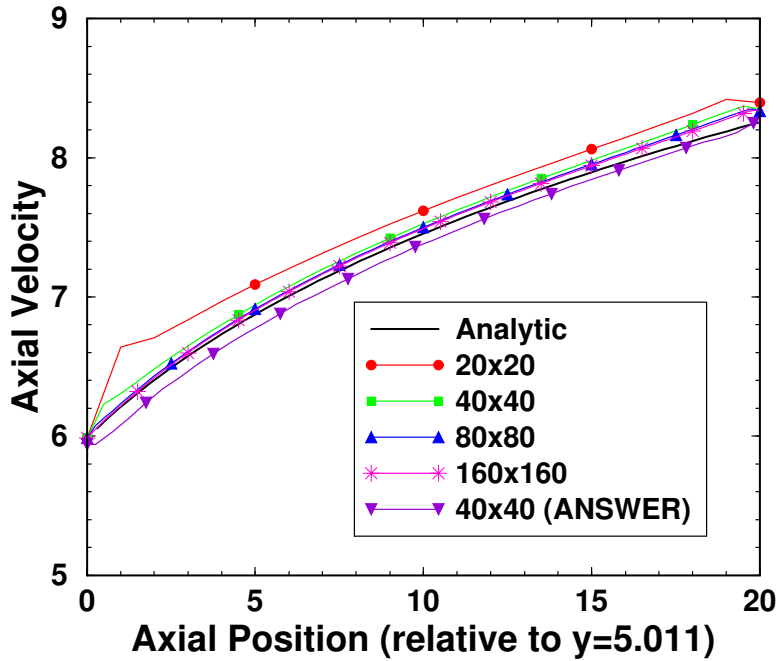


Figure 3.7-3.. Centerline vertical velocity for the laminar, buoyant plume with hybrid first-order upwinding. Temperature equation with  $\text{Pr}=2$ ,  $\text{Re}=10$ ,  $\text{Ra}=30500$ . Additional benchmark with cell-centered ANSWER code,  $x=0.25$ .

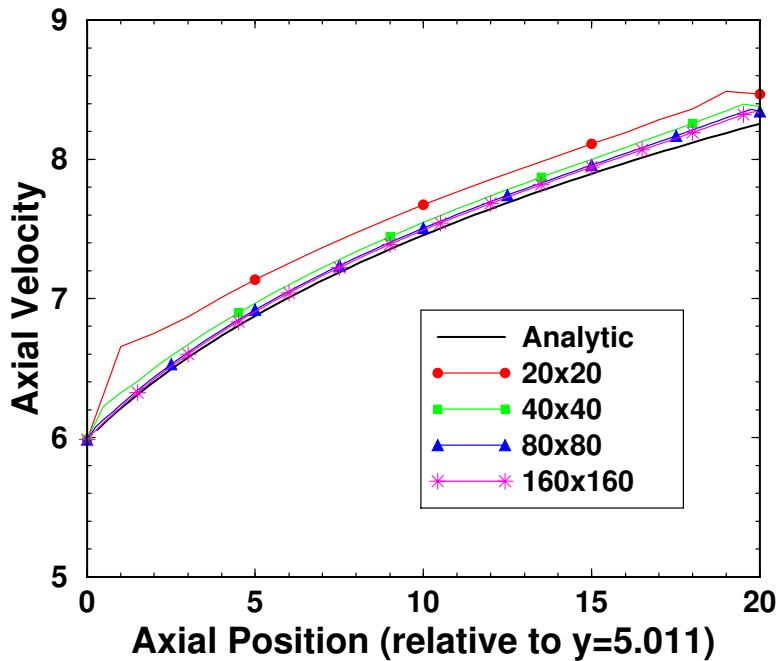
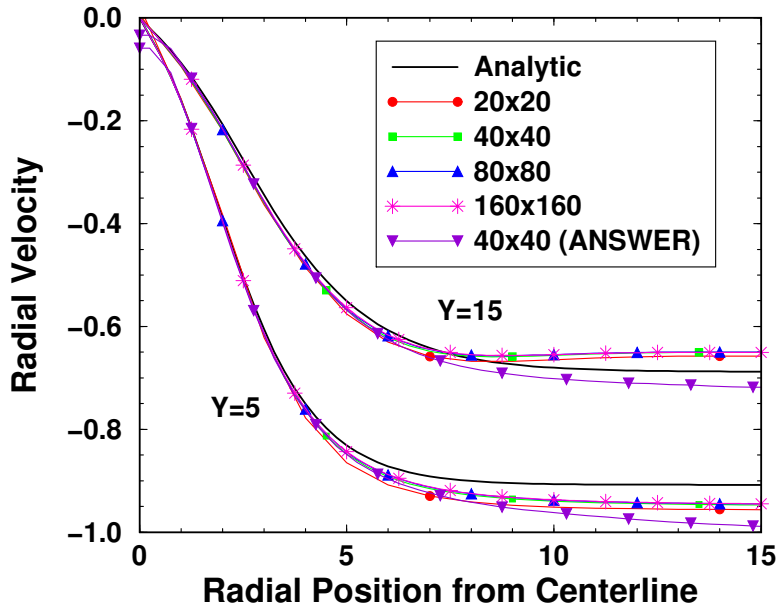
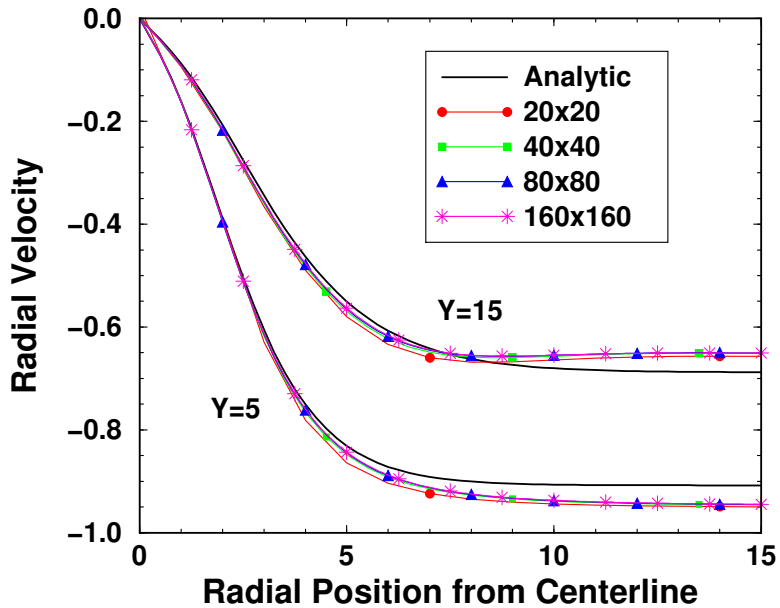


Figure 3.7-4.. Centerline vertical velocity for the laminar, buoyant plume with hybrid MUSCL upwinding. Temperature equation with  $\text{Pr}=2$ ,  $\text{Re}=10$ ,  $\text{Ra}=30500$ .



**Figure 3.7-5..** Horizontal velocity for the laminar, buoyant plume with hybrid first-order upwinding. Horizontal cuts at  $y=5$  and  $y=15$  relative to the inflow plane. Temperature equation with  $Pr=2$ ,  $Re=10$ ,  $Ra=30500$ . Additional benchmark with cell-centered ANSWER code,  $y=4.75$  and  $y=14.75$ .



**Figure 3.7-6..** Horizontal velocity for the laminar, buoyant plume with hybrid MUSCL upwinding. Horizontal cuts at  $y=5$  and  $y=15$  relative to the inflow plane. Temperature equation with  $Pr=2$ ,  $Re=10$ ,  $Ra=30500$ .

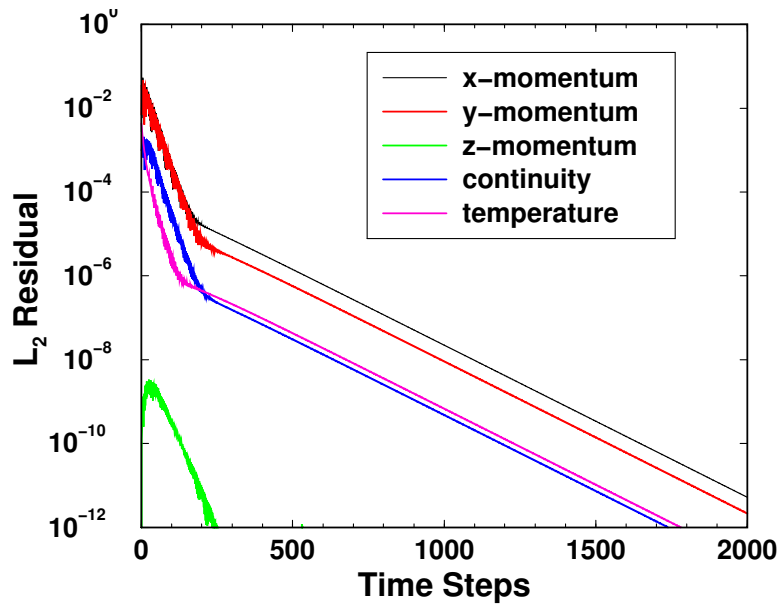


**Figure 3.7-7.. Nonlinear convergence for the 80x80 mesh, temperature equation.**

**Table 3.7-2.. Error norms for Test 1 (temperature equation) with hybrid first-order upwind scheme. Errors are relative to the boundary layer solution.**

	$\Delta$	U	V	T
$L_\infty$	1.0	5.40513e-01	4.31224e-01	2.43656e-01
	0.5	5.94183e-01	1.46283e-01	8.23834e-02
	0.25	5.73291e-01	1.12101e-01	3.14658e-02
	0.125	5.23882e-01	9.83572e-02	1.96103e-02
$L_1$	1.0	3.33501e-02	2.46857e-02	1.25595e-02
	0.5	2.82248e-02	1.49606e-02	4.64873e-03
	0.25	2.60829e-02	1.24171e-02	2.28129e-03
	0.125	2.48070e-02	1.16122e-02	1.64718e-03
$L_2$	1.0	6.37143e-02	5.47223e-02	4.18634e-02
	0.5	5.43105e-02	2.65467e-02	1.32591e-02
	0.25	4.70979e-02	2.03004e-02	5.61024e-03
	0.125	4.22387e-02	1.83907e-02	3.87271e-03

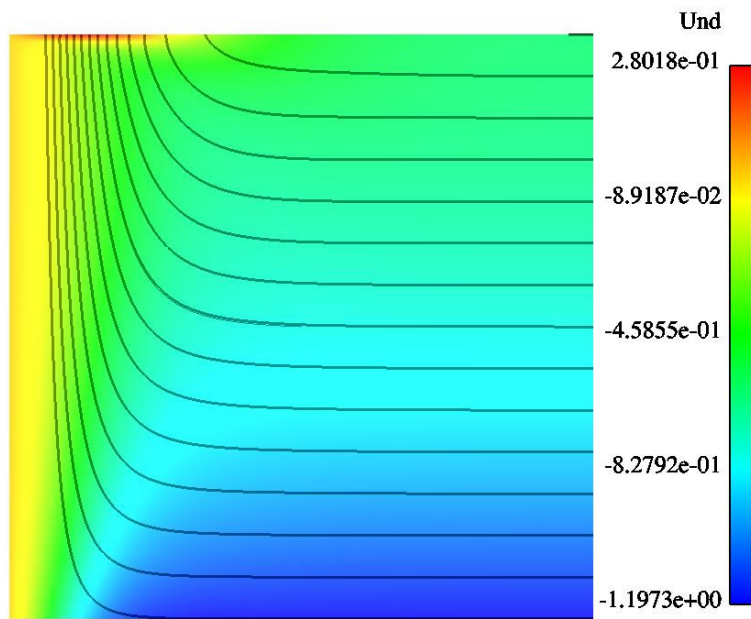


**Figure 3.7-8.. Horizontal velocity contours for  $Pr=2$ ,  $Re=10$ ,  $Ra=30500$ , temperature equation.**

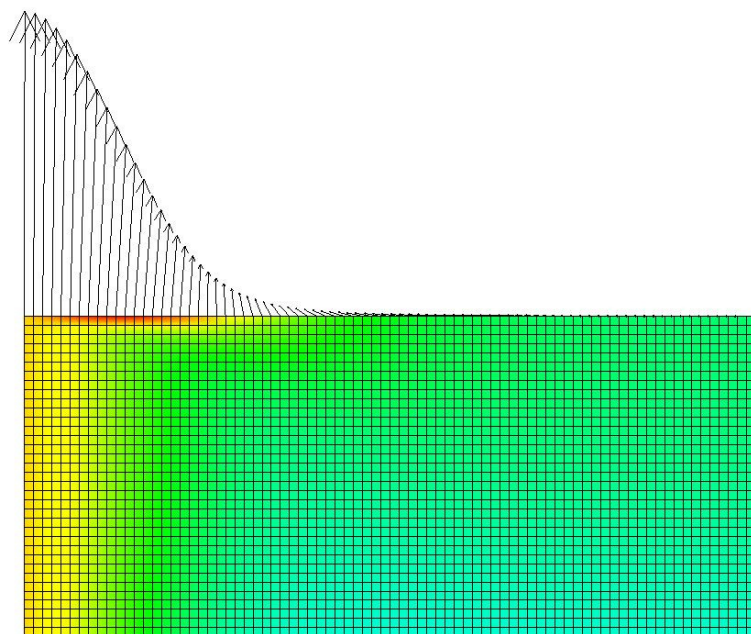


**Figure 3.7-9.. Horizontal velocity contours with outflow velocity vectors for  $Pr=2$ ,  $Re=10$ ,  $Ra=30500$ , temperature equation.**

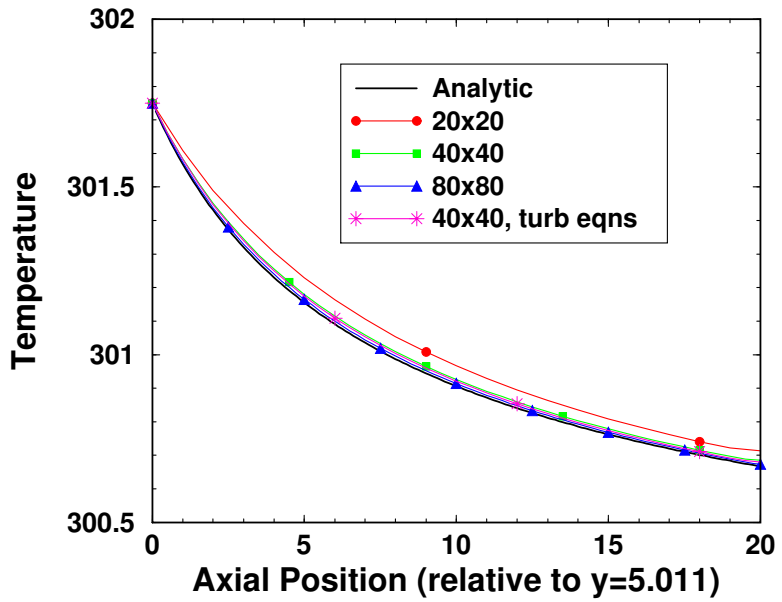


**Figure 3.7-10.. Centerline temperature for the laminar, buoyant plume with hybrid first-order upwinding. Enthalpy equation with  $\text{Pr}=2$ ,  $\text{Re}=10$ ,  $\text{Ra}=30500$ .**

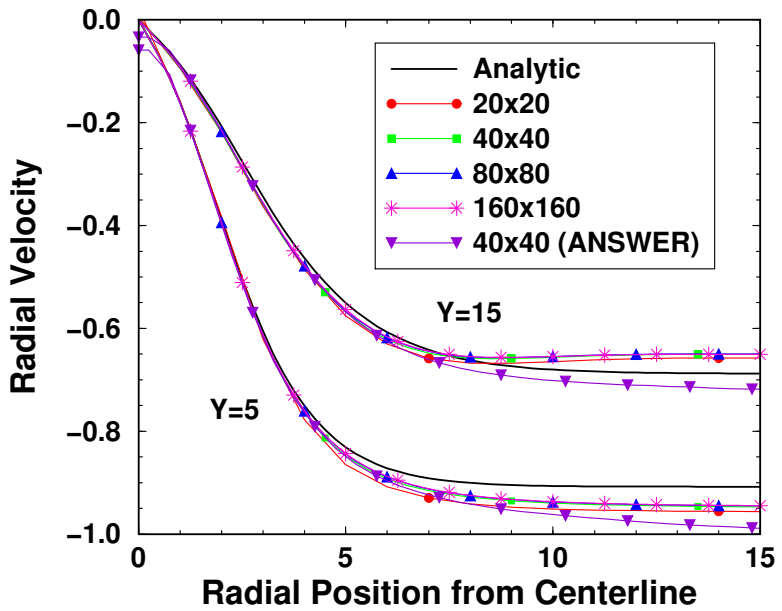


**Figure 3.7-11.. Horizontal velocity for the laminar, buoyant plume with hybrid first-order upwinding. Horizontal cut at  $y=15$  relative to the inflow plane. Enthalpy equation with  $\text{Pr}=2$ ,  $\text{Re}=10$ ,  $\text{Ra}=30500$ .**

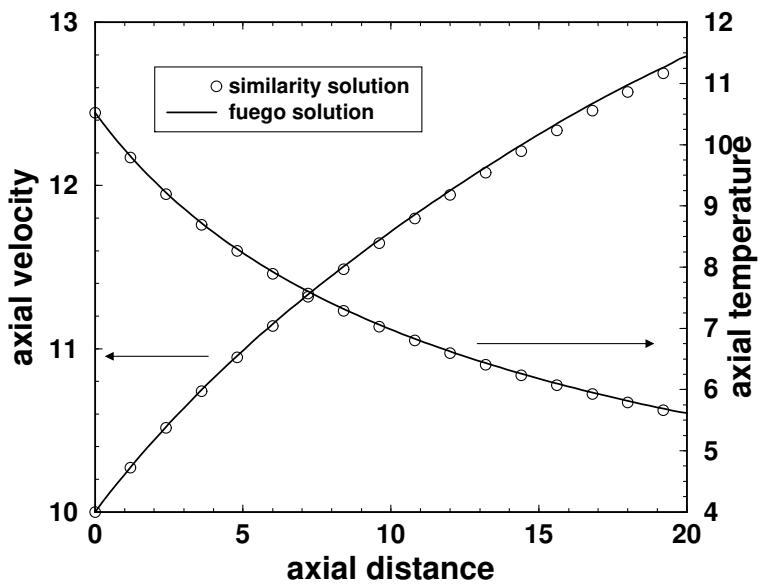


**Figure 3.7-12.. Centerline temperature and velocity for the laminar, buoyant plume. Temperature equation with  $Pr=2$ ,  $Re=16.7$ ,  $Ra=85000$ .**

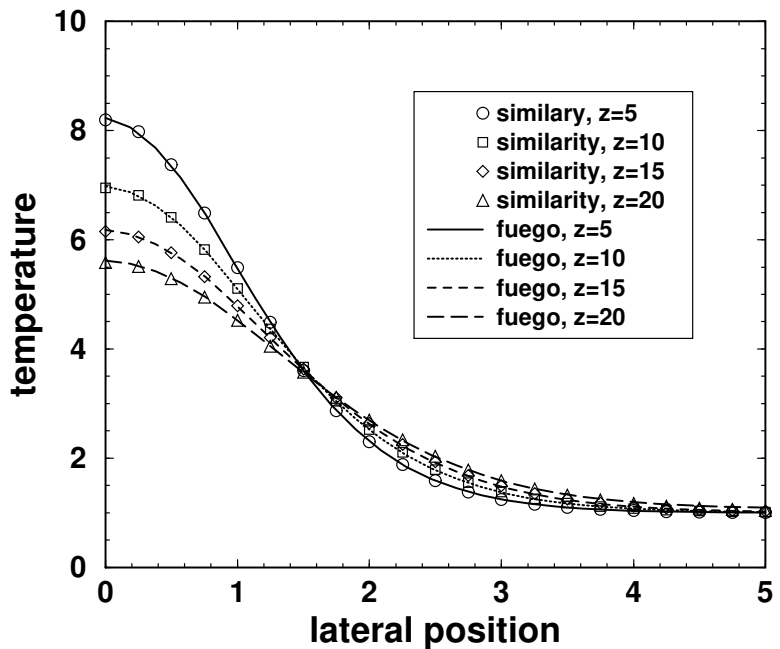


**Figure 3.7-13.. Lateral profiles of temperature for the laminar, buoyant plume. Temperature equation with  $Pr=2$ ,  $Re=16.7$ ,  $Ra=85000$ .**

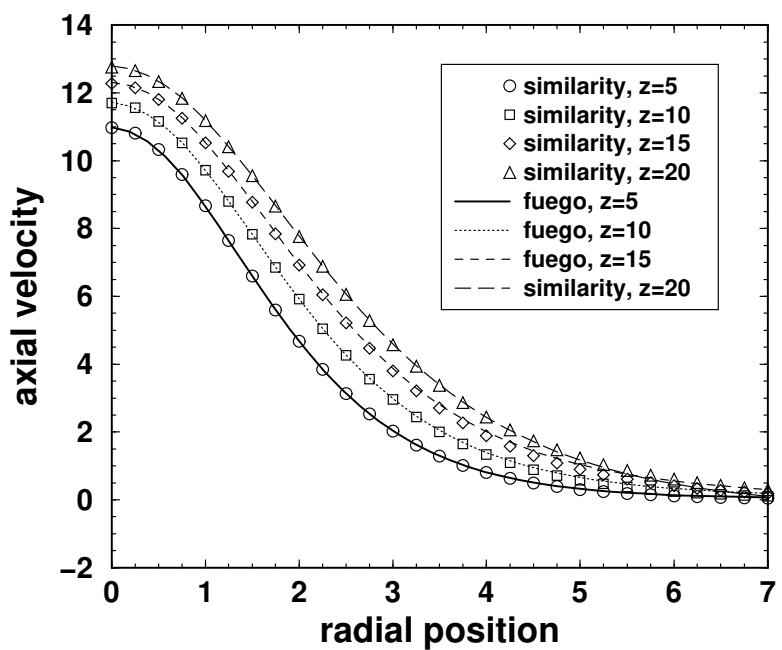


**Figure 3.7-14.. Horizontal profiles of vertical velocity for the laminar, buoyant plume. Temperature equation with  $Pr=2$ ,  $Re=16.7$ ,  $Ra=85000$ .**

This page intentionally left blank.

# 4. LAMINAR, CONCENTRATION-DRIVEN BUOYANT PLUME

<b>Dimension:</b>	3D (quasi 2D)
<b>Transient/Steady:</b>	steady
<b>Laminar/Turbulent:</b>	laminar
<b>Isothermal/Thermal:</b>	isothermal
<b>Temperature/Enthalpy:</b>	n/a
<b>Uniform/Nonuniform:</b>	nonuniform mixture
<b>Combustion:</b>	no
<b>Soot:</b>	no
<b>Coupled Mechanics:</b>	no
<b>Regression Test:</b>	fuego/concentration_plumeA_lam fuego/concentration_plumeB_lam fuego/concentration_plumeB_trb

An analytical solution for a concentration-driven plume due to a line source is used as a verification problem. Yih (1977) gave a similarity solution, using boundary layer equations, for the buoyant plume above a line source. Since this solution is not based on the full Navier-Stokes equations, problem parameters have to be specified such that the full flow equations approximate the boundary layer equations. The purpose of this test is to verify the species transport with buoyancy body forces and open boundaries. The most appropriate equation set for this analytic solution is the laminar Navier-Stokes equations with a species transport equation. The fluid is assumed to be a binary mixture of ideal gas. In order to achieve some degree of verification for the terms in the turbulent species transport equation set, results are included for both laminar species transport and species enthalpy transport (with zero eddy viscosity).

## 4.1. ANALYTIC OR BENCHMARK SOLUTION

Yih [4] presents similarity solutions for buoyant convection above a point source (Chapter 8, Section 7) and a line source (Chapter 8, Section 8). We consider the latter problem which is two-dimensional and

planar. These solutions were first published by Yih [5] in 1952 (corrections in 1953 [6]). Apparently unaware of Yih's work, Brand and Lahey [7] reproduced the same solutions some 15 years later.

Yih found two similarity solutions in closed form for Schmidt numbers of 5/9 and 2. With reference to the coordinate system in Figure 3.1-1, the boundary layer equations are:

$$u \frac{\partial u}{\partial x} + v \frac{\partial u}{\partial y} = \nu \frac{\partial^2 u}{\partial y^2} - g \frac{\Delta \gamma}{\gamma_0}, \quad (4.1)$$

$$u \frac{\partial \Delta \gamma}{\partial x} + v \frac{\partial \Delta \gamma}{\partial y} = \alpha \frac{\partial^2 \Delta \gamma}{\partial y^2}, \quad (4.2)$$

$$\frac{\partial u}{\partial x} + \frac{\partial v}{\partial y} = 0, \quad (4.3)$$

where  $\gamma = \rho g$  is the specific weight. Use of the ideal gas law gives the following relation between specific weight and mass fraction of species 1 in a binary mixture:

$$-\text{MW}_0 \left( \frac{1}{\text{MW}_1} - \frac{1}{\text{MW}_2} \right) \Delta Y_1 = \frac{\Delta \gamma}{\gamma}, \quad (4.4)$$

where  $\text{MW}_1$  is the molecular weight of species 1,  $\text{MW}_2$  is the molecular weight of species 2,  $\text{MW}_0$  is the ambient mixture molecular weight,  $\gamma_0$  the corresponding mixture specific weight,  $\Delta \gamma = \gamma - \gamma_0$ , and  $\Delta Y_1 = Y_1 - Y_1, 0$ . In this problem, it is assumed that the concentration variations are small enough to approximate physical properties as constant. The boundary conditions for the problem are:

$$v = \frac{\partial u}{\partial y} = \frac{\partial \Delta \gamma}{\partial y} = 0, \quad \text{for } y = 0, \quad (4.5)$$

$$u = \Delta \gamma = 0, \quad \text{for } y \rightarrow \pm\infty. \quad (4.6)$$

There is an integral quantity which should be independent of  $x$ , namely a measure of the strength of the line source,

$$G = - \int_{-\infty}^{\infty} u \Delta \gamma dy. \quad (4.7)$$

The similarity variable found by Yih is,

$$\xi = \frac{1}{5} \left( \frac{\rho^2 G}{\mu^3 x^2} \right)^{\frac{1}{5}} y, \quad (4.8)$$

and the corresponding similarity solution is sought in terms of the stream function and specific weight

$$\left( \frac{\rho^3}{G \mu^2 x^3} \right)^{\frac{1}{5}} \psi = f(\xi), \quad (4.9)$$

$$\left( \frac{\mu^2 x^3}{G^4 \rho^3} \right)^{\frac{1}{5}} \Delta \gamma = - \frac{1}{125} \theta(\xi), \quad (4.10)$$

which results in the similarity solution

$$f(\xi) = A \tanh(B\xi), \quad (4.11)$$

$$\theta(\xi) = C \operatorname{sech}^n(B\xi). \quad (4.12)$$

The constants are given in Table 4.1-1 for the two values of Schmidt number which admit similarity. The velocity components can be computed from the stream function,  $\psi$ , resulting in

$$5 \left( \frac{\rho\mu}{G^2 x} \right)^{\frac{1}{5}} u = f' = AB \operatorname{sech}^2(B\xi), \quad (4.13)$$

$$5 \left( \frac{\rho^3 x^2}{G\mu^2} \right)^{\frac{1}{5}} v = 2\xi f' - 3f. \quad (4.14)$$

**Table 4.1-1.. Constants in concentration plume similarity solution for two Schmidt numbers (Sc).**

Sc	n	A	B	C
5/9	2	$(405/8)^{1/5}$	$5A/6$	$50A^4/27$
2	4	$5/(240)^{1/5}$	$3A/2$	$9A^4$

Several assumptions were made at the outset in order to arrive at this analytical solution. In order to use the solution as a benchmark against the full Navier-Stokes equations, the parameters governing the motion must be specified so that the approximations embodied in the analytical solution are closely approximated in the full equations. One of the major assumptions was that the motion can be described by the boundary layer approximation to the full equations.

This requires that the flow Reynolds (Re) and Richardson (Ri) numbers be large compared to unity ( $Re \gg 1, Ri \gg 1$ ). There is no intrinsic length scale in the concentration plume problem. However, a (somewhat artificial) length scale can be defined by considering the solution in a region above the source, i.e., by introducing a virtual origin for the line source location at some position beneath the computational region. In this interpretation of Yih's solution for the upper half plane, one considers the solution in a truncated computational domain as a combined concentration/momentu

The volume flux through the plume depends on elevation, and can be computed using the expressions for the vertical velocity with the result,

$$U = \int_{-\infty}^{\infty} u dy = 2A \left( \frac{Gx^3\mu^2}{\rho^3} \right)^{\frac{1}{5}}. \quad (4.15)$$

The Reynolds number at any elevation can then be defined by

$$\text{Re} = \frac{\rho U}{2\mu} = A \left( \frac{\rho^2 G x^3}{\mu^3} \right)^{\frac{1}{5}}. \quad (4.16)$$

The definition of the width of the jet is somewhat arbitrary. We define it, for a given elevation, as the lateral dimension where the vertical velocity component is some small fraction,  $\epsilon$ , of the centerline velocity,

$$\epsilon = \frac{f'(\xi(h))}{f'(0)}, \quad (4.17)$$

which leads to

$$h = \frac{5E}{B} \left( \frac{x^2 \mu^3}{\rho^2 G} \right)^{\frac{1}{5}}, \quad (4.18)$$

$$E = \text{acosh}(\epsilon^{-1/2}). \quad (4.19)$$

The Richardson number is defined with respect to this length scale and in terms of the source strength,

$$\text{Ri} = \frac{\Delta\gamma}{\gamma} \frac{2hg}{u^2} = 8 \frac{G}{\rho} \frac{h^3}{U^3}. \quad (4.20)$$

Using the definition of the jet half-width and comparing to the definition of the Reynolds number, we find a definite relationship between the Richardson number and the Reynolds number,

$$\text{RiRe} = \left( \frac{5E}{B} \right)^3 \frac{1}{A^2}. \quad (4.21)$$

Thus, we now have expressions for  $G$  and the virtual origin,  $x_0$ , as functions of the jet half-width,  $h$ , and key dimensionless numbers,

$$G = \rho \left( \frac{\nu}{h} \right)^3 \text{RiRe}^3, \quad (4.22)$$

$$x_0 = \rho \left( \frac{G}{\mu^3} \right)^{\frac{1}{2}} \left( \frac{Bh}{5E} \right)^{\frac{5}{2}}. \quad (4.23)$$

These formulae allow us to specify  $\text{Re}$  (and therefore  $\text{Ri}$  via Equation 4.21) and  $h$  and compute the corresponding source strength and virtual origin such that the assumptions made in the similarity solution should be met by the Navier-Stokes solution for these parameters. The Schmidt number is restricted to either  $5/9$  or  $2$  in order to admit a self-similar solution that is analytic rather than numeric.

## 4.2. MESH DEFINITION

There are four three-dimensional meshes with uniform, hexahedral elements. There is only one element in the  $z$ -direction since the  $z$ -planes act as symmetry planes to achieve two-dimensionality. The  $x$  and

y-dimensions are the same in each mesh, 20 units by 20 units. The z-depth is 0.25 units. (Note that the coordinate system for the mesh is different from the derivation of the boundary layer solution.) Mesh A is  $20 \times 20 \times 1$  elements, mesh B is  $40 \times 40 \times 1$  elements, mesh C is  $80 \times 80 \times 1$  elements, and mesh D is  $160 \times 160 \times 1$  elements. The x and y-plane of the mesh each have a side-set defined for a total of four. The element faces of the two z-planes make up the fifth side-set.

## 4.3. MATERIAL SPECIFICATIONS

The material properties are constant for the species transport equation. The units are unimportant as long as they are consistent. The density is 1.0, the viscosity is 1.0, and the mass diffusivity is conductivity is 0.5. The Schmidt number is 2.0. The gravitational acceleration is 1.0. The buoyancy body force is approximated using the Boussinesq approximation.

## 4.4. INITIAL CONDITIONS

The velocities and mass fractions are initialized to the inflow profiles. The inflow profiles are specified as a function of the lateral coordinate. The inflow functions are applied at every node. The pressure is zero.

## 4.5. BOUNDARY CONDITIONS

The boundary conditions are applied over five side-sets. Note that the coordinate system for the mesh is different from the derivation of the boundary layer solution. In the mesh, the vertical direction is along the y-axis and the horizontal is along the x-axis. The analytic solution is derived in a coordinate system rotated by 90 degrees (see Figure 3.1-1). The bottom plane at  $y=0$  is the inflow boundary. The analytic velocities and mass fractions are enforced at the nodes of the inflow side-set using Dirichlet conditions. The  $x=0$  plane is a symmetry plane since the solution is symmetric about the vertical centerline. The  $x=x_{\max}$  plane is the entrainment plane. The pressure is specified as zero and the flow is required to enter the domain normal to the boundary. There is no shear velocity specified since the vertical velocity is negligible far from the plume. The mass fractions are entrained at the reference conditions used in the buoyancy model. The  $y=y_{\max}$  plane is the outflow plane. It is applied in the same manner as the entrainment plane. Additionally, the “OMIT DIFFUSION TERMS” command is required at the outflow boundary in order to get a converged steady-state solution. If the diffusion terms are retained on the outflow boundary, the outflow velocities tend to oscillate and the nonlinear residuals hang up. The horizontal velocity will also behave strangely. The  $z=0$  and  $z=z_{\max}$  planes make up the fifth side-set. These boundary conditions are applied as symmetry planes to make the flow quasi-two-dimensional.

## 4.6. SOLUTION PROCEDURE

The equations are time-marched to steady state with an adaptive time step. The time steps adapt to a fixed maximum CFL number of 5.0. The projection method is the “stabilized method” with no under-relaxation. The hybrid first-order upwind scheme was used for convection.

The linearized continuity equation is solved with the stabilized biconjugate gradient method with two steps of symmetric Gauss-Seidel preconditioning. The linear residuals are reduced by six orders of magnitude at each solve. The linearized momentum equations are solved with the GMRES method with three steps of Jacobi preconditioning. The GMRES method is restarted after 50 iterations. The linear residuals are reduced four orders of magnitude at each solve. Dirichlet boundary conditions are enforced exactly. The linearized temperature equation is solved with the GMRES method with three steps of symmetric Gauss-Seidel preconditioning. The GMRES method is restarted after 50 iterations. The linear residuals are reduced four orders of magnitude at each solve. Dirichlet boundary conditions are enforced exactly. The linearized enthalpy equations are solved in the same manner as the temperature equation.

## 4.7. VERIFICATION EXPERIMENTS

The behavior of the concentration-driven buoyant plume problem is similar to the thermally-driven buoyant plume. The velocity and scalar values look good near the plume core. The entrainment velocity asymptotes to a value different from the similarity solution far from the plume. The mesh refinement study was performed with the laminar mechanics. A solution was run with the turbulent mechanics with forced laminar inputs to verify the turbulent mass transport equation.

The cases are run with Fuego-0.9.0.

### 4.7.1. Laminar Mechanics

The concentration-driven buoyant plume problem was run with  $Sc=2$ , half-width=5, and  $Re=10$ . This corresponds to  $G=61.03$ ,  $Ri=7.6281$ ,  $B=2.506$ ,  $E=2.993$ , and  $x_o = 5.011$ . Recall that  $\rho = \mu = 1$  and the gravitational acceleration is 1.0. There are two chemical species:  $H_2$  (mw=2) and  $O_2$  (mw=32).

The centerline  $H_2$  mass fractions of  $H_2$ , Figure 4.7-1, track the analytic solution as the mesh is refined. Similar behavior is noted for the radial  $H_2$  distributions, shown in Figure 4.7-2. Radial distributions of the radial velocity are shown in Figure 4.7-3. The asymptotic entrainment velocity does not match the similarity solution. Centerline distributions of the axial velocity are shown in Figure 4.7-4.

The order of accuracy of the solution is estimated using a Richardson extrapolation technique. Nodal solutions on a sequence of three uniformly refined meshes are compared. The expected order of accuracy is one since the first-order upwind convection scheme was used. The convection scheme is hybrid in the sense that it switches to a second-order accurate centered scheme in regions where the cell Peclet number is below a threshold value near two. On the coarsest mesh, the maximum cell Reynolds number was 10. Contours of the order of accuracy of the nodal velocities are shown in Figures 4.7-5

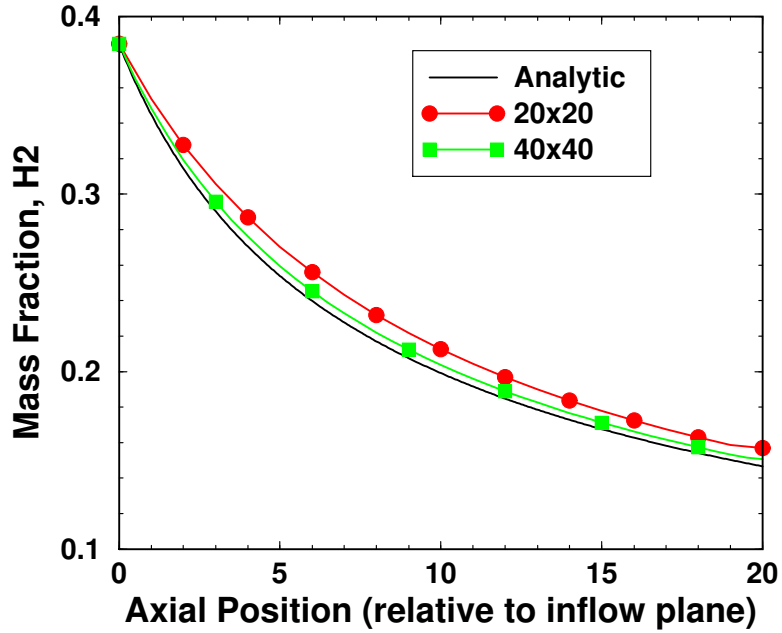


**Figure 4.7-1.. Centerline H2 mass fractions.**

and 4.7-6. The velocities have an order-one accuracy within the plume where the velocities are highest and change the most. The analysis indicates the order of accuracy is closer to two out in the entrainment region where velocities are lower and more smooth. The order of accuracy of the species mass fraction is shown in Figure 4.7-7. The analysis indicates that the order of accuracy for the mass fractions is near one throughout the domain.

## 4.7.2. Turbulent Mechanics

The zero eddy viscosity is achieved by setting initial values of  $k = 10^{-15}$ ,  $\epsilon = 10^{-9}$ ,  $\text{Pr}_t = 10^{12}$ , and an explicit relaxation parameter of 0.0 for the turbulence model equations.

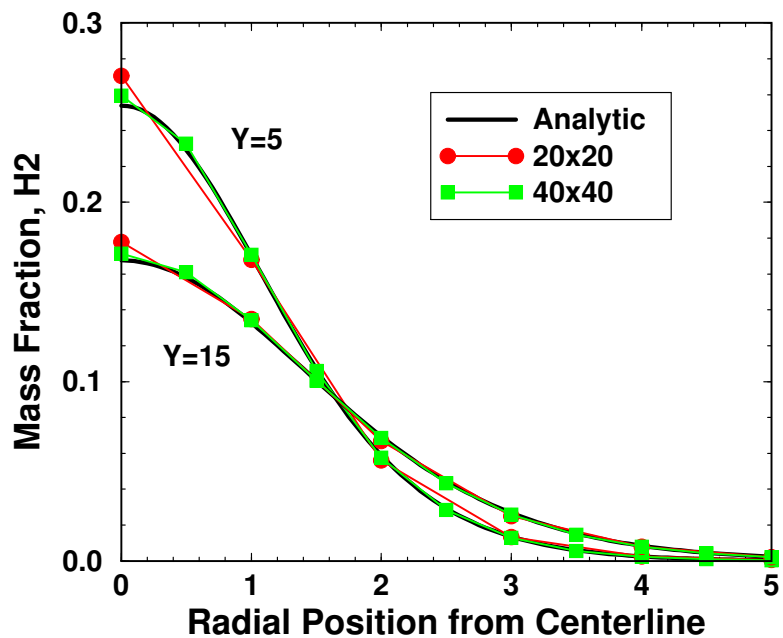


Figure 4.7-2.. Radial H<sub>2</sub> mass fractions at two axial stations.

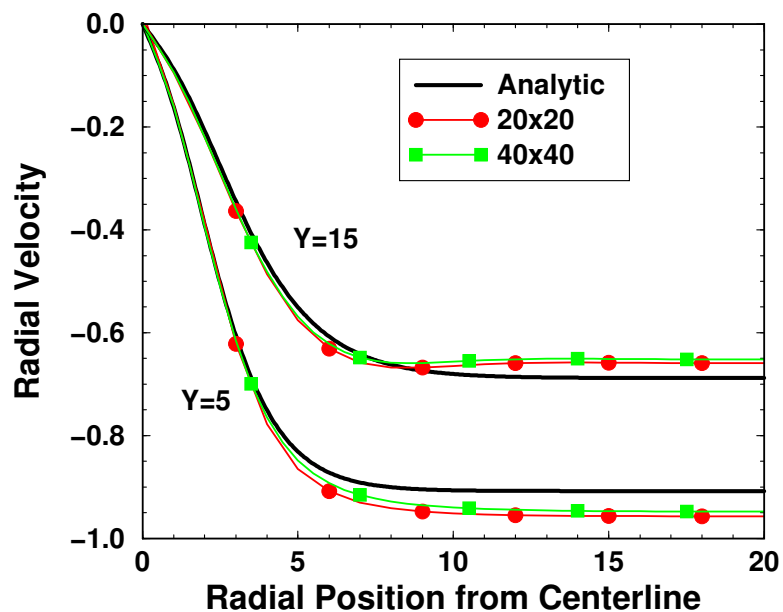
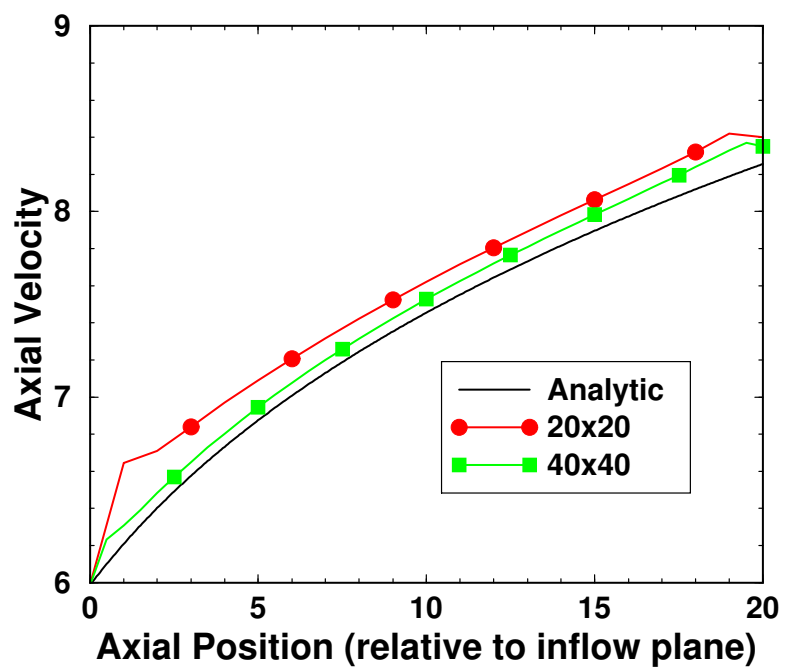
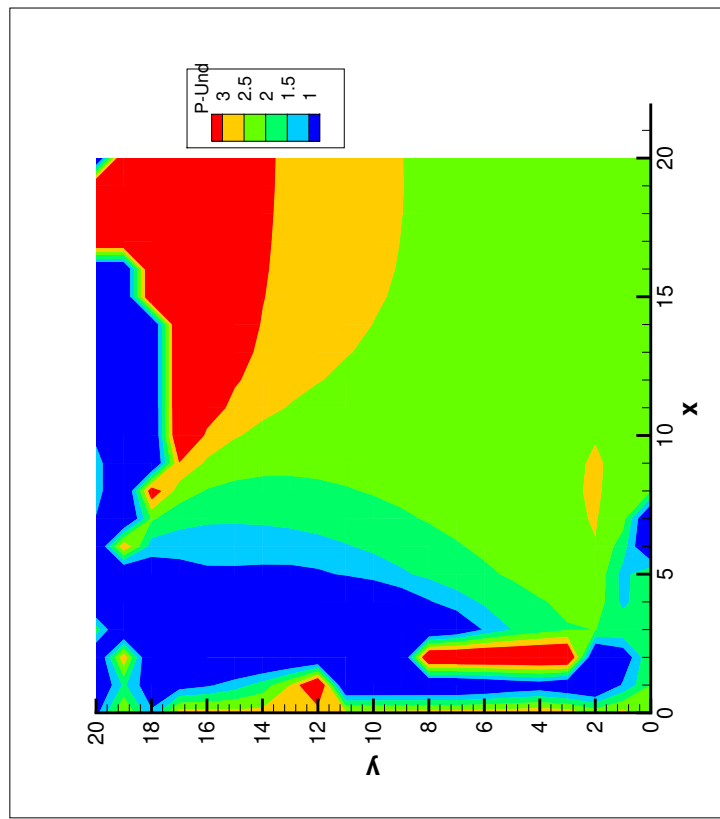


Figure 4.7-3.. Radial distribution of radial velocity at two axial stations.



**Figure 4.7-4.. Centerline velocity.**



**Figure 4.7-5.. Order of accuracy contours, x-velocity.**

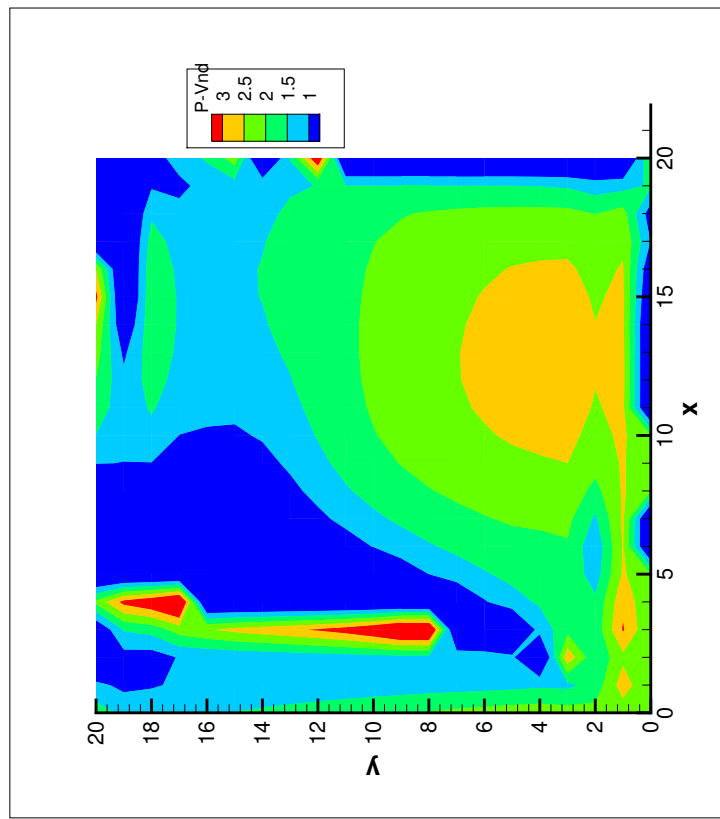


**Figure 4.7-6.. Order of accuracy contours, y-velocity.**

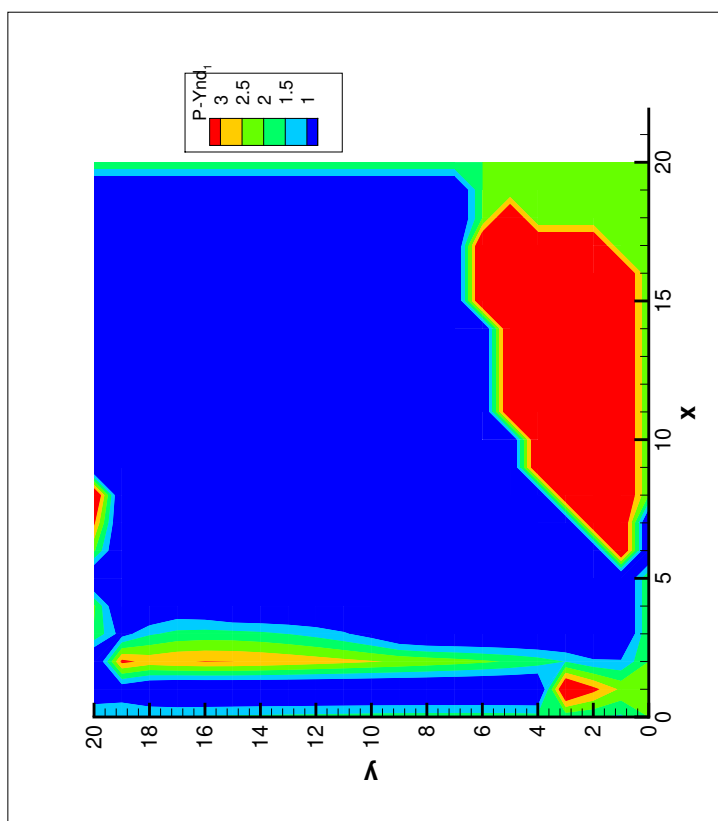


**Figure 4.7-7.. Order of accuracy contours, mass fraction of species 1.**

# 5. PRESSURE-DRIVEN LAMINAR DUCT

<b>Dimension:</b>	3D
<b>Transient/Steady:</b>	steady
<b>Laminar/Turbulent:</b>	laminar
<b>Isothermal/Thermal:</b>	isothermal
<b>Temperature/Enthalpy:</b>	N/A
<b>Uniform/Nonuniform:</b>	uniform
<b>Combustion:</b>	no
<b>Soot:</b>	no
<b>Coupled Mechanics:</b>	no
<b>Regression Test:</b>	fuego/laminar_duct_2xi

This problem is used to verify the implementation of fixed pressure inlet and outlet boundary conditions for laminar isothermal uniform flow. The verification approach is to compare between Fuego-0.8.0 and an analytical solution of this problem by Berker [8]. The geometry was selected to be a channel rectangular channel of width 1 m, height 2 m, and length 20 m. A detailed refinement study (to 2 million nodes) has been completed with version 2.0beta.

## 5.1. MATERIAL SPECIFICATIONS

The material properties in Fuego are a fluid with a density of 1E-3 kg/m<sup>3</sup> and a viscosity of 1E-4 kg/m s.

## 5.2. INITIAL CONDITIONS

The initial conditions used in Fuego were a  $x$ ,  $y$ , and  $z$  components of velocity of 0 m/s, 0 m/s, 0.914 m/s respectively. The channel was aligned with the flow in the  $z$  direction and the initial velocity is the analytical average velocity through the duct.

## 5.3. BOUNDARY CONDITIONS

The boundary conditions used in Fuego were a fixed inflow and outflow pressure of 0.032 Pa and 0.0 Pa respectively. No slip walls were used for the channel wall.

## 5.4. ANALYTIC OR BENCHMARK SOLUTION

An analytical solution to fully-developed laminar flow in a rectangular duct is given by Berker [8]. The axial velocity distribution is

$$v = -\frac{1}{2\mu} \frac{dp}{dz} \left[ b^2 - y^2 - \frac{4}{b} \sum_{n=0}^{\infty} (-1)^n \frac{1}{m^3} \frac{\cos(my) \cosh(mx)}{\cosh(ma)} \right] \quad (5.1)$$

where

$$m = \frac{(2n+1)\pi}{2b} \quad (5.2)$$

The half-width in the  $x$ -direction is  $a$  and the half-width in the  $y$ -direction is  $b$ . The axial direction down the duct is  $z$ .

The volumetric flow rate is

$$Q = -\frac{ab^3}{4\mu} \frac{dp}{dz} f\left(\frac{a}{b}\right) \quad (5.3)$$

where

$$f\left(\frac{a}{b}\right) = \frac{16}{3} - \frac{1024}{\pi^5} \frac{b}{a} \sum_{n=0}^{\infty} \frac{\tanh(ma)}{(2n+1)^5} \quad (5.4)$$

Values of the function,  $f(a/b)$ , are given in Table 5.4-1. For comparison to Fuego values of  $f(a/b)$  were computed using 100 terms in the summation. The average velocity is a function of the pressure gradient, the viscosity, and the duct cross-section.

$$\bar{v} = -\frac{b^2}{16\mu} \frac{dp}{dz} f\left(\frac{a}{b}\right) \quad (5.5)$$

The centerline velocity, at  $x = y = 0$ , is

$$v(0,0) = -\frac{1}{2\mu} \frac{dp}{dz} \left[ b^2 - \frac{4}{b} \sum_{n=0}^{\infty} (-1)^n \frac{1}{m^3} \frac{1}{\cosh(ma)} \right] \quad (5.6)$$

For the special case of a square duct,

$$v(0,0) = 2.096\bar{v} \quad (5.7)$$

To show convergence of the solution we show the L<sub>2</sub> norm of the residuals for the highest resolution case in Figure 5.4-1.

**Table 5.4-1.. Function values in similarity solution by Berker**

$a/b$	$f(a/b)$
1	2.253
2	3.664
3	4.203
4	4.498
5	4.665
6	4.777
7	4.842
8	4.916
10	5.000
12	5.059
100	5.299
$\infty$	5.333

To show that the solution has reached steady state and that the velocity profile is the expected parabolic one that matches the analytical solution, the  $z$  velocity for a cross section at  $z = 10.0$  m is shown in the  $x$  direction, Figure 5.4-2, and in the  $y$  direction, Figure 5.4-3. Along with the computed solution for the highest resolution the analytical result is shown as well in both figures.

For the specified pressure difference across the duct the analytical solution gives the velocity at the centerline  $v(0,0) = 1.8219$  where the summations are carried to 100 terms. Comparison of the Fuego results at the centerline for the three different mesh resolutions are shown in Table 5.4-2. It is seen that the velocities are converging to the analytical solution at a rate equal to second order. Note that these results are made with 2.0beta with a first order upwind factor of 0.0 with a CFL of 5. As the pressure field is linear, smoothing error (proportional to the fourth derivative of pressure) is not expected to affect steady results.

**Table 5.4-2.. Computed Centerline Velocity**

Mesh Resolution	Computed Velocity
20x40x40	1.82252
40x80x80	1.82209
80x160x160	1.82199

A comparison to analytical results is made by looking at the pressure down the centerline of the duct. The analytical and computed results for a mesh of 20x40x40 are shown in Figure 29.4-1. The computed outlet pressure was found to be 1e-9 Pa instead of 0.0 Pa.

An arbitrary revolution was made using grepos: revolve x, 123.; revolve y, 25., revolve z, 12. for the 20x40x40 mesh. The resulting outlet velocity profile was  $u(x,y,z) = -9.25387e - 02i - 1.58231e + 00j - 8.99616e - 01k$ , at a position of  $p(x,y,z) = 4.03180e - 01i - 1.36483e + 00j + 5.48784e - 01k$ . The velocity magnitude for the above position is 1.82252. This confirms the verification of arbitrary mesh revolution.

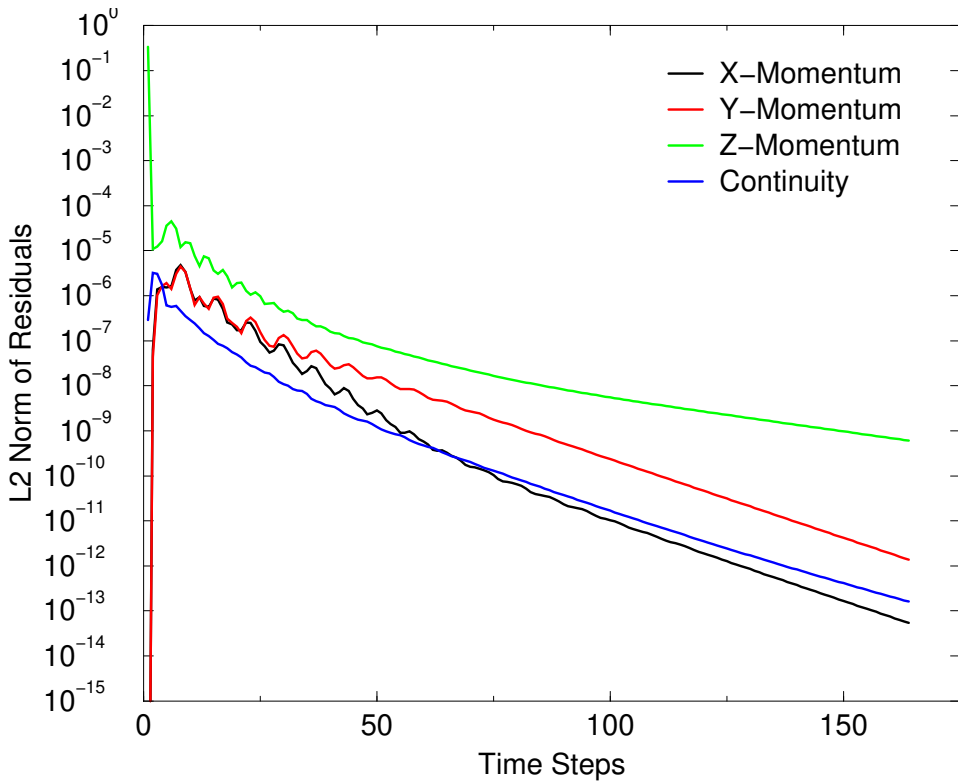


**Figure 5.4-1.. L2 norm of residuals for 20x40x40 mesh.**

## 5.5. MESH DEFINITION

Three different meshes were used for the Fuego calculations. The three different mesh sizes for the  $x$ ,  $y$ , and  $z$ , directions are 20x40x40, 40x80x80, and 80x160x160. The meshes consist of 3D hexahedral elements. The arbitrary revolution simulation was performed on the 20x40x40 mesh.

## 5.6. SOLUTION PROCEDURE

Options selected in the Fuego run were: **CFL LIMIT** = 0.1, **TIME STEP CHANGE FACTOR** = 1.25, **TRANSIENT STEP TYPE** IS automatic, **UPWIND METHOD** IS MUSCL, one nonlinear iteration per time step. For  $u$ ,  $v$ ,  $w$ , **SOLUTION METHOD** IS bicgstab, **PRECONDITIIONING METHOD** IS jacobi, **RESIDUAL NORM TOLERANCE** = 1.0e-6. For continuity **SOLUTION METHOD** IS gmres, **PRECONDITIONING METHOD** IS jacobi, **RESIDUAL NORM TOLERANCE** = 1.0e-8.

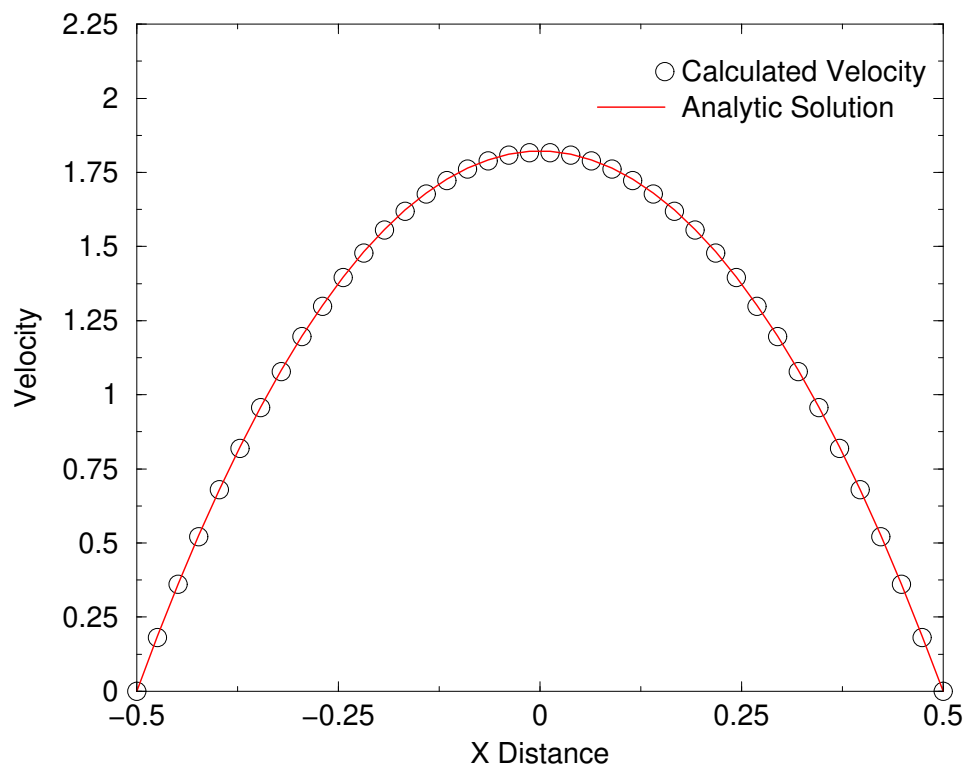


**Figure 5.4-2.. Parabolic velocity profile across  $x$  axis at  $y = 0$  m,  $z = 10$  m.**

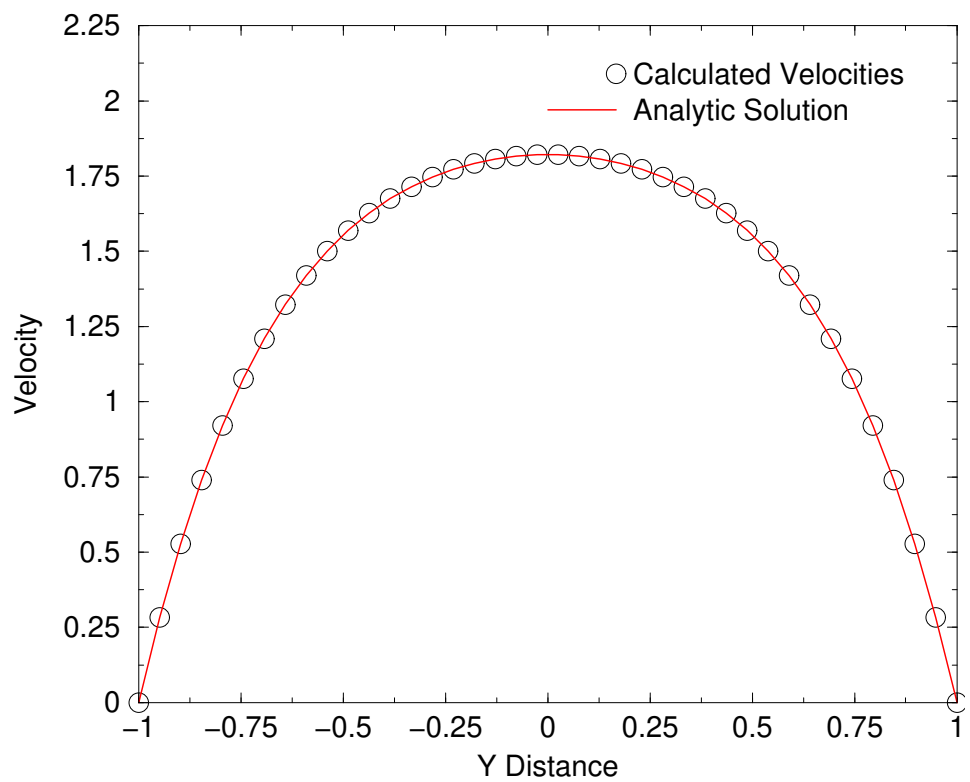


**Figure 5.4-3.. Parabolic velocity profile across  $y$  axis at  $x = 0$  m,  $z = 10$  m.**

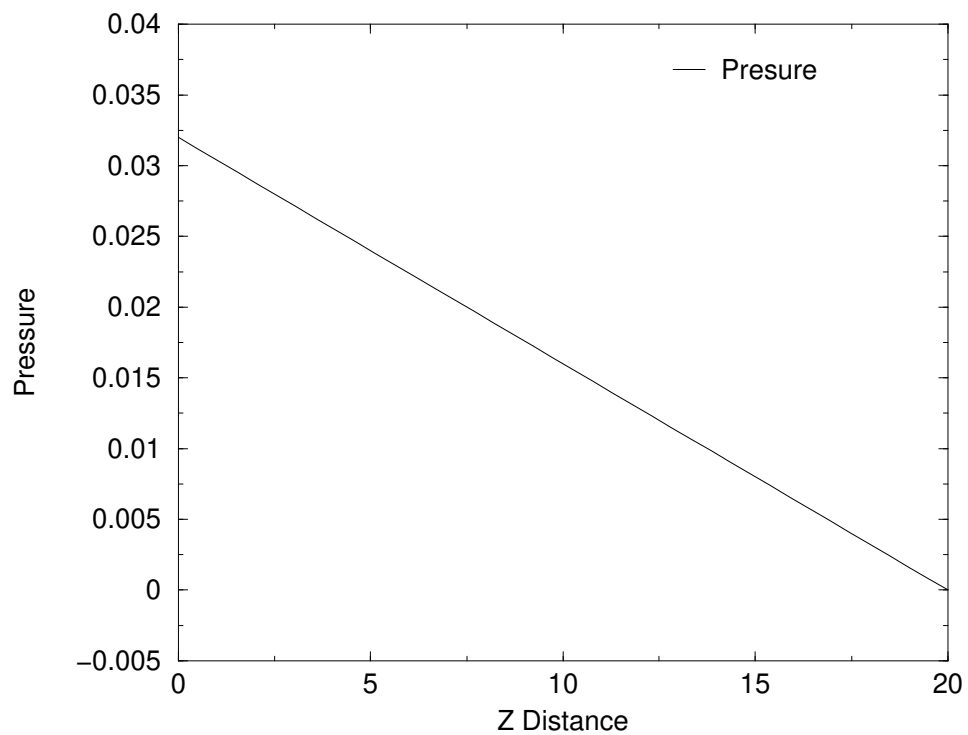


**Figure 5.4-4.. Centerline pressure in duct showing linear change.**

This page intentionally left blank.

# 6. TURBULENT HEATED DUCT

<b>Dimension:</b>	3D (1 element in z direction; symmetry on z boundaries)
<b>Transient/Steady:</b>	steady
<b>Laminar/Turbulent:</b>	turbulent
<b>Isothermal/Thermal:</b>	thermal with unheated entrance section
<b>Temperature/Enthalpy:</b>	enthalpy
<b>Uniform/Nonuniform:</b>	uniform
<b>Combustion:</b>	no
<b>Soot:</b>	no
<b>Coupled Mechanics:</b>	no
<b>Regression Test:</b>	fuego/heated_turb_duct_re50k

## 6.1. EXECUTIVE SUMMARY

Heat transfer in a turbulent channel flow is used to verify the implementation of turbulent wall functions for momentum and heat transfer in the computational fluid dynamics (CFD) code Fuego. The verification approach is a benchmark comparison of the predicted heat transfer between Fuego-0.8.0 and the commercial code CFX5. The problem is air flowing in a planar heated channel; an upstream section is unheated and at the same temperature as the inflowing air, allowing for velocity profile development; a downstream section is heated to a higher temperature. In the downstream section predictions of the heat transfer from the channel wall to the flowing air are compared. Besides the code to code predictions the results are compared with an empirical correlation of Shah and Bhatti [9] and, for specified turbulent velocity and eddy viscosity profiles and for turbulent Prandtl number  $Pr_t = 1.0$ , an analytical solution of Özışık et al. [10]. The results for the asymptotic heat transfer are shown in Table 6.1-1. The Fuego and CFX5 calculations were made for  $Pr_t = 0.9$ ; the CFX5 result was made with a thermal law of the wall modified by a function of  $Pr$  [11].

Due to the complex nature of turbulent convective heat transfer and the lack of detailed understanding, it appears that heat transfer predictions within 10% of the data are generally considered to be quite good. Furthermore, the large number of differences in models and their numerical implementations will undoubtedly result in differences in the heat transfer predicted by the two codes. The results of the code to code comparison as well as the comparison with empirical correlation and analytical solution presented in this study are proposed to be sufficient for verification of turbulent wall functions for heat transfer in Fuego.

source	Nu <sub>asymptotic</sub>
Fuego-0.8.0:	104
CFX5:	107
Özişik et al. [10]:	101
Shah and Bhatti [9]:	105.8

**Table 6.1-1.. Asymptotic Nusselt numbers in turbulent channel flow**

## 6.2. INTRODUCTION

The purpose of this study is to provide verification of the wall function implementation in Fuego for the prediction of turbulent heat transfer. Due to the complex nature of turbulent convective heat transfer and the lack of detailed understanding and exact solutions, the verification of model predictions is difficult. The approach has been to find a problem that has been the focus of significant earlier research where results are established (i.e., correlations and approximate analytical solutions are available, and numerical solutions have been obtained using mathematical models similar to those in Fuego). The heat transfer in a fully developed turbulent channel flow where the channel wall temperature undergoes a step change (the turbulent Graetz problem) is such a problem. Experiments have been performed ([12]; [13]) and standard  $k - \epsilon$  model predictions have been obtained ([14]) for the turbulent heat transfer to air flowing in a channel with a half-height of 2.54 cm. Correlations of the turbulent heat transfer for flow in a channel with a sudden increase in the channel wall temperature have been obtained by Shah and Bhatti [9]. Furthermore, for specified turbulent velocity and eddy viscosity profiles and for turbulent Prandtl number  $Pr_t = 1.0$ , an analytical solution to the turbulent Graetz problem in a channel flow has been obtained by Özişik et al. [10].

The primary objective of the verification problem is to compare the local heat transfer predicted by Fuego with that predicted by another code that has the same turbulence model and the same numerical algorithm. Due to complexities in turbulence models and their numerical implementation in combination with the complexities in solving CFD problems numerically, finding another code that completely meets these requirements is unlikely. The commercial CFD code, CFX5, was chosen for verification of Fuego on this problem because it uses essentially the same turbulence model and numerical algorithm. However, there are some differences which affect the results; these differences and the results will be discussed and shown below.

## 6.3. PROBLEM DESCRIPTION

The problem is shown in Fig. 6.3-1. Air at atmospheric pressure and 300 K enters a 12 m long planar channel (half-height,  $b=2.54$  cm) with a flat velocity profile, the magnitude of which produces the desired Reynolds number. The Reynolds number based on this velocity, which is also the average velocity  $u_{avg}$ , and the hydraulic diameter  $4b$  is  $Re=u_{avg} \cdot 4b/\nu = 50,000$  (10,000 and 100,000 are also shown in comparisons between CFX5 and results given in [10] and the correlation [9]). The turbulent velocity profile develops in the upstream unheated section of the channel ( $L_u = 4$ m) which has a wall

temperature of 300 K. Between  $x = 4$  m and the channel exit at  $x = 12$  m ( $L_d = 8$  m), the channel wall temperature is 310 K, the air temperature increases, and the dimensionless heat transfer (Nusselt number,  $Nu = h \cdot 4b/k$ ) from the heated channel wall to the flowing air first decreases and then reaches an asymptotic value upstream of the exit.

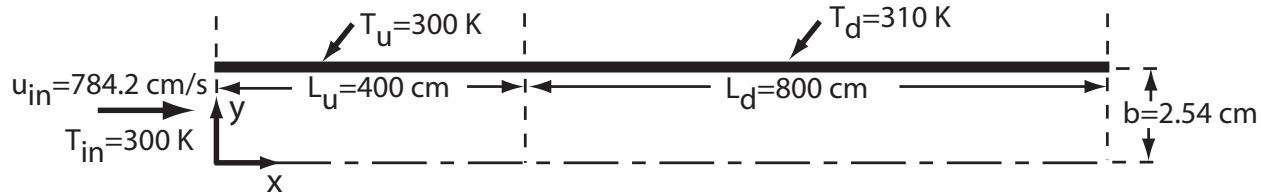


**Figure 6.3-1.. Description of the problem (not to scale,  $L_d/b = 315$ ).**

## 6.4. MATERIAL SPECIFICATIONS

### 6.4.1. CFX5

The CFX5 option “Air Ideal Gas” was used in all calculations, except for one case where Fuego/ChemkinIII values were used to verify that only the Reynolds number and Prandtl number need to be exactly duplicated for dimensionless parameter comparisons such as the Nusselt number in the present study. At 300 K and 1 atmosphere, the density selected by the code was 1.1764 kg/m<sup>3</sup> using a molecular weight of 28.96 kg/kmol. The viscosity was 1.79E-5 kg/m s, the heat capacity was 1000.0 J/kg K, and the thermal conductivity was 0.0252 W/m K. These are the values listed at the top of the CFX5 problem definition file.

### 6.4.2. Fuego

The material properties in Fuego were evaluated using ChemkinIII. Air was simulated as a binary mixture of O<sub>2</sub> and N<sub>2</sub>, with mole fractions of 0.2095 and 0.7905, respectively. At 300 K and 1 atmosphere, the mixture density, viscosity, and constant pressure specific heat are 1.172 kg/m<sup>3</sup>, 1.868E-5 kg/(m-s), and 1009.7 J/(kg-K), respectively. The molecular Prandtl number was specified to be 0.72. This results in a thermal conductivity of 0.02619 W/(m-K).

### 6.4.3. Comments

The evaluation of the viscosity of air in Fuego and CFX5 differs by approximately 4%; thus for the results presented here that compare CFX5 with Fuego, all of the properties were modified in CFX5 so that both Fuego and CFX5 used the same inlet velocity of 7.842 m/s as well as the same Reynolds number of 50,000 to prove that the 4% difference was not causing any significant differences.

## 6.5. INITIAL CONDITIONS

### 6.5.1. CFX5

The default “automatic” initial condition option was used along with the CFX5 “Smart Start” option. This sets the entire field to stagnant, 1 atmosphere, 306.7 K [ a weighted average( $300/3+310x2/3$ )], and then it maintains laminar flow for 5 iterations prior to activating the turbulence calculations.

### 6.5.2. Fuego

The initial conditions used in Fuego were uniform values of temperature, turbulent kinetic energy, turbulent dissipation rate, and  $x$ ,  $y$ , and  $z$  components of velocity of 307 K, 121.5  $\text{cm}^2/\text{s}^2$ , 2636.  $\text{cm}^2/\text{s}^3$ , 784.2  $\text{cm}/\text{s}$ , 0  $\text{cm}/\text{s}$ , and 0  $\text{cm}/\text{s}$ , respectively. The channel was aligned with the flow in the  $x$  direction. The turbulence quantities were determined by assuming an isotropic turbulence field, a 1.2% turbulence intensity, and a turbulence length scale of 0.508 cm (20% of  $b$ , the half-height of the channel).

## 6.6. BOUNDARY CONDITIONS

### 6.6.1. Common elements

Uniform velocity and temperature of 784.2  $\text{cm}/\text{s}$  and 300 K were applied at the inlet ( $x=0$ ) of the channel. Only half of the duct width was simulated: symmetry was assumed at the channel centerline ( $y=0$ ). The upstream 4.0 m of the channel was unheated and was simulated to allow the flow to adjust toward a fully developed turbulent flow from the uniform conditions applied at the inlet. The downstream 8.0 m of the channel had a uniform channel wall temperature  $T_d=310$  K. The small temperature difference of 10 K was chosen so the effects of variable fluid properties would be minimal.

### 6.6.2. CFX5

Besides the inlet velocity of 7.842 m/s, three other inlet velocity conditions were computed with CFX5(air ideal gas): 1.5, 7.5 and 15.0 m/s. The turbulent “default intensity and autocompute length scale” option was invoked. The inlet turbulence conditions here are irrelevant, however, because a 4.0 m long adiabatic entrance region was used to produce fully developed velocity profiles prior to the 8.0 m long heat transfer region. No slip conditions were applied to all walls. The CFX5 default  $k - \epsilon$  turbulence model with “scalable wall functions” was used for all calculations. The outlet of the 12.0 m long duct was given mass flow rate values of 0.0011384, 0.005692 and 0.011384  $\text{kg}/\text{s}$ , respectively, corresponding to the 1.5, 7.5 and 15.0 m/s inlet velocities. For the 7.842 m/s inlet velocity case, the outlet mass flow rate was 0.0058628  $\text{kg}/\text{s}$ . The simulation was 2D; “periodic pair” symmetry conditions were applied on the transverse planes in the  $z$  direction.

### 6.6.3. Fuego

Uniform turbulence conditions applied at the inlet of the channel were turbulent kinetic energy and turbulent dissipation rate of  $121.5 \text{ cm}^2/\text{s}^2$  and  $2636 \text{ cm}^2/\text{s}^3$ , respectively. Wall functions were applied at the channel wall ( $y=2.54 \text{ cm}$ ); the turbulent kinetic energy equation was solved at the wall node and the Fuego option *USE EQUILIBRIUM PRODUCTION MODEL* was selected. A Dirichlet condition was applied to the dissipation rate equation at the wall node as described in the Fuego theory manual. At the outlet of the channel ( $x=1200 \text{ cm}$ ), an outflow condition with pressure set to zero was applied. Since Fuego is a 3D code and the interest here is to simulate a 2D channel flow in which the transverse ( $z$ ) dimension of the channel is large relative to the half-height, the  $z$  dimension was arbitrarily set to  $1.0 \text{ cm}$  and symmetry conditions were applied at the transverse boundaries (at  $z=0, 1 \text{ cm}$ ).

## 6.7. ANALYTIC OR BENCHMARK SOLUTION

Three nominal CFX5 steady-state simulations were performed with inlet velocities of  $1.5, 7.5$  and  $15.0 \text{ m/s}$  yielding Reynolds numbers of  $10,000, 50,000$  and  $100,000$ , respectively, which correspond to results given by Özışık et al. [10]. The wall heat flux was examined in the  $8.0 \text{ m}$  heat transfer section of the duct. For comparison purposes, the results were placed in a non-dimensional form corresponding to the correlation of Shah and Bhatti [9] and also to the analysis of Özışık et al. [10]. These comparisons are shown in Figure 6.7-1 for Prandtl number  $0.72$ . It can be observed that the CFX5 results accurately approach the fully developed Shah and Bhatti correlation as an asymptote and are also in good agreement with the analysis of Özışık et al. Note that the Özışık solution is for  $\text{Pr}_t=1.0$  and the CFX5 results are for  $\text{Pr}_t=0.9$  where  $\text{Pr}_t$  is the turbulent Prandtl number. The sensitivity of the calculated results to turbulent Prandtl number will be presented later.

## 6.8. MESH DEFINITION

### 6.8.1. CFX5

The benchmark mesh was uniform and hexagonal. It was imported to CFX5 from CFX4, where it had been successfully used to solve the same problem. It covers the duct half-width of  $0.0254 \text{ m}$ , and the entire duct length of  $12.0 \text{ m}$ , and it was  $42 \times 800 \times 1$ . Some experiments were also conducted with  $12, 22$  and  $32$  grids in the duct half-width direction to test sensitivity of results to different  $y^+$  values for both the default “scalable” and the optional “standard” wall functions in the  $k - \epsilon$  turbulence model options. These results are shown in Figures 6.8-1 and 6.8-2.

### 6.8.2. Fuego

For the Fuego calculation, the mesh spacing in the  $x$  direction was uniform at  $\Delta x=1.5 \text{ cm}$ , resulting in  $800$  elements in this direction. The mesh consists of 3D hexahedral elements. The implementation of wall functions in Fuego is described in the Fuego theory manual. Effectively the first node off the wall

## LOCAL NUSSELT NUMBER $\text{Pr} = 0.72$

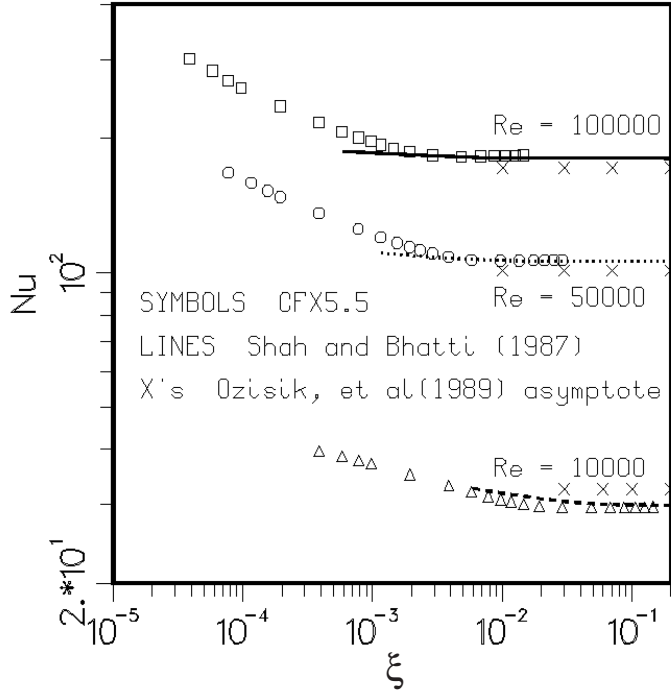


**Figure 6.7-1.. Nusselt numbers: analytic solution and CFX5 benchmark; horizontal coordinate defined in eqn. 6.3.**

must be placed in a region where the logarithmic law of the wall is applicable. An appropriate place is  $y^+ \approx 20$  (this is where the assumptions used to derive the form of the wall functions used in Fuego are highly consistent; this is also near the peak in the turbulent kinetic energy profile; see the Fuego theory manual section on turbulent verification problems). The wall function is applied to the wall node control volume with  $y^+$  defined as the dimensionless distance normal from the wall to the subcontrol volume center. In CFX5, the wall function is applied at the wall node using an assumed  $y^+$  value of 11.1 when the scalable wall function approach (used here) is selected. The CFX5 scalable wall function implementation decouples the mesh from the application of the wall function, whereas in Fuego the mesh is coupled to the wall function implementation. In order for the Fuego and CFX5 simulations to have the same mesh in the wall normal ( $y$ ) direction and still have the wall function applied appropriately in Fuego, the first node next to the wall was 4 times the  $y$  mesh spacing otherwise used. The  $y$  mesh spacing used in Fuego was uniform with  $\Delta y = 0.0605$  cm, except next to the wall where  $\Delta y = 0.242$  cm, resulting in 38 uniformly spaced elements (with  $\Delta y = 0.0605$  cm) plus the single near-wall element with 4 times this uniform spacing ( $\Delta y_{\text{wall}} = 0.242$  cm). For  $\text{Re} = 50,000$  this mesh resulted in  $y^+ \approx 16$  for application of the Fuego wall function. An early Fuego simulation with a uniform  $y$  mesh ( $\Delta y = 0.0605$  cm), including the near wall node, resulted in  $y^+$  being below the laminar cutoff in Fuego and an asymptotic heat transfer (Nusselt number) that was 65% too large. Only one element was used in the  $z$  direction since the simulation was effectively 2D.

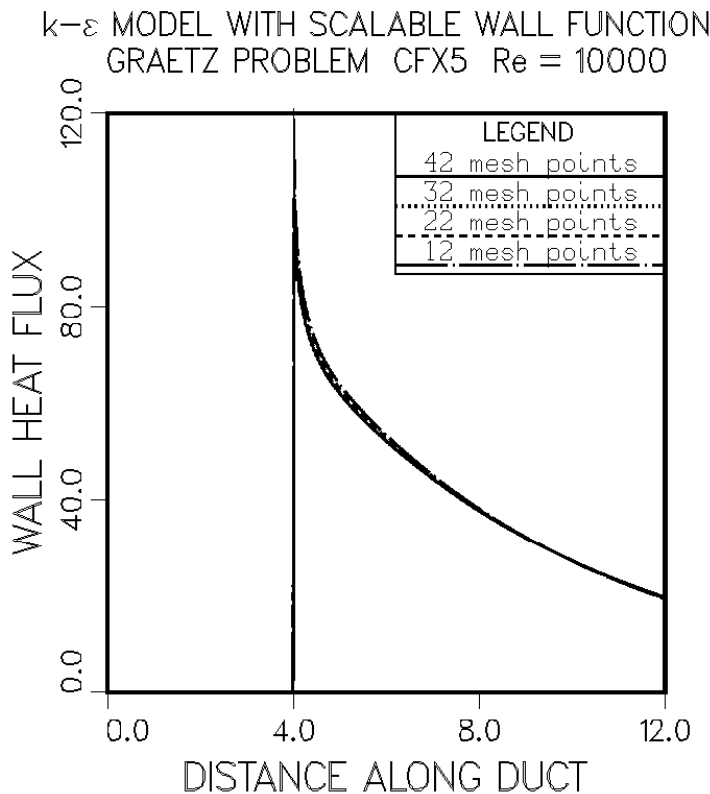


**Figure 6.8-1.. Local heat flux distribution on heated channel wall: CFX results with different mesh spacing.**

## 6.9. SOLUTION PROCEDURE

Options selected in the Fuego run are listed in Table 6.9-1. The calculation was run to a stop time of 15 seconds. This time was significantly beyond steady-state and corresponds to approximately 10 flow through times in the channel.

## 6.10. VERIFICATION EXPERIMENTS

### 6.10.1. Code comparisons

Predictions of the local heat transfer along the heated wall of the channel from Fuego, CFX5, and Özışık et al. [10] are shown in dimensionless form in Fig. 6.10-1 for Re=50,000.

Here the local Nusselt number is given by:

$$\text{Nu}_{\text{local}} = \frac{4b q_w}{k(T_w - T_b)} \quad (6.1)$$

k- $\varepsilon$  MODEL COMPARISON OF STANDARD AND SCALABLE  
GRAETZ PROBLEM CFX5 Re = 10000

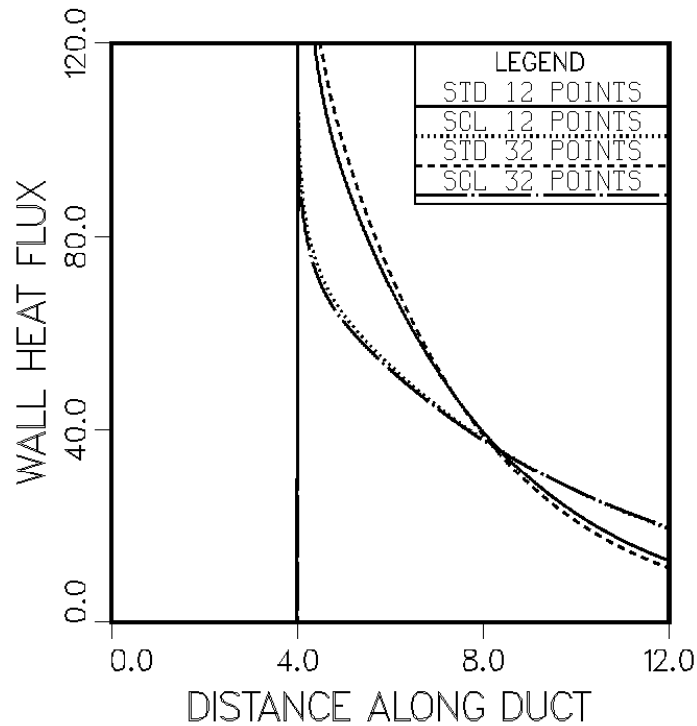


**Figure 6.8-2.. Local heat flux distribution on heated channel wall: CFX results with different mesh spacing and different wall functions.**

where  $b$  is the half-height of the channel (2.54 cm);  $q_w$  and  $T_w$  are the heat flux and temperature at the wall, respectively;  $k$  and  $T_b$  are the thermal conductivity and bulk temperature of the flowing gas, respectively, where

$$T_b(x) = \frac{1}{u_{\text{avg}} b} \int_0^b u T dy \quad (6.2)$$

The dimensionless axial coordinate,  $\xi$ , is given by:

$$\xi = \frac{16x}{4b C \text{Re} \text{Pr}} \quad (6.3)$$

where  $x$  is the axial coordinate measured from the start of the heated section,  $C = u_{\text{max}}/u_{\text{avg}}$ ,  $\text{Re} = u_{\text{avg}} 4b/\nu$  is the Reynolds number, and  $\text{Pr} = \nu/\alpha$  is the Prandtl number. In these equations,  $u_{\text{max}}$  is the maximum axial velocity,  $u_{\text{avg}}$  is the average axial velocity, and  $\nu$  and  $\alpha$  are the kinematic viscosity and thermal diffusivity of the gas, respectively. Özişik et al. [10] give  $C = 1.139$  for  $\text{Re}=50,000$ ; the relation between  $\xi$  and  $x$  for  $\text{Pr}=0.72$  and  $b=2.54$  cm is:

$$\xi = 3.841 \times 10^{-5} x \quad (6.4)$$

where  $x$  is given in units of cm. Using the velocity profile calculated in Fuego,  $C = 1.118$ , which is a difference of 1.8% from [10]. This difference arises from differences between the velocity profile

<b>CFL LIMIT:</b>	5.0
<b>TIME STEP CHANGE FACTOR:</b>	1.25
<b>TRANSIENT STEP TYPE:</b>	automatic
<b>PROJECTION METHOD:</b>	smoothed WITH timestep SCALING
<b>UPWIND METHOD:</b>	UPW
<b>FIRST ORDER UPWIND FACTOR:</b>	1.0
<b>underrelaxation factors:</b>	0.3 on $k$ , $\epsilon$ , and $h$
<b>nonlinear iterations per time step:</b>	1
<b>SOLUTION METHOD:</b>	gmres
<b>PRECONDITIONING METHOD:</b>	symmetric-gauss-seidel
<b>PRECONDITIONING STEPS:</b>	continuity:3; all other equations:1
<b>RESTART ITERATIONS:</b>	continuity:50; all other equations:25
<b>MAXIMUM ITERATIONS:</b>	continuity:150; all other equations:50
<b>RESIDUAL NORM TOLERANCE:</b>	continuity:1.0e-3; all other equations:1.0e-2
<b>RESIDUAL NORM SCALING:</b>	Ro

**Table 6.9-1.. Fuego job parameters**

calculated in Fuego and that assumed in [10]. The velocity profile changes from the plug velocity profile used as the boundary condition at the inlet of the channel in the Fuego and CFX5 simulations to a fully developed profile at  $x \approx 275$  cm (approximately 27 channel hydraulic diameters, where the channel hydraulic diameter is given by four times the channel half-height) after an overshoot in the centerline velocity of approximately 3.5%.

Profiles of the axial component of velocity across the half-height of the channel at  $x=350$  cm (upstream of the start of the heated surface) and at  $x=1100$  cm from Fuego and CFX5 are shown in Fig. 6.10-2. Although the temperature difference between the channel wall and inlet air flow was limited to 10 K to minimize the effects of variable properties, there is a small increase in the axial velocity of about 2% seen in Fig. 6.10-2 due to the density decrease that accompanies the bulk air temperature rise from 300 K at  $x=400$  cm to approximately 306 K at the outlet of the channel ( $x=1200$  cm).

Profiles of the turbulent kinetic energy and dissipation rate across the half-height of the channel at  $x=350$  cm (upstream of the start of the heated surface) and at  $x=1100$  cm from Fuego and CFX5 calculations are shown in Figs. 6.10-3 and 6.10-4, respectively. The pressure drop along the centerline of the channel from Fuego and CFX5 calculations is compared in Fig. 6.10-5.

## 6.10.2. Sensitivity of heat transfer to wall function parameters

Both Fuego and CFX5 used a turbulent Prandtl number,  $Pr_t$ , of 0.9; the analytical solution [10] is for  $Pr_t=1.0$ . The so-called ‘pee-function’ (Launder [15]), which is used to modify the heat transfer law of the wall when  $Pr_t \neq Pr$  and which is supported in Fuego, was removed from Fuego for the heat transfer comparisons shown in Fig. 6.10-1. This was done to reduce model differences when comparing with the analytical solution. However, CFX5 contains an expression due to Kader [11] that modifies the thermal law of the wall and differs in functional form from the ‘pee-function’ implemented in Fuego,

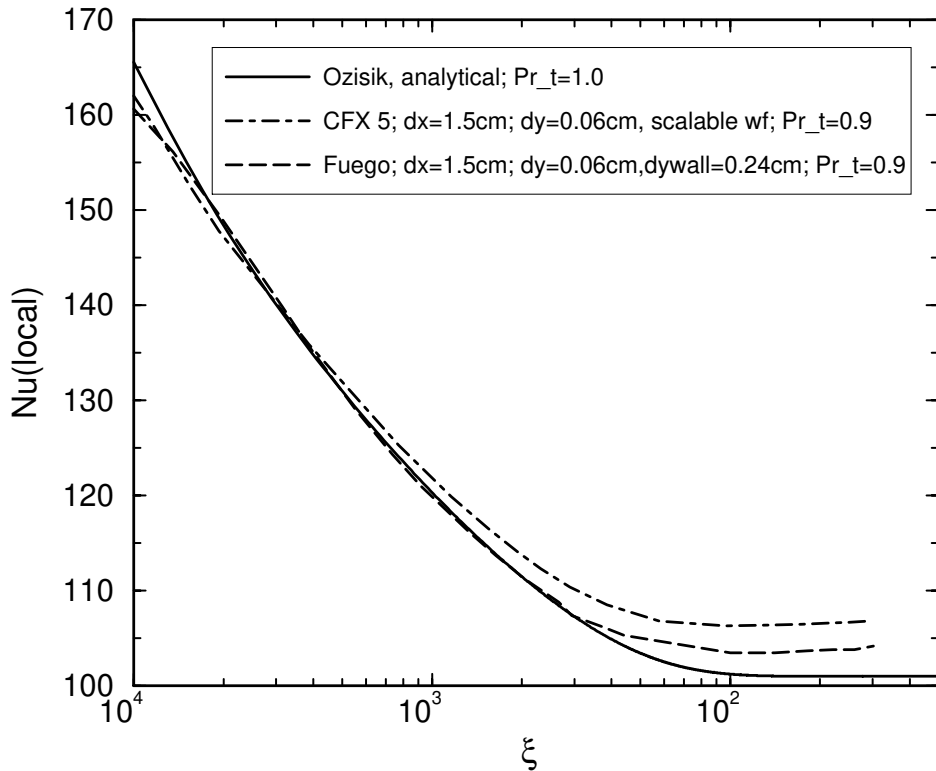


**Figure 6.10-1.. Local Nusselt number distribution on heated channel wall: Fuego, CFX5, and Özişik solutions at  $Re=50,000$ .**

making comparisons of the heat transfer between the two codes subject to model differences. Currently there are outstanding questions concerning the functional form of the thermal law of the wall in CFX5. Contacts have been made with CFX staff to resolve these issues.

As a result of these different parameters, several Fuego simulations were made where  $Pr_t$  was changed from 0.8 to 1.0, with and without the ‘pee-function’. The results for the local Nusselt number are shown in Fig. 6.10-6.

Increasing  $Pr_t$  by approximately 10% results in a reduction in  $Nu_{local}$  by approximately the same amount. Including the ‘pee-function’, which is a function of  $Pr_t/Pr_t$ , results in an increase in  $Nu_{local}$  of a similar amount. Finally, a calculation with  $Pr_t=1.0$  and the ‘pee-function’ results in an increase in  $Nu_{local}$  over the base case ( $Pr_t=0.9$  with no ‘pee-function’) result; this increase is larger in the thermally developing region than in the asymptotic region.

Variations of  $Nu_{local}$  with  $Pr_t$  calculated with CFX5 are shown in Fig. 6.10-7. Although the trends are the same as seen with Fuego(cf. Fig. 6.10-6), the magnitudes of the variations are smaller in CFX5.

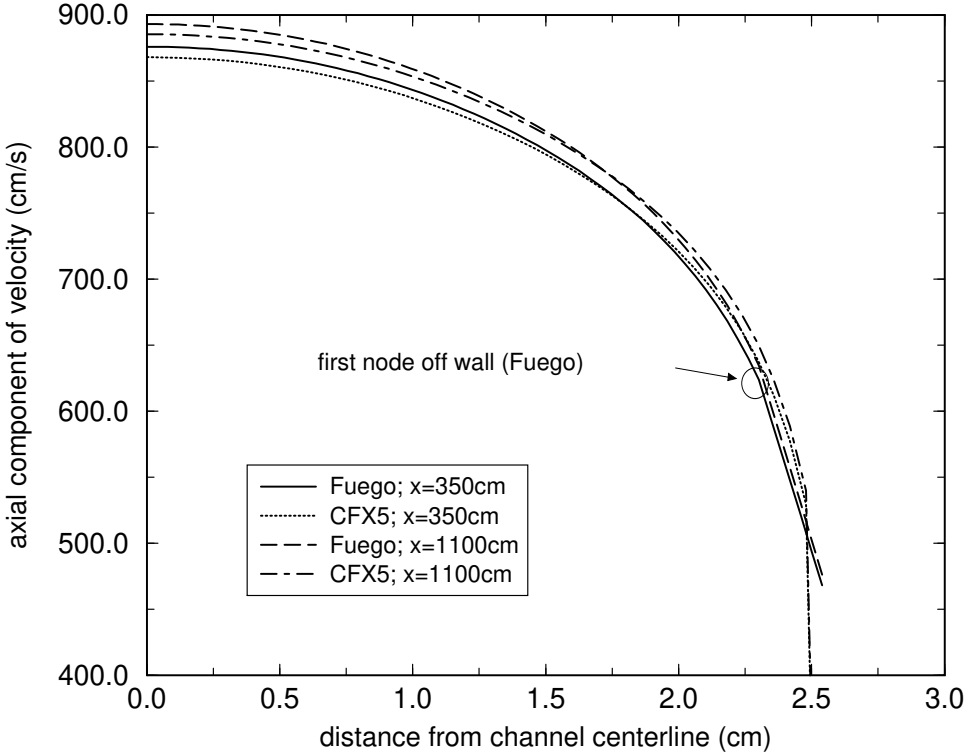


**Figure 6.10-2.. Axial component of velocity profiles across channel half-width upstream and downstream of start of heated channel wall; comparisons between Fuego and CFX5;  $Re=50,000$ .**

### 6.10.3. Sensitivity of heat transfer to mesh spacing and mesh rotation

The sensitivity of  $Nu_{local}$  calculated in Fuego to mesh spacing is shown in Fig. 6.10-8. First the  $x$  and  $y$  mesh spacing was increased by approximately 20% over the base case mesh, but the single near-wall  $\Delta y_{wall}$  value was fixed at the base case mesh value of 0.242 cm. Changing the mesh by 20% resulted in changes to  $Nu_{asym}$  of much less than 1% and changes to  $Nu_{local}$  on the order of 1% in the thermally developing region. Next the near-wall mesh spacing was increased by approximately 30% so that  $y^+$  increased from about 16 to about 21. This result had a negligible effect on  $Nu_{asym}$ ; a decrease in  $Nu_{local}$  of less than 5% was noted near the location of the step change in wall temperature.

The effects of mesh rotation on  $Nu_{local}$  were examined for two configurations. The effects of gravity were not considered in the present study. In the first configuration the mesh was rotated about the  $z$  axis by 90 degrees so that the channel was oriented in the  $+y$  direction. In the second configuration the mesh was rotated about the  $z$  axis by 45 degrees so that the channel was inclined by 45 degrees to the  $+x$  axis. This latter configuration resulted in the inlet velocity to the channel having both  $x$  and  $y$  components; also both  $x$  and  $y$  components of momentum were affected by the wall function formulation. The Fuego results (not shown) for  $Nu_{local}$  for these two mesh rotations agreed to within a fraction of a percent with the unrotated base case results; these small differences can easily be attributed to the extensive post processing required to obtain  $Nu_{local}$ .

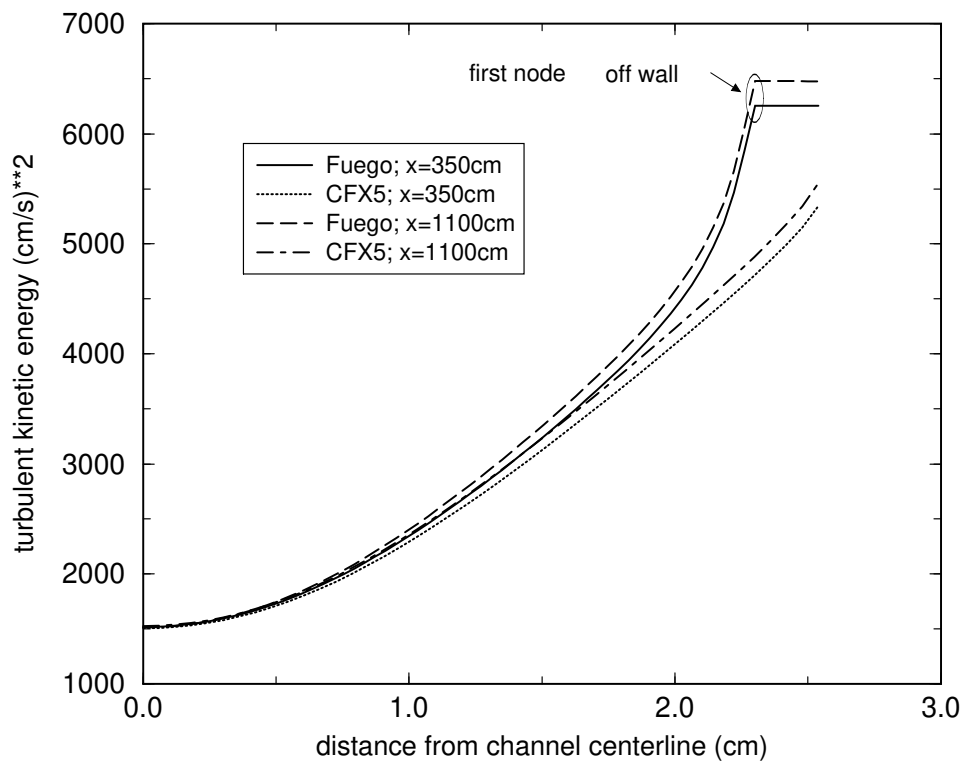


**Figure 6.10-3.. Turbulent kinetic energy profiles across channel half-width, upstream and downstream of start of heated channel wall; comparisons between Fuego and CFX5;  $\text{Re}=50,000$ .**

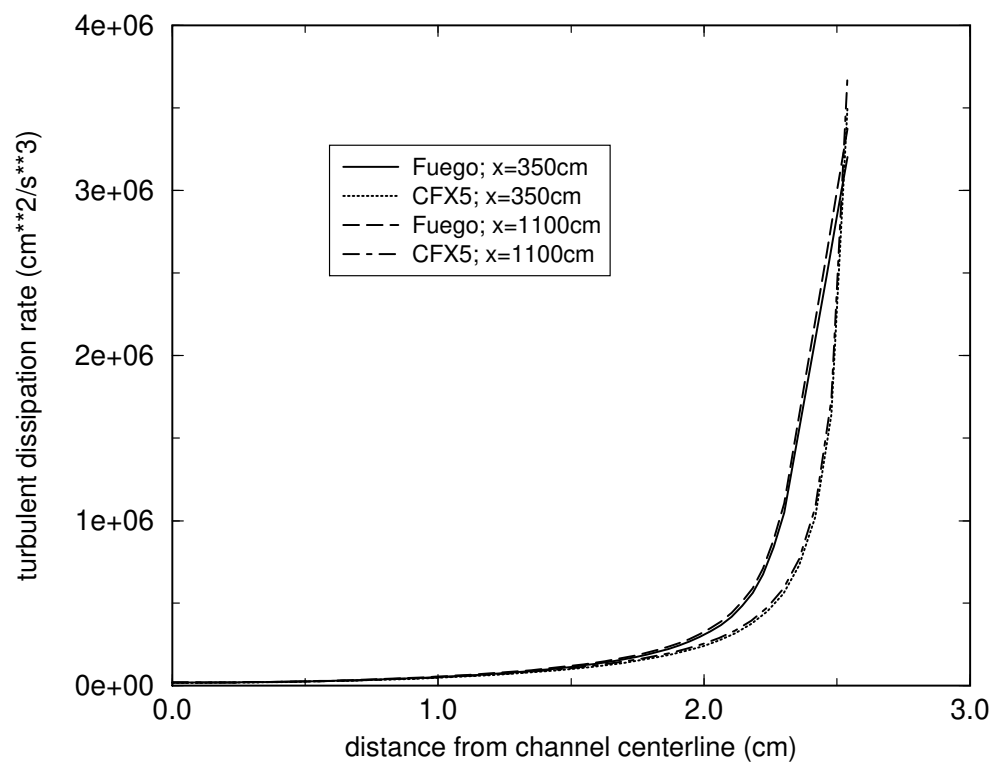


**Figure 6.10-4.. Turbulent dissipation rate profiles across channel half-width, upstream and downstream of start of heated channel wall; comparisons between Fuego and CFX5;  $Re=50,000$ .**

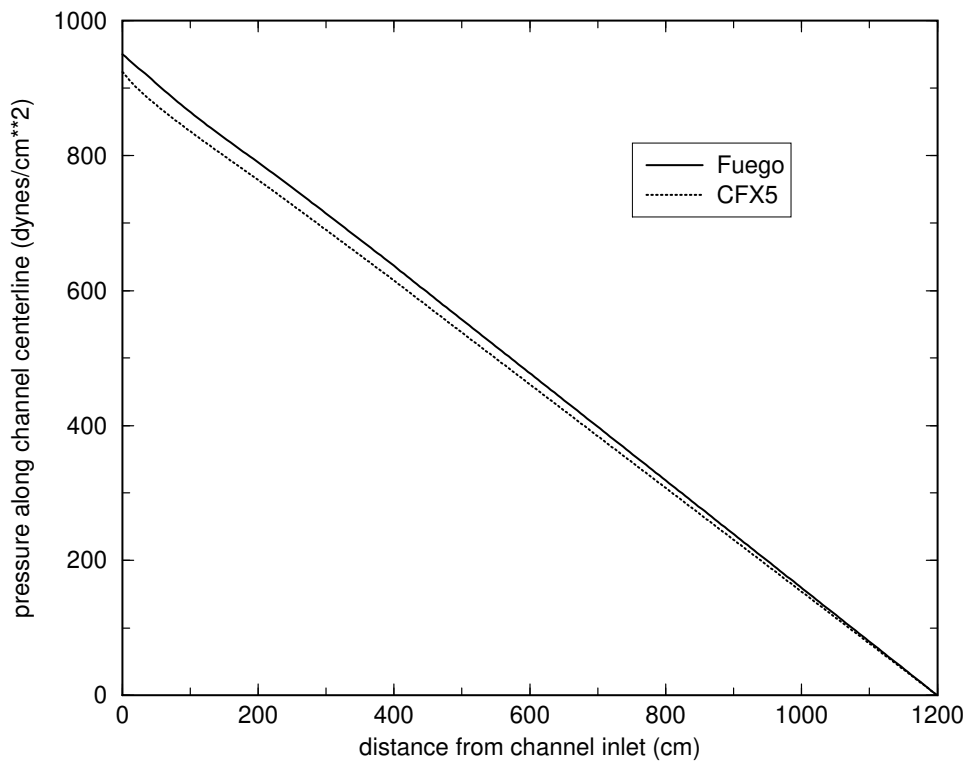


**Figure 6.10-5.. Pressure drop along the centerline of the channel; comparison between Fuego and CFX5; Re=50,000.**

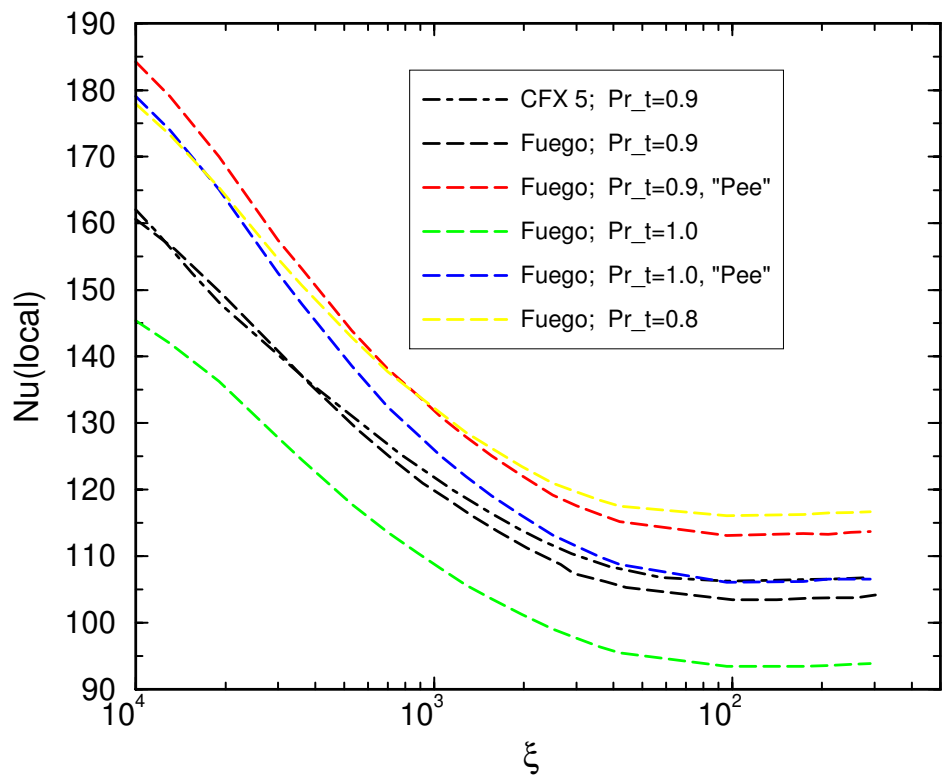


**Figure 6.10-6.. Local Nusselt number distribution on heated channel wall: Fuego results for various thermal wall law parameters;  $Re=50,000$ ; CFX5 result at  $Pr_t=0.9$  shown for comparison.**

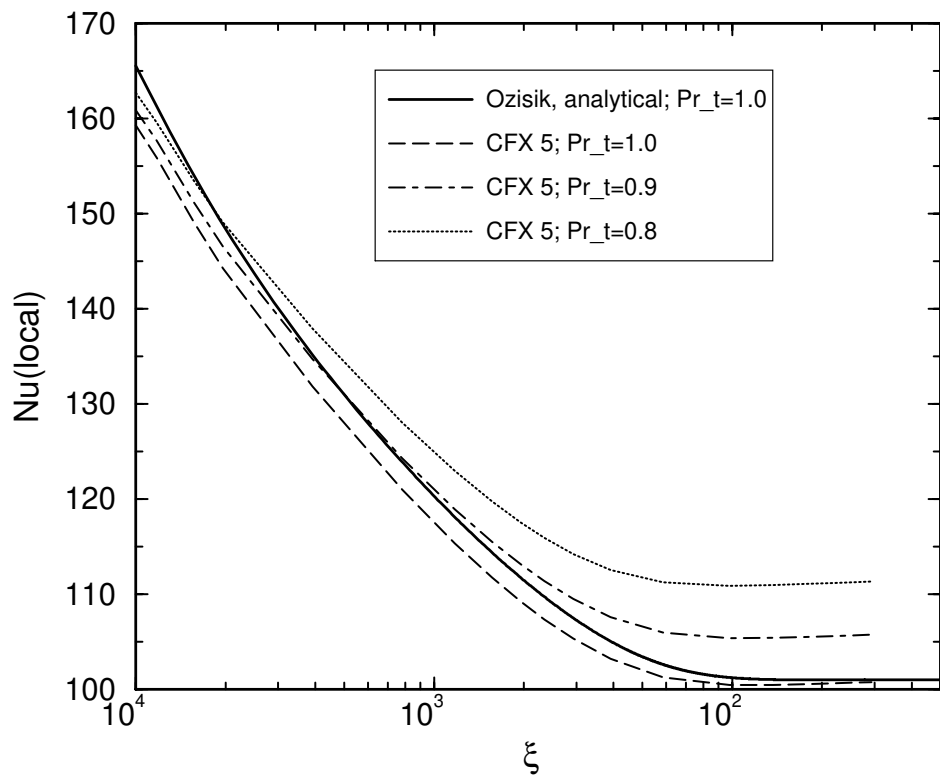


**Figure 6.10-7.. Local Nusselt number distribution on heated channel wall: CFX5 results for three values of  $Pr_t$ ; analytical solution for  $Pr_t=1.0$ ;  $Re=50,000$ .**

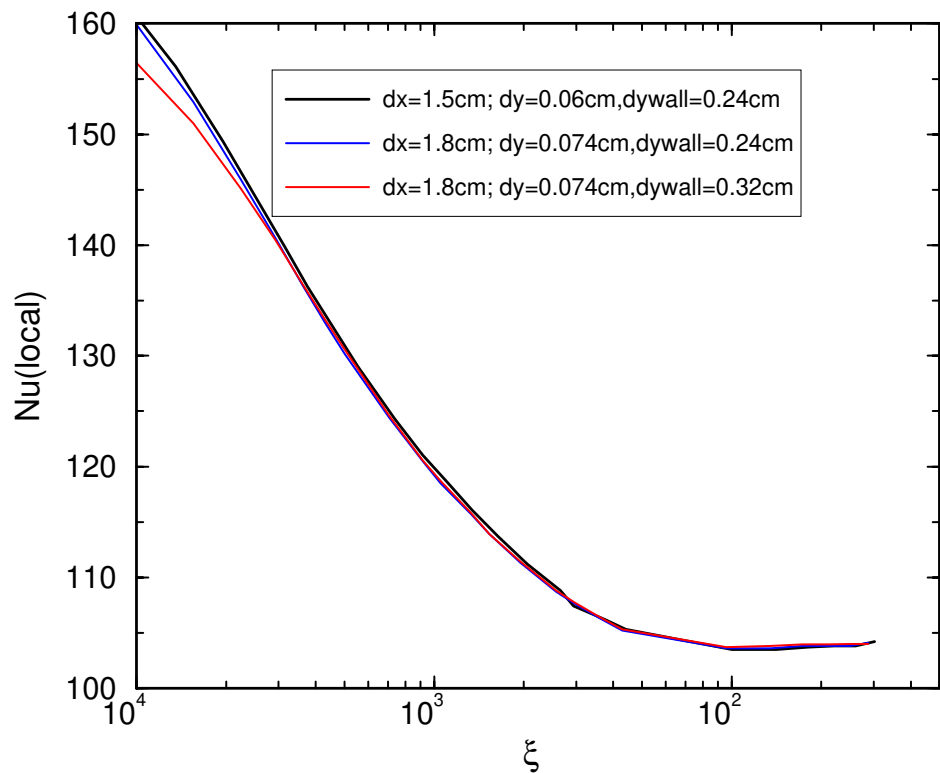


**Figure 6.10-8.. Local Nusselt number distribution on heated channel wall: sensitivity of Fuego results to mesh spacing;  $\text{Re}=50,000$ ;  $\text{Pr}_t=0.9$ .**

This page intentionally left blank.

# 7. EDC COMBUSTION MODEL

<b>Dimension:</b>	oD
<b>Transient/Steady:</b>	N/A
<b>Laminar/Turbulent:</b>	N/A
<b>Isothermal/Thermal:</b>	N/A
<b>Temperature/Enthalpy:</b>	N/A
<b>Uniform/Nonuniform:</b>	N/A
<b>Combustion:</b>	EDC
<b>Soot:</b>	N/A
<b>Coupled Mechanics:</b>	N/A
<b>Regression Test:</b>	no

The EDC model verification strategy is to use a unit test. The unit test queries the Afgo::Region method responsible for computing the EDC source terms.

The unit test expects inputs and provides outputs.

## 7.1. EXECUTIVE SUMMARY

The verification effort for the EDC Turbulent Combustion Model in FUEGO 1.0 has been completed. Verification, as defined for this effort, has been conducted as a comparison of hand calculated values utilizing the equations defined in the Draft FUEGO Theory Manual, Version 0.8.0, with identified output from the EDC model code modules. A unit test routine, written by Warren Tauber and modified by Stefan Domino, Chris Moen and myself, was utilized to exercise the EDC model and produce the code output. The verification effort identified a couple of minor discrepancies and these are reported in this memo. Further, the unit test routine has been coded to be used as a regression test for future verification work on the EDC model. In addition to the verification work, a concerted effort was made to evaluate the Fortran modules used in the EDC model with the goal to streamline and potentially speed-up the code. This effort identified such issues as variables passed through argument lists that are no longer used in the module and variables passed through as arrays that are used as single constants within the module. These will also be articulated within this memo. FUEGO Verification Effort The preliminary step to the verification effort required running FUEGO on a sample problem to develop single point states from the simulation to be used as input to the unit test. The sample problem selected was an open 5m JP-8 pool fire. The simulation was allowed to run approximately one minute to achieve a reasonably steady fire. Discrete points were queried within the final graphic output using

EnSight and several data states within the fire simulation (ie, fuel rich, fuel lean, etc.) were saved as input to the unit test code. The results of the verification work are presented sequentially by Fortran module. The output variables from each module are identified and the verification comparisons are made. Discrepancies among the comparisons are rectified. Additionally, code streamlining issues will be reported for each Fortran module as appropriate.

The first module encountered in the EDC model is *Afgo\_EDC\_Initialize.F*. This module initializes (or populates) the indices and stoichiometric coefficients for the combustion equations to be solved based on the specific hydrocarbon fuel for the application problem. Calls are made to Chemkin routines from this module to evaluate the stoichiometric coefficients. Primarily, this routine establishes a code implementation system for a standardized numbering scheme and therefore no comparison to theory is required.

The next module evaluated is *Afgo\_EDC\_Ignite.F*. This module calculates product mass fractions in cells that have been identified for ignition. The output variable from this module is YPROD, which is the mass fraction of products from the secondary combustion (CO<sub>2</sub> and H<sub>2</sub>O only, neglecting the diluents). There are two branches for calculating YPROD, depending on the value of a flag that determines whether a transport equation is used during the solve or not. When a transport equation is not used, the value of YPROD calculated by *Afgo\_EDC\_Ignite.F* is 0.86883348. A hand calculation, using Equation 2.153 from the Theory Manual, yields a value of 0.868191 for YPROD. The small difference in values is due to the number of significant digits of constants used in the computations (ie, 2 in the Theory Manual and 3 in the Fortran routine). Also, it should be noted that the mass normalization used in Equation 2.153 was not used during this calculation. When the flag determines that a transport equation is used during the calculation of YPROD, there are two possible solutions for YPROD. The first branch determines that the cell is currently undergoing combustion. When this condition exists, the value of YPROD "falls through" the routine and yields the input value to the routine, in this case a value of 0.869 from the Unit test file. When combustion has not been initiated in the cell, then *Afgo\_EDC\_Ignite.F* calculates a value of YPROD of 0.0259055. The hand calculated value for YPROD under these conditions is 0.025906, which compares favorably with the code calculated value. The hand calculation was computed based on a discussion in the "Ignition Criteria" section of the Theory Manual. It is recommended that the equation for this YPROD parameter under these conditions be explicitly defined in the Theory Manual.

Regarding the code streamlining effort, there are two recommendations for this Fortran module. First, the variable TEMP has been passed through the argument list in this subroutine call. There is no indication that TEMP is being used in the routine and therefore can be eliminated from the argument list. The second recommendation is not definitive and is left to a code developer to innovate a solution. It was noted that the routine completes all calculations for the initial ignition of the cell, even though the cell may currently be experiencing combustion (hence the calculations are spurious). Suggestions to check for existing combustion include cell temperature and incoming values of YPROD (since the potential product mass fraction calculated at the initiation of cell combustion is generally small).

The third module evaluated in the EDC model is *Afgo\_EDC\_TurbTime.F*. This routine evaluates the characteristic scales for the combustion model. There are two output variables for this routine: TRES, which is the residence time in the fine structure (flame region), and GAMMA, which is the dissipative to integral length scale ratio. The calculation of the variables is straightforward and there are no additional logical branches in this routine. The Fortran routine calculates a value of 0.0008475 for

TRES. The hand calculation, using Equation 2.177 from the Theory Manual, yields a value of 0.000851. The small discrepancy is due to the Fortran routine implementation rounding off the inverse of a constant to two decimal places. The Fortran routine calculates a value of 0.0056207 for GAMMA, while the hand calculation, using Equation 2.166 from the Theory Manual, yields a value of 0.005621.

The streamlining effort suggests that the parameter TCHAR in the subroutine call signature and the computation performed in the Fortran routine be eliminated. Greg Evans confirms that the parameter was used in an earlier version, but is no longer utilized.

The fourth module evaluated in the EDC model is *Afgo\_EDC\_Limit.F*. This routine calculates a limiter on the EDC combustion model, termed CHI, and a reaction rate multiplier, termed ETA. There are two logical paths through this routine. The first path considers the case of no primary or secondary fuel. In this case, the values for CHI and ETA are fixed at 0 and 1, respectively, and a quick check of this case confirms the implementation of the default values. For the case when there is fuel present, the routine calculates a value of 4.2943926 for CHI. The hand calculation for CHI, which utilizes Equations 2.144, 2.145, 2.164 and several supporting arguments, yields a value of 4.29439, which is comparable to the same significant digits. The value of ETA calculated by the Fortran routine is 5.62432445, while the hand calculation, using Equation 2.169 from the Theory Manual, yields a value of 5.6243.

Regarding the streamlining effort, there is only one suggestion. A significant amount of effort is undertaken within this routine to calculate the variable CHI. However, outside of the EDCLIM subroutine in *Afgo\_Region.C*, the value of CHI is limited to 0.99. During the current evaluation, the calculated value of CHI always exceeded 0.99, hence it was limited. Perhaps there is a method to approximate CHI to determine if it would be limited and therefore minimize the computations.

The fifth module evaluated in the EDC model is *Afgo\_EDC\_IrrevChem.F*. This routine calculates SPECFS(), which is the array of mass fractions of each species as the two chemical reactions occur in the fine structure. There is only one logical path through this routine. The hand calculations employed Equations 2.106, 2.107, 2.120 and 2.121 from the Theory Manual. The comparison of the fine structure mass fractions for all the species are shown in Table 1. It should be noted for this particular unit test case that the first reaction is fuel limited, while the second reaction is oxygen limited. As observed, the comparisons are favorable, considering the hand calculations use only a few significant digits during the computations. Of mild interest is the appearance of zeros, which result from a limiter in the routine which redefines negative values (albeit small negative values) to be zero.

<b>Fuel:</b>	0.0, 0.0
<b>Oxygen:</b>	1.626e-18, 0.0
<b>Carbon Monoxide:</b>	0.0228379, 0.022753
<b>Carbon Dioxide:</b>	0.19510527, 0.195266
<b>Hydrogen:</b>	0.001848915, 0.001843
<b>Water Vapor:</b>	0.08986685, 0.089941
<b>Nitrogen:</b>	0.6903, 0.6903

There are no recommendations for streamlining this module. However, consideration should be given to cleaning up write statements at the bottom of the module which may be leftover from early versions when the module was undergoing debug testing.

The sixth module evaluated in the EDC model is *Afgo\_EDC\_FineStruct.F*. This routine calculates the state properties of the fine structure region, including the temperature TFS, the density RHOFS, and the kinematic viscosity NUFS. There is only one logical path through this routine, although the solution methodology uses an iterative technique. The routine calculates a value of 1967.997 for TFS, while the hand calculation yields a value of 1968.02. The hand calculation employs Equation 2.180 from the Theory Manual, enthalpy values from the Chemkin routine and a standard thermodynamic relationship between temperature, enthalpy and specific heat. The routine calculates a value of 1.7299087e-04 for RHOFS, while the hand calculation produced a value of 1.735e-04. Equation 2.183 from the Theory Manual was used for this calculation. Round-off error associated with the species molecular weights contributed to the small discrepancies in the two values. Finally, the routine calculates a value of 3.7605 for the kinematic viscosity NUFS, while the hand calculation produces a value of 3.756. The standard thermodynamic relationship between dynamic viscosity, density and kinematic viscosity was used in the hand calculation. The dynamic viscosity values for the mixture constituents were obtained from the Chemkin routines. The difference in values is attributed to the small difference in the density values.

There are a couple of recommendations for streamlining this routine. First, computations are performed to calculate the fine structure kinematic viscosity and then the kinematic viscosity is redefined as the cell kinematic viscosity (consistent with VULCAN implementation). Rather than performing the computations, the fine structure implementation should be commented until the implementation becomes the default method. Second, there should be consideration given to relaxing the tolerance limit established for the iterative procedure. Specifically, the current tolerance value is 1.e-08, which when combined with a typical flame temperature requires a convergence of the flame temperature to the fifth decimal place (order of magnitude). In stepping through this routine, I noted that at least 1 or 2 iterations could be eliminated and still achieve convergence to 2 or 3 decimal places (ie, convergence to 0.0005 percent).

The seventh module evaluated in the EDC model is *Afgo\_EDC\_Surround.F*. This routine calculates the state properties of the surrounding region, including the temperature TSU and the density RHOSU. The calculations performed in this routine mirror those of the previous routine, with the exception that the kinematic viscosity calculations have been omitted. The routine calculates a value of 1705.763 for TSU, while the hand calculation yields a value of 1705.527 (the difference results from rounding off the enthalpy and specific heat values obtained from Chemkin). The hand calculation utilized Equation 2.181 from the Theory Manual. The routine calculates a value of 1.97955 for RHOSU, while the hand calculation yields a value of 1.9786. Equation 2.184 from the Theory Manual was used for this calculation, with the small difference in values attributed to rounding off species molecular weight values used in the computation.

There are a couple of recommendations for streamlining this routine. First, several variables are passed through the main subroutine call that are currently extraneous. Specifically, the variables are NU, TKE and EPSILON, which were used previously for calculation of the turbulent and low Reynolds numbers. However, these computations are currently commented out, therefore the aforementioned variables can be removed from the call signature. Second, the first computations performed in this routine ensure that the fine structure species mass fractions are greater than zero by at least 1.D-50. These logical checks and assignments could be eliminated since the computations are being duplicated

upstream in the *Afgo\_EDC\_IrrevChem.F* module, with one modification. Within the IrrevChem routine, modify the statement of MAX (ZERO, SPECFS()) to be MAX(1.D-50, SPECFS()).

The eighth module evaluated in the EDC model is *Afgo\_EDC\_Average.F*. This routine calculates the average cell properties, including the cell temperature TCELL, the cell density RHOCELL, and the average radiation emission QRAD. There is only one logical path through this routine. The routine calculates a value of 1707.223 for TCELL. The hand calculation, using Equation 2.171 from the Theory Manual, yields a comparable value of 1707.219 for TCELL. The routine calculates a value of 1.9779e-04 for RHOCELL, while the hand calculation produces a value of 1.98e-04 using Equation 2.173 from the Theory Manual. Finally, the routine calculates a value of 8.50752e+12 for QRAD, while the hand calculation yields a value of 8.514e+12 using Equation 2.182 (excluding the absorptivity parameter and the Stefan Boltzmann constant, which are factors applied outside of this routine).

There is one recommendation for streamlining this routine. The local parameter TAVGB is calculated but never used in the routine and therefore should be eliminated or commented out.

The ninth and final module evaluated in the EDC model is *Afgo\_EDC\_Source.F*. This routine calculates the chemical production rates of the species per unit volume, denoted as the variable RATE. There are two paths through this module, based on the nodal temperature passed into the routine. If the temperature exceeds 2500 degrees, the source term is set to zero. Along the alternate path, the module calculates a value of 0.0073377 for the variable RATE. The hand calculation, using Equation 2.179 from the Theory Manual, yields a value of 0.007338. It should be noted that the RATE variable calculated by this routine does not include the mass fraction species difference term, as this calculation is done in *Afgo\_ElemSolverWS.C* (because of the way that the species transport equation is cast for solution). Also, the Theory Manual has an error in the species mass conservation, Equation 2.125, where the time averaged mixture density was not included in the source term integral. For purposes of this verification work, the average cell density was incorporated in the calculation, as implemented in the routine.

There is only one recommendation for streamlining this routine. Several variables are passed in the call statement to the subroutine that are not utilized in the routine and should be removed. These variables include SPEC, SPECFS and RHOSU.

## 7.2. SOLUTION PROCEDURE

hand Calculation

## 7.3. SAMPLE OUTPUT

Sample Output from the current Unit Test Code for the EDC Model in FUEGO

DistributionChemkin Universal Gas Constant is 8.31451e+07 erg/mol/K Chemkin Atmospheric Pressure is 1.01325e+06 dyne/cm\*\*2

Chemkin Species Molecular Weight IC8H18 114.233 O2 31.9988 CO 28.0106 CO2 44.01 H2 2.01594 H2O 18.0153 N2 28.0134

DENSITY = 0.00117787 VISCOSITY = 0.000185546 ENTHALPY = -1.17691e+06 SPECIFIC HEAT = 1.01099e+07 k = 0 spec[0] = -4.29869e-20 fracFS[0] = 1e-50 fracSU[0] = 0.0036664 spec[1] = 1.6263e-18 fracFS[1] = 1.6263e-18 fracSU[1] = 0.0258639 spec[2] = 0.0228379 fracFS[2] = 0.0228379 fracSU[2] = 0.0335697 spec[3] = 0.195105 fracFS[3] = 0.195105 fracSU[3] = 0.166943 spec[4] = 0.00184892 fracFS[4] = 0.00184892 fracSU[4] = 0.00271784 spec[5] = 0.0898669 fracFS[5] = 0.0898669 fracSU[5] = 0.0768978 spec[6] = 0.6903 fracFS[6] = 0.6903 fracSU[6] = 0.6903 local max chi = 4.29439 local chi count = 1 tempFS = 1968 tempSU = 1705.76 densFS = 0.000172991 densSU = 0.000197955 nuFS = 5581.98 tres = 0.000847509 eta = 5.62432 gammachi = 0.00556447 yproduct = 0.869 rate = 0.00733771 emission = 1.53559e+08

# 8. EDC SOOT MODEL

<b>Dimension:</b>	oD
<b>Transient/Steady:</b>	N/A
<b>Laminar/Turbulent:</b>	N/A
<b>Isothermal/Thermal:</b>	N/A
<b>Temperature/Enthalpy:</b>	N/A
<b>Uniform/Nonuniform:</b>	N/A
<b>Combustion:</b>	EDC
<b>Soot:</b>	yes
<b>Coupled Mechanics:</b>	no
<b>Regression Test:</b>	no

## 8.1. MATERIAL SPECIFICATIONS

## 8.2. INITIAL CONDITIONS

## 8.3. BOUNDARY CONDITIONS

## 8.4. ANALYTIC OR BENCHMARK SOLUTION

## 8.5. MESH DEFINITION

## 8.6. SOLUTION PROCEDURE

## 8.7. VERIFICATION EXPERIMENTS

This page intentionally left blank.

# 9. PROGRESS VARIABLE MODEL FOR SOOT

<b>Dimension:</b>	1D
<b>Transient/Steady:</b>	Steady
<b>Laminar/Turbulent:</b>	Laminar
<b>Isothermal/Thermal:</b>	Thermal
<b>Temperature/Enthalpy:</b>	Yes
<b>Uniform/Nonuniform:</b>	Nonuniform
<b>Combustion:</b>	Mixture Fraction
<b>Soot:</b>	Yes
<b>Coupled Mechanics:</b>	no
<b>Regression Test:</b>	no

For the Aksit-Moss soot model [16] using progress variables we integrate the following equation set

$$\rho \frac{DZ}{Dt} = \nabla \cdot \left( \frac{\mu}{Sc} \nabla Z \right) + \dot{S}_Z \quad (9.1)$$

$$\rho \frac{DN}{Dt} = \dot{S}_N = \dot{S}_{\text{nucl.}} + \dot{S}_{\text{coag.}} \quad (9.2)$$

$$\rho \frac{DM}{Dt} = \dot{S}_M = W_s \dot{S}_{\text{nucl.}} + \dot{S}_{\text{surf.}} - \dot{S}_{\text{oxid.}} \quad (9.3)$$

$$\rho \frac{Dh}{Dt} = \nabla \cdot \left( \frac{\mu}{Pr} \nabla h \right) + \nabla \cdot q_{\text{ext}} \quad (9.4)$$

$$\rho \frac{Dh_c}{Dt} = \nabla \cdot \left( \frac{\mu}{Pr} \nabla h_c \right) \quad (9.5)$$

$$Z_{\text{lookup}} = \frac{Z}{1 - M/\rho} \quad (9.6)$$

with source terms for the progress variables (soot number density and soot mass concentration,  $N$  and  $M$  respectively) determined partially from tabulated flamelet solutions and progress variables. The modification to the density to account for soot accumulation

$\rho = \rho(Z, \chi, h - h_c) + \left(1 - \frac{\rho_g(Z, \chi, h - h_c)}{\rho_s}\right) M$  is turned off to compare with a simple ODE system.

The mixture fraction source is defined from the Bilger definition of the mixture fraction, which is

defined through the atomic mass fractions of carbon, hydrogen, and oxygen ( $Y_C$ ,  $Y_H$ , and  $Y_O$ ) as

$$Z = \frac{\gamma_C(Y_C - Y_{C,ox})/W_C + \gamma_H(Y_H - Y_{H,ox})/W_H + \gamma_O(Y_O - Y_{O,ox})/W_O}{\gamma_C(Y_{C,fuel} - Y_{C,ox})/W_C + \gamma_H(Y_{H,fuel} - Y_{H,ox})/W_H + \gamma_O(Y_{O,fuel} - Y_{O,ox})/W_O}. \quad (9.7)$$

With the formation of soot, the mixture fraction describes the gas-phase fuel alone. The atomic mixture fractions are individually leaned proportionally to the growth of soot mass fraction in order to represent the change of composition. For the mass fraction of carbon in the gas-phase, the transport equation is

$$\rho \frac{DY_C^g}{Dt} = \alpha_C(\phi, N, M) \dot{S}_M, \quad (9.8)$$

where  $\alpha_C$  represents the average mass fraction of carbon atoms within a soot particle as a function of the thermochemical gas composition and various soot moments ( $\phi, N, M$ ). Replacing the elemental mass fractions in Eq. (9.7) with their equivalent gas-phase mass fractions and taking the material derivative, with a constant atomic composition of soot, the source term for the gas-phase mixture fraction is directly proportional the source for the mass concentration of soot:

$$\rho \frac{DZ^g}{Dt} = \frac{\gamma_C \alpha_C/W_C + \gamma_H \alpha_H/W_H + \gamma_O \alpha_O/W_O}{\gamma_C(Y_{C,fuel} - Y_{C,ox})/W_C + \gamma_H(Y_{H,fuel} - Y_{H,ox})/W_H + \gamma_O(Y_{O,fuel} - Y_{O,ox})/W_O} \dot{S}_M. \quad (9.9)$$

With typical atomic mass fractions of soot ( $\sim 97\%$  carbon) and a pure ethylene fuel stream mixing with air, the coefficient multiplying the mass concentration source is  $\sim 0.73$ . As the flamelet database does not account for the loss of mass to soot, a modified “lookup” mixture fraction is defined, normalized by the mass of gas ( $1 - Y_s$ ) to compensate.

The fine particle model is composed of terms describing nucleation, coagulation, surface growth, and oxidation. The nucleation is taken to be proportional to the molar concentration of acetylene:

$$\dot{S}_{\text{nucl.}} = C_{\text{nucl.}} X_{\text{C}_2\text{H}_2} \frac{P}{RT} \exp(-21, 100/T) [\text{mol m}^{-3} \text{s}^{-1}], \quad (9.10)$$

The value of  $C_\alpha$  is chosen based on empirical results as  $54.0 \text{ s}^{-1}$ . The coagulation model affects only the number density source and uses the similarity solution for coagulation in the free-molecular regime assuming spherical particles with an average diameter  $D = (6M/(\pi \rho_s N))^{1/3}$

$$\dot{S}_{\text{coag.}} = \left( \frac{24RT}{\rho_s N_a} \right)^{1/2} \left( \frac{6}{\rho_s \pi} \right)^{1/6} N_A^{5/6} N^{11/6} M^{1/6}. \quad (9.11)$$

Surface growth is also considered to be proportional to the acetylene concentration and affects the mass concentration as

$$\dot{S}_{\text{surf.}} = C_{\text{surf.}} X_{\text{C}_2\text{H}_2} \frac{P}{RT} \left( \frac{6}{\rho_s} \right)^{1/6} (\pi N_A)^{1/3} \exp(-12, 100/T) N^{1/3} M^{2/3}. \quad (9.12)$$

The value of  $C_\gamma$  is also empirical in origin and is taken to be  $11.7 \times 10^3 \text{ m}^{-2} \text{s}^{-1}$ .

The oxidation model consists of both OH and O<sub>2</sub> oxidation terms. The OH oxidation is

$$\dot{S}_{\text{oxid.,OH}} = C_{\text{OH}} X_{\text{OH}} \frac{P}{RT} \left( \frac{6}{\rho_s} \right)^{2/3} (\pi N_A)^{1/3} T^{1/2} N^{1/3} M^{2/3}, \text{ and} \quad (9.13)$$

$$\dot{S}_{\text{oxid.,O}_2} = C_{\text{O}_2} X_{\text{O}_2} \frac{P}{RT} \left( \frac{6}{\rho_s} \right)^{2/3} (\pi N_A)^{1/3} T^{1/2} \exp(-19,680/T) N^{1/3} M^{2/3}. \quad (9.14)$$

The O<sub>2</sub> oxidation was ignored by [16], and so the O<sub>2</sub> oxidation was taken from [17] instead, with constants  $C_{\text{OH}} = 4.23$  and  $C_{\text{O}_2} = 500$ .

## 9.1. INITIAL CONDITION

A velocity of 0.001 m/s is initialized. The mixture fraction is kept constant at  $Z = 0.153333$  and a temperature of  $T = 1641$  is chosen to match the value of temperature for the corresponding mixture fraction at the lowest value of scalar dissipation and heat loss, as well as zero scalar variance.

## 9.2. BOUNDARY CONDITIONS

The domain is long rectangular prism with an inflow/outflow condition at the front and back and symmetry conditions at the sides.

## 9.3. ANALYTIC OR BENCHMARK SOLUTION

The steady solution is compared with a numerical integration of the corresponding nonlinear ODE system in Matlab using the exact values from the underlying flamelet simulation.

## 9.4. SAMPLE OUTPUT

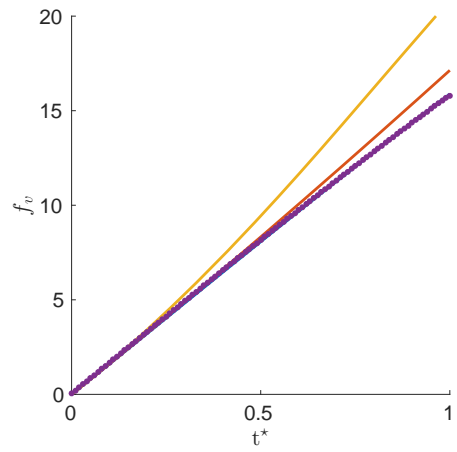


**Figure 9.4-1.. Comparison of results (Blue: solution with leaning and a change to the mixture fraction lookup; Orange, no lookup mixture fraction modification; Yellow, no mixture fraction sink or lookup mixture fraction; Fuego, purple circles;)** for a short time. Mapping ignores density variation.

# 10. RADIATION PROPERTIES

<b>Dimension:</b>	oD
<b>Transient/Steady:</b>	N/A
<b>Laminar/Turbulent:</b>	N/A
<b>Isothermal/Thermal:</b>	N/A
<b>Temperature/Enthalpy:</b>	N/A
<b>Uniform/Nonuniform:</b>	N/A
<b>Combustion:</b>	EDC
<b>Soot:</b>	yes
<b>Coupled Mechanics:</b>	N/A
<b>Regression Test:</b>	no

## 10.1. MATERIAL SPECIFICATIONS

## 10.2. INITIAL CONDITIONS

## 10.3. BOUNDARY CONDITIONS

## 10.4. ANALYTIC OR BENCHMARK SOLUTION

## 10.5. MESH DEFINITION

## 10.6. SOLUTION PROCEDURE

## 10.7. VERIFICATION EXPERIMENTS

This page intentionally left blank.

# 11. TURBULENT DIFFUSION FLAME

<b>Dimension:</b>	3D
<b>Transient/Steady:</b>	steady
<b>Laminar/Turbulent:</b>	turbulent
<b>Isothermal/Thermal:</b>	thermal
<b>Temperature/Enthalpy:</b>	enthalpy
<b>Uniform/Nonuniform:</b>	nonuniform
<b>Combustion:</b>	EDC
<b>Soot:</b>	no
<b>Coupled Mechanics:</b>	no
<b>Regression Test:</b>	no

## 11.1. MATERIAL SPECIFICATIONS

## 11.2. INITIAL CONDITIONS

## 11.3. BOUNDARY CONDITIONS

## 11.4. ANALYTIC OR BENCHMARK SOLUTION

## 11.5. MESH DEFINITION

## 11.6. SOLUTION PROCEDURE

## 11.7. VERIFICATION EXPERIMENTS

This page intentionally left blank.

# 12. GAS PROPERTIES

<b>Dimension:</b>	oD
<b>Transient/Steady:</b>	N/A
<b>Laminar/Turbulent:</b>	N/A
<b>Isothermal/Thermal:</b>	N/A
<b>Temperature/Enthalpy:</b>	N/A
<b>Uniform/Nonuniform:</b>	N/A
<b>Combustion:</b>	N/A
<b>Soot:</b>	N/A
<b>Coupled Mechanics:</b>	N/A
<b>Regression Test:</b>	fuego/gas_props_helium fuego/gas_props_methane fuego/gas_props_octane

Thermodynamic and transport properties can be specified three ways in Fuego: by constant value, by a piecewise linear function of temperature, and by using the ChemkinIII libraries [18, 19]. For turbulent heat and/or mass transport, we always use the ChemkinIII libraries. This unit test will verify property evaluations for three different problems using ChemkinIII: a turbulent helium plume in air, a turbulent methane pool fire, and a turbulent JP-8 (octane) fuel fire.

The material property evaluations follow different pathways in the code depending on how the state is defined. We allow the use of either a constant reference temperature, a constant reference composition, constant reference temperature and reference composition, or no reference states. Three of the modes most commonly used are tested.

The ChemkinIII libraries have been modified relative to the original version in order to properly function with SIERRA; namely, the FORTRAN common blocks have been replaced with one-dimensional data arrays. All properties evaluated with the ChemkinIII routines in Fuego are verified to match to within the four significant digits reported by an external ChemkinIII material evaluation program called DATA.

## 12.1. ANALYTIC OR BENCHMARK SOLUTION

The property evaluations performed with the SIERRA implementation of ChemkinIII are compared against a stand-alone ChemkinIII application, DATA. This program computes properties for gas

mixtures: version 1.01 of July 1993 by J. F. Grcar.

## 12.2. MESH DEFINITION

Not applicable.

## 12.3. MATERIAL SPECIFICATIONS

helium/air: He, O<sub>2</sub>, and N<sub>2</sub>.

methane/air: CH<sub>4</sub>, CO<sub>2</sub>, CO, H<sub>2</sub>, H<sub>2</sub>O, O<sub>2</sub>, and N<sub>2</sub>.

octane/air: C<sub>8</sub>H<sub>18</sub>, CO<sub>2</sub>, CO, H<sub>2</sub>, H<sub>2</sub>O, O<sub>2</sub>, and N<sub>2</sub>.

Material properties for each chemical species are computed from curve fits maintained by ChemkinIII [20], though we use a variation of the curve fits available from the Combustion and Reaction Simulation (CRSIM) group at the University of Utah. The numbers from the thermodynamic database are shown in Table 12.7-4 and the numbers from the transport database are shown in Table 12.7-5. Ready-made Chemkin “linking files” for the different gas mixtures are available at <http://www.engsci.sandia.gov/fuego/chemkin>. The linking files contain specific data from the tables for a particular gas composition.

The thermal conductivity and mass diffusivity are derived from a constant Prandtl number and Schmidt number when the turbulence model is active. Values for these properties are not reported since they are derived.

The universal gas constant is  $8.31451 \times 10^7$  erg/mole/K. One atmospheric pressure is  $1.01325 \times 10^6$  dyne/cm<sup>2</sup>.

## 12.4. INITIAL CONDITIONS

Not applicable.

## 12.5. BOUNDARY CONDITIONS

Not applicable.

## 12.6. SOLUTION PROCEDURE

During the initialization of the material property evaluator in Fuego, material properties corresponding to the reference state are reported. The reference material properties are evaluated using a similar code pathway as nodal material properties. The test procedure is to compare several reference states against an external ChemkinIII material evaluation program.

The Fuego test is carried out by setting a particular reference state, an equation configuration option, and then running a one-element problem.

The properties are evaluated using the stable version Fuego-0.07.

## 12.7. VERIFICATION EXPERIMENTS

Three different gas mixtures are used to test three different property evaluation modes. All properties compare to within the four significant figures reported by the benchmark program, DATA. All properties are reported in cgs units.

### 12.7.1. Helium/Air

The helium/air property evaluations are performed using the isothermal, nonuniform composition pathway. Two states are considered, shown in Table 12.7-1. The reference pressure is one atmosphere for both evaluations. Composition is in mole fractions.

State 1:  $T=500$  K,  $X_{he} = 0.2$ ,  $X_{o2} = 0.2$ , and  $X_{n2} = 0.6$ .

State 2:  $T=2000$  K,  $X_{he} = 0.5$ ,  $X_{o2} = 0.3$ , and  $X_{n2} = 0.2$ .

**Table 12.7-1.. Properties for helium/air, cgs units.**

	State 1	State 2
$\rho$	0.000585156	0.000104826
$\mu$	0.000277165	0.000747441
$h$	2.33727e+09	2.71249e+10
$C_p$	1.173e+07	1.68148e+07

### 12.7.2. Methane/Air

The methane/air property evaluations are performed using the thermal, uniform composition pathway. Two states are considered, shown in Table 12.7-2. The reference pressure is one atmosphere for both evaluations. Composition is in mole fractions.

State 1:  $T=500$  K,  $X_{ch4} = 0.05$ ,  $X_{o2} = 0.2$ ,  $X_{n2} = 0.7$ ,  $X_{h2} = 0.0125$ ,  $X_{h2o} = 0.0125$ ,  $X_{co} = 0.0125$ , and  $X_{co2} = 0.0125$ .

State 2:  $T=2000$  K,  $X_{ch4} = 0.15$ ,  $X_{o2} = 0.15$ ,  $X_{n2} = 0.15$ ,  $X_{h2} = 0.15$ ,  $X_{h2o} = 0.1$ ,  $X_{co} = 0.15$ , and  $X_{co2} = 0.15$ .

**Table 12.7-2.. Properties for methane/air, cgs units.**

	State 1	State 2
$\rho$	0.000681518	0.000148159
$\mu$	0.000263207	0.000638855
$h$	-2.4862e+09	-1.55268e+10
$C_p$	1.10996e+07	2.05619e+07

### 12.7.3. Octane/Air

The octane/air property evaluations are performed using the thermal, nonuniform composition pathway. Two states are considered, shown in Table 12.7-3. The reference pressure is one atmosphere for both evaluations. Composition is in mole fractions.

State 1:  $T=500$  K,  $X_{c8h18} = 0.05$ ,  $X_{o2} = 0.2$ ,  $X_{n2} = 0.7$ ,  $X_{h2} = 0.0125$ ,  $X_{h2o} = 0.0125$ ,  $X_{co} = 0.0125$ , and  $X_{co2} = 0.0125$ .

State 2:  $T=2000$  K,  $X_{c8h18} = 0.15$ ,  $X_{o2} = 0.15$ ,  $X_{n2} = 0.15$ ,  $X_{h2} = 0.15$ ,  $X_{h2o} = 0.1$ ,  $X_{co} = 0.15$ , and  $X_{co2} = 0.15$ .

**Table 12.7-3.. Properties for octane/air, cgs units.**

	State 1	State 2
$\rho$	0.000801177	0.000237904
$\mu$	0.000240797	0.000544745
$h$	-3.75596e+09	8.28101e+09
$C_p$	1.31727e+07	3.00535e+07

**Table 12.7-4.. Thermodynamic curve fit data for ChemkinIII.**  
**Source: CRSIM, University of Utah.**

HE	0.02500000E+02	0.00000000E+00	0.00000000E+00	0.00000000E+00
	0.00000000E+00	-0.07453750E+04	0.09153489E+01	0.02500000E+02
	0.00000000E+00	0.00000000E+00	0.00000000E+00	0.00000000E+00
	-0.07453750E+04	0.09153488E+01		
O <sub>2</sub>	0.03697578E+02	0.06135197E-02	-0.12588420E-06	0.01775281E-09
	-0.11364354E-14	-0.12339301E+04	0.03189165E+02	0.03212936E+02
	0.11274864E-02	-0.05756150E-05	0.13138773E-08	-0.08768554E-11
	-0.10052490E+04	0.06034737E+02		
N <sub>2</sub>	0.02926640E+02	0.14879768E-02	-0.05684760E-05	0.10097038E-09
	-0.06753351E-13	-0.09227977E+04	0.05980528E+02	0.03298677E+02
	0.14082404E-02	-0.03963222E-04	0.05641515E-07	-0.02444854E-10
	-0.10208999E+04	0.03950372E+02		
CO	0.03025078E+02	0.14426885E-02	-0.05630827E-05	0.10185813E-09
	-0.06910951E-13	-0.14268350E+05	0.06108217E+02	0.03262451E+02
	0.15119409E-02	-0.03881755E-04	0.05581944E-07	-0.02474951E-10
	-0.14310539E+05	0.04848897E+02		
CO <sub>2</sub>	0.04453623E+02	0.03140168E-01	-0.12784105E-05	0.02393996E-08
	-0.16690333E-13	-0.04896696E+06	-0.09553959E+01	0.02275724E+02
	0.09922072E-01	-0.10409113E-04	0.06866686E-07	-0.02117280E-10
	-0.04837314E+06	0.10188488E+02		
H <sub>2</sub>	0.02991423E+02	0.07000644E-02	-0.05633828E-06	-0.09231578E-10
	0.15827519E-14	-0.08350340E+04	-0.13551101E+01	0.03298124E+02
	0.08249441E-02	-0.08143015E-05	-0.09475434E-09	0.04134872E-11
	-0.10125209E+04	-0.03294094E+02		
H <sub>2</sub> O	0.02672145E+02	0.03056293E-01	-0.08730260E-05	0.12009964E-09
	-0.06391618E-13	-0.02989921E+06	0.06862817E+02	0.03386842E+02
	0.03474982E-01	-0.06354696E-04	0.06968581E-07	-0.02506588E-10
	-0.03020811E+06	0.02590232E+02		
CH <sub>4</sub>	0.01683478E+02	0.10237236E-01	-0.03875128E-04	0.06785585E-08
	-0.04503423E-12	-0.10080787E+05	0.09623395E+02	0.07787415E+01
	0.01747668E+00	-0.02783409E-03	0.03049708E-06	-0.12239307E-10
	-0.09825229E+05	0.13722195E+02		
C <sub>8</sub> H <sub>18</sub>	2.71373590E+01	3.79004890E-02	-1.29437358E-05	2.00760372E-09
	-1.16400580E-13	-4.07958177E+04	-1.23277495E+02	-4.20868893E+00
	1.11440581E-01	-7.91346582E-05	2.92406242E-08	-4.43743191E-12
	-2.99446875E+04	4.49521701E+01		

**Table 12.7-5.. Transport property data for ChemkinIII. Source: CRSIM, University of Utah.**

HE	0	10.200	2.576	0.000	0.000	0.000
O <sub>2</sub>	1	107.400	3.458	0.000	1.600	3.800
N <sub>2</sub>	1	97.530	3.621	0.000	1.760	4.000
CO	1	98.100	3.650	0.000	1.950	1.800
CO <sub>2</sub>	1	244.000	3.763	0.000	2.650	2.100
H <sub>2</sub>	1	38.000	2.920	0.000	0.790	280.000
H <sub>2</sub> O	2	572.400	2.605	1.844	0.000	4.000
CH <sub>4</sub>	2	141.400	3.746	0.000	2.600	13.000
C <sub>8</sub> H <sub>18</sub>	2	458.500	6.414	0.000	0.000	1.000

# 13. TRANSIENT BUOYANT FLOW

<b>Dimension:</b>	3D
<b>Transient/Steady:</b>	unsteady
<b>Laminar/Turbulent:</b>	laminar
<b>Isothermal/Thermal:</b>	thermal
<b>Temperature/Enthalpy:</b>	enthalpy
<b>Uniform/Nonuniform:</b>	uniform
<b>Combustion:</b>	no
<b>Soot:</b>	no
<b>Coupled Mechanics:</b>	no
<b>Regression Test:</b>	no

## 13.1. MATERIAL SPECIFICATIONS

## 13.2. INITIAL CONDITIONS

## 13.3. BOUNDARY CONDITIONS

## 13.4. ANALYTIC OR BENCHMARK SOLUTION

## 13.5. MESH DEFINITION

## 13.6. SOLUTION PROCEDURE

## 13.7. VERIFICATION EXPERIMENTS

This page intentionally left blank.

# 14. BUOYANT FLOW WITH PMR

<b>Dimension:</b>	3D
<b>Transient/Steady:</b>	steady
<b>Laminar/Turbulent:</b>	laminar
<b>Isothermal/Thermal:</b>	thermal
<b>Temperature/Enthalpy:</b>	temperature
<b>Uniform/Nonuniform:</b>	uniform
<b>Combustion:</b>	no
<b>Soot:</b>	no
<b>Coupled Mechanics:</b>	syrinx
<b>Regression Test:</b>	fuego/pmrA_sk_0.125 fuego/pmrA_sk_1.25 fuego/pmrB_sk_0.125 fuego/pmrB_sk_1.25

Coupling between the buoyant flow and PMR components is tested using a two-dimensional, buoyant flow/participating media radiation benchmark problem in a horizontal annulus. An absorbing/emitting fluid is bounded by two isothermal surfaces (inner  $T_i$ , and outer  $T_o$ ) within an annular gap. The surfaces are modeled as gray, diffuse with surface emissivity values of unity. The resultant temperature gradient gives rise to natural convection.

## 14.1. MATERIAL SPECIFICATIONS

The physical parameters that define the problem are  $\text{Pr}=0.71$ ,  $T_i = 300 \text{ K}$ ,  $T_o = 150 \text{ K}$ ,  $r_i = 1.0 \text{ cm}$ ,  $r_o = 2.6 \text{ cm}$ ,  $Z = 10.0 \text{ cm}$ ,  $K = 1.0 \text{ cm}^{-1}$ , and  $\text{Ra}_L = 10^4$ .

The Stark number represents the ratio of the conductive to radiative heat flux,

$$\text{Sk} = \frac{\kappa K}{\sigma T_i^3}, \quad (14.1)$$

where  $\kappa$  is the thermal conductivity,  $K$  is the extinction coefficient, and  $\sigma$  is the Stefan-Boltzmann coefficient. The other parameter that defines the extent of the buoyancy driven flow is the Rayleigh number,

$$\text{Ra}_L = \frac{g\beta(T_i - T_o)L^3}{\text{Pr} \alpha^2}, \quad (14.2)$$

where  $g$  is the gravitational acceleration,  $\beta = 1/T_i$  is the coefficient of volume expansion for an ideal gas,  $L$  is the annular gap distance,  $\text{Pr}$  is the Prandtl number, and  $\alpha$  is the thermal diffusivity of the fluid. In practice, Eq.(14.1) is manipulated such that the Stefan-Boltzmann parameter becomes the dependent variable which is modified to match the Stark number of choice. Likewise, the annular Rayleigh number Eq.(14.2) is rearranged and simplified such that the desired Rayleigh number, is obtained through manipulation of the gravity field. Table 14.1-1 outlines the appropriate values for the Stefan-Boltzmann parameter, gravity, thermal diffusivity, and thermal conductivity.

**Table 14.1-1.. Physical properties for natural convection/radiation problem for  $\text{Ra}_L = 10^4$ .**

Sk	$g$ $\text{cm}/\text{s}^2$	$\sigma$ $\text{erg}/\text{cm}^2/\text{s}/K^4$	$\kappa$ $\text{erg}/\text{cm}/\text{s}/K$	$\alpha$ $\text{cm}^2/\text{s}$
1.25	173.6395	$7.774815 \times 10^{-5}$	2624	0.2238
0.125	173.6395	$7.774815 \times 10^{-4}$	2624	0.2238

## 14.2. INITIAL CONDITIONS

The pressure and velocities are initialized to zero. The initial temperature is 250 K.

## 14.3. BOUNDARY CONDITIONS

For the fluid mechanics equations, the inner and outer cylinders are isothermal, no-slip surfaces. The nodal velocities are fixed to zero. The nodal temperatures are set to the surface temperatures. The end-caps are treated as symmetry planes.

For the radiation transport, all boundary surfaces are black.

## 14.4. ANALYTIC OR BENCHMARK SOLUTION

The benchmark metric is the average Nusselt number evaluated at the inner surface,

$$\overline{\text{Nu}}_i = \frac{r_i \int q_t dA}{\kappa A (T_o - T_i)}, \quad (14.3)$$

where  $q_t$  is the total heat flux to the inner surface including conduction and radiation,  $dA$  is the differential surface area, and  $A$  is the total area of the inner surface. Our results are summarized in Table 14.7-1 along with results from other two-dimensional studies. In the study of Burns [21], a two-dimensional mesh consisting of 20x30 biquadratic elements was used. The  $S_9$  discrete ordnance approximation was employed and the radiative energy equation was solved using a finite element formulation. The results of Morales and Campo [22] reflect the use of the less accurate P-1 formulation.

## 14.5. MESH DEFINITION

Several nonuniform grids are used in this problem and listed in Table 14.7-1. The meshes consist of 3D hexahedral elements.

In order to achieve two-dimensionality with the three-dimensional code, we make the annulus sufficiently long ( $Z$ ) such that black boundary conditions on the end caps have little effect on the radiation field at the center plane [23]. The end caps are treated as slip planes with no heat conduction.

## 14.6. SOLUTION PROCEDURE

Most calculations are run with the  $S_{10}$  approximation. The  $Sk=1.25$  case updates the radiation field every 5 time steps. The  $Sk=0.125$  case is more sensitive to the radiation field and is updated every 3 time steps. The convection scheme is the MUSCL scheme, but large portions of the mesh meet the conditions for transition to the centered scheme.

The linear solver for the continuity equation was GMRES with two steps of symmetric Gauss-Seidel preconditioning. The linear convergence tolerance was 1.oe-8 with  $R_o$  scaling. The linear solver for the momentum equations was GMRES with five steps of Jacobi preconditioning. The linear convergence tolerance was 1.oe-4 with  $R_o$  scaling. The linear solver for the temperature equation was GMRES with five steps of Jacobi preconditioning. The linear convergence tolerance was 1.oe-5 with  $R_o$  scaling. The linear solver for the PMR equations was stabilized bi-conjugate gradient with a third-order polynomial preconditioning. The linear convergence tolerance was 1.oe-6 with  $R_o$  scaling. Dirichlet boundary conditions are enforced exactly in all cases.

## 14.7. VERIFICATION EXPERIMENTS

The average inner Nusselt number is given in Table 14.7-1 for a series of mesh refinements. The Fuego/Syrinx solutions are run with the  $S_{10}$  approximation which proved to be more than enough ordinate directions. The  $S_4$  approximation has five times fewer ordinate directions than the  $S_{10}$  approximation, but changes the average Nusselt number by less than a percent.

The coarse mesh was run with 8 processors on a SUN Enterprise server. The medium mesh was run with 64 processors on the Intel Teraflop machine. The fine mesh was run with 256 processors and the  $S_6$  approximation on the Intel Teraflop machine. The fraction of time spent between the equation evaluations and linear solves is shown in Table 14.7-2. In each of the mesh refinements (coarse to fine), the Fuego code took 17%, 14%, and 25% of the total compute time. Note that the fine mesh was run with fewer ordinate directions and required roughly 40% less work in the Syrinx module. We feel that the element assembly times for the Fuego code are excessive. A hexahedral element has twelve interior sub-faces, each an integration point. Much of the time is dominated by computing shape function derivatives at integration points. Storage of the gradients would cost 288 floating-point numbers per element. A more desirable numerical approach is to use an edge-connected difference stencil with an

**Table 14.7-1.. Average inner surface Nusselt number,  $\text{Ra}_L = 10^4$ , on different grids (radial  $\times$  azimuthal  $\times$  axial).**

	$\overline{\text{Nu}}_i$ $\text{Sk}=1.25$	$\overline{\text{Nu}}_i$ $\text{Sk}=0.125$
Fuego/Syrinx (16x64x24)	2.74	10.6
Fuego/Syrinx (32x128x40)	2.84	11.0
Fuego/Syrinx (64x256x80)	2.86	—
Burns [21]	2.96	11.4
Morales and Campo [22]	3.16	14.5

edge assembly procedure. The geometry can then be stored on edges, reducing the number of integration points. The speed of the code increases because the assembly work decreases (no geometry evaluation and fewer integration points) and the linear system is smaller.

**Table 14.7-2.. Computing resource expenditure for  $\text{Sk}=1.25$ . Fraction of time spent in assembling the linear systems and solving the linear systems for the different meshes.**

	Fuego Assemble	Fuego Solve	Syrinx Assemble	Syrinx Solve
(16x64x24)	0.09	0.78	0.02	0.98
(32x128x40)	0.09	0.78	0.02	0.98
(64x256x80)	0.05	0.83	0.01	0.99

Each of the aforementioned benchmark studies predicted the migration of the vortex center to below the annulus centerline for decreasing Stark number and the approach to one dimensional heat transfer, evident by the flattening of the temperature contours, as radiation effects are increased. Contour plots of the steady-state temperature and stream function contours at the center plane of the horizontal annulus, shown in Figures 14.7-1 and 14.7-2, also indicate the downward migration of the vortex center as radiation effects become more important (decreasing Stark number).

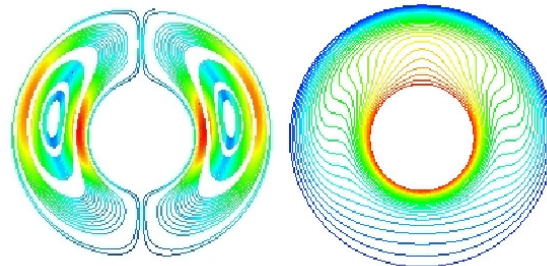


**Figure 14.7-1.. Stream function (left image; colored by velocity vector magnitude) and temperature (right image; colored by temperature) contours for (79x120x20);  $\text{Sk} = 1.25$  and  $\text{Ra}_L = 10^4$ .**

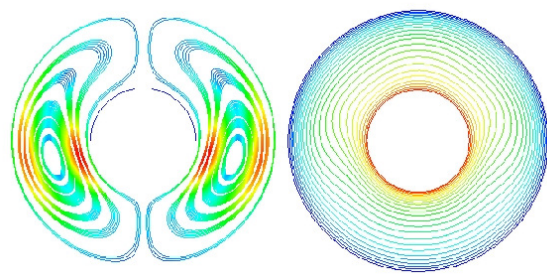


**Figure 14.7-2.. Stream function (left image; colored by velocity vector magnitude) and temperature (right image; colored by temperature) contours for (79x120x20);  $Sk = 0.125$  and  $Ra_L = 10^4$ .**

This page intentionally left blank.

# 15. FIVE-METER POOL FIRE

<b>Dimension:</b>	3D
<b>Transient/Steady:</b>	steady
<b>Laminar/Turbulent:</b>	turbulent
<b>Isothermal/Thermal:</b>	thermal
<b>Temperature/Enthalpy:</b>	enthalpy
<b>Uniform/Nonuniform:</b>	nonuniform
<b>Combustion:</b>	EDC
<b>Soot:</b>	yes
<b>Coupled Mechanics:</b>	no
<b>Regression Test:</b>	fuego/5m_jp8_13K_S4 fuego/5m_jp8_F65K_S13K_S4

## 15.1. MATERIAL SPECIFICATIONS

## 15.2. INITIAL CONDITIONS

## 15.3. BOUNDARY CONDITIONS

## 15.4. ANALYTIC OR BENCHMARK SOLUTION

## 15.5. MESH DEFINITION

## 15.6. SOLUTION PROCEDURE

## 15.7. VERIFICATION EXPERIMENTS

This page intentionally left blank.

# 16. MANUFACTURED SOLUTION

<b>Dimension:</b>	3D
<b>Transient/Steady:</b>	steady
<b>Laminar/Turbulent:</b>	laminar
<b>Isothermal/Thermal:</b>	isothermal
<b>Temperature/Enthalpy:</b>	N/A
<b>Uniform/Nonuniform:</b>	uniform
<b>Combustion:</b>	no
<b>Soot:</b>	no
<b>Coupled Mechanics:</b>	no
<b>Regression Test:</b>	fuego/mms_convection_1 fuego/mms_convection_2 fuego/mms_convection_3 fuego/mms_convection_4 fuego/mms_convection_1b fuego/mms_convection_2b fuego/mms_convection_3b fuego/mms_convection_4b

Manufactured solutions are derived to test the momentum and continuity equations at steady state. There are two tests for this problem.

The first test is at a low Reynolds number where the viscous terms dominate. The convected values are approximated using linear averaging (analogous to central differences). The velocity field is not divergence-free. Difficulties are encountered in running the manufactured solutions at higher Reynolds numbers with upwind schemes where the convection terms dominate. Other MMS studies for the incompressible Navier-Stokes equations have also only been performed for low Reynolds numbers [24] or for meshes with small cell Peclet numbers (Domino and Voth for the FAA code verification).

The higher Reynolds number cases work if the manufactured solution is modified such that the velocity is divergence-free.

The errors are computed by comparing the error between the computed solution and the manufactured solution. The errors are computed at nodes.

This series of tests is run with `fuego-0.8.o`.

## 16.1. ANALYTIC OR BENCHMARK SOLUTION

Problem 1:

$$u(x, y, z) = U_0 \cos(\pi x) \sin(\pi y) \sin(\pi z) \quad (16.1)$$

$$v(x, y, z) = U_0 \cos(\pi x) \sin(\pi y) \sin(\pi z) \quad (16.2)$$

$$w(x, y, z) = U_0 \cos(\pi x) \sin(\pi y) \sin(\pi z) \quad (16.3)$$

$$p(x, y, z) = P_0 \quad (16.4)$$

where  $P_0 = 0.0$  and  $U_0 = 0.1$ .

Problem 2:

$$u(x, y, z) = \sin(\pi x) \cos(\pi y) \sin(\pi z) \quad (16.5)$$

$$v(x, y, z) = -\cos(\pi x) \sin(\pi y) \sin(\pi z) \quad (16.6)$$

$$w(x, y, z) = \sin(\pi x) \sin(\pi y) \quad (16.7)$$

$$p(x, y, z) = P_0 \quad (16.8)$$

where  $P_0 = 0.0$ .

The problems are defined for the cubic domain:  $0.0 \leq y, z \leq 1.0$  and  $-0.5 \leq x \leq 0.5$ .

## 16.2. MESH DEFINITION

Four meshes are used in this problem. The geometry is a unit cube, centered at  $(0, \frac{1}{2}, \frac{1}{2})$ . The cube is uniformly meshed with element resolutions of:  $10 \times 10 \times 10$ ,  $20 \times 20 \times 20$ ,  $40 \times 40 \times 40$ , and  $80 \times 80 \times 80$ . The meshes consist of 3D hexahedral elements.

## 16.3. MATERIAL SPECIFICATIONS

Constant properties.

Test 1:  $\rho = 23$ , and  $\mu = 3$ .

Test 2:  $\rho = 1$ , and  $\mu = 0.001$ .

## 16.4. INITIAL CONDITIONS

The manufactured solution is applied as the initial condition.

## 16.5. BOUNDARY CONDITIONS

The domain is fully enclosed by no-slip walls. The velocities are fixed to a value of zero at all the nodes on the walls using the “WALL” boundary condition. There is no explicit condition for the continuity equation since there is no mass flow rate through the wall. Note, if the solution is such that the velocities are non-zero at the boundaries, then an “INFLOW” boundary condition should be used in order to enforce the proper mass flow rate.

## 16.6. SOLUTION PROCEDURE

The projection method is pressure-smoothed with a scaling proportional to time step. Since the analytic solution has a uniform pressure field, there should be little error from the pressure smoothing. The solution is sensitive to the choice of projection method and linear solver parameters. The unsmoothed and stabilized schemes exhibit poor convergence for the continuity equation. The mesh refinement study is performed with a constant maximum CFL number of 0.5. The linear systems for the momentum equation are solved with bicgstab/jacobi(2), exact boundary condition enforcement, Ro residual norm scaling, and a solver tolerance of  $10^{-6}$ . The linear system for the continuity equation is solved with cg/icc, Ro residual norm scaling, and a solver tolerance of  $10^{-8}$ . The convergence for the continuity equation can intermittently lock up or jump. The convergence is sensitive to the right-hand side scaling and the initial solver guess. A randomly-generated vector was used for the pressure system initial guess.

## 16.7. VERIFICATION EXPERIMENTS

Test 1: The problem is run with the laminar element mechanics routines. The residual norms during the time-stepping to steady state are shown in Figure 16.7-1. The error norms of the computational velocity solution against the manufactured velocity solution are shown in Figure 16.7-2. Only the interior nodes are used for the error analysis of the velocity. The boundary conditions are imposed as Dirichlet conditions and contribute no information to the error analysis. The peak velocity is  $U_0 = 0.1$ . All the nodes are used for the error analysis for pressure. Since the pressure can float in this closed domain, the nodal pressure is first normalized to zero. The error norms for pressure are shown in Figure 16.7-3. The spatial errors are greater than first order, but less than second order. The errors are probably due to the near-boundary implementation of the continuity equation. The control volumes associated with boundary nodes are one-sided in the sense that the boundary node sits on a control volume face.

Test 2: The problem is run with the laminar element mechanics routines. The Reynolds number for this problem is 1000 which is well above the range for which we can use a centered scheme. The convection terms dominate at this level, so two of the convection operators are tested – first-order upwind and a second-order upwind (MUSCL). Only the interior nodes are used for the error analysis. The boundary conditions are imposed as Dirichlet conditions and contribute no information to the error analysis.

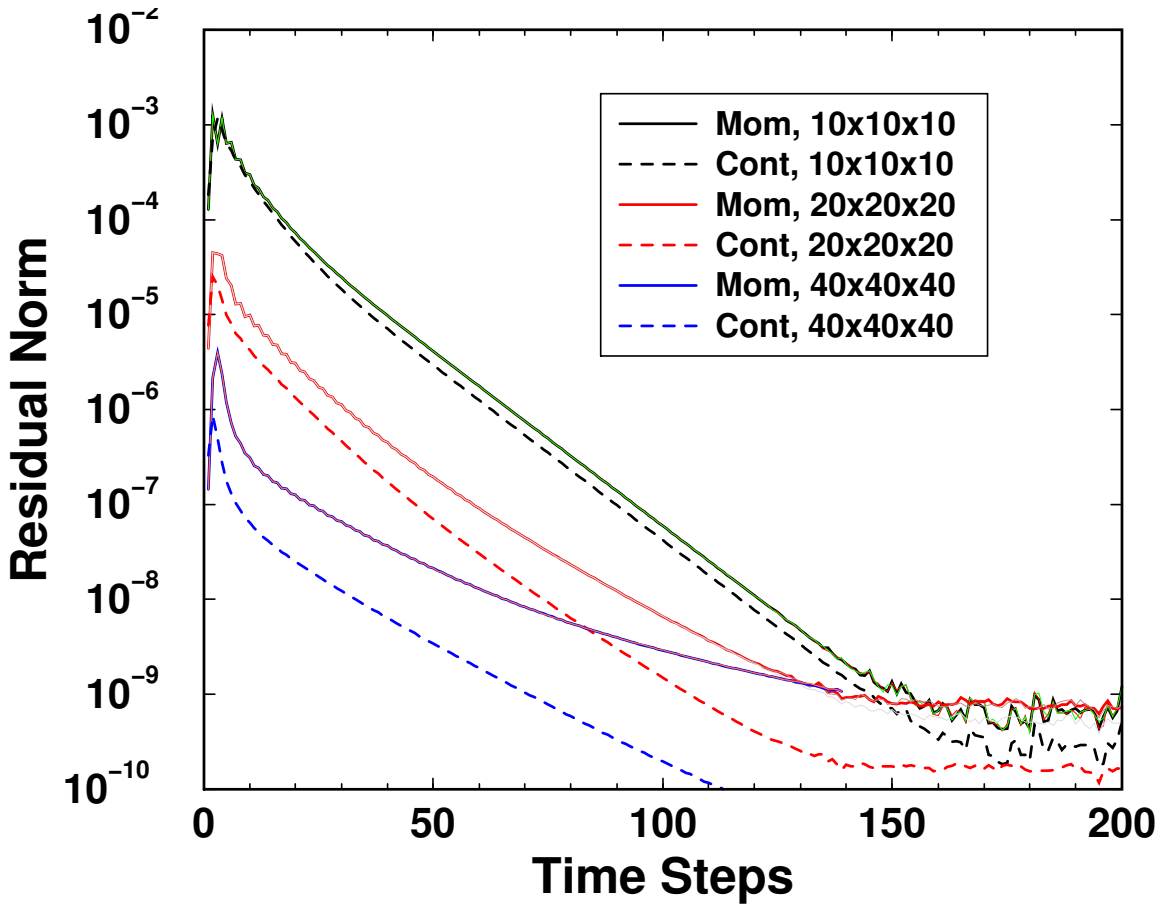


**Figure 16.7-1.. Convergence performance of the nonlinear equations,  $L_2$  norms of the nonlinear residuals. Low Reynolds number test.**

The error norms using the first-order scheme are shown in Table 16.7-1. The errors reduce in a linear fashion with the mesh spacing which supports that the scheme is truly first-order accurate. The error norms using the second-order scheme are shown in Table 16.7-2. The errors also reduce in a linear fashion with the mesh spacing which indicates that the scheme is only first-order accurate when it should be second-order accurate. The MUSCL scheme interpolates convected values to faces using nodal gradients. The nodal gradients at the boundary are only first-order accurate. Also, we only use a first-order accurate flux at subfaces adjacent or opposite and inflow, outflow, or wall boundary.

**Table 16.7-1.. Error norms for Test 2 with first order upwind scheme.**

	$\Delta$	U	V	W	P
$L_\infty$	1.0	1.11655e-01	1.83055e-01	1.19931e-01	3.40577e-01
	0.5	1.40566e-01	1.62851e-01	1.23414e-01	1.47678e-01
	0.25	1.07699e-01	1.16247e-01	8.27482e-02	7.85193e-02
	0.125	6.90864e-02	6.70982e-02	5.03993e-02	4.00601e-02
$L_1$	1.0	2.35476e-02	3.53337e-02	3.23702e-02	7.85616e-02
	0.5	1.56146e-02	2.61142e-02	2.58322e-02	3.29448e-02
	0.25	1.00535e-02	1.64651e-02	1.62824e-02	1.57647e-02
	0.125	5.77453e-03	9.26977e-03	9.04649e-03	7.84826e-03
$L_2$	1.0	2.94769e-02	4.77228e-02	4.17084e-02	9.66346e-02
	0.5	2.18673e-02	3.68794e-02	3.46250e-02	3.92651e-02
	0.25	1.50626e-02	2.40395e-02	2.23377e-02	1.86694e-02
	0.125	8.90935e-03	1.37886e-02	1.26167e-02	9.30629e-03

**Table 16.7-2.. Error norms for Test 2 with MUSCL scheme.**

	$\Delta$	U	V	W	P
$L_\infty$	1.0	1.63694e-01	1.92194e-01	1.69980e-01	2.90509e-01
	0.5	1.11331e-01	1.03616e-01	9.79579e-02	1.33196e-01
	0.25	5.72565e-02	4.45556e-02	4.59224e-02	7.14460e-02
	0.125	2.67767e-02	1.91510e-02	2.09098e-02	3.78585e-02
$L_1$	1.0	3.89306e-02	5.48025e-02	3.89359e-02	5.03472e-02
	0.5	2.00116e-02	2.88929e-02	1.99812e-02	1.86900e-02
	0.25	9.07859e-03	1.29956e-02	9.07545e-03	7.84653e-03
	0.125	4.03974e-03	5.69528e-03	4.06873e-03	3.41206e-03
$L_2$	1.0	5.15657e-02	7.25655e-02	5.43943e-02	6.75761e-02
	0.5	2.63307e-02	3.70622e-02	2.84043e-02	2.35882e-02
	0.25	1.21258e-02	1.66389e-02	1.27256e-02	9.66442e-03
	0.125	5.40602e-03	7.28248e-03	5.67433e-03	4.15270e-03

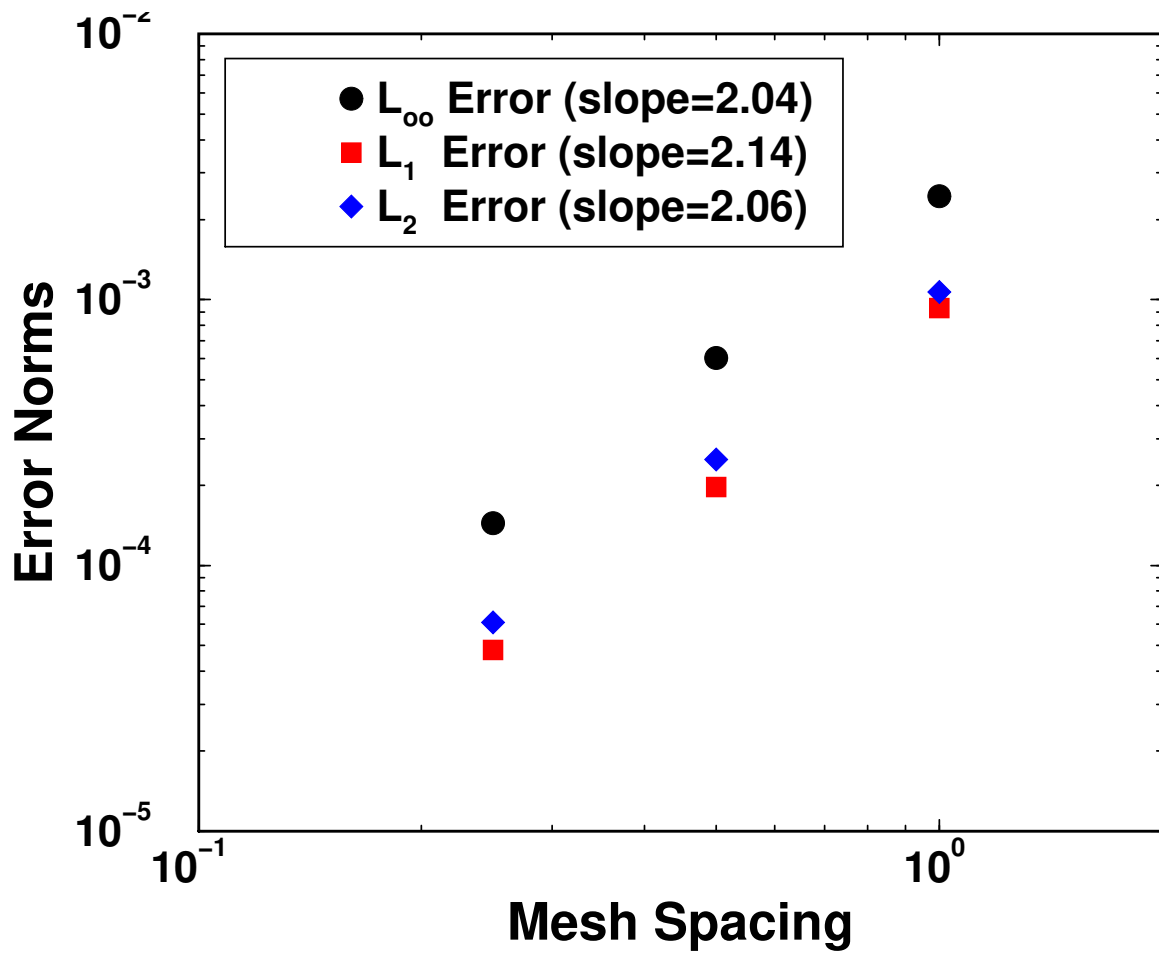


**Figure 16.7-2.. Velocity solution: error analysis for low Reynolds number test with second order convection and diffusion. Error slopes indicate second order spatial accuracy, as expected. Mesh spacing of 1.0 in this plot corresponds to the  $10 \times 10 \times 10$  mesh.**

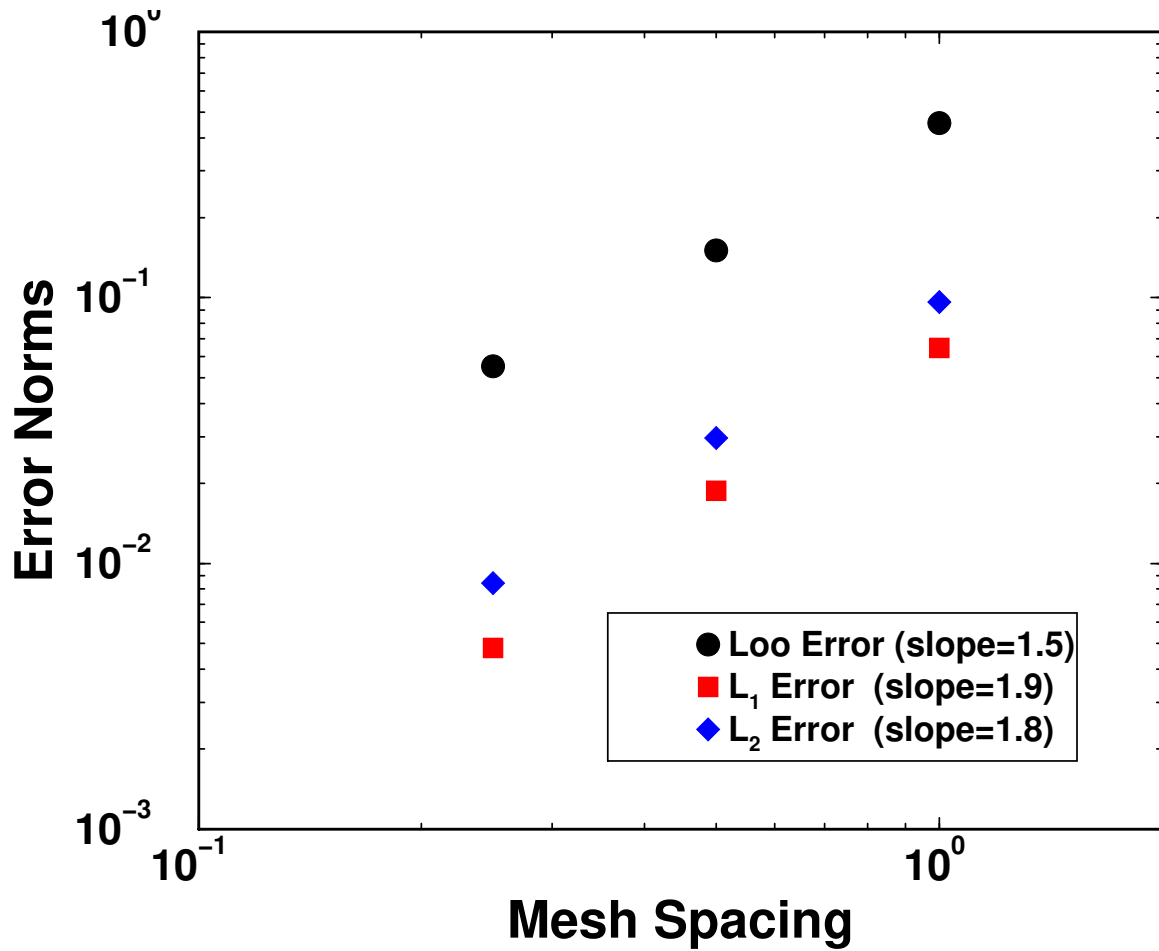


Figure 16.7-3.. Pressure solution: error analysis for low Reynolds number test with second order convection and diffusion. Error slopes indicate less than second order spatial accuracy. Mesh spacing of 1.0 in this plot corresponds to the  $10 \times 10 \times 10$  mesh.

This page intentionally left blank.

# 17. TURBULENT FREE JET

<b>Dimension:</b>	3D
<b>Transient/Steady:</b>	steady
<b>Laminar/Turbulent:</b>	turbulent
<b>Isothermal/Thermal:</b>	isothermal
<b>Temperature/Enthalpy:</b>	N/A
<b>Uniform/Nonuniform:</b>	uniform
<b>Combustion:</b>	no
<b>Soot:</b>	no
<b>Coupled Mechanics:</b>	no
<b>Regression Test:</b>	fuego/turbulent_roundjetA fuego/turbulent_roundjetB fuego/turbulent_roundjetB

## 17.1. EXECUTIVE SUMMARY

An open,  $Re=13200$ , turbulent round jet problem based on the work of Abdel [25] is used to verify the implementation of the turbulence mechanics within SIERRA/Feugo. The verification approach is a benchmark comparison between SIERRA/Fuego 0.9.0 and the commercial code CFX5 using a set of three common meshes ranging from node size of approximately 61K to 246K.

The metric of success is the closeness between the two codes when comparing predicted centerline quantities such as normalized axial velocity and turbulence quantities, i.e., turbulent kinetic energy and turbulence dissipation. Mesh refinement and an informal grid independence study is presented for the two codes.

Results of the SIERRA/Fuego CFX5 code comparisons indicate that on like meshes, results in quantities of interest are within 1 percent. Moreover, results indicate that the two code solutions are convergent to each other given that the exact form of the mathematical models in question are not precisely unknown.

Comparisons to an ad-hoc similarity solution taken from White [26] are also presented for the 61K node mesh SIERRA/Fuego simulation. This solution provides the test to determine if the velocity profiles become self-similar even at downstream locations near the numerical specified pressure

boundary condition. The simulated jet spreading rate is compared to the experimental data set of Abdel [25] and shows excellent agreement (an uncanny 0.5 percent descrepency).

This study also includes a set of SIERRA/Fuego scoping simulations on a smaller mesh (approximately 35K) where sensitivities to simulation time step, mesh rotations, projection methods, and boundary conditions are explored. Results of the SIERRA/Fuego scoping study on the coarser mesh indicate that the stabilized projection methodology provides results independent of time step and relaxation factors. Moreover, the simulations were found to be independent of principle axis rotation. The stabilized and characteristic projection algorithm were found to yield, as expected, the same results at steady state. Lastly, it was found that simulation results are not sensitive to the inclusion of diffusion terms at the specified pressure outflow condition. However, the use of the Dirichlet inflow boundary condition on the coarse scoping study mesh precluded mixing due to diffusion and convection effects within the first one-half control volume at the inflow boundary face. Therefore, the jet core collapse was pushed further downstream when using the inlet Dirichlet condition.

When appropriate, the tool 'exodiff' was used to determine differences between two simulation output files.

## 17.2. MATERIAL SPECIFICATIONS

Since this simulation is of an isothermal flow, constant properties for density and viscosity were chosen to be  $1.1814e-3 \text{ g/cm}^3$  and  $1.79e-4 \text{ g/cm} - \text{s}$  that provided for the appropriate Reynolds number of  $1.32e4$  based on a  $2 \text{ cm}$  jet inlet.

## 17.3. INITIAL CONDITIONS

### 17.3.1. SIERRA/Fuego Initial Conditions

The initial conditions used in SIERRA/Fuego were uniform values of turbulent kinetic energy and turbulent dissipation rate,  $1.50 \text{ cm}^2/\text{s}^2$  and  $215.62e2 \text{ cm}^2/\text{s}^3$  respectively. These turbulence quantities were determined by assuming an isotropic turbulence field based on a 1.0 percent turbulence intensity, and a turbulence length scale of  $2.0 \text{ cm}$  that corresponds to the inlet jet diameter.

Initial velocity components were specified to be zero. For the initial scoping study, the jet was aligned with the flow in the  $-x$ ,  $y$ , and  $z$  directions. For the final code comparison study, the jet was aligned in the  $z$  direction only.

### 17.3.2. CFX5 Initial Conditions

The default "automatic" initial condition option was used along with the CFX5 "Smart Start" option.

## 17.4. BOUNDARY CONDITIONS

### 17.4.1. Common elements

A uniform velocity of  $1000.0 \text{ cm/s}$  was applied at the inlet of the jet. Constant total pressures were specified at all open sidesets to be zero. Simulations were also run with a non-zero specified total pressure condition to verify that specified values do not effect the final result, as would be expected in a low Mach number code without errors (these results are not shown). For the scoping solutions, a no-slip wall condition (using the standard law-of-the-wall) was used for the  $4 \text{ cm}$  inlet pipe section.

Inlet conditions for the turbulent kinetic energy and turbulence dissipation equation were based on a 10 percent turbulence intensity and  $2.0 \text{ cm}$  length scale that corresponded to the inlet jet diameter. The corresponding values of turbulent kinetic energy and turbulence dissipation were  $1.5e2 \text{ cm}^2/\text{s}^2$  and  $215.62e4 \text{ cm}^2/\text{s}^3$ , respectively.

Entrainment values of turbulent kinetic energy and turbulence dissipation were set to  $1.0 \text{ e-2 cm}^2/\text{s}^2$  and  $\text{cm}^2/\text{s}^3$ , respectively.

### 17.4.2. SIERRA/Fuego BC's

The flux inlet boundary condition was primarily used in all code comparison simulations. The sensitivity to this boundary condition and the omission of diffusion was explored in the scoping study). The code comparison simulation included diffusion effects at all free boundaries and the use of the flux inflow condition in lieu of an inlet Dirichlet condition.

### 17.4.3. CFX5 BC's

The exact numerical implementation of the boundary conditions, i.e., flux, omit diffusion, etc., is not formally known.

## 17.5. ANALYTIC OR BENCHMARK SOLUTION

The analysis of the turbulent round jet is taken from White [26]. The derivation begins with the assumption that the flow can be resolved at a location sufficiently down stream from the inlet such that the flow is self similar. In this self similar region, with the absence of walls in the numerical domain, the centerline axial velocity and width of the jet should be strictly a function of distance from the inlet and the momentum of the jet.

Following the standard similarity solution to the scaled-down Navier Stokes equations, the analytical self similar velocity profiles have been shown to be

$$\frac{u}{U_{max}} = \left(1 + \frac{\eta^2}{4}\right), \quad (17.1)$$

where

$$\eta = 15.2 \frac{y}{x} \quad (17.2)$$

and

$$U_{max} = 7.4 \frac{\left(\frac{J}{\rho}\right)^{1/2}}{x}. \quad (17.3)$$

Although the above similarity solution has been shown to match experimental data well, a better form is given by the solution of the plane jet with an alternative constant,  $\sigma$  (see [26])

$$\frac{u}{U_{max}} = \operatorname{sech}^2 \left( 10.4 \frac{y}{x} \right). \quad (17.4)$$

## 17.6. MESH DEFINITION

A variety of different meshes were used for this simulation study and shall now be outlined.

### 17.6.1. Initial Scoping Study Mesh

To explore sensitivity to CFL, projection algorithm, and mesh rotations, a mesh of 35,532 nodes was used to provide fast simulation turn around. The mesh includes a 4 cm pipe section, of diameter 2 cm, entering a cylindrical domain. The physical dimensions of the cylindrical mesh are 41 cm x 26 cm in the axial and radial directions, respectively with 40x20x60 nodes (again in the axial, radial, and azimuthal directions, respectively). Three orientations were used to explore sensitivity to mesh revolution: principle  $-x$ ,  $y$ , and  $z$ .

### 17.6.2. Common Meshes Between SIERRA/Fuego and CFX5

For the code-to-code comparison, three cylindrical mesh resolutions were used: 61,251; 120,411; 246,013. Each were aligned with the  $z$ -principle axis. The physical dimension of the mesh was 100.0 cm in height and 60.0 cm in diameter. The inlet jet diameter was again 2 cm. In the code to code comparisons, no walls were included to simplify the comparison. An extremely fine mesh (631,881) solution was run using SIERRA/Fuego only.

<b>CFL LIMIT:</b>	50.0 or 100.0
<b>TIME STEP CHANGE FACTOR:</b>	10.0
<b>TRANSIENT STEP TYPE:</b>	automatic
<b>PROJECTION METHOD:</b>	stabilized or characteristic
<b>UPWIND METHOD:</b>	UPW
<b>FIRST ORDER UPWIND FACTOR:</b>	1.0
<b>underrelaxation factors:</b>	0.5 for $u, v, w, p$ ; 0.80 for $k$ and eddy viscosity; dissipation rate, 0.75
<b>nonlinear iterations per time step:</b>	1
<b>SOLUTION METHOD:</b>	gmres
<b>PRECONDITIONING METHOD:</b>	symmetric-gauss-seidel
<b>PRECONDITIONING STEPS:</b>	continuity:2; all other equations:1
<b>RESTART ITERATIONS:</b>	continuity:100; all other equations:50
<b>MAXIMUM ITERATIONS:</b>	continuity:200; all other equations:100
<b>RESIDUAL NORM TOLERANCE:</b>	continuity:1.0e-5; all other equations:1.0e-4
<b>RESIDUAL NORM SCALING:</b>	Ro

**Table 17.7-1.. Fuego job parameters from scoping simulation study**

## 17.7. SOLUTION PROCEDURE

Options selected in the scoping SIERRA/Fuego run and code comparison study are listed in Table 17.7-1 and Table 17.7-2.

## 17.8. VERIFICATION EXPERIMENTS

### 17.8.1. Scoping Study

A series of simulation cases were run for the 35,532 node mesh that included sensitivity to mesh rotation, CFL, relaxation, projection algorithm and outflow boundary conditions. In each of simulations, residuals were reduced approximately eight to twelve orders in magnitude.

Figure 17.8-1 shows the results of three cases run using a CFL of 50 using the stabilized projection algorithm (see Table 17.7-1 input specifics) in three principle axis directions,  $-x$ ,  $y$ , and  $z$ . To the precision of the mesh rotation, the answers are precisely matching.

Computational fluid dynamics codes that utilize colocation of the primitive values can sometimes show steady state results that are sensitive to the chosen CFL number or momentum relaxation parameters. To verify that SIERRA/Fuego does not suffer from such algorithmic issues, a series of simulations were run that vary both CFL and relaxation parameters while using the stabilized projection algorithm. Figure 17.8-2 displays three simulations with varying CFL and relaxation parameters (shown is normalized axial velocity):

<b>CFL LIMIT:</b>	50.0
<b>TIME STEP CHANGE FACTOR:</b>	10.
<b>TRANSIENT STEP TYPE:</b>	automatic
<b>PROJECTION METHOD:</b>	stabilized
<b>UPWIND METHOD:</b>	UPW
<b>FIRST ORDER UPWIND FACTOR:</b>	1.0
<b>underrelaxation factors:</b>	0.5 for $u, v, w, p$ ; 0.80 for $k$ and eddy viscosity; dissipation rate, 0.75
<b>nonlinear iterations per time step:</b>	1
<b>SOLUTION METHOD:</b>	gmres
<b>PRECONDITIONING METHOD:</b>	symmetric-gauss-seidel
<b>PRECONDITIONING STEPS:</b>	continuity:2; all other equations:1
<b>RESTART ITERATIONS:</b>	continuity:100; all other equations:50
<b>MAXIMUM ITERATIONS:</b>	continuity:200; all other equations:100
<b>RESIDUAL NORM TOLERANCE:</b>	continuity:1.0e-5; all other equations:1.0e-4
<b>RESIDUAL NORM SCALING:</b>	Ro

**Table 17.7-2.. Fuego job parameters for code comparison simulation study**

- $CFL = 50.0, \alpha_{mom} = 0.50, \alpha_p = 0.50$
- $CFL = 50.0, \alpha_{mom} = 0.75, \alpha_p = 0.25$
- $CFL = 100.0, \alpha_{mom} = 0.50, \alpha_p = 0.50$

As shown, the displayed normalized streamwise velocities as a function of axial distance for each of the above three simulations are indistinguishable. Rather than spot probing of the data set, the tool 'exodiff' was used to determine differences. Results using this tool indicate that all differences were less than 1e-16.

The next study using the 35,532 node mesh varied the projection method. Typically, the stabilized algorithm is used since it includes terms (proportional to the simulation time step) that augments the diagonal dominance of the continuity pressure solve that adds stability. However, this stabilizing factor is scaled by the change in pressure gradient, so at steady state, its effect on the final answer vanish.

Using the following option: 'PROJECTION METHOD = smoothed WITH characteristic SCALING' uses the same form as above for the convecting velocity without the stabilizing term. Therefore, the steady state results using either of the two methodologies should be same provided that nonlinear convergence has been obtained. Figure 17.8-3 shows the normalized axial data as a function of axial distance. Again, the plot indicates that the two methodologies do, in fact, provide exactly the same answers at numerical convergence (verified by running 'exodiff' whose results indicate no differences to within 1e-16).

For reference, Figure 17.8-4 shows the nonlinear residual plot for the streamwise velocity and the continuity equation for both the stabilized and characteristic scaling projection method (input file reflected parameters outlined in Table 17.7-1 with  $CFL = 50$ ). For this particular case, both methods

perform very well with a total reduction in nonlinear residual of over eleven orders in magnitude. For reasons not explored, the characteristic scaling algorithm seems to have performed better during the duration of the flow hitting the outflow boundary condition.

The sensitivities to the chosen outflow and inflow boundary conditions are now presented. Figure 17.8-5 displays the sensitivity of the chosen outflow and inflow boundary condition ('use fluxes' vs. 'dirichlet inlet'; 'omit diffusion terms' and 'include diffusion terms') on the centerline profile of normalized streamwise velocity. Results indicate no substantial differences, both in stability (nonlinear residuals not shown) and results when the use of diffusion terms at the outflow are omitted or included.

However, on this coarse mesh, the use of the flux inlet condition does show a faster core collapse than the Dirichlet inflow condition. The Dirichlet condition removes the half-control volume equation at the inflow boundary face thereby not allowing convection or diffusion through the top and side faces. As the mesh is refined, it would be expected that results would not be sensitive to removal of a half-control volume equation, however, this is not formally shown in this study. The user should note that the current default behavior of SIERRA/Fuego's boundary conditions are to include diffusion terms at specified pressure boundary conditions and use Dirichlet conditions at inflow boundaries.

Lastly, the use of the time step scaling algorithm for turbulent flows is addressed. As noted within the SIERRA/Fuego theory manual, the use of smoothing within the convecting velocity interpolation admits smoothing error that is not "erased" at full convergence. The option exists to allow the scaling term be the time step taken for the simulation. As such, steady results will depend on the timestep taken to reach steady state. As with other smoothing algorithms, this error will be proportional to the fourth derivative of pressure multiplied by a length scale to the third power. Therefore, the effects of the smoothing error will be most noticeable when using large timesteps on a coarse mesh (when the pressure does not vary linearly).

Figure 17.8-6 is a plot of normalized streamwise velocity as a function of normalized axial distance downstream. The figure compares the use of the time step scaling projection method for three CFLs, 25, 50, and 100. Also shown for comparison is a plot obtained from the characteristic scaling projection method (CFL = 50, with relaxation). The plot indicates that the entrance region is different between the three simulations.

Figure 17.8-7 represents a close up of the above figure. It is now apparent that the smoothing error is greatest at the inlet when pressure gradients are the highest. Moreover, with decreasing time step, one notes that the two projection methods approach each other. This plot suggests that the time step projection method incorporates more smoothing.

Lastly, the effect of projection method scaling on the global convergence is presented. Figure 17.8-8 outlines the nonlinear streamwise velocity residual history for the three simulations using the time step scaling projection method and the characteristic scaling scheme. The plot again indicates that with increased smoothing, the code can converge much faster. However, this converged solution may show increased smoothing error as shown in Figure 17.8-7.

It should be noted that this scoping study resolution is on the coarse side, so increased mesh resolution would presumably decrease the smoothing error (again due to the third order dependence on mesh spacing).

## 17.8.2. Code Comparison Study

This section will be organized by presentation of SIERRA/Fuego simulations first, followed by comparison plots with the experimental data set and CFX second.

## 17.8.3. SIERRA/Fuego Results

The degree of convergence for the SIERRA/Fuego simulation code comparison study was found to be good for each of the mesh resolutions run. Figure 17.8-9 shows the  $\|L_2\|$  norm of the nonlinear residuals for  $u$ ,  $v$ ,  $w$ ,  $p$ , turbulent kinetic energy, and turbulence dissipation rate for the 246,013 node simulation study. The degree of convergence varies from eleven orders of magnitude reduction for the turbulence dissipation rate variable to six orders of magnitude reduction for the off-velocity components,  $u$  and  $v$ . In general, pointwise variables became constant after a nonlinear residual drop of approximately four orders in magnitude. Given the difficulty of problem (due to the numerous specified pressure boundary conditions) the residual plots are as good as can be expected when using a segregated solution algorithm.

Figure 17.8-10, Figure 17.8-11, and Figure 17.8-12 show results from SIERRA/Fuego, specifically showing, normalized streamwise velocity, turbulent kinetic energy, and turbulence dissipation rate for the three meshes used in this study.

## 17.8.4. Self-Similarity and Jet Spreading Rates

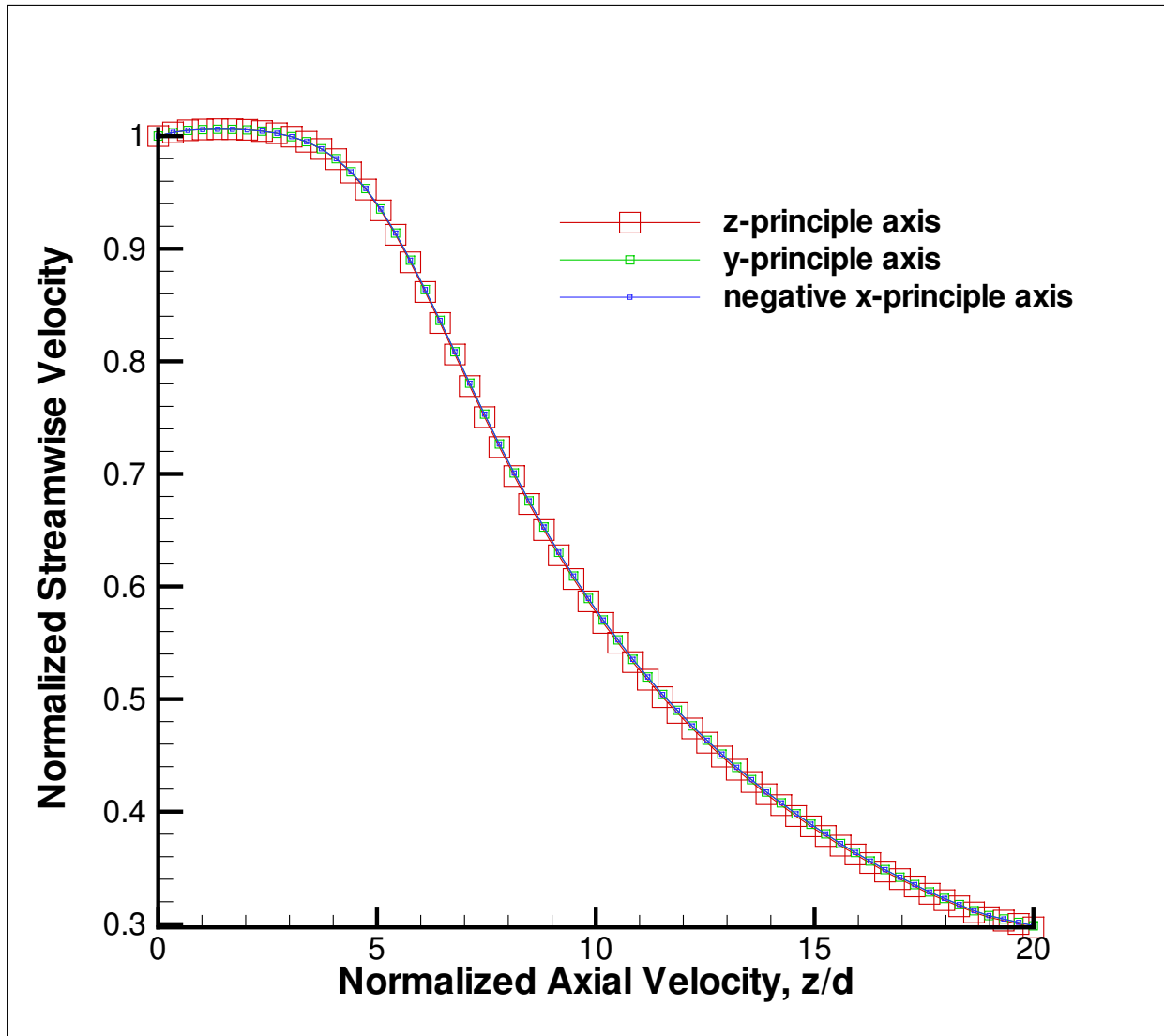
To explore the self similar nature of the streamwise velocity radial profiles, Figure 17.8-13 is a plot of the normalized streamwise velocity as a function of the radial distance normalized by the radius half width for a series of four downstream diameters (20, 40, and 60, and 80). For reference, the radius half-width represents the radial distance that corresponds to the value of the velocity that is one-half its maximum center value. Of particular significance is the lack of similarity profile deflection near the outflow boundary thus indicating a “non intrusive” numerical boundary condition..

Figure 17.8-14 is a plot of the radial half width as a function of normalized downstream position. The slope of this curve represents the spreading rate of the jet. The simulation results indicate a perfectly linear variation of the jet spreading rate whose slope is 0.0975. As a reference, the spreading rate of the free jet ( $Re = 1.32e4$ ) given by Abdel [25] is 0.097. The lack of boundary condition sensitivity to the spreading rate is again noted, specifically for the  $z/d = 80$  position.

## 17.8.5. SIERRA/Fuego as Compared to CFX

Code comparisons between SIERRA/Fuego and CFX were run using three mesh resolutions. Figure 17.8-15, Figure 17.8-16, and Figure 17.8-17 show comparisons of normalized streamwise velocity, turbulent kinetic energy, and turbulence dissipation rate for the three meshes used in this study.

Results clearly demonstrate that the order of difference between the two codes are extremely small. Within the range of uncertainty of the exact form of the mathematical models used in CFX, the fine mesh results are well within the acceptance criteria outlined verification via code comparison.



**Figure 17.8-1.. Scoping study simulation plot of normalized streamwise velocity at three mesh rotations.**

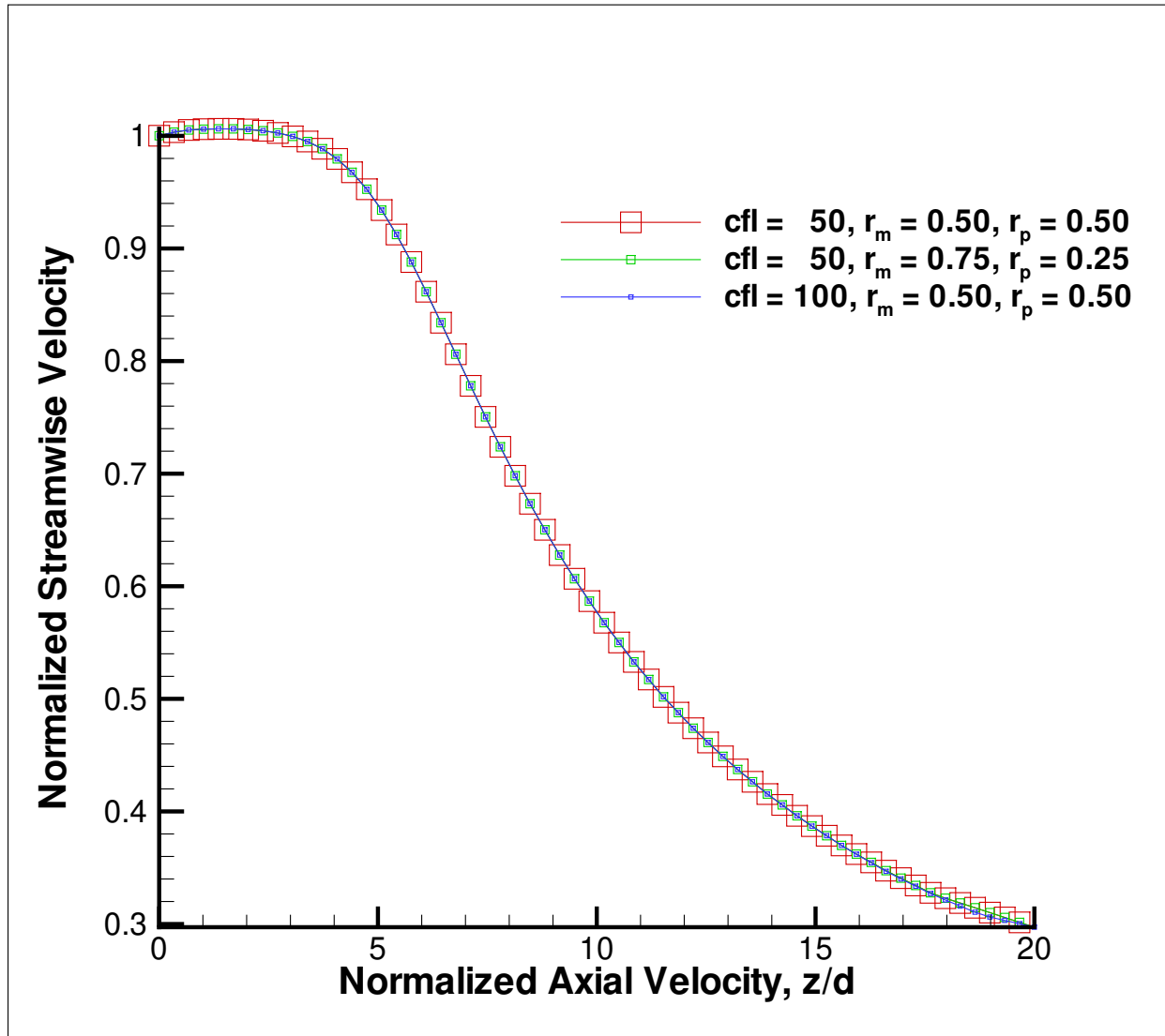
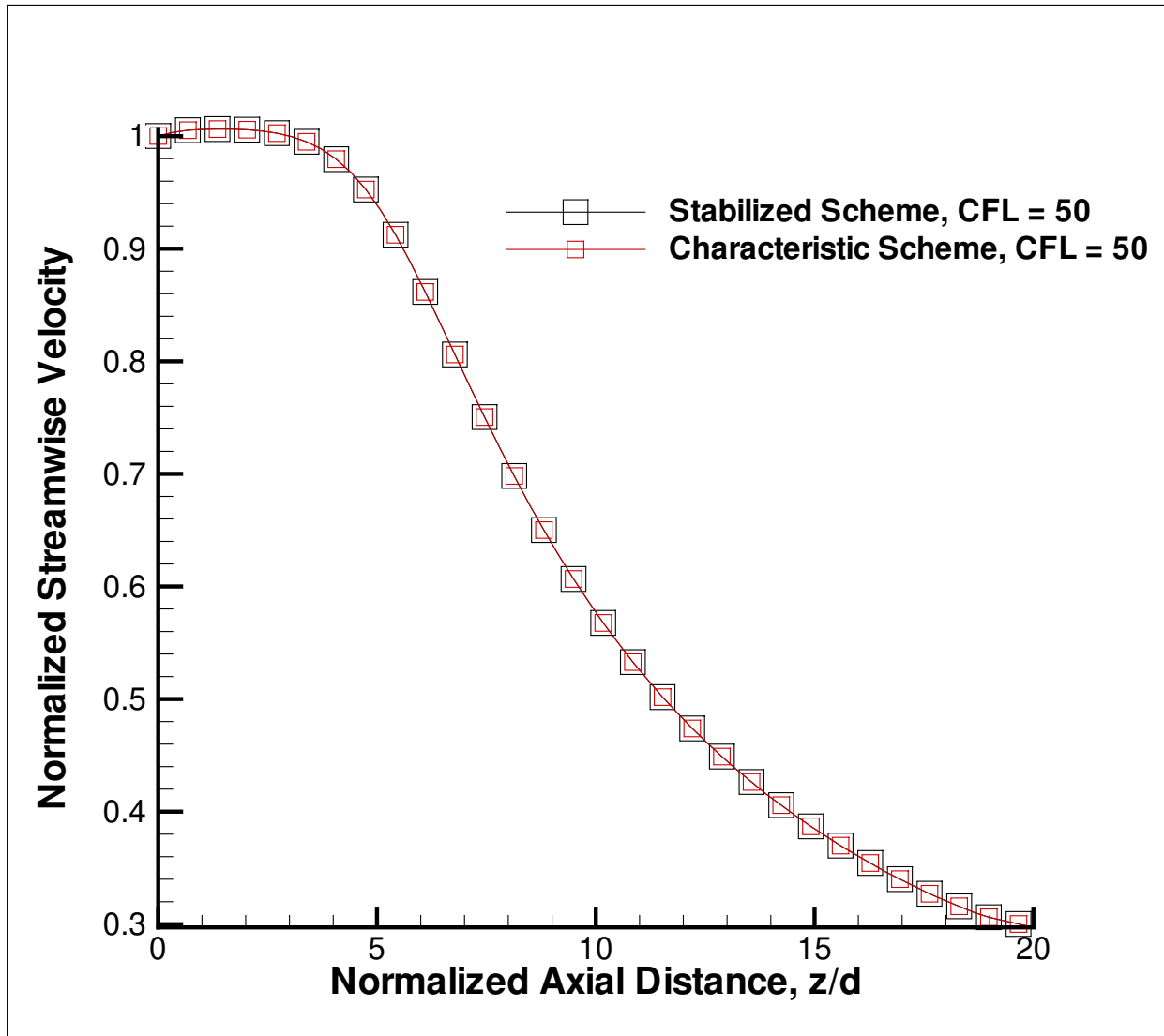
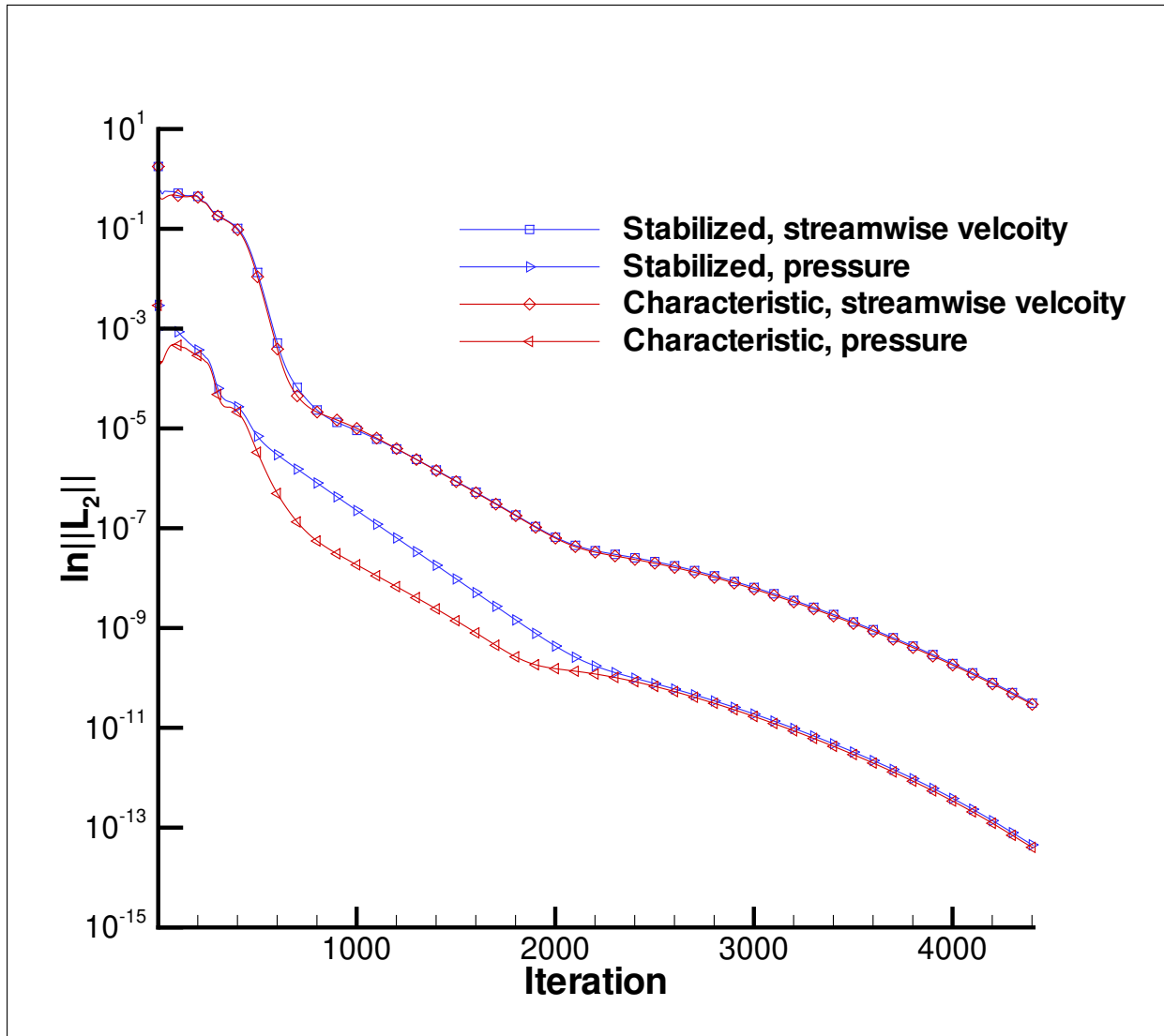


Figure 17.8-2.. Scoping study simulation plot of normalized streamwise velocity with varying CFL and relaxation parameters.



**Figure 17.8-3.. Scoping study simulation plot of normalized streamwise velocity with varying projection algorithms in use.**



**Figure 17.8-4.. Scoping study simulation plot of nonlinear residuals with varying projection algorithms in use.**

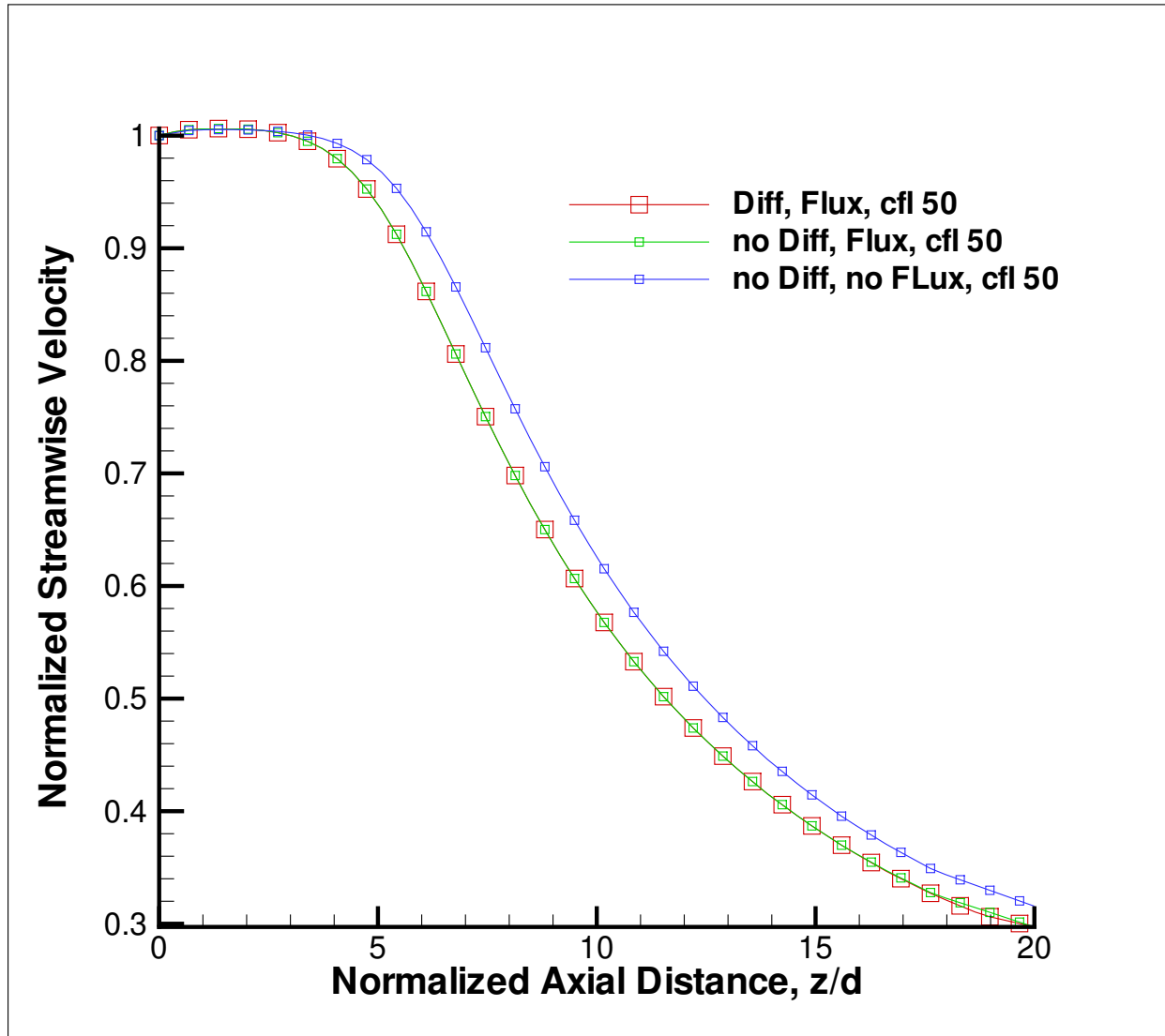


**Figure 17.8-5..** Scoping study simulation plot of normalized streamwise velocity as a function of normalized axial distance. Shown are the sensitivities to chosen inflow and outflow boundary conditions.

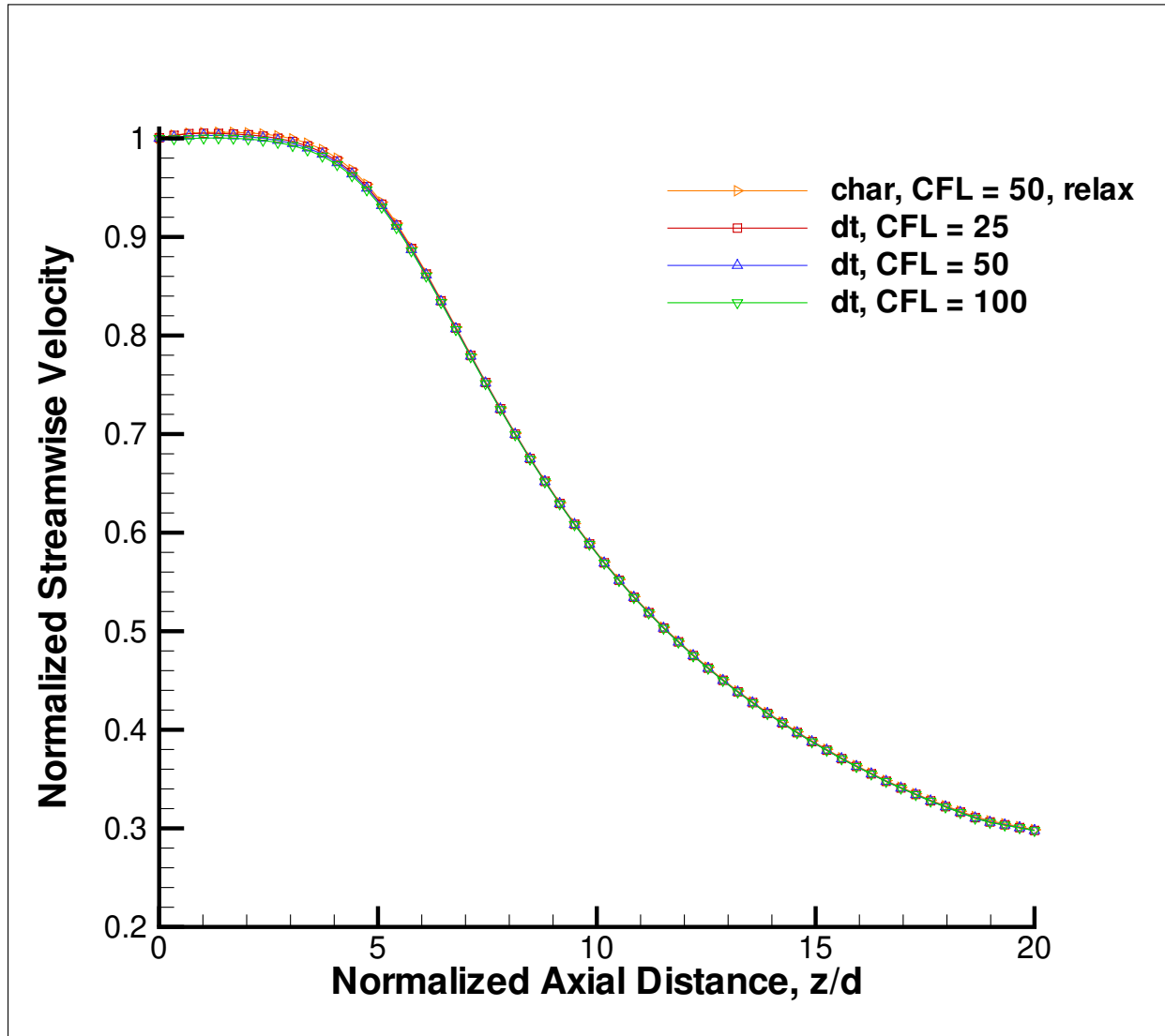


**Figure 17.8-6..** Scoping study simulation plot of normalized streamwise velocity as a function of normalized axial distance. Shown are the sensitivities to chosen projection methods with varying time steps.

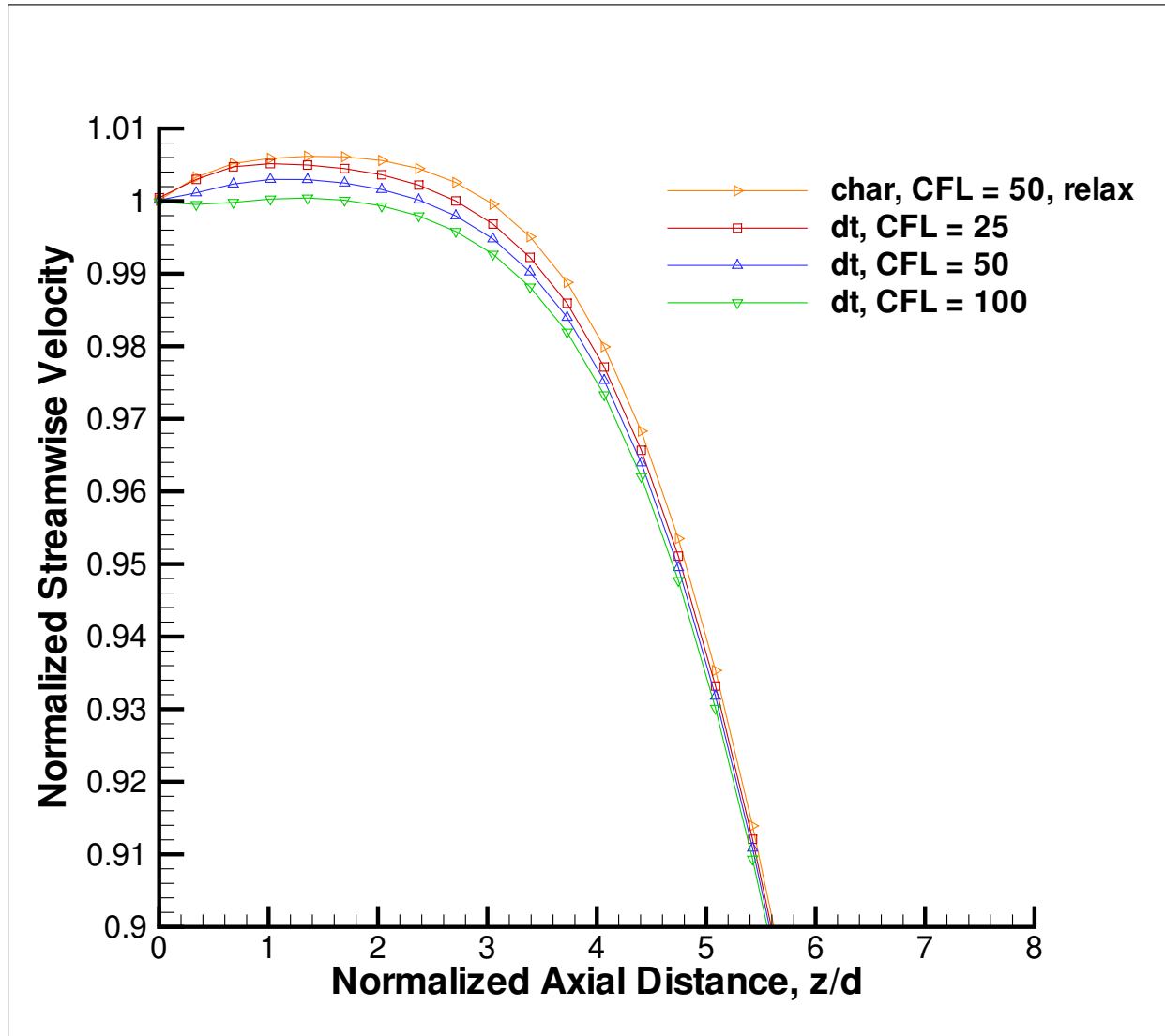


**Figure 17.8-7.. Scoping study simulation plot of normalized streamwise velocity as a function of normalized axial distance. Shown are the sensitivities to chosen projection methods with varying time steps, close-up of entry region.**

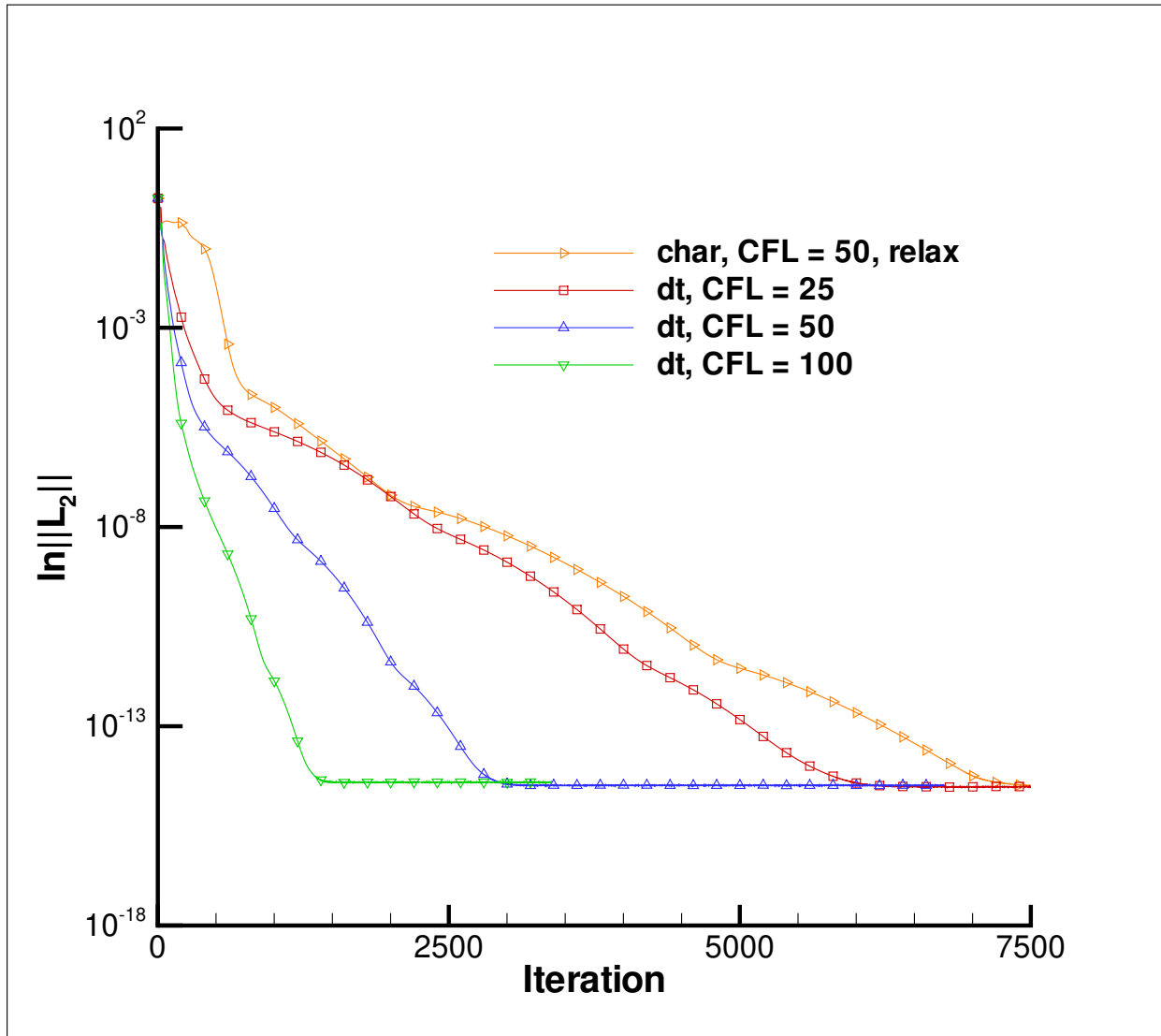


**Figure 17.8-8.. Scoping study simulation plot of streamwise non-linear residuals with varying projection algorithms in use; time step and characteristic.**

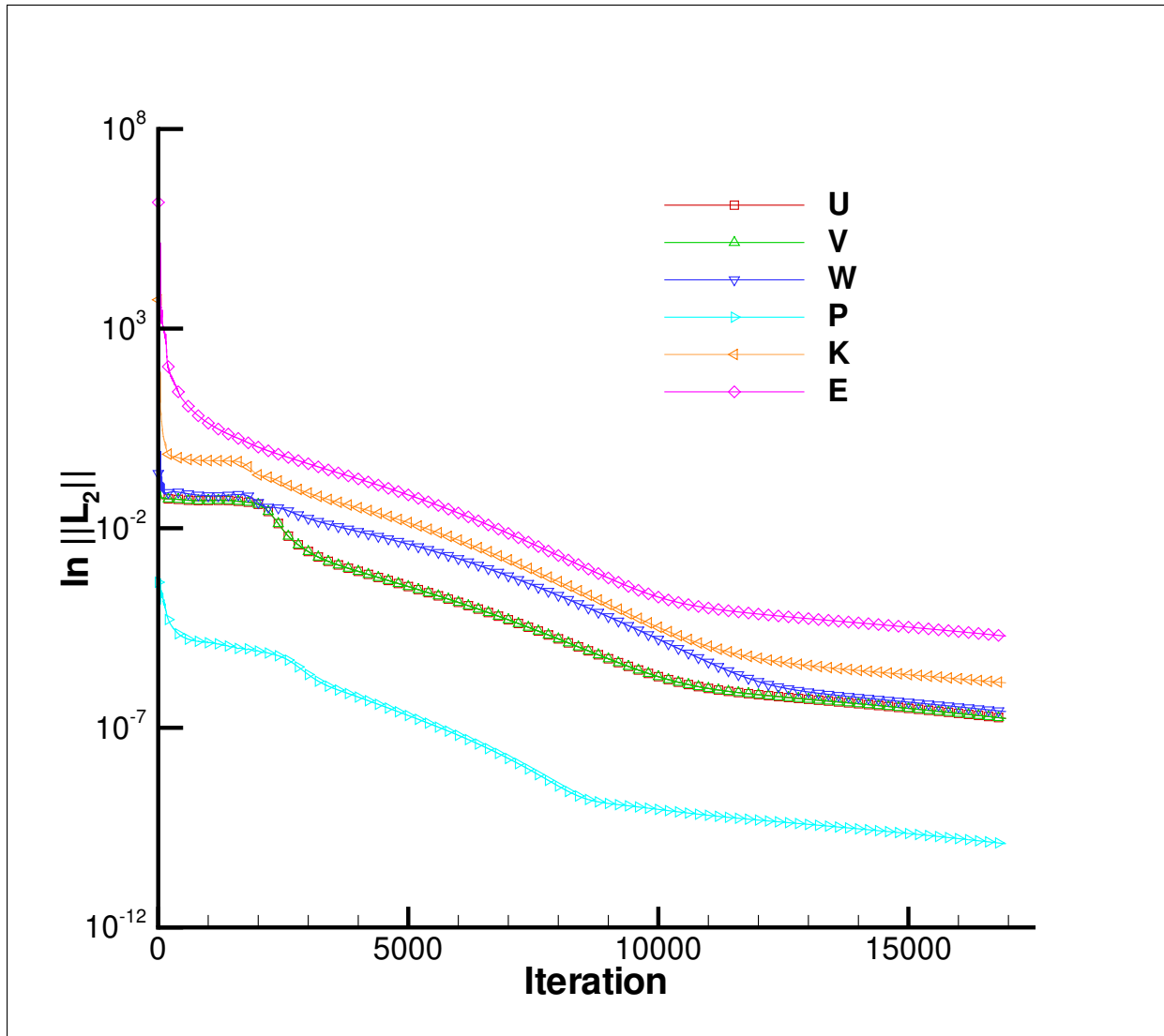


**Figure 17.8-9..**  $||L_2||$  norm as a function of iteration for the 246,013 node turbulent open jet simulation.

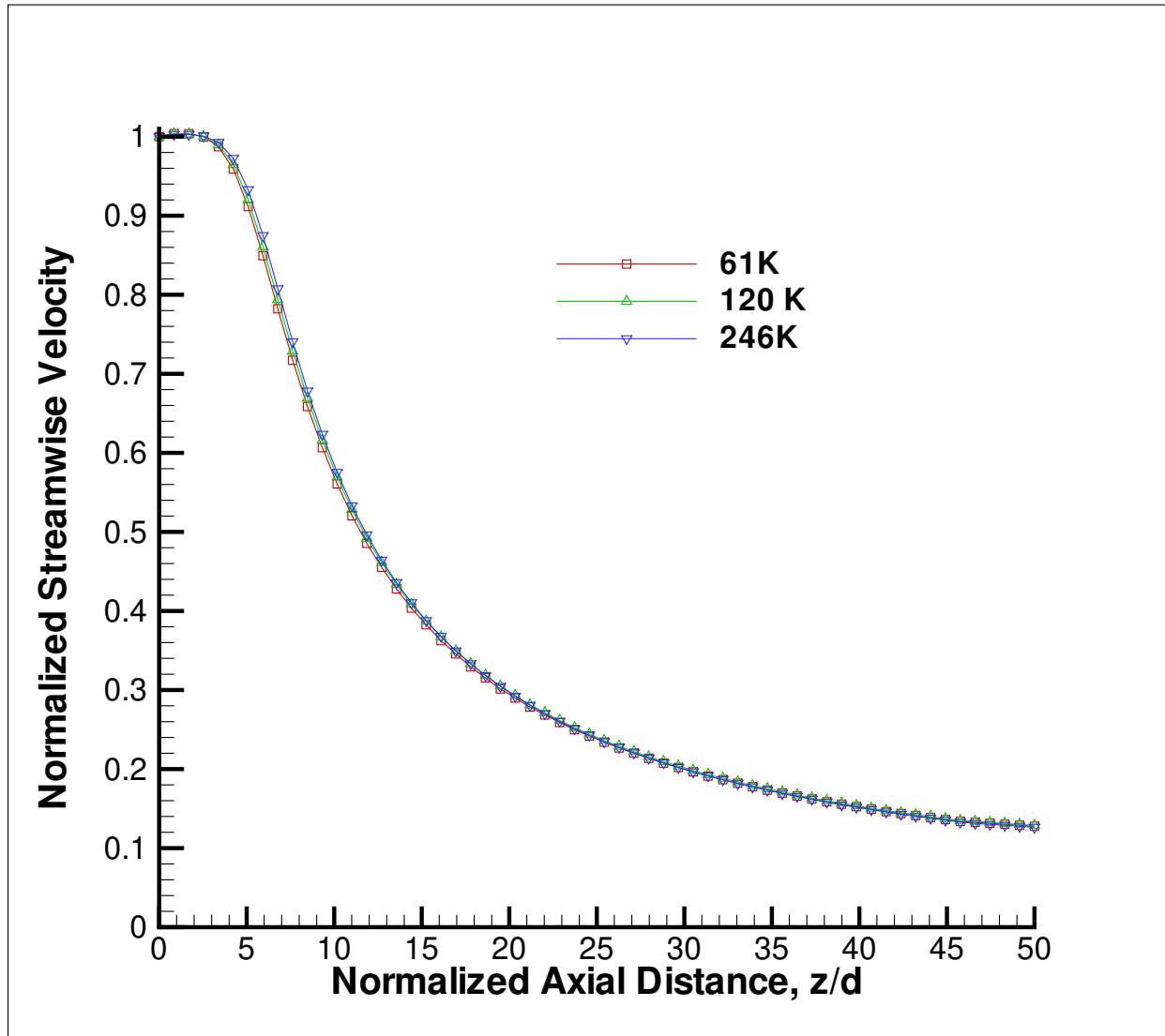


Figure 17.8-10.. Normalized streamwise velocity as a function of normalized axial distance for the SIERRA/Fuego mesh refinement study of the turbulent round jet.

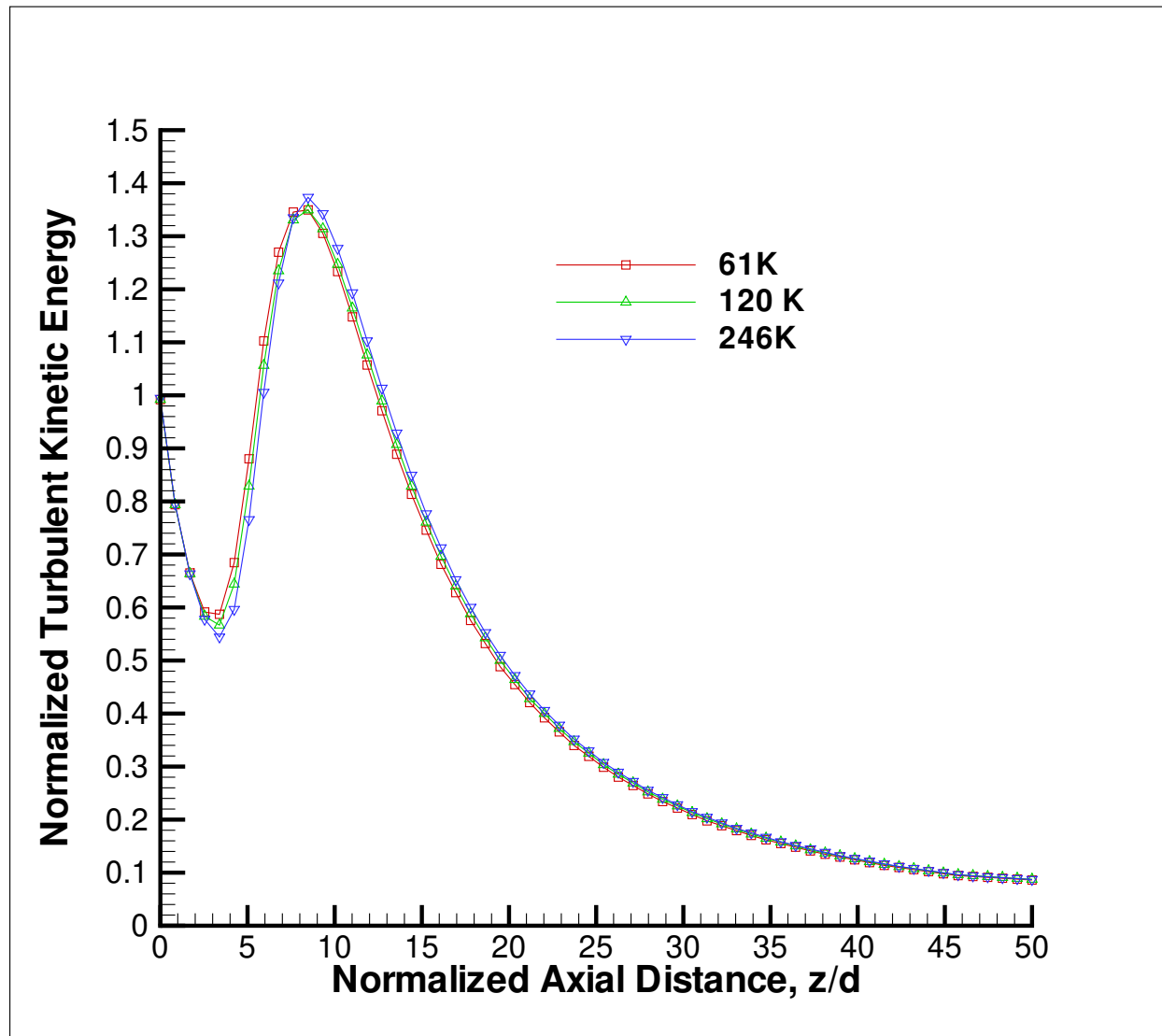
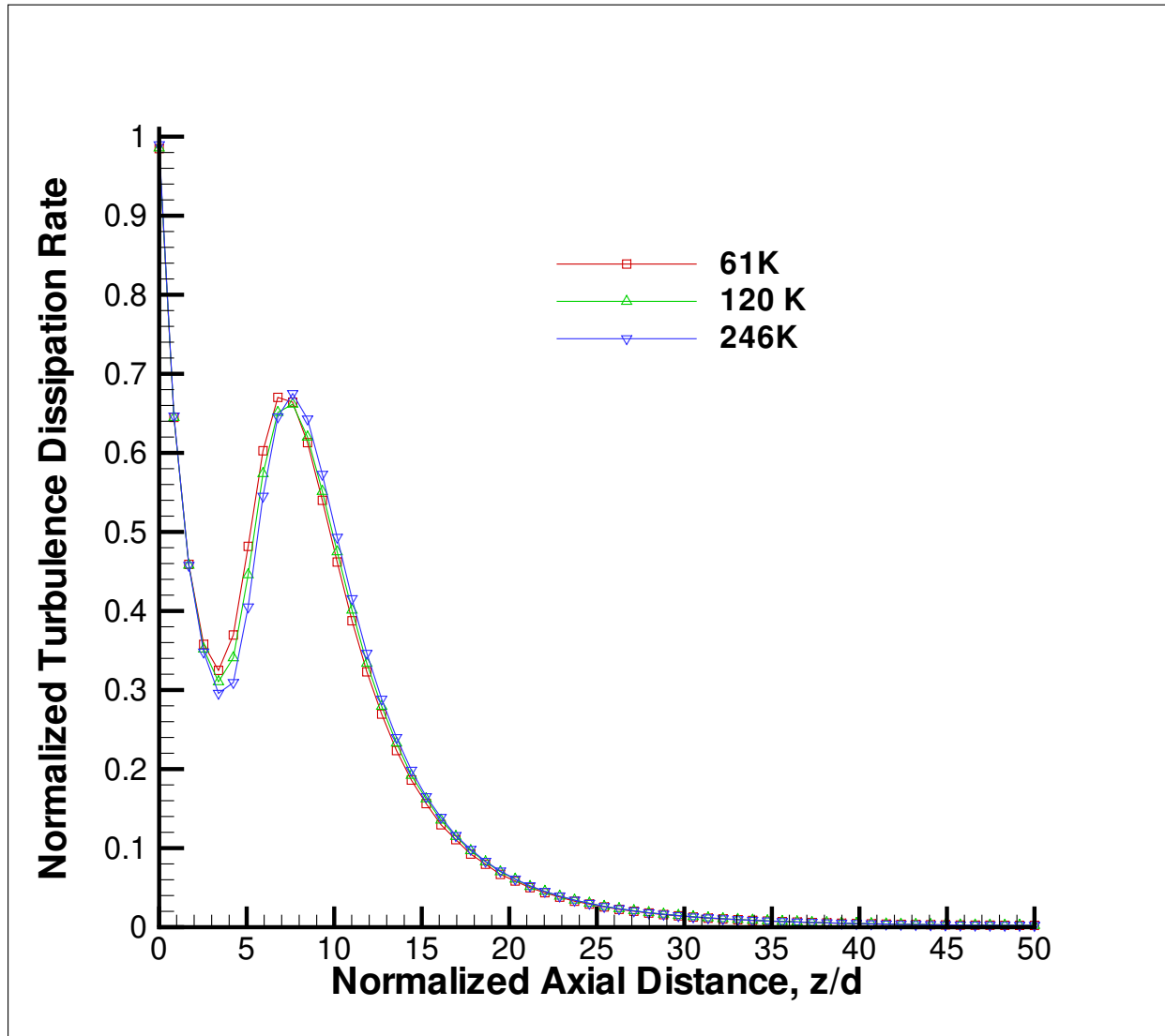
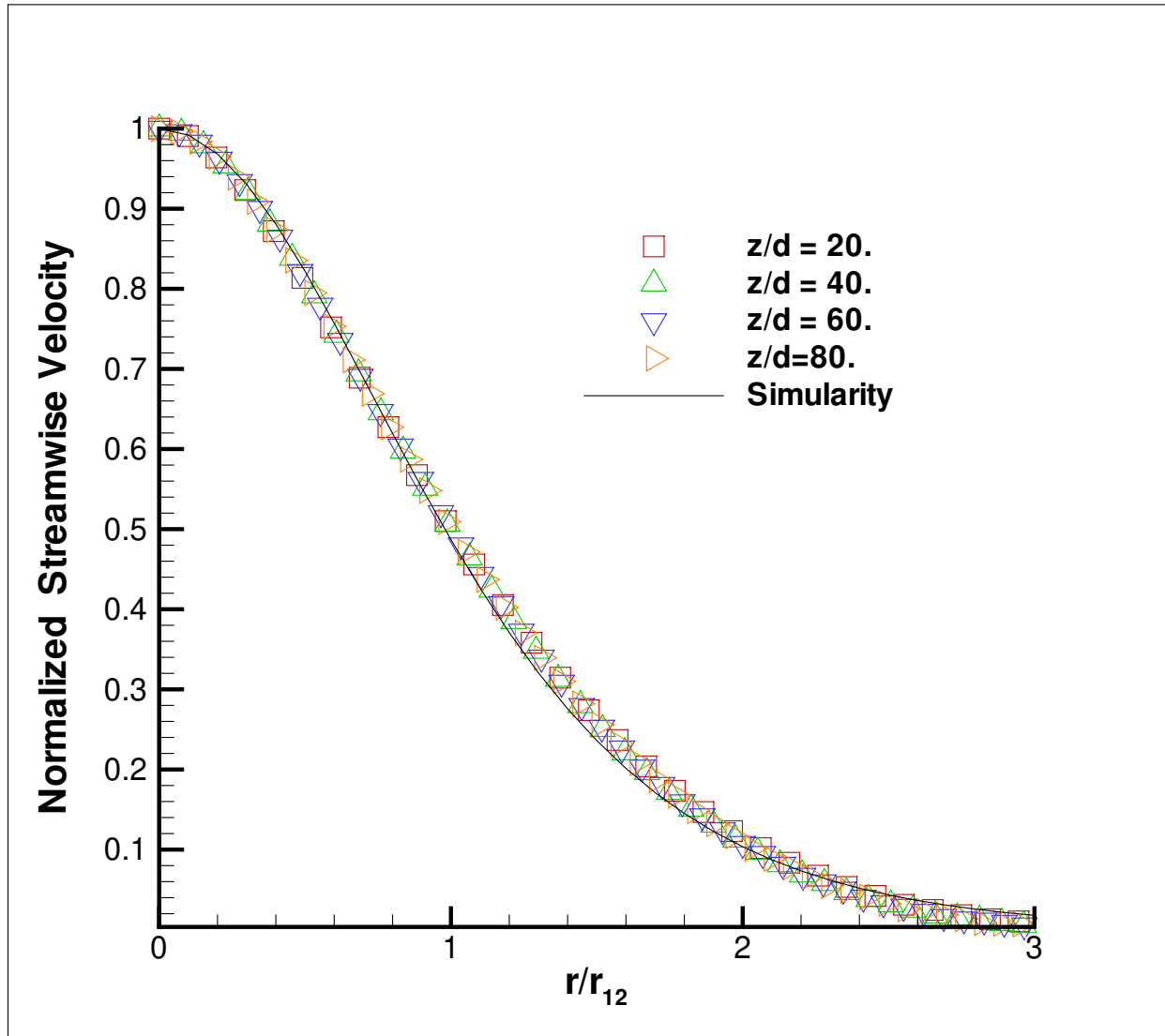


Figure 17.8-11.. Normalized turbulent kinetic energy as a function of normalized axial distance for the SIERRA/Fuego mesh refinement study of the turbulent round jet.



**Figure 17.8-12.. Normalized turbulence dissipation as a function of normalized axial distance for the SIERRA/Fuego mesh refinement study of the turbulent round jet.**



**Figure 17.8-13.. Normalized streamwise velocity as a function of normalized radial distance for the 61,251 node mesh comparison study of the turbulent round jet. Shown are profiles  $z/d = 20, 40$ , and  $60$ .**

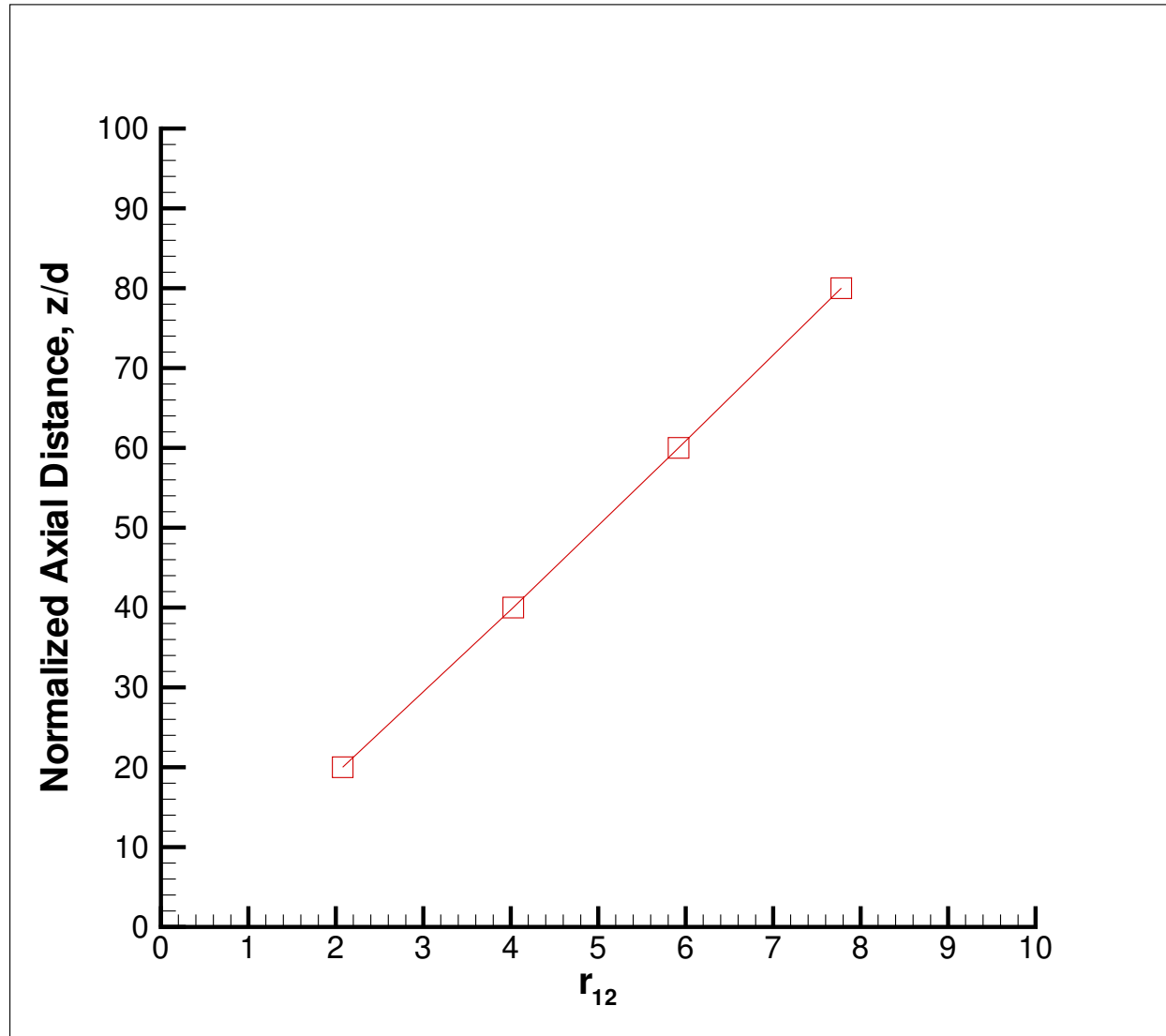


**Figure 17.8-14.. Radius half-width as a function of normalized axial distance for the 61,251 node mesh comparison study of the turbulent round jet. The slope of this curve represents the “jet spreading rate” and is 0.0975.**

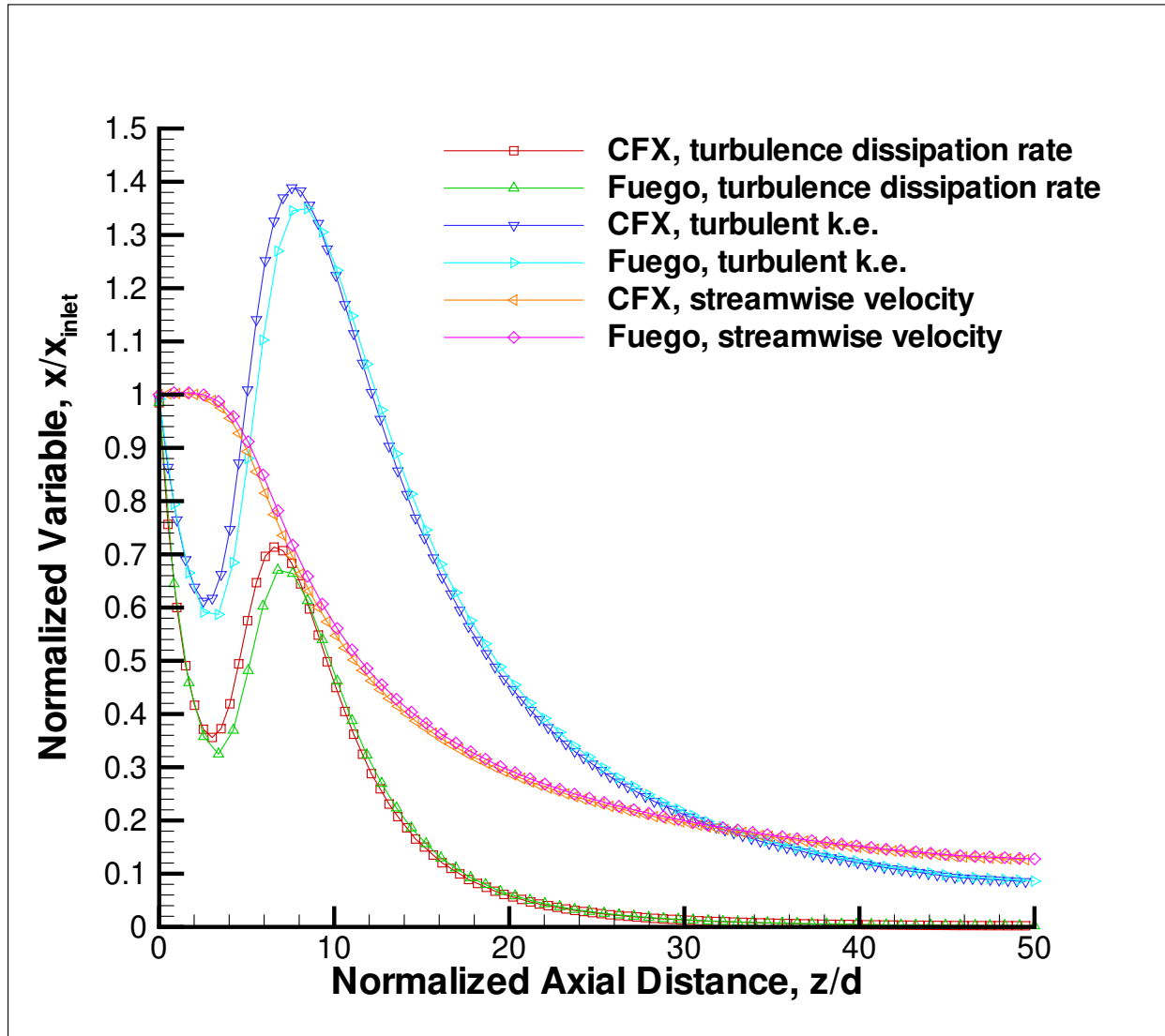


**Figure 17.8-15..** Normalized streamwise velocity, turbulent kinetic energy, and turbulence dissipation rate as a function of normalized axial distance for the 61,251 node mesh comparison study of the turbulent round jet.

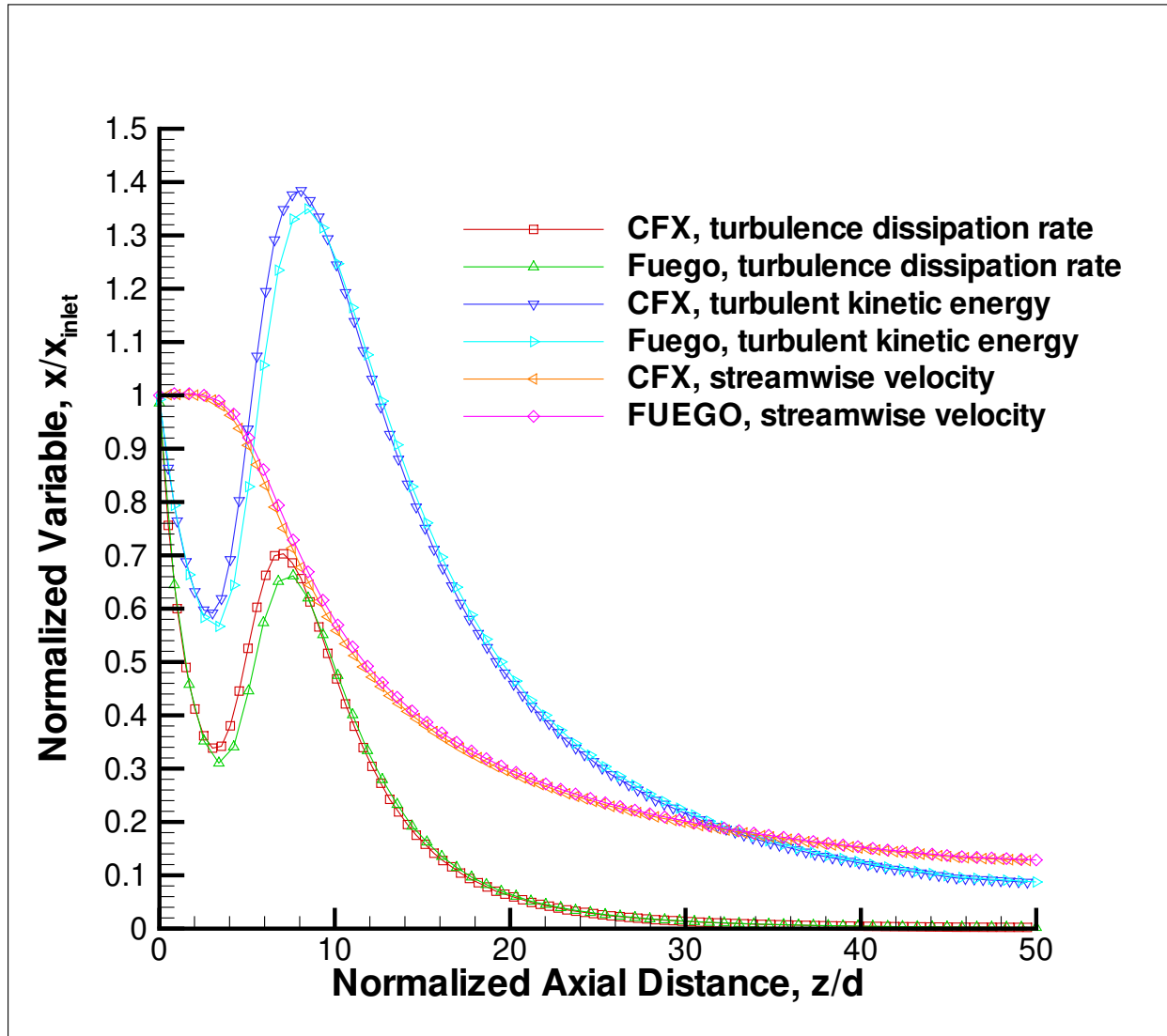


**Figure 17.8-16..** Normalized streamwise velocity, turbulent kinetic energy, and turbulence dissipation rate as a function of normalized axial distance for the 120,411 node mesh comparison study of the turbulent round jet.

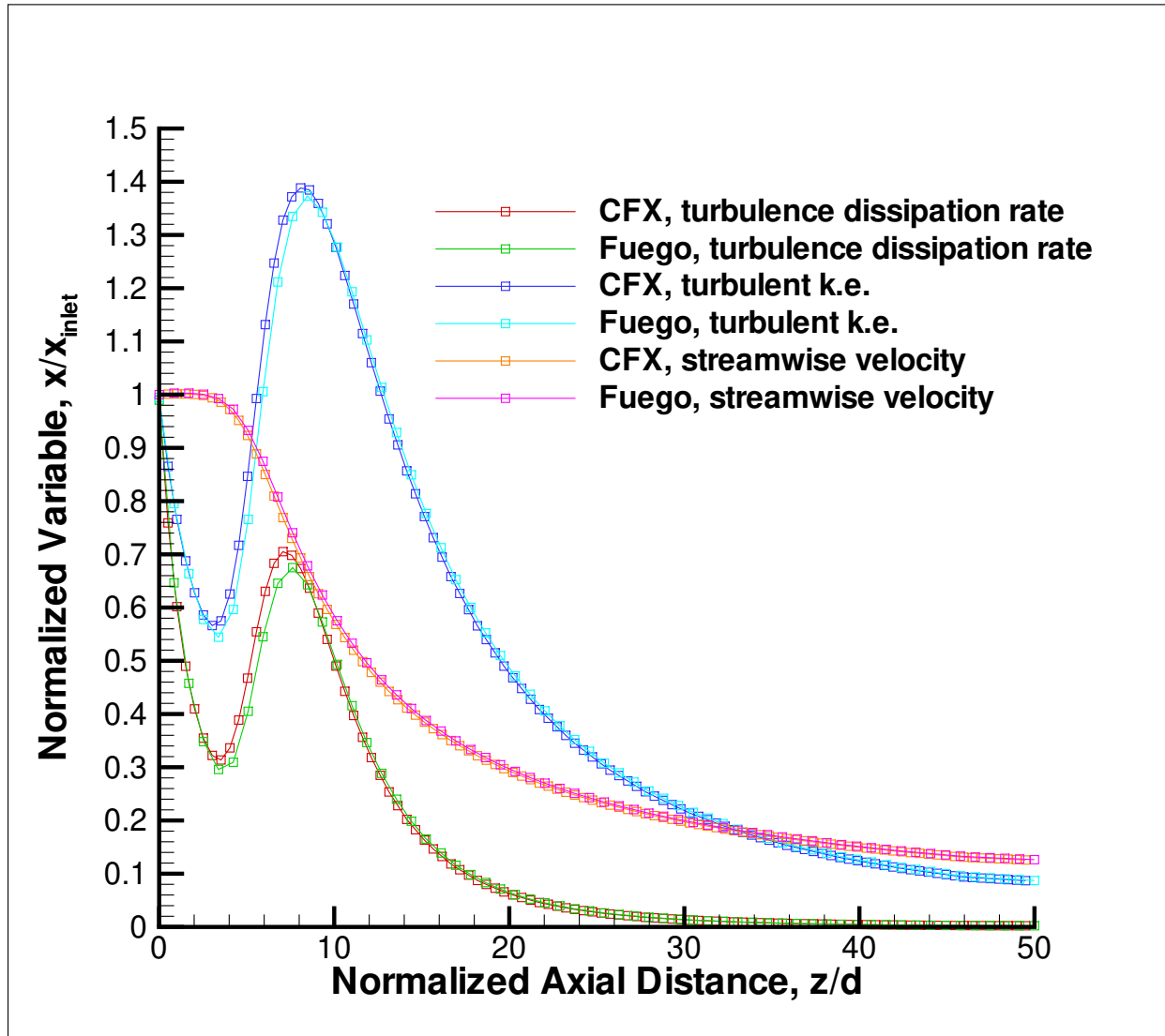


**Figure 17.8-17..** Normalized streamwise velocity, turbulent kinetic energy, and turbulence dissipation rate as a function of normalized axial distance for the 246,013 node mesh comparison study of the turbulent round jet.

# 18. SURFACE TRANSFER VERIFICATION

<b>Dimension:</b>	3D
<b>Transient/Steady:</b>	steady
<b>Laminar/Turbulent:</b>	laminar
<b>Isothermal/Thermal:</b>	thermal
<b>Temperature/Enthalpy:</b>	temperature
<b>Uniform/Nonuniform:</b>	uniform
<b>Combustion:</b>	no
<b>Soot:</b>	no
<b>Coupled Mechanics:</b>	no
<b>Regression Test:</b>	fuego/tetHexFluidCond

This problem is used to verify the implementation for surface transfers used for fluid/solid (laminar and turbulent) and solid/pmr fire mechanics transfers.

The first problem represents testing of a heterogeneous surface transfer (quad:triangle) for the laminar heat transfer boundary condition. The fluid region is a hex topology while the conduction region is a tetrahedral topology. The fluid domain has boundary conditions that result in a quiescent flow with a wall temperature of 10. The conduction region has a temperature specification of 0. Each of the regions share the same conduction coefficient, thereby allowing a perfectly linear temperature profile.

## 18.1. MATERIAL SPECIFICATIONS

The material properties in Fuego are a fluid with a density of 1.0, viscosity of 1.e-4, conductivity of 1.0, and specific heat of 1.0. The conduction region has a density of 1.0, conductivity of 1.0, and specific heat of 1.0.

## 18.2. INITIAL CONDITIONS

## 18.3. BOUNDARY CONDITIONS

The boundary conditions used in the fluid were a wall (10) surrounded by symmetry with one wall interface bc. The conduction region shared the interface bc, a wall of temperature equal to 0.0, and adibatic bcs.

## 18.4. ANALYTIC OR BENCHMARK SOLUTION

An analytical solution is given by the simple diffusion equation,  $T = C_1 x + C_2$

## 18.5. MESH DEFINITION

Hex and Tet mesh.

## 18.6. SOLUTION PROCEDURE

THIS IS WRONG Options selected in the Fuego run were: **CFL LIMIT** = 0.1, **TIME STEP CHANGE FACTOR** = 1.25, **TRANSIENT STEP TYPE IS** automatic, **UPWIND METHOD IS** MUSCL, one nonlinear iteration per time step. For  $u$ ,  $v$ ,  $w$ , **SOLUTION METHOD IS** bicgstab, **PRECONDITIIONING METHOD IS** jacobi, **RESIDUAL NORM TOLERANCE** = 1.0e-6. For continuity **SOLUTION METHOD IS** gmres, **PRECONDITIONING METHOD IS** jacobi, **RESIDIAL NORM TOLERANCE** = 1.0e-8.

## 18.7. VERIFICATION EXPERIMENTS

### 18.7.1. Laminar Heat Transfer BC

Figure 18.7-1 shows the temperature profile.

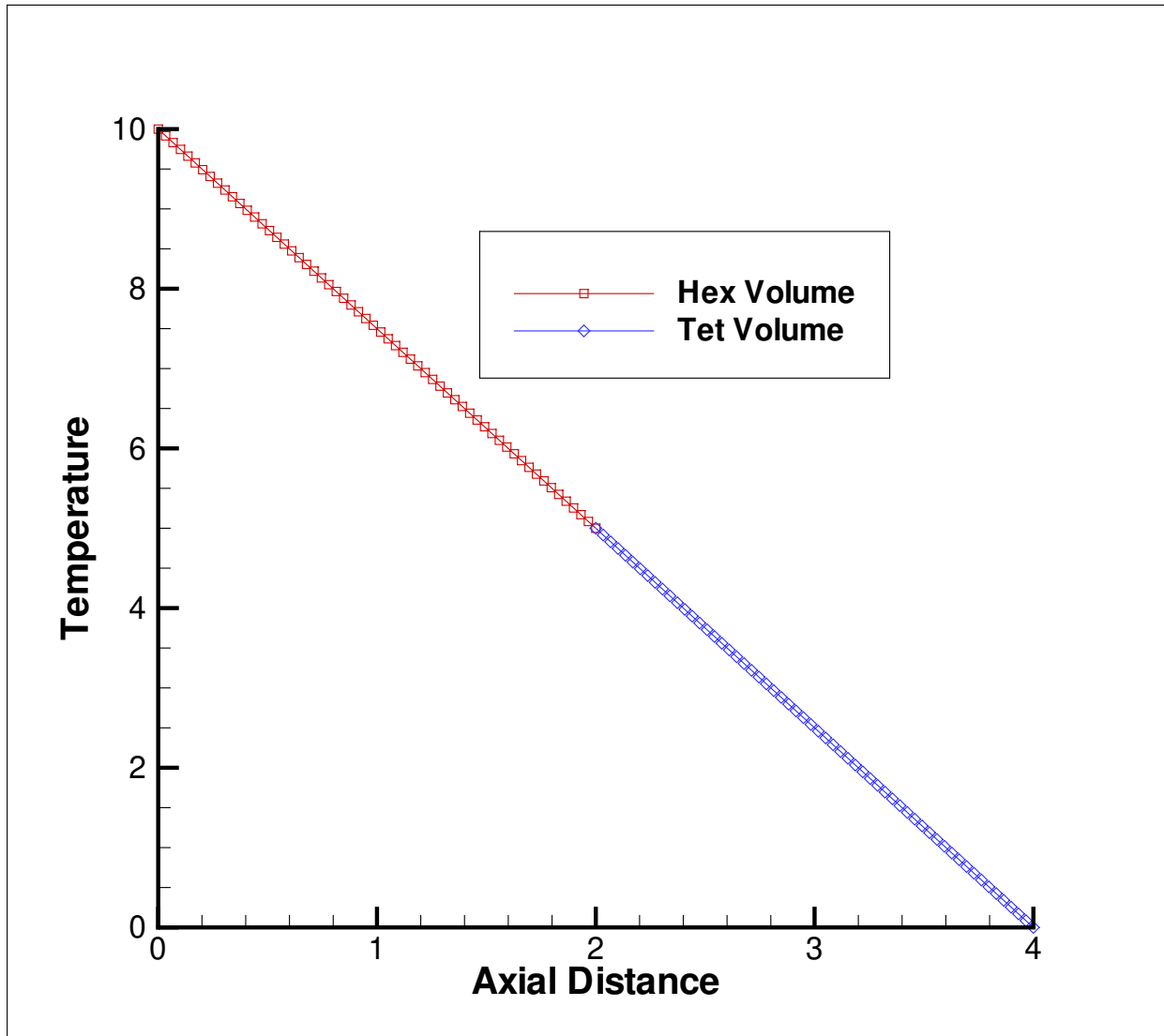


**Figure 18.7-1.. Scoping study simulation plot of normalized streamwise velocity at three mesh rotations.**

This page intentionally left blank.

# 19. BUOYANCY VORTICITY GENERATION MODEL

<b>Dimension:</b>	oD
<b>Transient/Steady:</b>	
<b>Laminar/Turbulent:</b>	
<b>Isothermal/Thermal:</b>	
<b>Temperature/Enthalpy:</b>	
<b>Uniform/Nonuniform:</b>	
<b>Combustion:</b>	no
<b>Soot:</b>	no
<b>Coupled Mechanics:</b>	no
<b>Regression Test:</b>	1mHeBVG

## 19.1. EXECUTIVE SUMMARY

The buoyancy vorticity generation (BVG) model has been verified to be implemented correctly within SIERRA/Fuego (starting at version 0.9.0) when appropriate buoyancy models are in use, i.e., 'Differential' and 'Buoyant'. The verification approach is a modified unit test of the BVG model. Specifically, an actual SIERRA/Fuego simulation is performed and point wise values of the subcontrol volume weighed production term are viewed in an output file using the SIERRA Frameworks 'History' functionality and checked against hand-calculations.

The simulation input file is used to prescribe constant initial values of turbulent kinetic energy, turbulence dissipation rate, and linear profiles of temperature and pressure. Based on the linear profiles of both pressure and temperature (through which density is calculated using the ideal gas law) and given the initial conditions for turbulence quantities (through which eddy viscosity is calculated), the subcontrol volume assembled value of the turbulence production rate due to buoyancy vorticity generation is given at all locations within the domain. The mesh used to determine base metrics is the standard 'duct.g' mesh.

To avoid contamination of the BVG production term by the standard shear-based production term, velocity gradients are guaranteed to be numerically zero through initialization of the flow field to zero and using a relaxation parameter of 1.0e-300 that is used during the velocity update. Given that the turbulence fields are calculated after the pressure solve and update, a relaxation value of 0.0 is used to

insure that the nodal pressure gradient used in the calculation of the BVG production term is based on the values specified within the initial condition block.

This unit test procedure ensures a non-invasive methodology to check the values of the calculated BVG production term against a hand calculation. Moreover, given that any solid mesh rotation will result in a constant value of production term (assuming the initial conditions for temperature and pressure are properly rotated repectively with the mesh), the model implementation has been verified even for mesh rotations.

Finaly, verification experiments demonstrate that the BVG model is implemented correctly. Refinement studies are carried out to demonstrate that the numerical implementation is convergent to the analytical model.

## 19.2. MATERIAL SPECIFICATIONS

The material properties in SIERRA/Fuego were evaluated using ChemkinIII. Air was simulated as a binary mixture of O<sub>2</sub> and N<sub>2</sub>, with mole fractions of 0.2095 and 0.7905, respectively.

## 19.3. INITIAL CONDITIONS

### 19.4. STANDARD MESH

The standard mesh used was aligned in the principle  $z$  direction. The length, width and height, corresponding to the  $z$ ,  $x$ , and  $y$  directions are 20 cm x 2 cm x 2 cm. The initial conditions used in Fuego for turbulent kinetic energy and turbulence dissipation rate were specified to be uniform values, which were arbitrarily chosen, of 120.0 cm<sup>2</sup>/s<sup>2</sup> and 20.0 cm<sup>2</sup>/s<sup>3</sup>, respectively.

A linear profile of temperature was implemented using linear functions within the initial condition block,  $T(z) = 75z + 500$ , that yielded a temperature of 500 and 2000 K at  $z = 0$  and  $z = 20$  cm, respectively. Since the density gradient is required, the non-zero analytical gradient in the  $z$ -principle direction was  $d/dz(P^{ref}MW/R(75z + 500))$ , or  $-75\alpha/(75z + 500)^2$  (note the quadratic functionality) where  $\alpha$  is  $P^{ref}MW/R$ . The pressure was initialized to be a function of  $y$  and its linear equation was  $P(y) = 250Y + 1000$  that yielded a pressure of 1000 and 1500 dyne/cm<sup>2</sup> at  $y = 0$  and  $y = 2$ , respectively. The analytical pressure gradient, in the  $y$ -principle direction, therefore, was (convieniently) a constant value of 250 dyne/cm<sup>2</sup>/cm.

When the 'Differential' buoyancy model is in use, the above specified pressure gradient does not include the hydrostatic component since it is convieniently combined with the right hand side buoyancy term,  $(\rho - \rho^{ref})g$ , that appears within the respective momentum equation. Therefore, the above pressure is perceived to be the "motion pressure" and does not yet include the hydrostatic component, i.e.,  $(\rho^{ref}gh_y)$ . However, when using the 'Buoyant' model, the above specified pressure, in fact, includes both the hyrostatic and motion contributions since the right hand side buoyancy source that appears within the respective momentum equations is simply  $\rho^{ref}g$ .

Given the constant values of turbulent kinetic energy and turbulence dissipation rate and a variable profile ( $z$ -direction) in density, eddy viscosity was given as a strict function of  $z$  alone.

## 19.5. ROTATED MESH

Using the SEACAS tools 'grepos', see <http://www.jal.sandia.gov/SEACAS/SEACAS.html>, the standard mesh was rotated by angle  $\alpha$ . Constant initial conditions of turbulent kinetic energy and turbulence dissipation rate were again chosen to be  $120.0 \text{ cm}^2/\text{s}^2$  and  $20.0 \text{ cm}^2/\text{s}^3$ , respectively.

The initial conditions for pressure and temperature were specified by user subroutine. The user subroutine rotated the given rotated simulation mesh back to the non rotated mesh and prescribed the conditions as described above. Therefore, the profiles of temperature and pressure were again linear along the axis of rotation. However, in this rotated reference frame all cross derivatives appeared in the BVG production term.

Given the constant values of turbulent kinetic energy and turbulence dissipation rate and the variable profile in density, eddy viscosity was given as a function of  $x$ ,  $y$ , and  $z$ .

As a side note, revolutions of a given mesh by an arbitrary angle can introduce slight metric errors.

## 19.6. BOUNDARY CONDITIONS

Since no variable update was performed for any variables, specific types of boundary conditions were arbitrary. Nevertheless, the three dimensional duct used and inflow, outflow and wall condition.

## 19.7. ANALYTIC OR BENCHMARK SOLUTION

The BVG model is formally described in the SIERRA/Fuego theory document. For clarity, the final form of the model is given by,

$$P_{bvg} = C_{bvg} (\mu + \mu_{eddy}) \frac{((\nabla \rho \times \nabla P)^2)^{1/2}}{\rho^2} \quad (19.1)$$

where  $\nabla P$  represents the combine pressure gradient, i.e., motion + hydrostatic,  $\mu + \mu_{eddy}$  is the combination of the molecular and eddy viscosity, and  $C_{bvg}$  is a user defined constant and is currently taken to be five.

The SIERRA/Fuego implementation is to use subcontrol volume variables for the density and pressure gradient terms, while all other variables, e.g., density, and turbulence properties, i.e.,  $k$ ,  $\epsilon$ , and  $\mu^{eddy}$ , are chosen to be nodal.

The right hand side nodal contribution to the turbulent kinetic energy equation is given by,

$$P_{bvg_i} scvol_i \quad (19.2)$$

while the right hand side nodal contribution for the turbulence dissipation rate equation is

$$\frac{\epsilon}{k} C_{\epsilon 3} P_{bvg_i} scvol_i \quad (19.3)$$

where  $C_{\epsilon 3}$  is a user defined constant and is currently set to 1.3. The above two formulas stress the assembly over all subcontrol volumes by summation over repeated indices.

For the unit test, a center mesh point, corresponding to  $(x, y, z)^T = (1, 1, 10) \text{ cm}$ , was used to calculate, using a separate c++ program, the production of turbulent kinetic energy due to buoyancy vorticity generation. The simple scaling of the production term required for the turbulent dissipation rate right hand side contribution was also calculated using the c++ program. In the discussion that follows, each model term is described and shown to four significant figures. Where appropriate, the full precision obtained from the c++ code is provided.

### 19.7.1. Analytic Form of the Buoyancy Production Term

Given the point wise location of  $(x, y, z)^T = (1, 1, 10) \text{ cm}$ , the analytical value of the BVG production term can be obtained by using analytical derivatives for density and pressure. The calculation of the germane required values follows (shown below are intermediate calculations from a c++ program).

### 19.7.2. Set of Material Properties

The values of mixture molecular weights, densities, and viscosities used in the analytical calculation of the BVG production term will now be presented.

- Mixture molecular weight is given by  $MW_i Y_i = 28.848341 \text{ g/gmol}$ , where Einsteinien notation is assumed. Here,  $MW_{O_2} = 31.9988 \text{ g/gmol}$  and  $MW_{N_2} = 28.0134 \text{ g/gmol}$ .
- Reference density is given by  $P^{ref} MW / RT^{ref}$ , where  $P^{ref}$ ,  $T^{ref}$  are 1.0 atm and 298.0 K, repectively, while the universal gas constant is taken to be  $83145100 \text{ erg/gmolK}$ . The reference density is therefore  $1.1797e-3 \text{ g/cm}^3$ . The density at  $z = 10 \text{ cm}$ , coressponding to a temperature of  $T(z = 10\text{cm}) = 1250K$  (recall  $T(z) = 75z + 500$ ) is  $2.8125e-4 \text{ g/cm}^3$ .
- The eddy viscosity at  $z = 10 \text{ cm}$  is given by  $C_\mu \rho_{z=10\text{cm}} k^2 / \epsilon$  where  $C_\mu$  is 0.09 while  $k$  and  $\epsilon$  represent the initial conditions, i.e.,  $120.0 \text{ cm}^2/\text{s}^2$  and  $20.0 \text{ cm}^2/\text{s}^3$ , respectively. The value is, therefore, 1.8225 cP.
- The molecular viscosity at  $z = 10 \text{ cm}$ ,  $T = 1250 \text{ K}$  is  $0.049601 \text{ cP}$  (calculated from ChemkinIII).

### 19.7.3. Analytical Density and Pressure Gradients

The values of mixture density and pressure gradients used in the analytical calculation of the BVG production term will now be presented.

- Density derivative at  $z = 10 \text{ cm}$  is given by  $-75\alpha/(75z + 500)^2$ , or  $-1.6875e-05 \text{ g/cm}^3/\text{cm}$ .
- The Pressure gradient at  $y = 1.0 \text{ cm}$  is given by  $250 + \beta \rho^{ref} g$ , where  $g$  is the gravitational vector and taken to be  $-981.0j \text{ cm/s}^2$  and  $\beta$  assumes a value of unity or zero depending on the buoyancy model in use. The pressure gradient in the  $y$ -direction is a constant  $248.8427$  and  $250.0 \text{ dyne/cm}^3$  for the 'Differential' and 'Buoyant' mode, respectively.

### 19.7.4. Mesh Geometric Properties

The set of mesh geometric properties used in the analytical calculation of the BVG production term will now be presented.

- The total volume at the center node is given by  $\Delta x \Delta y \Delta z = 1/8 \text{ cm}^3$ , where (for the coarse mesh)  $\Delta x = \Delta y = 2/8 \text{ cm} = 1/4 \text{ cm}$  and  $\Delta z = 20/10 \text{ cm} = 2 \text{ cm}$ . Subsequent refinements drop the total volume by  $(1/8)(1/2)^3 n$  where  $n$  represents the number of refinements, e.g., 0, 1, 2, and 3. Therefore, the total volumes for each refinement level are,  $1/8$ ,  $1/64$ ,  $1/512$ , and  $1/4096 \text{ cm}^3$ .

### 19.7.5. Analytical Normalized Cross Product

The form of the analytical cross product, normalized by the square of the density is given by,

$$\frac{\frac{d\rho}{dz} \times \frac{dP}{dy}}{\rho^2} \Big|_{z=10\text{cm}} \quad (19.4)$$

- The precise value of the analytical normalized cross product term is  $53086.65155872068 \text{ s}^{-2}$ .

### 19.7.6. Analytical BVG Production Source Term

The analytical BVG production term at  $(x, y, z)^T = (1, 1, 10) \text{ cm}$  for the series of refinements are:

- Refinement level 0:  $621.1450469872418 \text{ gcm}^2/\text{s}^3$ .
- Refinement level 1:  $77.64313087340523 \text{ gcm}^2/\text{s}^3$ .
- Refinement level 2:  $9.705391359175653 \text{ gcm}^2/\text{s}^3$ .
- Refinement level 3:  $1.213173919896957 \text{ gcm}^2/\text{s}^3$ .

The analytical BVG production term for the turbulence dissipation rate, at  $(x, y, z)^T = (1, 1, 10) \text{ cm}$ , for the series of refinements are:

- Refinement level 0:  $134.5814268472357 \text{ gcm}^2/\text{s}^4$ .
- Refinement level 1:  $16.82267835590446 \text{ gcm}^2/\text{s}^4$ .
- Refinement level 2:  $2.102834794488058 \text{ gcm}^2/\text{s}^4$ .
- Refinement level 3:  $0.2628543493110073 \text{ gcm}^2/\text{s}^4$ .

### 19.7.7. Discretized Form of the Buoyancy Production Term

Given the above form of the production of turbulent kinetic energy by buoyancy vorticity generation, Equation 19.1, the precise numerical value of the term can be calculated given the aforementioned quadrature rules. For example, the density and pressure gradients could be evaluated at the coordinates specific to the eight sub control volume centers and assembled to the nodes by weighing the values with nodal viscosities, nodal densities and subcontrol volumes. However, since the density is actually a quadratic function and the code uses linear shape functions, such a procedure would not provide means to verify the model implementation when compared to the above analytical result.

In fact, the difference between the above analytical result and the SIERRA/Fuego's result represents model discretization error. Therefore, the above analytical refinement results were provided to establish that refinement of the coarse mesh will yield a numerical discretized model value that is convergent to the analytical result (shown later).

Therefore the hand calculations of the numerically implemented model, with its associated quadrature rules and both linear shape functions and derivatives, will now be presented.

We begin by reviewing the quadrature point locations for the nodal control volume corresponding to the coordinates  $(x, y, z)^T = (1, 1, 10) \text{ cm}$ . The density derivatives need only be computed at the  $z$  location of  $9.5$  and  $10.5 \text{ cm}$  while the  $y$ -component of the pressure gradient has already been shown to be constant at all locations, i.e.,  $248.843$  and  $250.0 \text{ dyne/cm}^3$ .

A total of eight subcontrol volume contributions should be included for the full assembly. However, given the convenient choice of pressure and density gradients, the overall term can be broken down into two separate terms: the set of four contributions at  $z=9.5 \text{ cm}$  and the set of four contributions at  $z=10.5 \text{ cm}$ . Each of the subcontrol volume values, for the coarse mesh, are given by  $\Delta x \Delta y \Delta z / 8$  or  $1/64 \text{ cm}^3$ .

### 19.7.8. Set of Material Properties

The values of mixture molecular weights, densities, and viscosities used in the numerical hand calculation of the BVG production term will now be presented.

- Mixture molecular weight is given by  $MW_i Y_i = 28.8483413 \text{ g/gmol}$ , where Einsteinien notation is assumed. Here,  $MW_{O_2} = 31.9988 \text{ g/gmol}$  and  $MW_{N_2} = 28.0134 \text{ g/gmol}$ .
- Reference density is given by  $P^{ref} MW / RT^{ref}$ , where  $P^{ref}$ ,  $T^{ref}$  are  $1.0 \text{ atm}$  and  $298.0 \text{ K}$ , respectively, while the universal gas constant is taken to be  $82.0575 \text{ atmcm}^3/\text{gmolK}$ . The reference density is

therefore  $1.1797e-3 \text{ g/cm}^3$ . The density at  $z = 10$ , corresponding to a temperature of  $T(z = 10\text{cm}) = 1250\text{K}$ , is  $2.8125e-4 \text{ g/cm}^3$ .

- The eddy viscosity at  $z = 10 \text{ cm}$  is given by  $C_\mu \rho_{z=10\text{cm}} k^2 / \epsilon$  where  $C_\mu$  is 0.09 while  $k$  and  $\epsilon$  represent the initial conditions, i.e.,  $120.0 \text{ cm}^2/\text{s}^2$  and  $20.0 \text{ cm}^2/\text{s}^3$ , respectively. The value is, therefore,  $1.8225 \text{ cP}$ .
- The molecular viscosity at  $z = 10 \text{ cm}$ ,  $T = 1250 \text{ K}$  is  $0.04960 \text{ cP}$  (calculated from ChemkinIII).

### 19.7.9. Numerical Density and Pressure Gradients

The values of mixture density and pressure gradients used in the numerical calculation of the BVG production term will now be presented.

- Density derivative at  $z = 9.5$  and  $z = 10.5 \text{ cm}$  are  $1.9176e-05$  and  $1.5067e-05 \text{ g/cm}^3/\text{cm}$  respectively. These values are obtained by using shape function derivatives for a hexahedral element with integration points at  $(\xi, \eta, \zeta)^T = (-0.5, -0.5, -0.5)$  and  $(0.5, -0.5, -0.5)$ , respectively. Values of nodal density, used for the shape function derivative evaluations, for the  $z = 8, 10$ , and  $12 \text{ cm}$  locations are calculated to be  $0.0003196, 0.0002812, 0.0002511 \text{ g/cm}^3$ , respectively.
- Pressure gradients, at all locations, should be constant. The pressure gradient in the  $y$ -direction is a constant  $248.843$  and  $250 \text{ dyne/cm}^3$  for the 'Differential' and 'Buoyant' model, respectively.

### 19.7.10. Mesh Geometric Properties

The set of mesh geometric properties used in the numerical calculation of the BVG production term will now be presented.

- The volume of the individual subcontrol volumes are a given above,  $\Delta x \Delta y \Delta z / 8$  or  $1/64 \text{ cm}^3$ .

### 19.7.11. Numerical Normalized Cross Product

The precise cross product term (evaluated at  $z = 9.5$  and  $10.5 \text{ cm}$ ) normalized by the square of the density (evaluated at  $z = 10 \text{ cm}$ ) are  $60325.74040763712$  and  $47398.79603457203 \text{ s}^{-2}$ , respectively. Note that these values, as expected, bracket the analytical value of  $53086.65155872068 \text{ s}^{-2}$ .

### 19.7.12. Numerical BVG Production Source Term

The final numerical BVG source term is comprised of two values:

$$\frac{4 * C_{bvg} * Scvol * (\mu + \mu^{eddy})}{\rho^2} \Big|_{z=10\text{cm}} (\nabla \rho \times \nabla P|_{z=9.5\text{cm}} + \nabla \rho \times \nabla P|_{z=10.5\text{cm}}) \quad (19.5)$$

- When using the 'Differential' model, evaluation of the above term for node  $(x, y, z)^T = (1, 1, 10) \text{ cm}$  (for refinement level 0) yields a right hand side source term for turbulent kinetic energy source term of

$630.220218128289 \text{ gcm}^2/\text{s}^3$ , while the right hand source term for the turbulence dissipation rate is  $136.547713927796 \text{ gcm}^2/\text{s}^4$ .

- When using the 'Buoyant' model, evaluation of the above term for node  $(x, y, z)^T = (1, 1, 10) \text{ cm}$  (for refinement level 0) yields a right hand side source term for turbulent kinetic energy source term of  $633.151253134033 \text{ gcm}^2/\text{s}^3$ , while the right hand source term for the turbulence dissipation rate is  $137.182771512374 \text{ gcm}^2/\text{s}^4$ .

## 19.8. MESH DEFINITION FOR THE SIERRA/FUEGO CASE STUDY

The standard mesh used was a rectangular domain oriented in the principle  $z$  direction. The length, width and height, corresponding to the  $z$ ,  $x$ , and  $y$  directions was  $20 \text{ cm} \times 2 \text{ cm} \times 2 \text{ cm}$ . The dimension of the mesh was  $11 \times 9 \times 9$  in the  $z$ ,  $x$  and  $y$  direction, respectively. A three dimensional mesh was chosen to verify the correct assembly of the BVG production term. For review, there are eight contributions per node for an interior node that is surrounded by eight hex elements.

For the refinement study, the 'Uniform Refinement' capability within SIERRA/Fuego was used to refine the original mesh three levels.

The standard mesh was rotated about the  $x$ -axis by  $\alpha = -45$  degrees to yield a mesh of the same proportions, however, aligned with the axis of rotation to exercise the cross derivatives that would be missed by simple orthogonal rotations.

The rotation transformation matrix, in the  $x$ -direction, is defined by,

$$R^{x'} = \begin{pmatrix} 1 & 0 & 0 \\ 0 & \cos(\alpha) & \sin(\alpha) \\ 0 & -\sin(\alpha) & \cos(\alpha) \end{pmatrix} \quad (19.6)$$

while the inverse of the transformation, which provides the mapping from the transformed variable back to the original frame, is

$$R^{x'^{-1}} = \begin{pmatrix} 1 & 0 & 0 \\ 0 & \cos(\alpha) & -\sin(\alpha) \\ 0 & \sin(\alpha) & \cos(\alpha) \end{pmatrix} \quad (19.7)$$

## 19.9. SOLUTION PROCEDURE

The simulation was run for one time step and values of the turbulent production of kinetic energy for both the standard and rotated mesh were viewed within EnSight7. Actual values reported, however, were obtained using the SIERRA Frameworks, 'History' functionality to provide the full precision of

the nodal variables to be compared. The transformed central coordinate was simply determined by  $(x^t, y^t, z^t)^T = R^{x'}(x, y, z)^T$ .

## 19.10. VERIFICATION EXPERIMENTS

### 19.10.1. Standard Mesh Numerical BVG Source Term

Results for the nodal pointwise location of  $(x, y, z)^T = (1, 1, 10) \text{ cm}$  were viewed in an output file that was obtained using the 'History' output functionality. The values of the assembled BVG production term for turbulent kinetic energy and turbulence dissipation rate, when using the 'Differential' model, for the series of mesh refinement levels are:

- Refinement Level 0:  $630.22021812829 \text{ gcm}^2/\text{s}^3, 136.547713927796 \text{ gcm}^2/\text{s}^4$
- Refinement Level 1:  $77.9236560351318 \text{ gcm}^2/\text{s}^3, 16.8834588076119 \text{ gcm}^2/\text{s}^4$
- Refinement Level 2:  $9.71413407984749 \text{ gcm}^2/\text{s}^3, 2.10472905063362 \text{ gcm}^2/\text{s}^4$
- Refinement Level 3:  $1.21344694545969 \text{ gcm}^2/\text{s}^3, 0.262913504849598 \text{ gcm}^2/\text{s}^4$

The values of the assembled BVG production term for turbulent kinetic energy and turbulence dissipation rate for the base refinement level, when using the 'Buoyant' model, are:

- Refinement Level 0:  $633.151253134033 \text{ gcm}^2/\text{s}^3, 137.182771512374 \text{ gcm}^2/\text{s}^4$ .

It is noted that the above value for Refinement Level = 0 match exactly the values determined, and presented above for the hand calculation to 12 orders of precision. Given the above values, specifically shown for the 'Differential' model suite, the error between the numerical and analytical production term can be plotted against the mesh spacing to show order of convergence. Figure 19.10-1 demonstrates that the model is, in fact, convergent. Given that the BVG source term for the turbulence dissipation rate is a simple scaling of the BVG production term, convergence plots are, therefore, not shown.

Specifying the pressure gradient to be a function of  $x$  alone provides coverage of all shape function derivative evaluations for the standard mesh orientation. The values of the assembled BVG production term for turbulent kinetic energy and turbulence dissipation rate for the base refinement level using both the 'Differential' and 'Buoyancy' model, are:

- Refinement Level 0:  $630.22021812829 \text{ gcm}^2/\text{s}^3, 136.547713927796 \text{ gcm}^2/\text{s}^4$
- Refinement Level 0:  $633.151253134033 \text{ gcm}^2/\text{s}^3, 137.182771512374 \text{ gcm}^2/\text{s}^4$ .

As expected, the above values match, exactly, those values when the pressure gradient was a strict function of  $y$ .

## 19.10.2. Rotated Mesh

Rotation of the mesh in any arbitrary direction along with rotation of the former linear profiles of pressure and temperature should yield a production term that is equal to the unrotated mesh. Only one rotation study must be performed given that the shape function derivatives are gathered in the workset and used for all gradient calculations.

Simulation results from a rotation of the  $x$  axis by -45 degrees provide the following values, when using the 'Differential' model, for turbulent kinetic energy and turbulence dissipation rate:

- Refinement Level 0:  $630.219963758676 \text{ gcm}^2/\text{s}^3$ ,  $136.547658814381 \text{ gcm}^2/\text{s}^4$
- Refinement Level 1:  $77.9236532591145 \text{ gcm}^2/\text{s}^3$ ,  $16.8834582061415 \text{ gcm}^2/\text{s}^4$
- Refinement Level 2:  $9.7141181347671 \text{ gcm}^2/\text{s}^3$ ,  $2.10472559586621 \text{ gcm}^2/\text{s}^4$
- Refinement Level 3:  $1.21344641876017 \text{ gcm}^2/\text{s}^3$ ,  $0.262913390731369 \text{ gcm}^2/\text{s}^4$

The values of the assembled BVG production term for turbulent kinetic energy and turbulence dissipation rate for the base refinement level, when using the 'Buoyant' model, are:

- Refinement Level 0:  $633.150997581395 \text{ gcm}^2/\text{s}^3$ ,  $137.182716142636 \text{ gcm}^2/\text{s}^4$

It is noted that there are minor differences between the rotated and non rotated mesh results, however, this error is likely due to numerical error that has been introduced via the non-exact mesh revolution and in the specification of the rotated gravitational vector, i.e.,  $R^x' g$ . Moreover, the above refinement study indicates that the model is approaching a like value regardless of rotation.

The convergence of the scheme on the rotated mesh is shown in Figure 19.10-2. Again, it is demonstrated that the numerical implementation within Fuego is convergent.

Again, to exercise the  $x$ -shape function derivative evaluations, the pressure gradient was made to be a function of  $x$  and transformed in the direction of the mesh orientation. Results are as follows for the 'Differential' and 'Buoyant' model:

- Refinement Level 0:  $630.219963758676 \text{ gcm}^2/\text{s}^3$ ,  $136.547658814381 \text{ gcm}^2/\text{s}^4$
- Refinement Level 0:  $633.150997581395 \text{ gcm}^2/\text{s}^3$ ,  $137.182716142636 \text{ gcm}^2/\text{s}^4$

It is noted that there is perfect consistency of results between the like-rotated mesh study.

## 19.11. CONCLUDING REMARKS

A set of SIERRA/Fuego simulations, using a specialized input file that prescribed initial profile for turbulent kinetic energy, turbulence dissipation rate, temperature, and pressure, was used to verify the correct implementation of the production term due to buoyancy vorticity generation. Results show that the model is convergent to manufactured analytical production term and that the model is independent of mesh revolution.

The c++ program used to verify the fuego implementation has been archived (along with the simulation file) along with this documentation.

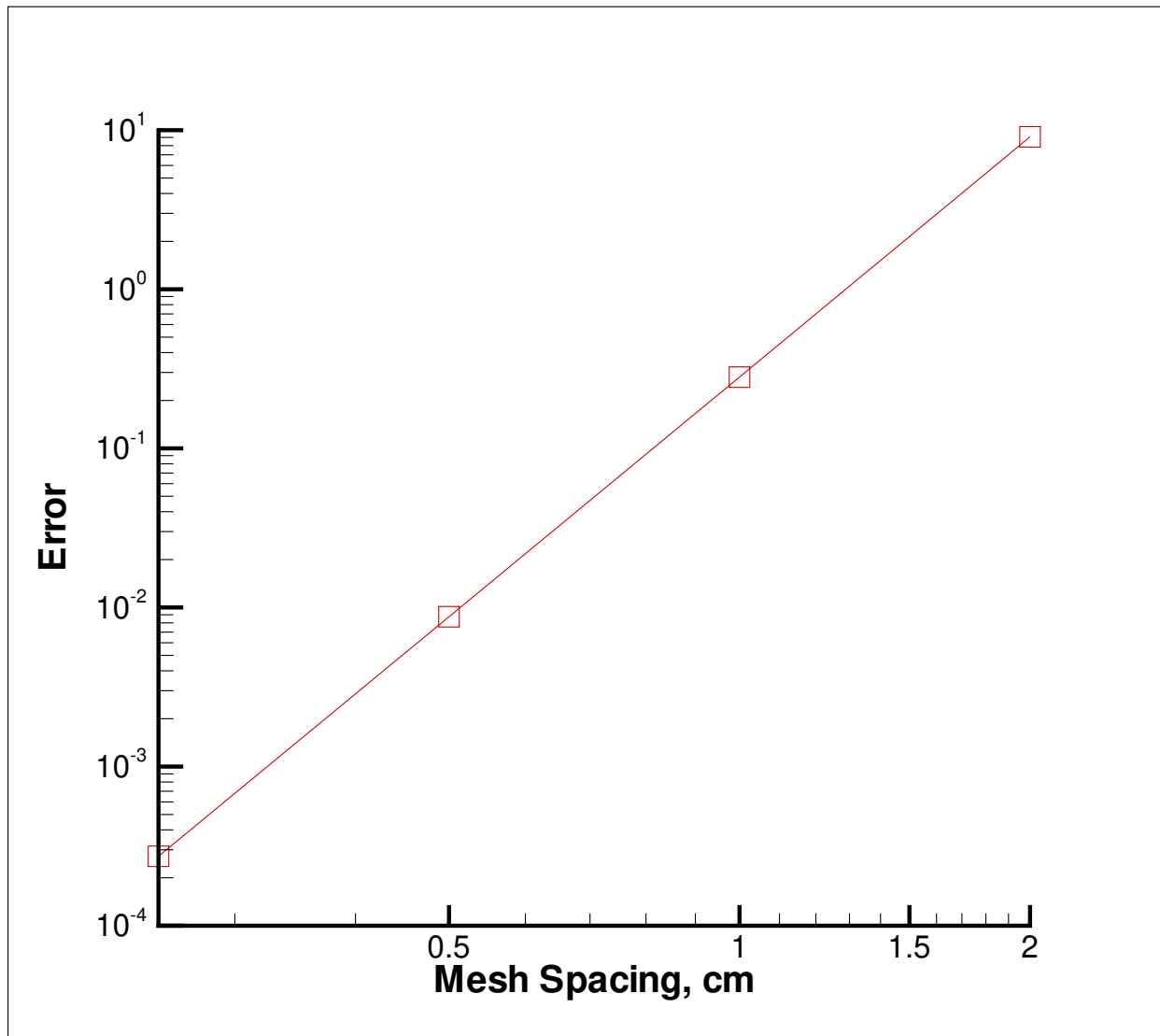


**Figure 19.10-1.. Plot of error vs mesh spacing to demonstrate convergence of the SIERRA/Fuego numerical model to the analytical result.**

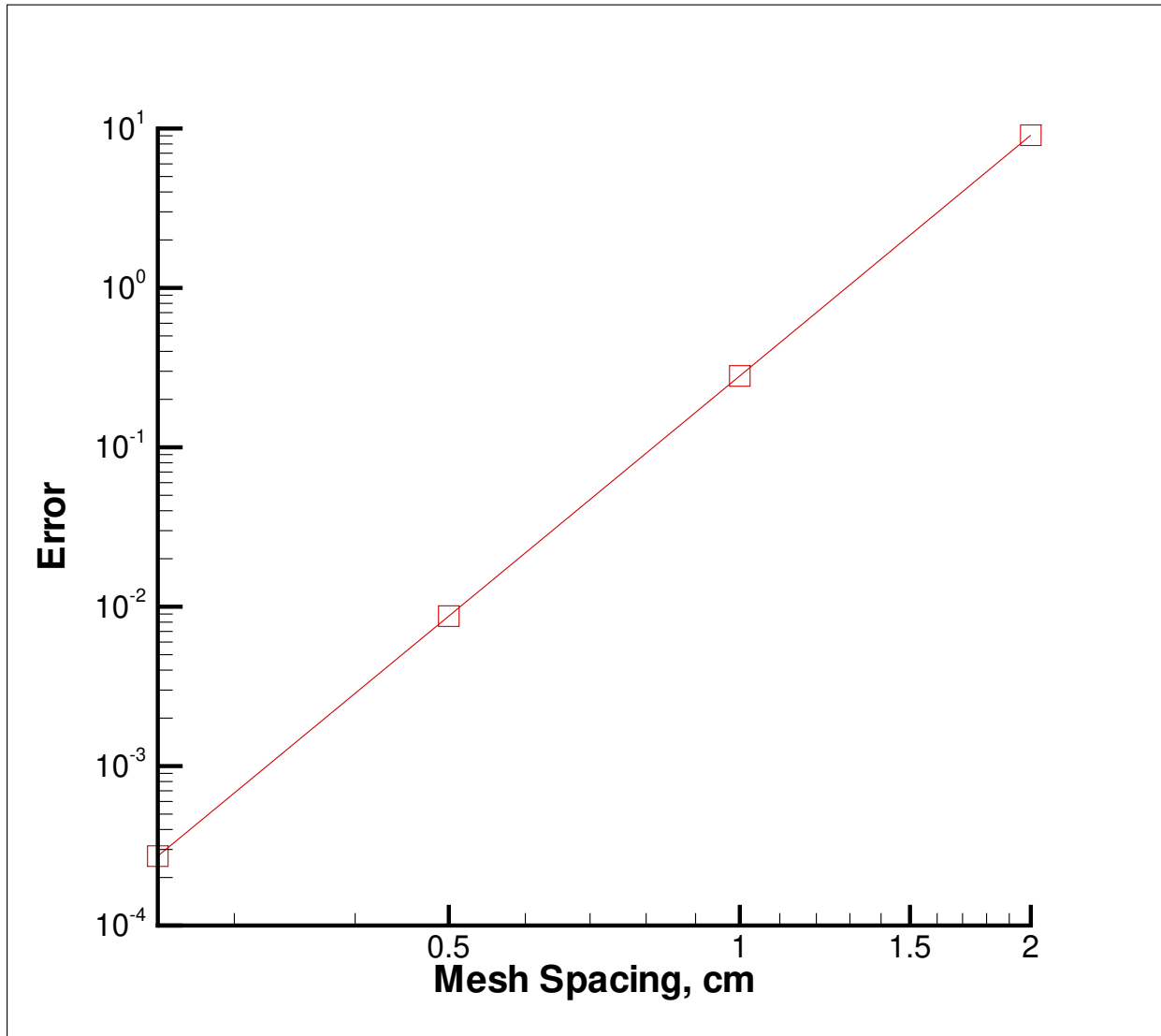


**Figure 19.10-2.. Plot of error vs mesh spacing to demonstrate convergence of the SIERRA/Fuego numerical model (using a rotated mesh) to the analytical result.**

This page intentionally left blank.

# 20. LAMINAR DUCT FLOW

<b>Dimension:</b>	3D
<b>Transient/Steady:</b>	steady
<b>Laminar/Turbulent:</b>	laminar
<b>Isothermal/Thermal:</b>	isothermal
<b>Temperature/Enthalpy:</b>	n/a
<b>Uniform/Nonuniform:</b>	uniform
<b>Combustion:</b>	no
<b>Soot:</b>	no
<b>Coupled Mechanics:</b>	no
<b>Regression Test:</b>	fuego/flat_ductA fuego/flat_ductB fuego/flat_ductC

This problem is used to verify the convection/diffusion operator with a laminar isothermal flow problem. The turbulence mechanics is used to solve this problem with the turbulence terms set to zero.

The 2-D flat duct geometry is 10 m long by 0.5 m high. A constant velocity of 1.0 m/s was specified at the inlet and a constant pressure of 0.0 Pa was specified at the outlet. The density was 1 kg/m<sup>3</sup>, the molecular viscosity was 0.002 kg/m·s, and the corresponding Reynolds number was 250 based on duct height. The entrance length was estimated to be 5.25 m such that fully developed flow existed over roughly half of the duct. In this region, the axial velocity profile is parabolic across the duct. At the inlet, the solution is singular at the two corners where the inlet intersects the walls.

Overall, the VIVID code has provided the solution order and solution error based on the Richardson extrapolated method. The results indicate that the numerical scheme is first order in the developing flow region and second order in the fully developed region of the duct. A finer mesh solution is required to accurately capture the gradients in the developing flow region. An additional mesh solution would also provide a better understanding of the behavior or the order as the mesh is refined.

The 2-D flat duct problem is not ideal for code verification due the singularities at the inlet-wall locations. In addition, the discretization error in the axial velocity is zero at some locations and Richardson extrapolation does not work at these points. In general, the calculated order of a numerical scheme is very sensitive to the properties of the problem (i.e. singularities), numerical error behavior (i.e., zero values), and the computational mesh (i.e., non-uniform spacing).

## 20.1. MATERIAL SPECIFICATIONS

The material properties in Fuego were specified to be constant air values. The density was  $1 \text{ kg/m}^3$ , the molecular viscosity was  $0.002 \text{ kg/m}\cdot\text{s}$ , and the corresponding Reynolds number was 250 based on duct height.

## 20.2. INITIAL CONDITIONS

The initial conditions used in Fuego were the reference pressure zero values of the  $x$ ,  $y$ , and  $z$  components of velocity, a turbulent kinetic energy value of  $1.0\text{e-}30$ , and a turbulent dissipation rate of  $1.0\text{e-}30$ . The turbulence quantities were set to very small values in order to simulate laminar flow conditions. The duct was aligned with the flow in the  $x$ -direction.

## 20.3. BOUNDARY CONDITIONS

A constant velocity of  $1.0 \text{ m/s}$  was specified at the inlet and a constant pressure of  $0.0 \text{ Pa}$  was specified at the outlet. Again, the turbulent kinetic energy and the turbulent dissipation were set to  $1.0\text{e-}30$ . Wall boundaries were specified along the top and bottom walls of the duct. Since Fuego is a 3-D code, two symmetry planes were specified in the  $z$ -coordinate direction to simulate a 2-D domain.

## 20.4. RICHARDSON EXTRAPOLATED SOLUTION

The VIVID code was used to determine the solution order and error for two dependent variables (axial velocity and pressure) in the 2-D flat duct problem. Exact analytical solutions do not exist for the developing duct flow problem; therefore, Richardson extrapolation method was used to estimate the exact solution. Second order accuracy was assumed in the Richardson extrapolated solution.

## 20.5. MESH DEFINITION

The 2-D flat duct problem was simulated with the Fuego code on three different non-uniform meshes: coarse ( $101 \times 21 \times 2$ ) with 2000 elements; medium ( $201 \times 41 \times 2$ ) with 8000 elements; and fine ( $401 \times 81 \times 2$ ) with 32000 elements.

The non-uniform meshes contained hexagonal elements. Geometric progression was used to cluster the grid points towards the inlet of the duct ( $x$ -direction) using an initial spacing of  $0.045697 \text{ m}$  for the fine mesh. Equal spacing was specified across the duct ( $y$ -direction). The medium and coarse meshes were created by removing every other grid point such that the meshes contain co-located grid points.

## 20.6. SOLUTION PROCEDURE

Options selected in the Fuego run were: CFL limit = 2.0; time step change factor = 1.25; transient step type is automatic; projection method = stabilized; upwind method = LPS; first order upwind factor = 0.0; underrelaxation factors = 1.0 for all variables; linear residual tolerances for continuity = 1.0e-5, flow equations = 1.0e-4, and k and  $\epsilon$  equations = 2.0; nonlinear residual tolerances = 1.0e-20 for all equations; and nonlinear iteration=1.

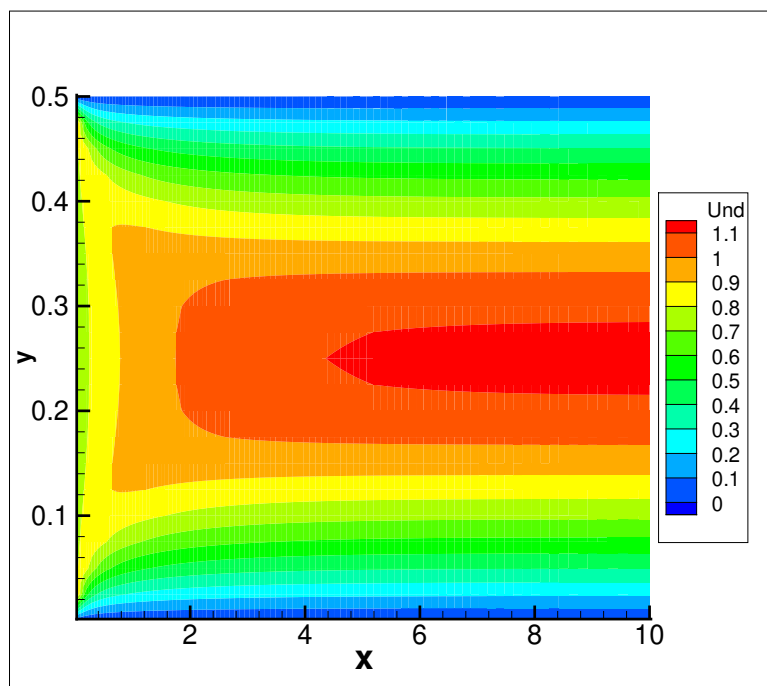
Each simulation was run until a steady state solution was obtained and all non-linear residuals were reduced below 1.0e-18. The calculations were performed using the turbulence mechanics in Fuego stable version 0.7.0 on a SUN computer platform. The turbulence terms were initialized to zero to simulate laminar flow. The LPS convection scheme was used in the Fuego simulation and the expected order of accuracy is between 1.0 and 2.0 based on the Peclet number of the flow. A second order accurate scheme was assumed in the Richardson extrapolated solution.

## 20.7. RESULTS

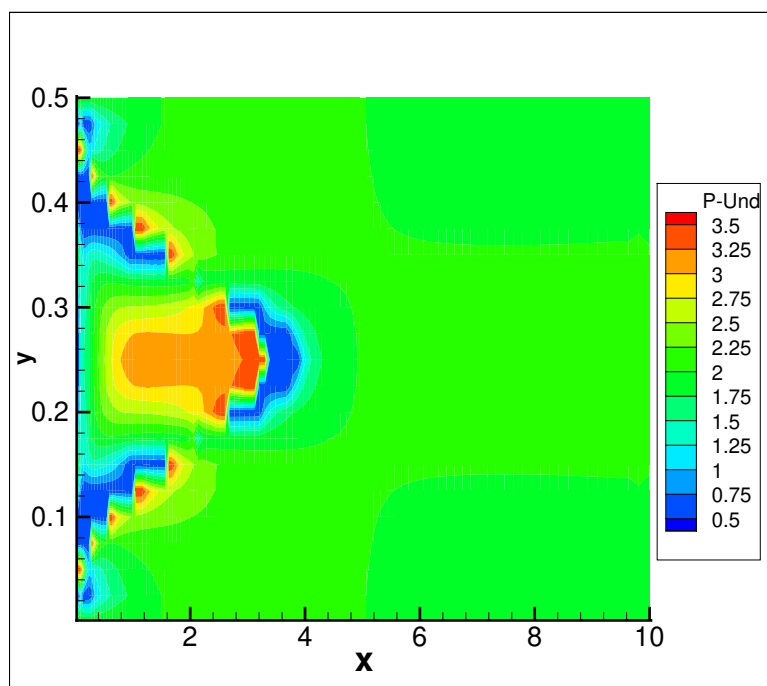
Figure 20.7-1 shows the axial velocity contour plot for the fine mesh solution. It should be noted that the  $y$ -axis has been expanded independently of the  $x$ -axis. As expected, there are sharp velocity gradients in the entrance region of the duct followed by a fully developed flow region.

Figure 20.7-2 shows the order of accuracy plot for the axial velocity along the duct. As expected, variable order values are shown in the entrance region of the duct. A much finer mesh is required near the singularities to capture the gradients in this region. In the fully developed region, the order values are closer to 2.0. A second order scheme should capture a parabolic velocity profile exactly. The calculated error between the Fuego fine mesh and the Richardson extrapolated solution is shown in Figure 20.7-3. Errors on the order of 1.0e-4 occur in the fully developed region while higher values occur near the inlet corners of the duct. Negative error values also occur in the entrance region of the duct and the dividing line where the error values are zero, Richardson extrapolation method will fail (see Figure 20.7-2). In addition to the local order value at discrete nodes, it is important to look at the order value based on integral variables. In Figure 20.7-4, the axial velocity  $L_1$ ,  $L_2$ ,  $L_{\infty}$  norms output from VIVID are shown as a function of grid cells in the  $x$ -direction. The slope of the  $L_1$  norm appears to be approaching second order accuracy. It is difficult to attain a value of 2 due to the lower order region near the inlet. Further grid refinement is required to approach second order behavior over the entire domain.

Figure 20.7-5, shows the order of accuracy plot for the pressure along the duct. Second order accuracy values appear over most of the duct, except near the inlet where the order values drop to one. The calculate error between the Fuego fine mesh solution and the Richardson extrapolated solution is shown in Figure 20.7-6. Again, the errors are on the order of 1.0e-4 beyond the entrance region. In Figure 20.7-7, the pressure  $L_1$ ,  $L_2$ ,  $L_{\infty}$  norms are shown as a function of grid cells in the  $x$ -direction. The slope of the norm curves suggest that the solution is converging a first order rate. The global order value is largely influenced by the low order values near the inlet of the duct. Finally, the change in slope of the norm curves suggest that the coarse mesh solution is not in the asymptotic region of convergence. Finer meshes are required to accurately capture the developing flow region in the duct.



**Figure 20.7-1.. Axial Velocity Contour Plot of Fine Mesh Solution**



**Figure 20.7-2.. Order Plot of Axial Velocity**

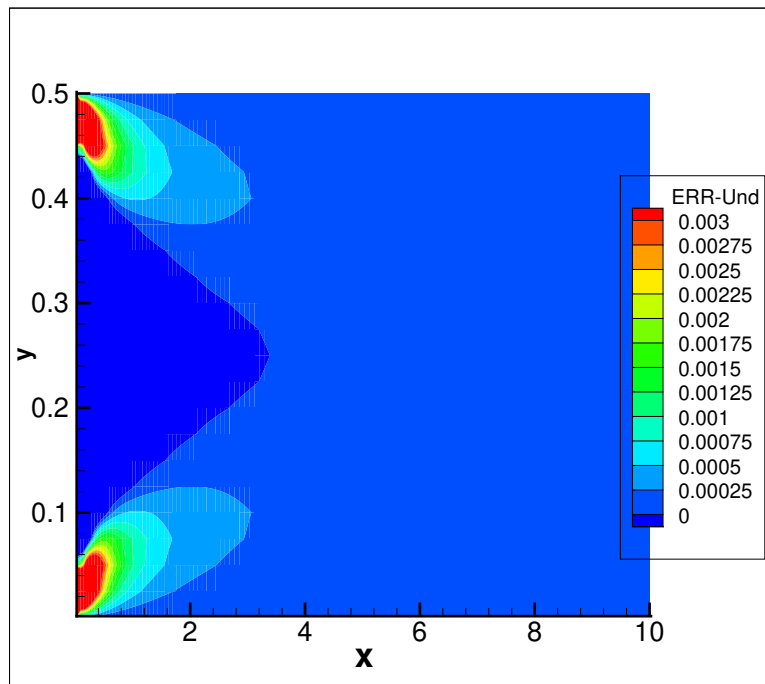


**Figure 20.7-3.. Error Plot of Axial Velocity (Fine Mesh Solution)**

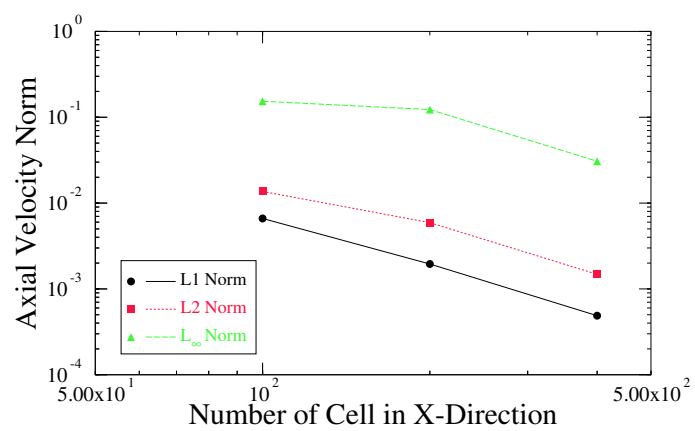


**Figure 20.7-4.. Axial Velocity Norms for Coarse, Medium, and Fine Mesh Solutions**

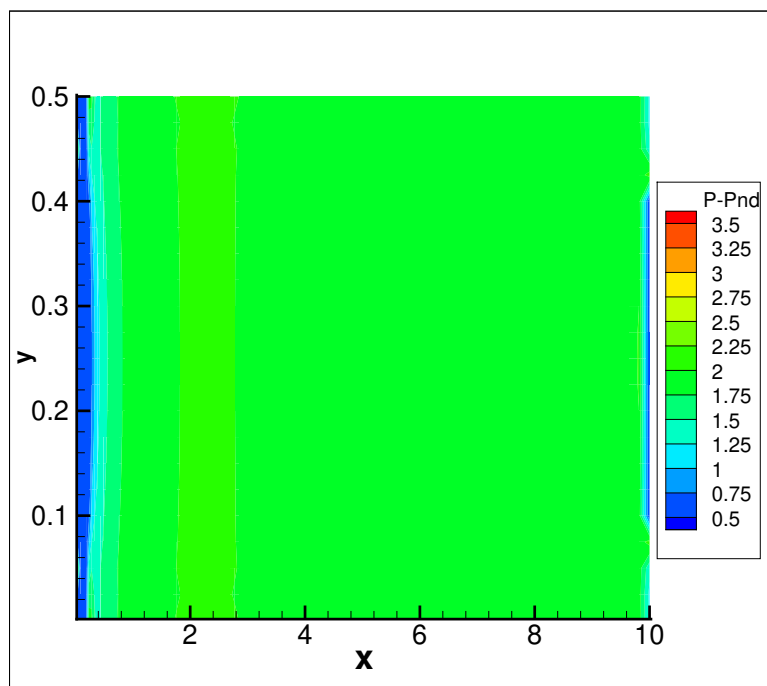


**Figure 20.7-5.. Order Plot of Pressure**

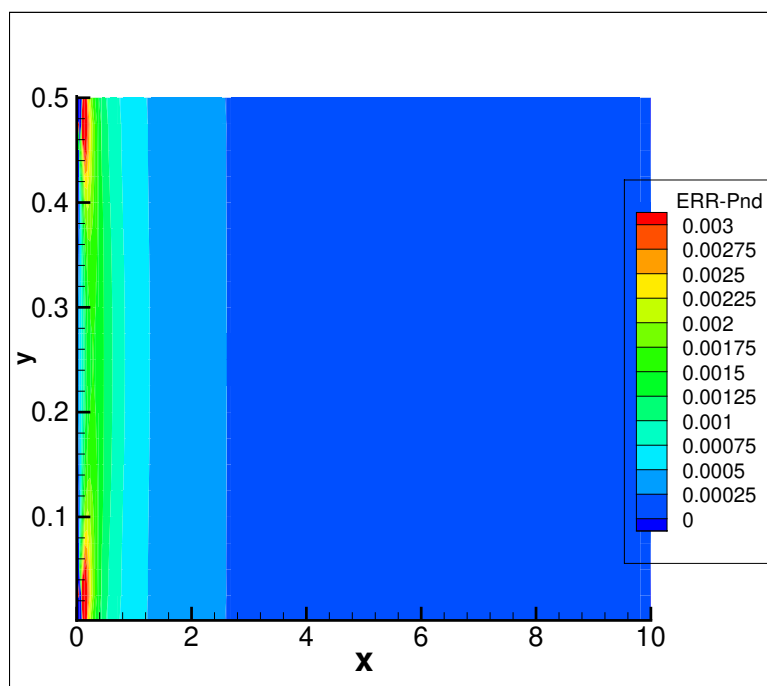


**Figure 20.7-6.. Error Plot of Pressure (Fine Mesh Solution)**

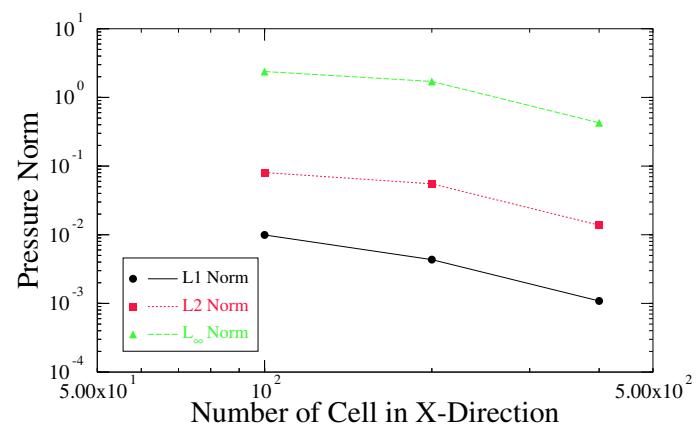


**Figure 20.7-7.. Pressure Norms for Coarse, Medium, and Fine Mesh Solutions**

This page intentionally left blank.

# 21. LAMINAR JET

<b>Dimension:</b>	3D (quasi 2D)
<b>Transient/Steady:</b>	steady
<b>Laminar/Turbulent:</b>	laminar
<b>Isothermal/Thermal:</b>	isothermal
<b>Temperature/Enthalpy:</b>	n/a
<b>Uniform/Nonuniform:</b>	uniform mixture
<b>Combustion:</b>	no
<b>Soot:</b>	no
<b>Coupled Mechanics:</b>	no
<b>Regression Test:</b>	fuego/laminar_jetA_40 fuego/laminar_jetB_40 fuego/laminar_jetC_40 fuego/laminar_jetD_40

The laminar jet issuing from a line source has a boundary layer solution. The boundary layer solution tests the implementation of the pressure-specified open boundary condition. The Reynolds number is 40 and the jet half-width at the inflow is 5. The Reynolds number is selected such that the jet width is within the computational domain at the outflow boundary.

## 21.1. ANALYTIC OR BENCHMARK SOLUTION

The boundary layer solution for a laminar jet issuing from a line source is given by Schlichting [27]. The streamwise (axial) direction is  $x$ , and the lateral direction is  $y$ . The axial velocity is  $u$  and the transverse velocity is  $v$ . The pressure is uniform. Infinitely far away in the lateral direction, the axial velocity is zero. The total specific momentum,  $K$ , is independent of streamwise position,

$$K = \int_{-\infty}^{\infty} u^2 dy. \quad (21.1)$$

The boundary layer solution is derived from a stream function

$$\psi = \sqrt{\nu} x^{1/3} f(\eta), \quad (21.2)$$

$$\eta = \frac{1}{3} \frac{1}{\sqrt{\nu}} \frac{y}{x^{2/3}}, \quad (21.3)$$

$$\alpha = \left( \frac{9}{16} \frac{K}{\sqrt{\nu}} \right)^{1/3}, \quad (21.4)$$

$$u = \frac{1}{3} x^{-1/3} f'(\eta), \quad (21.5)$$

$$v = -\frac{1}{3} \sqrt{\nu} x^{-2/3} (f(\eta) - 2\eta f'(\eta)). \quad (21.6)$$

The boundary layer equations satisfy the following ordinary differential equation

$$f''' + f f'' + f'^2 = 0, \quad (21.7)$$

$$f(0) = 0,$$

$$f''(0) = 0,$$

$$f'(\infty) = 0,$$

$$f(\eta) = 2\alpha \tanh(\alpha\eta), \quad (21.8)$$

$$f'(\eta) = 2\alpha^2 \operatorname{sech}^2(\alpha\eta). \quad (21.9)$$

The integrated Reynolds number is a function of axial position,

$$\operatorname{Re} = \frac{1}{\nu} \int_{-\infty}^{\infty} u dy = \left( 36 \frac{Kx}{\nu^2} \right)^{1/3}. \quad (21.10)$$

In order to establish a finite length scale for the boundary layer solution, define the jet half-width,  $h$ , to be the location at which the axial velocity has fallen to some fraction,  $\epsilon$ , of the velocity at the centerline (White [28], page 292),

$$\epsilon = \frac{u(\alpha\eta_h)}{u(0)} = \operatorname{sech}^2(\alpha\eta_h). \quad (21.11)$$

Define the a virtual origin such that at the inflow to the domain, the half-width is  $h$  and the inflow face is a distance  $x_o$  from the line source,

$$\begin{aligned} E &= \cosh^{-1} \left( \frac{1}{\sqrt{\epsilon}} \right) = \alpha\eta_h, \\ &= \frac{\alpha}{3} \frac{1}{\sqrt{\nu}} h x_o^{-2/3}, \end{aligned} \quad (21.12)$$

where the parameters are all defined at the inflow plane,  $x_o$ . The virtual origin is defined by the Reynolds number, the jet half-width, and the jet width parameter at the inflow plane. All other

parameters are derived from the inflow parameters,

$$\text{Re} = 12 \frac{x_o}{h} E, \quad (21.13)$$

$$\alpha = \frac{\sqrt{\nu}}{4} \text{Re} x_o^{-1/3}, \quad (21.14)$$

$$K = \frac{\nu^2}{36} \text{Re}^3 x_o^{-1}. \quad (21.15)$$

## 21.2. MESH DEFINITION

There are four three-dimensional meshes with uniform, hexahedral elements. There is only one element in the z-direction since the z-planes act as symmetry planes to achieve two-dimensionality. The x and y-dimensions are the same in each mesh, 20 units by 20 units. The z-depth is 0.25 units. (Note that the coordinate system for the mesh is different from the derivation of the boundary layer solution.) Mesh A is  $20 \times 20 \times 1$  elements, mesh B is  $40 \times 40 \times 1$  elements, mesh C is  $80 \times 80 \times 1$  elements, and mesh D is  $160 \times 160 \times 1$  elements. The x and y-planes of the mesh each have a side-set defined for a total of four. The element faces of the two z-planes make up the fifth side-set.

## 21.3. MATERIAL SPECIFICATIONS

The material properties are constant and the units are unimportant as long as they are consistent. The density is 1.0 and the viscosity is 1.0. The inflow plane Reynolds number is 40.

## 21.4. INITIAL CONDITIONS

The velocities are initialized to the inflow profiles. The inflow profiles are specified as a function of the lateral coordinate. The inflow functions are applied at every node. The pressure is zero.

## 21.5. BOUNDARY CONDITIONS

The boundary conditions are applied over five side-sets. Note that the coordinate system for the mesh is different from the derivation of the boundary layer solution. In the mesh, the axial direction is along the y-axis and the lateral is along the x-axis. The bottom plane at  $y=0$  is the inflow boundary. The analytic velocities are enforced at the nodes of the inflow side-set using Dirichlet conditions. The  $x=0$  plane is a symmetry plane since the solution is symmetric about the vertical centerline. The  $x=x_{\text{max}}$  plane is the entrainment plane. The pressure is specified as zero and the flow is required to enter the domain normal to the boundary. There is no shear velocity specified since the vertical velocity is negligible that far from the plume. The  $y=y_{\text{max}}$  plane is the outflow plane. It is applied in the same manner as the entrainment

plane. The  $z=0$  and  $z=z_{\max}$  planes make up the fifth side-set. These boundary conditions are applied as symmetry planes to make the flow quasi-two-dimensional.

## 21.6. SOLUTION PROCEDURE

The equations are time-marched to steady state with an adaptive time step. The time steps adapt to a fixed maximum CFL number of 5.0. The projection method is the “stabilized method” with no under-relaxation.

The linearized continuity equation is solved with the stabilized biconjugate gradient method with two steps of symmetric Gauss-Seidel preconditioning. The linear residuals are reduced by eight orders of magnitude at each solve. The linearized momentum equations are solved with the GMRES method with three steps of Jacobi preconditioning. The GMRES method is restarted after 50 iterations. The linear residuals are reduced five orders of magnitude at each solve. Dirichlet boundary conditions are enforced exactly.

The viscous stress terms terms are turned off at the outflow boundary ( $y_{\max}$ ) using the command “OMIT DIFFUSION TERMS”. This model was used in the laminar buoyant plume problem (see Chapter 3) in order to get a converged solution. The solution to the laminar jet will converge with the viscous stress terms on, but it takes longer than without. The inflow boundary condition applies the specified values as fluxes to a momentum balance rather than Dirichlet conditions. It was found that this approach gave better results for the entrainment values.

The results are generated using the development version Fuego-0.8.0, built on December 2, 2002.

## 21.7. VERIFICATION EXPERIMENTS

The laminar jet problem was run with a  $\text{half-width}=5$ , and  $\text{Re}=40$ . This corresponds to  $K=319.3$ ,  $E=2.993$ , and  $x_o = 5.568$ . Recall that  $\rho = \mu = 1$ .

It is difficult to match the lateral entrainment velocity, similar to the laminar buoyant plume test (see Chapter 3). The lateral entrainment velocity is sensitive to the outflow boundary conditions and the inflow boundary conditions. Several combinations of boundary conditions were explored and the entrainment velocity is plotted at two different axial stations in Figure 21.7-1. The plot contains comparisons between the analytic solution, flux inflow boundary conditions, fixed inflow boundary conditions, fixed inflow boundary conditions with no diffusion terms at the outflow, and flux inflow boundary conditions with no diffusion terms at the outflow. When the diffusion terms are turned off at the outflow boundary, the nodal velocities at the outflow plane are rotated outwards by about 30°.

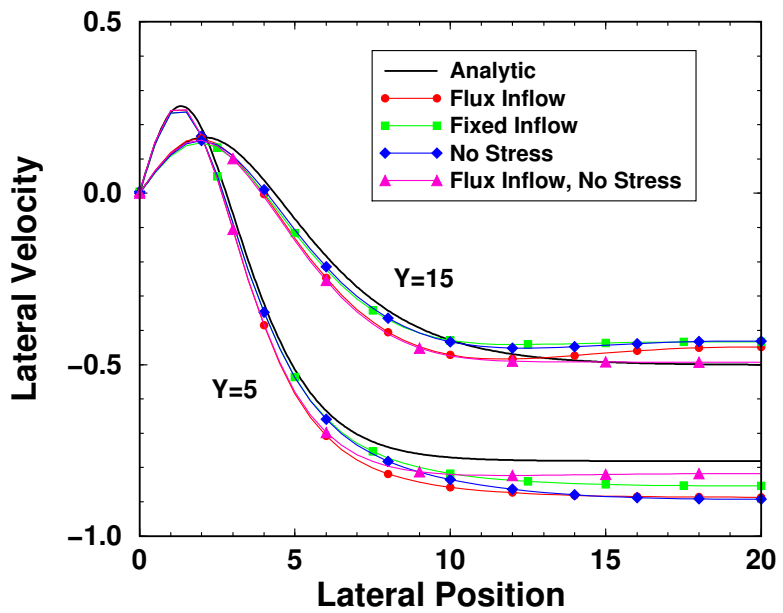


**Figure 21.7-1.. Lateral velocity profiles at axial stations 5 and 15 (relative to the inflow plane) for various boundary condition combinations.**

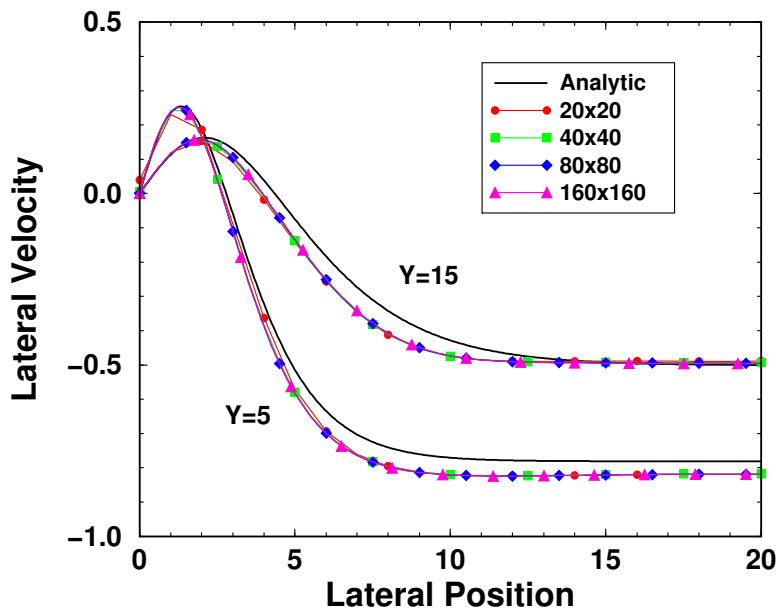


**Figure 21.7-2.. Lateral velocity profiles at axial stations 5 and 15 (relative to the inflow plane). Flux inflow and no viscous stress outflow conditions.**

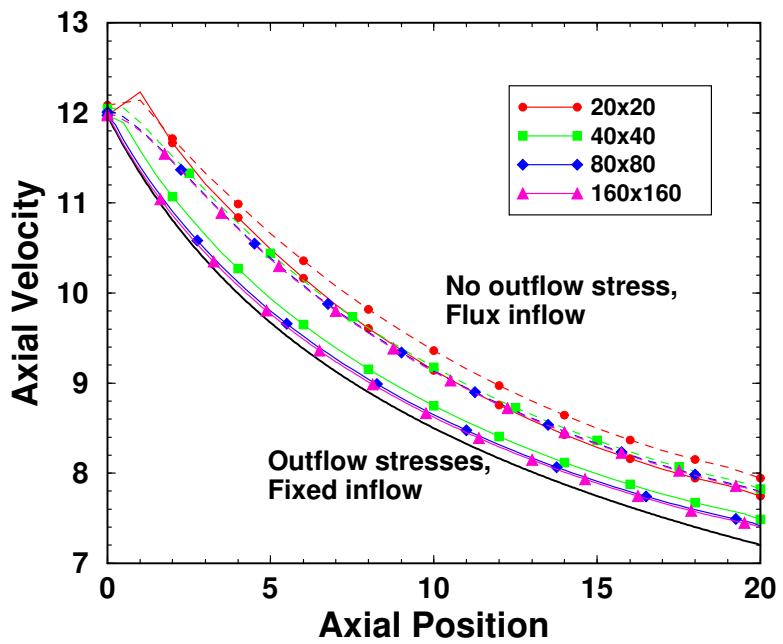


Figure 21.7-3.. Centerline axial velocity. Flux inflow and no viscous stress outflow conditions.

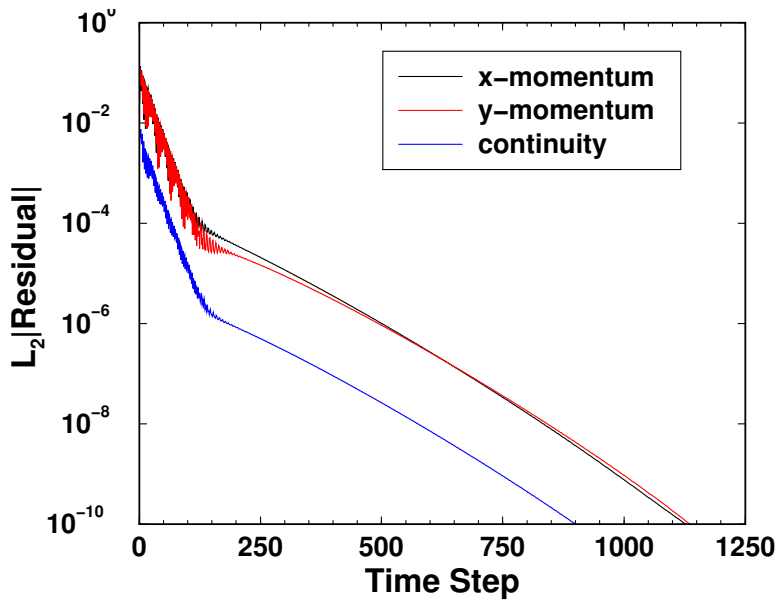


Figure 21.7-4.. Convergence history on the 40x40 mesh. Flux inflow and no viscous stress outflow conditions.

# 22. LID-DRIVEN CAVITY

<b>Dimension:</b>	3D
<b>Transient/Steady:</b>	steady
<b>Laminar/Turbulent:</b>	laminar
<b>Isothermal/Thermal:</b>	isothermal
<b>Temperature/Enthalpy:</b>	N/A
<b>Uniform/Nonuniform:</b>	uniform
<b>Combustion:</b>	no
<b>Soot:</b>	no
<b>Coupled Mechanics:</b>	no
<b>Regression Test:</b>	fuego/driven_cavity_40_smooth fuego/driven_cavity_80_smooth fuego/driven_cavity_160_smooth fuego/driven_cavity_40_stable fuego/driven_cavity_80_stable fuego/driven_cavity_160_stable fuego/driven_cavity_40_unsmooth fuego/driven_cavity_80_unsmooth fuego/driven_cavity_160_unsmooth

The lid-driven cavity is a popular benchmark solution. We use it here to study the behavior of several projection methods.

## 22.1. ANALYTIC OR BENCHMARK SOLUTION

Solutions by Ghia, Ghia, and Shinn [1]. We examine the  $Re=100$  case with the centerline profiles given in Table 22.1-1.

## 22.2. MESH DEFINITION

The geometry is a unit square cavity in the x- and y-directions. Three meshes are used with a uniform step refinement of two:  $40 \times 40 \times 1$ ,  $80 \times 80 \times 1$ , and  $160 \times 160 \times 1$ . The meshes are uniform in

**Table 22.1-1.. Lid-Driven Cavity: benchmark solution of Ghia and Ghia [1], Re=100.**

X	V	Y	U
0.0000	0.00000	0.0000	0.0
0.0625	0.09233	0.0547	-0.03717
0.0703	0.10091	0.0625	-0.04192
0.0781	0.10890	0.0703	-0.04775
0.0938	0.12317	0.1016	-0.06434
0.1563	0.16077	0.1719	-0.10150
0.2266	0.17507	0.2813	-0.15662
0.2344	0.17527	0.4531	-0.21090
0.5000	0.05454	0.5000	-0.20581
0.8047	-0.24533	0.6172	-0.13641
0.8594	-0.22445	0.7344	0.00332
0.9063	-0.16914	0.8516	0.23151
0.9453	-0.10313	0.9531	0.68717
0.9531	-0.08864	0.9609	0.73722
0.9609	-0.07391	0.9688	0.78871
0.9688	-0.05906	0.9766	0.84123
1.0000	0.00000	1.0000	1.00000

spacing. The one-element depth is in the z-direction. The z-spacing is equivalent to the xy-spacing in each mesh. The meshes consist of 3D hexahedral elements.

## 22.3. MATERIAL SPECIFICATIONS

Constant properties are used. The density is 1.0 and the viscosity is 0.01. The resulting Reynolds number for the cavity is 100.

## 22.4. INITIAL CONDITIONS

The flow is initialized to zero velocity and zero pressure.

## 22.5. BOUNDARY CONDITIONS

The z-min and z-max planes are treated as slip-planes using a symmetry plane boundary condition. The four remaining surfaces of the cavity are treated as no-slip walls. The velocity is specified to be 1.0 in the x-direction at the y-max surface.

## 22.6. SOLUTION PROCEDURE

The linear system for the pressure equation is singular. We solve it using the conjugate gradient iterative solver with an domain decomposition variation of the incomplete Cholesky preconditioner. To avoid linear solver problems with the singular system, we randomize the initial guess. The stopping tolerance is 1.oe-8 with Ro scaling.

The momentum equations are solved with GMRES using two steps of Jacobi preconditioning. The stopping tolerance is 1.oe-6 with Ro scaling. The Dirichlet boundary conditions for velocity are enforce exactly.

The initial time step is 0.01 and the solver adapts the time step to have a constant maximum nodal CFL number. Three projection algorithms are used. The smoothed pressure algorithm is run with time step scaling and a CFL=5.0. The unsmoothed pressure algorithm is run with time step scaling and a CFL=1.0. The stabilized algorithm is run with a CFL=1.0.

## 22.7. VERIFICATION EXPERIMENTS

...using VIVID-5.0 to extract the errors based on Richardson extrapolation, see Tables 22.7-1 and 22.7-2. These cases use the smoothed-pressure projection method with time-step scaling. The CFL number is held constant as the mesh is refined.

**Table 22.7-1.. Lid-Driven Cavity: Error Norms for X-Velocity, estimated order of accuracy is 1.5. Smoothed projection method with time-step scaling.**

	$L_1$	$L_2$	$L_\infty$
40x40x1	1.42409E-03	5.91235E-03	1.44453E-01
80x80x1	4.47619E-04	2.43744E-03	5.00603E-02
160x160x1	1.11905E-04	6.09360E-04	1.25151E-02

**Table 22.7-2.. Lid-Driven Cavity: Error Norms for Y-Velocity, estimated order of accuracy is 1.9. Smoothed projection method with time-step scaling.**

	$L_1$	$L_2$	$L_\infty$
40x40x1	1.33147E-03	5.29513E-03	-8.05509E-02
80x80x1	3.55459E-04	2.16876E-03	-5.26845E-02
160x160x1	8.88648E-05	5.42189E-04	-1.31711E-02

Test 2: The pressure smoothing affects the steady-state convergence rate of the equations. The smoothed and unsmoothed projection algorithms were both run with characteristic scaling, so under-relaxation was used to stabilize them. The resulting convergence history for the three methods is

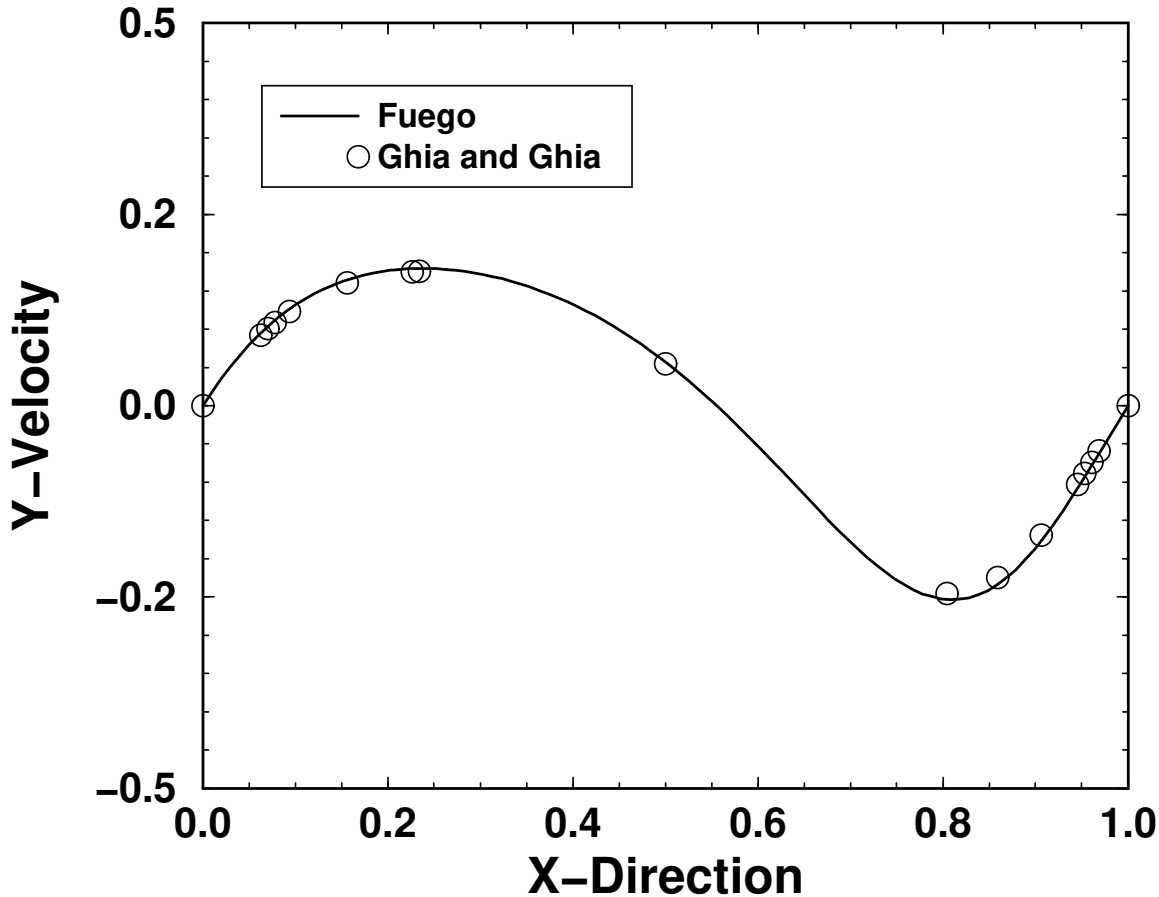


**Figure 22.7-1.. Comparison of computed x-velocity with benchmark solution along the vertical centerline,  $Re=100$ . The projection method is smoothed with time-step scaling.**

shown in Fig. 22.7-3. The velocity solutions for the smoothed, unsmoothed, and stabilized schemes are all the same at steady-state. The pressure fields are the same within a constant value.

The convergence rate of the smoothed and unsmoothed schemes is the same for the first 500 time steps, but then the momentum equations with the unsmoothed projection scheme stop converging.

The stabilized scheme out-performs the smoothed and unsmoothed schemes with characteristic scaling. Oscillations in the x-momentum residual are noted for the first 100 time steps. If we allow a solution that is dependent on the time step, then the smoothed method with time-step scaling gives the best convergence performance, shown in Fig. 22.7-4.

The convergence rate for the unsmoothed scheme is poor relative to the other schemes. The pressure field also shows oscillations. The oscillations are damped for larger scaling factors (or larger CFL numbers for time step scaling) as shown in Fig. 22.7-5, but the convergence rate is best for the smaller time steps as shown in Fig. 22.7-6.

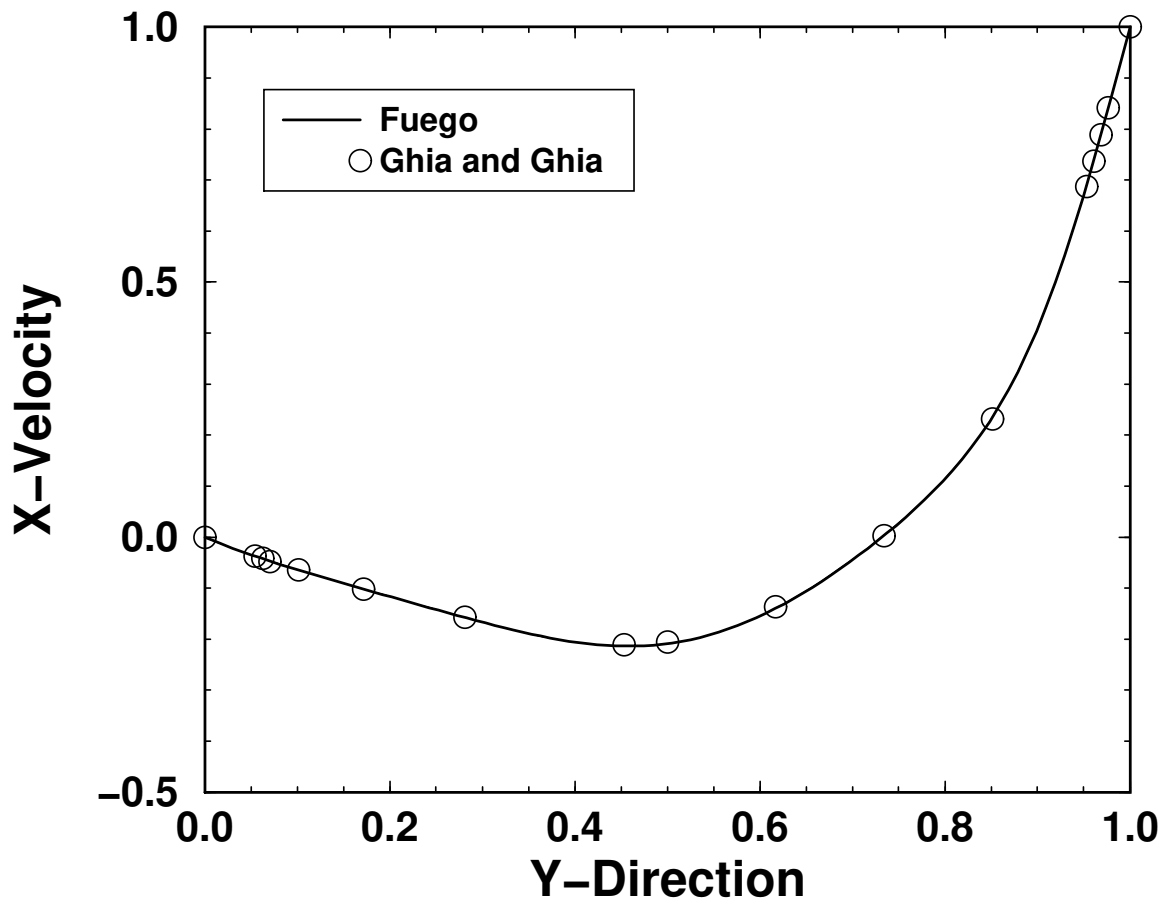
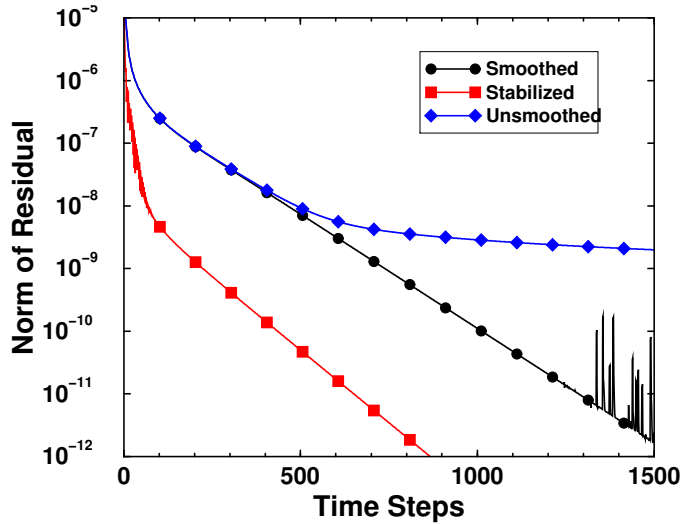
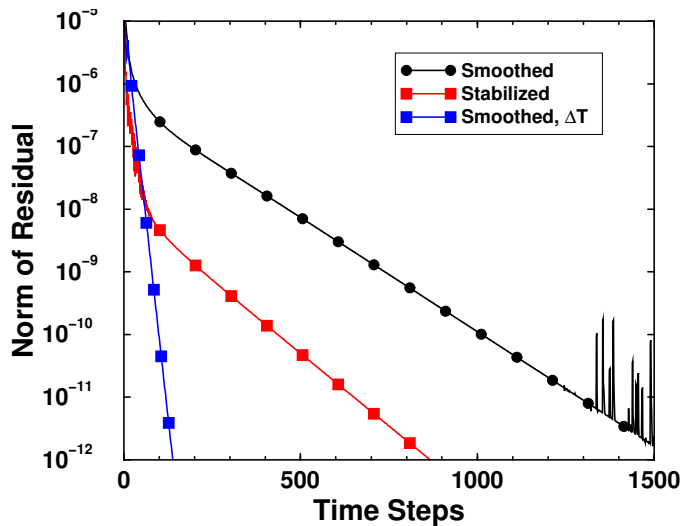


Figure 22.7-2.. Comparison of computed y-velocity with benchmark solution along the horizontal centerline,  $Re=100$ . The projection method is smoothed with time-step scaling.



**Figure 22.7-3..** Convergence history for the driven-cavity problem.  $L_2$  norm of the nonlinear residual of the x-momentum equation. The smoothed and unsmoothed projection methods use characteristic scaling with implicit momentum relaxation of 0.5 and explicit pressure relaxation of 0.5. All solutions are run at  $CFL=10$  and all solutions are the same at steady-state.



**Figure 22.7-4..** Convergence history for the driven-cavity problem.  $L_2$  norm of the nonlinear residual of the x-momentum equation. The smoothed method with characteristic scaling requires implicit momentum relaxation of 0.5 and explicit pressure relaxation of 0.5. The smoothed method with time step scaling requires no relaxation. All solutions were run at  $CFL=10$ .

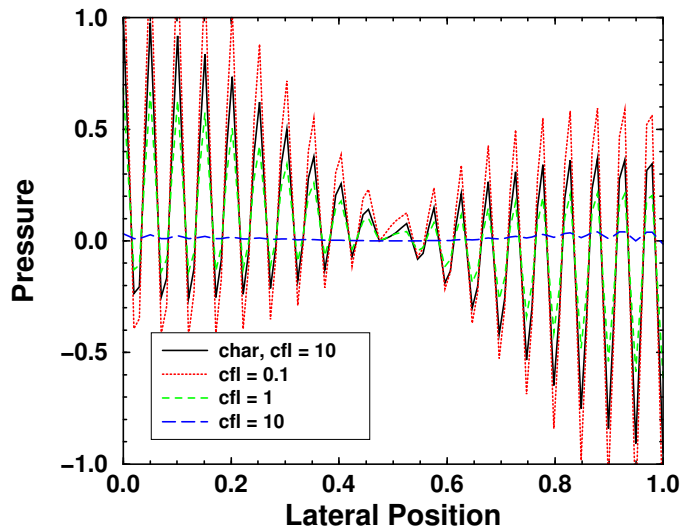


**Figure 22.7-5.. Pressure profile along the horizontal mid-line. Comparison of different scaling coefficients and time steps for the unsmoothed projection method.**

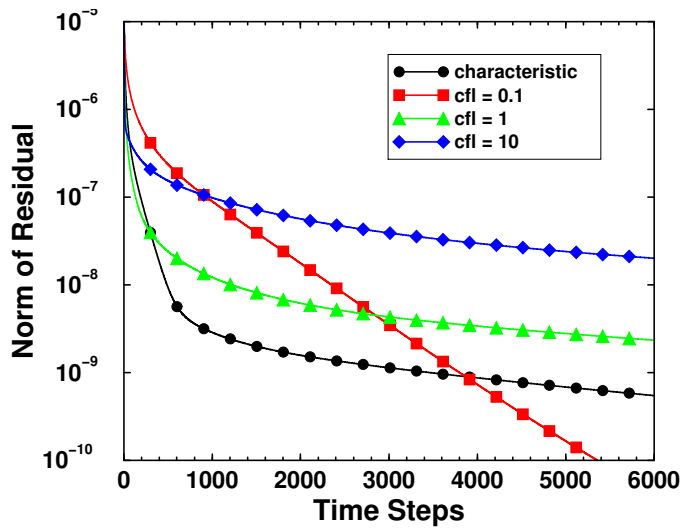


**Figure 22.7-6.. Convergence history for the driven-cavity problem.  $L_2$  norm of the nonlinear residual of the x-momentum equation. The unsmoothed method with characteristic scaling requires implicit momentum relaxation of 0.5 and explicit pressure relaxation of 0.5. The unsmoothed method with time step scaling requires no relaxation.**

This page intentionally left blank.

# 23. TURBULENT HELIUM PLUME

<b>Dimension:</b>	3D
<b>Transient/Steady:</b>	transient
<b>Laminar/Turbulent:</b>	turbulent
<b>Isothermal/Thermal:</b>	isothermal
<b>Temperature/Enthalpy:</b>	n/a
<b>Uniform/Nonuniform:</b>	nonuniform
<b>Combustion:</b>	no
<b>Soot:</b>	no
<b>Coupled Mechanics:</b>	no
<b>Regression Test:</b>	fuego/im_he_13K

## 23.1. MATERIAL SPECIFICATIONS

## 23.2. INITIAL CONDITIONS

## 23.3. BOUNDARY CONDITIONS

## 23.4. ANALYTIC OR BENCHMARK SOLUTION

## 23.5. MESH DEFINITION

## 23.6. SOLUTION PROCEDURE

## 23.7. VERIFICATION EXPERIMENTS

This page intentionally left blank.

# 24. LAMINAR SHEDDING FROM A SPHERE

<b>Dimension:</b>	3D
<b>Transient/Steady:</b>	transient
<b>Laminar/Turbulent:</b>	laminar
<b>Isothermal/Thermal:</b>	isothermal
<b>Temperature/Enthalpy:</b>	n/a
<b>Uniform/Nonuniform:</b>	uniform
<b>Combustion:</b>	no
<b>Soot:</b>	no
<b>Coupled Mechanics:</b>	no
<b>Regression Test:</b>	

## 24.1. MATERIAL SPECIFICATIONS

## 24.2. INITIAL CONDITIONS

## 24.3. BOUNDARY CONDITIONS

## 24.4. ANALYTIC OR BENCHMARK SOLUTION

The physics of flow over spherical droplets is described in Clift, Grace, and Weber [29] and Batchelor [30]. The flow over a spherical particle takes on various behaviors in different Reynolds number regimes. The Stokes flow regime occurs for  $Re < 1$  and flow looks symmetric about the particle. The flow remains unseparated for  $1 < Re < 20$ . The onset of separation occurs around a Reynolds number of 20, with a steady wake region for  $20 < Re < 130$ . The ratio of the length of the separation bubble to the sphere diameter in the steady region is correlated by

$$L_w/d = 0.565 \ln Re - 1.693. \quad (24.1)$$

The separation angle, measured from the aft stagnation point, is

$$\theta_s = 180 - 42.5 [\ln (Re/20)]^{0.483}, \quad (20 < Re < 400) \quad (24.2)$$

The separation point moves forward with increasing Reynolds number, up to the transition Reynolds number of  $2 \times 10^5$ , with the correlation for separation angle

$$\theta_s = 78 + 275Re^{-0.37}, \quad (400 < Re < 3 \times 10^5) \quad (24.3)$$

A correlations for the drag coefficient from Langmuir and Blodgett,

$$C_D = \frac{24}{Re} (1.0 + 0.197Re^{0.63} + 2.6 \times 10^{-4}Re^{1.38}) \quad (24.4)$$

$1 < Re < 100,$

with an error range on drag coefficient ranging from +6% to +1%. A correlation for the drag coefficient from Clift and Gauvin,

$$C_D = \frac{24}{Re} (1.0 + 0.15Re^{0.688}) + 0.42 / (1.0 + 4.25 \times 10^4 Re^{-1.16}) \quad (24.5)$$

$Re < 3 \times 10^5,$

with an error range on drag coefficient ranging from +6% to -4%. A correlation for the drag coefficient from Clift, Grace, and Weber,

$$C_D = \frac{24}{Re} \left[ 1 + 0.1315Re^{(0.82 - 0.05 \log_{10} Re)} \right], \quad 0.01 < Re < 20 \quad (24.6)$$

$$C_D = \frac{24}{Re} \left[ 1 + 0.1935Re^{0.6305} \right], \quad 20 < Re < 260 \quad (24.7)$$

$$\log_{10} C_D = 1.6435 - 1.1242 \log_{10} Re + 0.1558 (\log_{10} Re)^2, \quad 260 < Re < 1500 \quad (24.8)$$

The Nusselt number for heat transfer to air, Prandlt number of 0.7, is

$$Nu = 1.0 + 0.667Re^{0.47} \quad (100 < Re < 4000) \quad (24.9)$$

For natural convection over an isothermal sphere, the flow remains laminar for Rayleigh numbers less than XXX. The correlation for the mean Nusselt number is

$$Nu = 2 + \frac{0.589Ra_D^{1/4}}{\left[ 1 + (0.469/Pr)^{9/16} \right]^{4/9}}, \quad (24.10)$$

for  $Pr > 0.5$  and  $Ra_D < 10^{11}$ . The source is Mills [31].

## 24.5. MESH DEFINITION

## 24.6. SOLUTION PROCEDURE

## 24.7. VERIFICATION EXPERIMENTS

# 25. HEAT CONDUCTION MANUFACTURED SOLUTION

<b>Dimension:</b>	3D
<b>Transient/Steady:</b>	steady
<b>Laminar/Turbulent:</b>	n/a
<b>Isothermal/Thermal:</b>	thermal
<b>Temperature/Enthalpy:</b>	N/A
<b>Uniform/Nonuniform:</b>	uniform
<b>Combustion:</b>	no
<b>Soot:</b>	no
<b>Coupled Mechanics:</b>	no
<b>Regression Test:</b>	none

Manufactured solutions are derived to test the steady and transient heat conduction mechanics.

The steady manufactured solution is run on orthogonal and non-orthogonal (t-hex) meshes.

This series of tests is run with fuego-2.1Development

## 25.1. ANALYTIC OR BENCHMARK SOLUTION

Steady Manufactured Solution:

$$T(x, y, z) = \cos(a\kappa x) \sin(b\kappa y) \sin(c\kappa z) \quad (25.1)$$

where  $a = 3$ ,  $b = c = 2$ ; and  $\kappa = \pi$ .

The steady manufactured source terms, that are to be applied to the element assembled temperature transport equation is

$$S_{mms}(x, y, z) = ((a\kappa)^2 + (b\kappa)^2 + (c\kappa)^2) (\cos(a\kappa x) \sin(b\kappa y) \sin(c\kappa z)) \quad (25.2)$$

Problem 2:

$$T(x, y, z, t) = \sin(\omega t) \cos(a\kappa x) \sin(b\kappa y) \sin(c\kappa z) \quad (25.3)$$

where  $\omega = 2\pi$ .

The problems are defined for the cubic domain:  $0.0 \leq y, z \leq 1.0$  and  $-0.5 \leq x \leq 0.5$ .

## 25.2. MESH DEFINITION

The meshes consist of 3D hexahedral elements. One set of meshes represent an orthogonal hex mesh, with equal spacing, while the other represents a tetrahedral mesh that was “t-hexed”.

The total number of nodes for the set of orthogonal meshes are: 1,331, 9,261, 68,921, 531,441 while for the thex mesh: 17,349, 126,173, and 974,217. In each case the base mesh was used as an input for subsequent uniform mesh refinements.

## 25.3. MATERIAL SPECIFICATIONS

Constant properties.

Test 1:  $\rho = 1$ , and  $k = 1$ .

Test 2:  $\rho = 1$ , and  $k = 1$ .

## 25.4. INITIAL CONDITIONS

The manufactured solution is applied as the initial condition.

## 25.5. BOUNDARY CONDITIONS

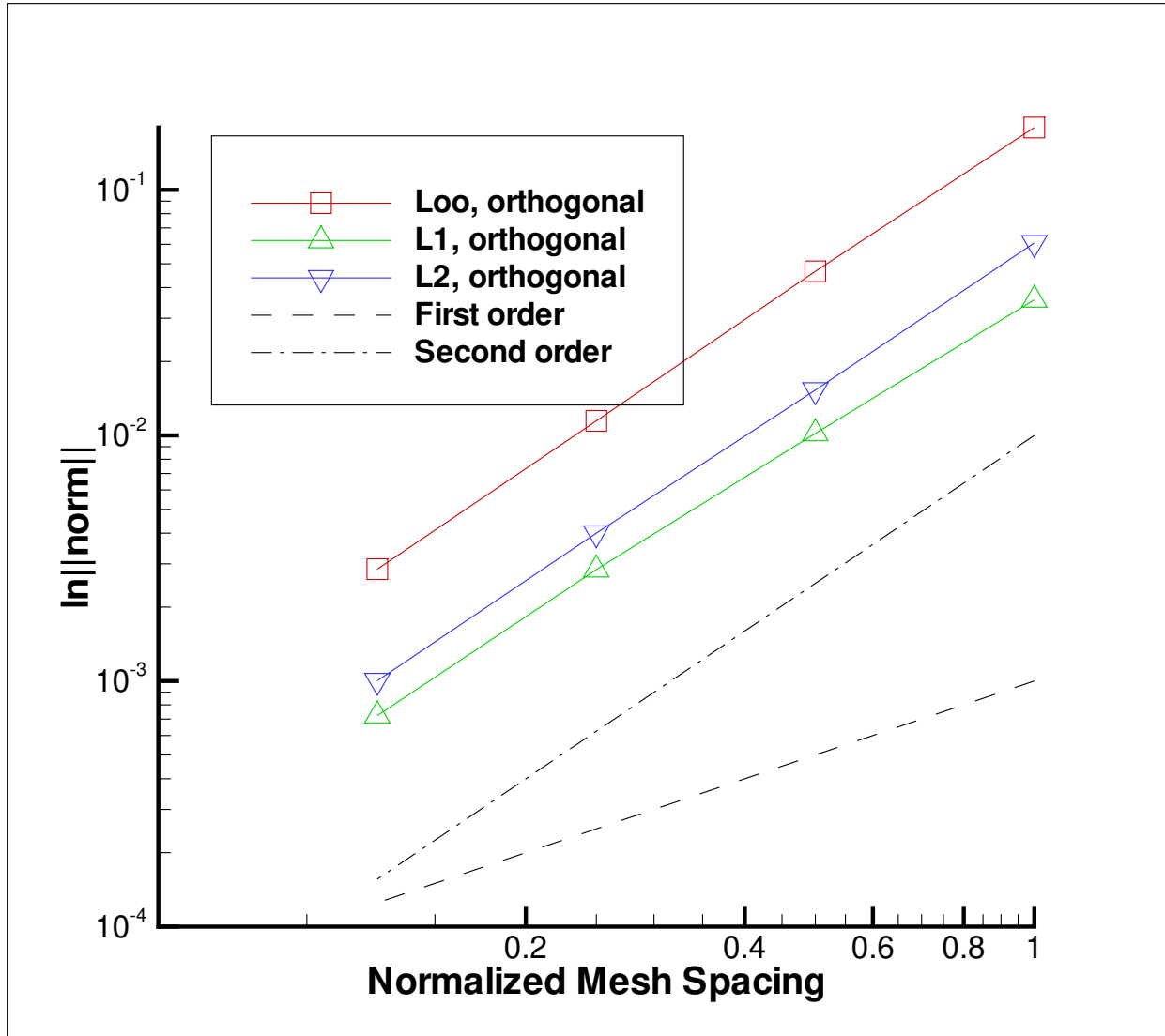
The domain is fully enclosed by walls. The temperatures are fixed to the manufactured solution, in this case zero.

## 25.6. SOLUTION PROCEDURE

A fixed time step of unity is used. All nonlinear residuals are converged to a tolerance of  $10^{-16}$ . Serial and parallel runs were made.

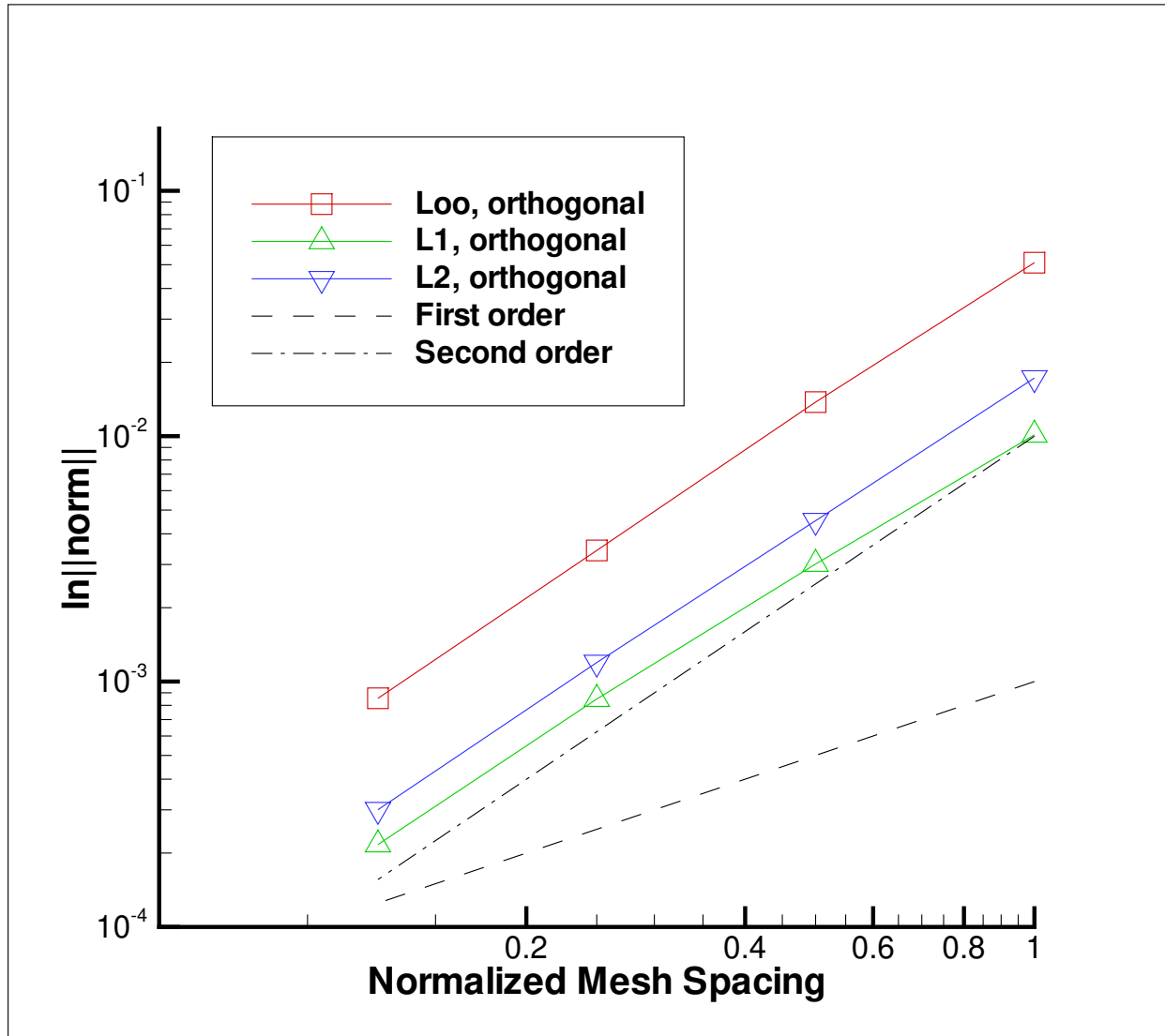
## 25.7. VERIFICATION EXPERIMENTS

Figure 25.7-1 shows the order of accuracy plot for the refinement case using an orthogonal mesh with the full control volume finite element diffusion stencil while Figure 25.7-2 are the results for the orthogonal mesh using the reduced stencil.



**Figure 25.7-1.. Plot of error vs normalized mesh spacing to demonstrate convergence of the SIERRA/Fuego method of outlined manufactured solution; results shown for the orthogonal study with full CVFEM diffusion operator.**

Figure 25.7-3 shows the order of accuracy plot for the refinement case using the non orthogonal thex mesh with the full control volume finite element diffusion stencil. Figure 25.7-4 is also an order of accuracy plot for the thex mesh, however, this time the reduced diffusion operator is used. Results indicate that the formal order of accuracy is first order.



**Figure 25.7-2..** Plot of error vs normalized mesh spacing to demonstrate convergence of the SIERRA/Fuego method of outlined manufactured solution; results shown for the orthogonal study with reduced diffusion operator.

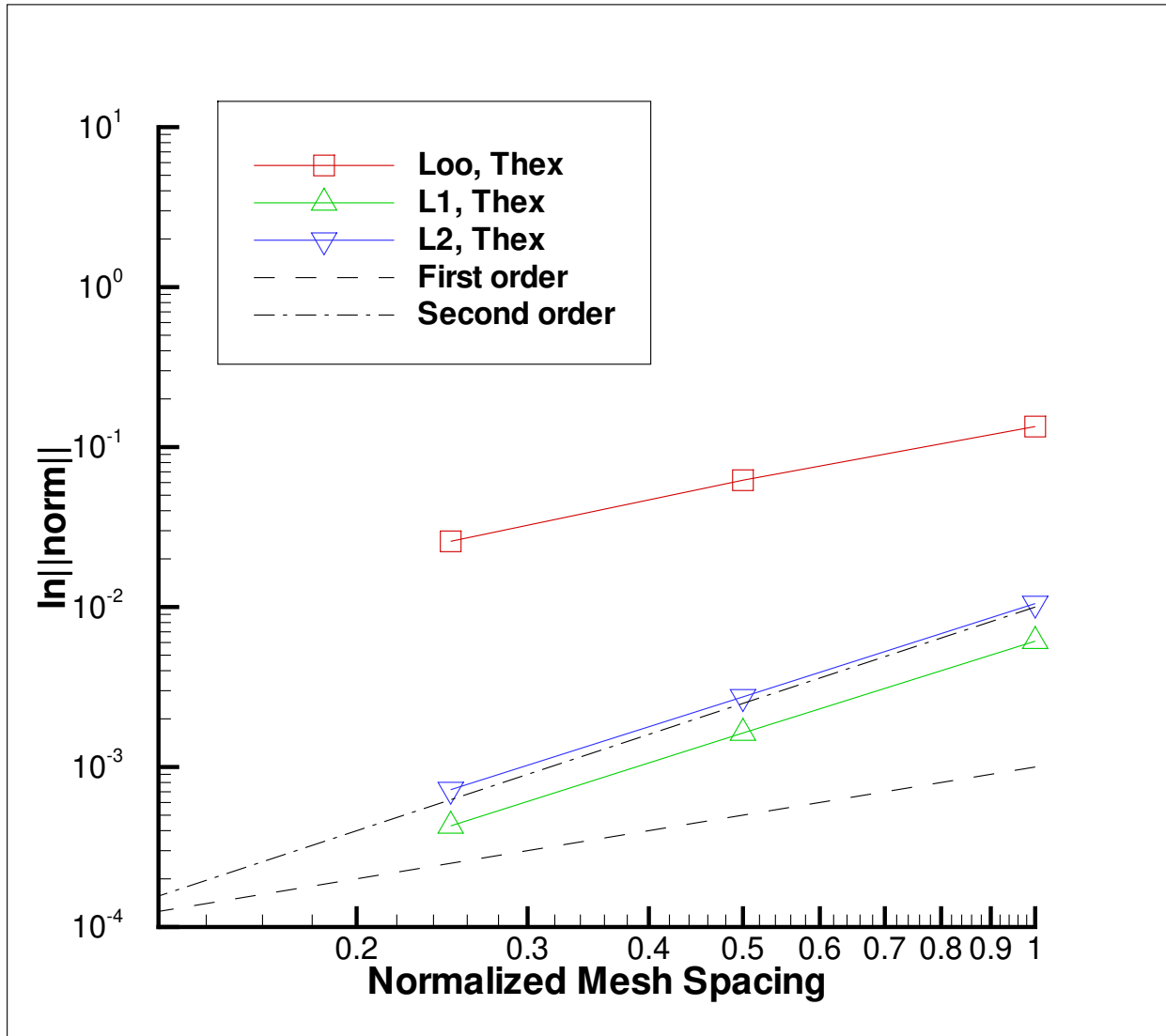


**Figure 25.7-3..** Plot of error vs normalized mesh spacing to demonstrate convergence of the SIERRA/Fuego method of outlined manufactured solution; results shown for the non orthogonal thex study with full CVFEM diffusion operator.

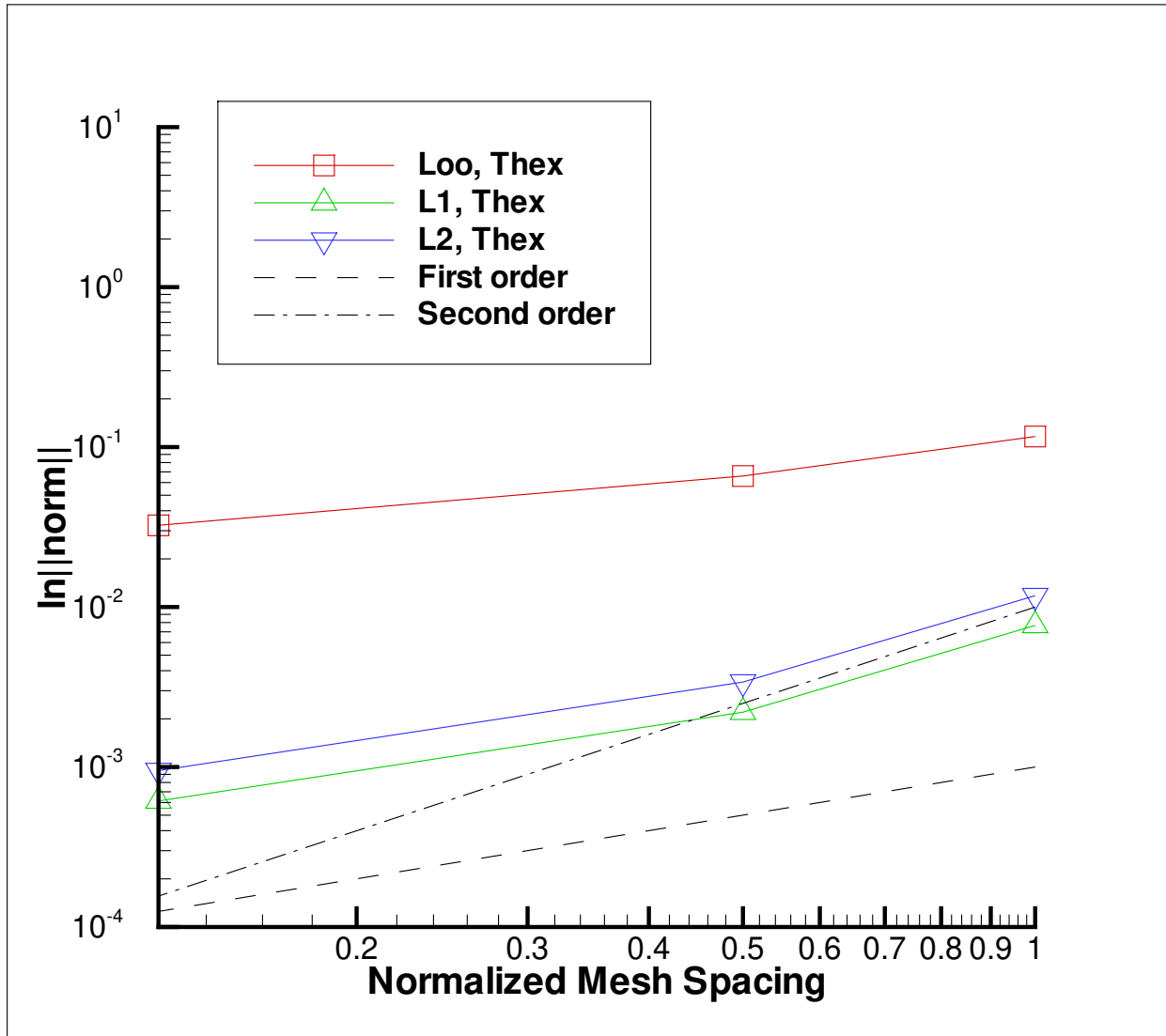


**Figure 25.7-4..** Plot of error vs normalized mesh spacing to demonstrate convergence of the SIERRA/Fuego method of outlined manufactured solution; results shown for the non orthogonal thex study with reduced CVFEM diffusion operator.

# 26. BUOYANT, VARIABLE DENSITY MANUFACTURED SOLUTION

<b>Dimension:</b>	3D
<b>Transient/Steady:</b>	steady
<b>Laminar/Turbulent:</b>	laminar
<b>Isothermal/Thermal:</b>	thermal
<b>Temperature/Enthalpy:</b>	enthalpy
<b>Uniform/Nonuniform:</b>	nonuniform
<b>Combustion:</b>	no
<b>Soot:</b>	no
<b>Coupled Mechanics:</b>	no
<b>Regression Test:</b>	fuego/mms_buoyant_flow

Manufactured solutions are derived to test the variable density momentum, continuity, and enthalpy/mixture fraction equations at steady state, with a differential buoyancy source term. There are two tests for this problem. The first test uses the enthalpy equation and the second uses the mixture fraction equation. The state relationships for each test are

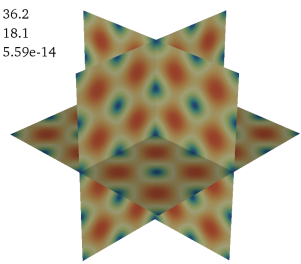
$$\rho_h(T) = \frac{\overline{MWP}_{\text{ref}}}{RT}, \quad T(h) = \frac{h}{c_p} + T_{\text{ref}}, \quad (26.1)$$

$$\rho_Z(Z) = \frac{1}{\frac{1-Z}{\rho_{\text{ref}}} + \frac{Z}{\rho_p}}. \quad (26.2)$$

The errors are computed by comparing the error between the computed solution and the manufactured solution. The errors are computed at nodes.

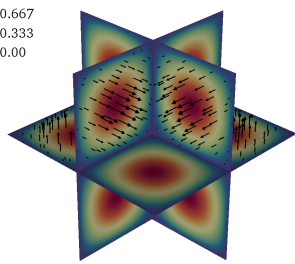
This series of tests is run with `fuego-4.42`.

Pseudocolor  
Var: dpdx\_magnitude  
54.4  
36.2  
18.1  
5.59e-14



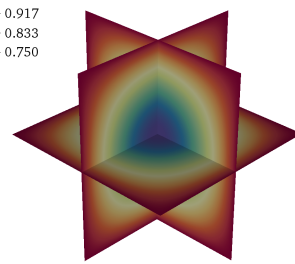
(a)  $|\nabla p|$

Pseudocolor  
Var: velocity\_magnitude  
1.00  
0.667  
0.333  
0.00



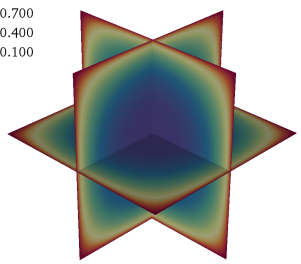
(b)  $|\mathbf{u}|$

Pseudocolor  
Var: density  
1.00  
0.917  
0.833  
0.750



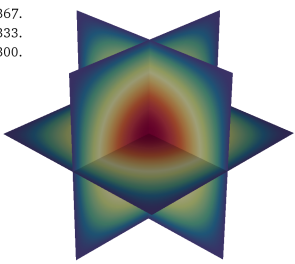
(c)  $\rho_h$

Pseudocolor  
Var: density  
1.00  
0.700  
0.400  
0.100



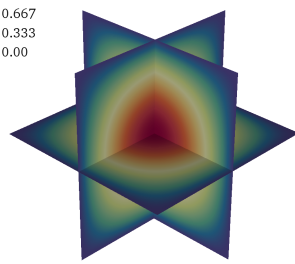
(d)  $\rho_Z$

Pseudocolor  
Var: temperature  
400.  
367.  
333.  
300.



(e)  $T$

Pseudocolor  
Var: mixture\_fraction  
1.00  
0.667  
0.333  
0.00



(f)  $Z$

	$\Delta$	$L^1$	Order	$L^2$	Order	$L^\infty$	Order
<b>u</b>	1	$2.99 \times 10^{-6}$	—	$1.05 \times 10^{-4}$	—	$9.98 \times 10^{-3}$	—
	$\frac{1}{2}$	$6.89 \times 10^{-7}$	2.12	$2.39 \times 10^{-5}$	2.13	$2.30 \times 10^{-3}$	2.11
	$\frac{1}{4}$	$1.66 \times 10^{-7}$	2.05	$5.73 \times 10^{-6}$	2.06	$5.05 \times 10^{-4}$	2.19
	$\frac{1}{8}$	$4.09 \times 10^{-8}$	2.02	$1.40 \times 10^{-6}$	2.03	$1.22 \times 10^{-4}$	2.06
$(\nabla p)_{\text{proj.}}$	1	$1.61 \times 10^{-3}$	—	$9.66 \times 10^{-2}$	—	$1.96 \times 10^{+1}$	—
	$\frac{1}{2}$	$5.24 \times 10^{-4}$	1.62	$4.41 \times 10^{-2}$	1.13	$1.24 \times 10^{+1}$	0.66
	$\frac{1}{4}$	$1.82 \times 10^{-4}$	1.53	$2.14 \times 10^{-2}$	1.04	$8.52 \times 10^{+0}$	0.55
	$\frac{1}{8}$	$6.59 \times 10^{-5}$	1.46	$1.07 \times 10^{-2}$	0.99	$5.88 \times 10^{+0}$	0.53
<b>T</b>	1	$4.38 \times 10^{-5}$	—	$2.03 \times 10^{-3}$	—	$2.36 \times 10^{-1}$	—
	$\frac{1}{2}$	$1.10 \times 10^{-5}$	1.99	$5.11 \times 10^{-4}$	2.13	$6.00 \times 10^{-2}$	1.98
	$\frac{1}{4}$	$2.75 \times 10^{-6}$	2.00	$1.28 \times 10^{-4}$	2.06	$1.51 \times 10^{-2}$	1.99
	$\frac{1}{8}$	$6.89 \times 10^{-7}$	2.00	$3.21 \times 10^{-5}$	2.03	$3.77 \times 10^{-3}$	2.00

**Table 26.1-1.. Error in velocity, projected pressure gradient, and temperature for the  $h$ -based formulation. Uniform mesh.**

	$\Delta$	$L^1$	Order	$L^2$	Order	$L^\infty$	Order
<b>u</b>	1	$2.66 \times 10^{-5}$	—	$1.01 \times 10^{-3}$	—	$1.17 \times 10^{-1}$	—
	$\frac{1}{2}$	$6.71 \times 10^{-6}$	1.99	$2.56 \times 10^{-4}$	1.98	$3.17 \times 10^{-2}$	1.89
	$\frac{1}{4}$	$1.67 \times 10^{-6}$	2.01	$6.35 \times 10^{-5}$	2.01	$7.90 \times 10^{-3}$	2.00
	$\frac{1}{8}$	$4.14 \times 10^{-7}$	2.01	$1.58 \times 10^{-5}$	2.01	$2.01 \times 10^{-3}$	1.97
$(\nabla p)_{\text{proj.}}$	1	$4.47 \times 10^{-3}$	—	$3.20 \times 10^{-1}$	—	$7.95 \times 10^{+1}$	—
	$\frac{1}{2}$	$1.80 \times 10^{-3}$	1.31	$1.93 \times 10^{-1}$	0.72	$6.87 \times 10^{+1}$	0.21
	$\frac{1}{4}$	$7.20 \times 10^{-4}$	1.32	$1.10 \times 10^{-1}$	0.81	$5.34 \times 10^{+1}$	0.36
	$\frac{1}{8}$	$2.87 \times 10^{-4}$	1.33	$6.09 \times 10^{-2}$	0.86	$3.93 \times 10^{+1}$	0.44
<b>Z</b>	1	$1.37 \times 10^{-6}$	—	$6.23 \times 10^{-5}$	—	$7.81 \times 10^{-3}$	—
	$\frac{1}{2}$	$3.61 \times 10^{-7}$	1.92	$1.66 \times 10^{-5}$	1.91	$2.13 \times 10^{-3}$	1.88
	$\frac{1}{4}$	$9.14 \times 10^{-8}$	1.98	$4.20 \times 10^{-6}$	1.98	$5.42 \times 10^{-4}$	1.97
	$\frac{1}{8}$	$2.29 \times 10^{-8}$	2.00	$1.05 \times 10^{-6}$	2.00	$1.35 \times 10^{-4}$	2.00

**Table 26.1-2.. Error in velocity, projected pressure gradient, and temperature for the  $Z$ -based formulation. Uniform mesh.**

	$\Delta$	$L^1$	Order	$L^2$	Order	$L^\infty$	Order
<b>u</b>	1	$6.99 \times 10^{-6}$	—	$2.47 \times 10^{-4}$	—	$2.47 \times 10^{-2}$	—
	$\frac{1}{2}$	$1.39 \times 10^{-6}$	2.33	$4.89 \times 10^{-5}$	2.34	$6.01 \times 10^{-3}$	2.04
	$\frac{1}{4}$	$3.46 \times 10^{-7}$	2.01	$1.25 \times 10^{-5}$	1.97	$2.73 \times 10^{-3}$	1.14
	$\frac{1}{8}$	$9.06 \times 10^{-8}$	1.93	$3.35 \times 10^{-6}$	1.89	$1.27 \times 10^{-3}$	1.10
$(\nabla p)_{\text{proj.}}$	1	$2.67 \times 10^{-3}$	—	$1.22 \times 10^{-1}$	—	$2.33 \times 10^{+1}$	—
	$\frac{1}{2}$	$1.03 \times 10^{-3}$	1.37	$5.33 \times 10^{-2}$	1.19	$1.50 \times 10^{+1}$	0.63
	$\frac{1}{4}$	$6.31 \times 10^{-4}$	0.71	$3.01 \times 10^{-2}$	0.82	$1.07 \times 10^{+1}$	0.49
	$\frac{1}{8}$	$3.64 \times 10^{-4}$	0.80	$1.69 \times 10^{-2}$	0.83	$7.82 \times 10^{+0}$	0.45
<b>T</b>	1	$9.78 \times 10^{-5}$	—	$4.32 \times 10^{-3}$	—	$7.46 \times 10^{-1}$	—
	$\frac{1}{2}$	$2.00 \times 10^{-5}$	2.29	$8.84 \times 10^{-4}$	2.29	$8.84 \times 10^{-1}$	1.39
	$\frac{1}{4}$	$4.78 \times 10^{-6}$	2.07	$2.12 \times 10^{-4}$	2.06	$2.12 \times 10^{-2}$	2.54
	$\frac{1}{8}$	$1.22 \times 10^{-6}$	1.97	$5.45 \times 10^{-5}$	1.96	$5.46 \times 10^{-2}$	0.89

**Table 26.1-3.. Error in velocity, projected pressure gradient, and temperature for the  $h$ -based formulation. THex mesh.**

	$\Delta$	$L^1$	Order	$L^2$	Order	$L^\infty$	Order
<b>u</b>	1	$3.48 \times 10^{-5}$	—	$1.25 \times 10^{-3}$	—	$1.44 \times 10^{-1}$	—
	$\frac{1}{2}$	$7.73 \times 10^{-6}$	2.17	$2.86 \times 10^{-4}$	2.13	$3.16 \times 10^{-2}$	2.19
	$\frac{1}{4}$	$1.76 \times 10^{-6}$	2.14	$6.56 \times 10^{-5}$	2.12	$8.58 \times 10^{-3}$	1.88
	$\frac{1}{8}$	$4.33 \times 10^{-7}$	2.02	$1.62 \times 10^{-5}$	2.02	$2.77 \times 10^{-3}$	1.63
$(\nabla p)_{\text{proj.}}$	1	$4.33 \times 10^{-3}$	—	$2.15 \times 10^{-1}$	—	$5.88 \times 10^{+1}$	—
	$\frac{1}{2}$	$1.72 \times 10^{-3}$	1.33	$1.19 \times 10^{-1}$	0.85	$4.70 \times 10^{+1}$	0.32
	$\frac{1}{4}$	$9.28 \times 10^{-4}$	0.89	$6.29 \times 10^{-2}$	0.92	$3.32 \times 10^{+1}$	0.50
	$\frac{1}{8}$	$5.16 \times 10^{-4}$	0.85	$3.43 \times 10^{-2}$	0.87	$2.54 \times 10^{+1}$	0.39
<b>Z</b>	1	$1.91 \times 10^{-6}$	—	$8.14 \times 10^{-5}$	—	$1.13 \times 10^{-2}$	—
	$\frac{1}{2}$	$4.53 \times 10^{-7}$	2.08	$1.94 \times 10^{-5}$	2.07	$6.20 \times 10^{-3}$	0.86
	$\frac{1}{4}$	$1.10 \times 10^{-7}$	2.05	$4.71 \times 10^{-6}$	2.04	$7.42 \times 10^{-4}$	3.06
	$\frac{1}{8}$	$2.77 \times 10^{-8}$	1.99	$1.19 \times 10^{-6}$	1.99	$2.64 \times 10^{-4}$	1.48

**Table 26.1-4.. Error in velocity, projected pressure gradient, and temperature for the  $Z$ -based formulation. THex mesh.**

## 26.1. ANALYTIC OR BENCHMARK SOLUTION

$$u(x, y, z) = \cos(2\pi kx) \sin(2\pi ky) \sin(2\pi kz) \quad (26.3)$$

$$v(x, y, z) = -\sin(2\pi kx) \cos(2\pi ky) \sin(2\pi kz) \quad (26.4)$$

$$w(x, y, z) = \sin(2\pi kx) \sin(2\pi ky) \cos(2\pi kz) \quad (26.5)$$

$$p(x, y, z) = \frac{1}{4} \cos(4\pi kx) \cos(4\pi ky) \cos(4\pi kz) \quad (26.6)$$

$$Z(x, y, z) = \cos(\pi kx) \cos(\pi ky) \cos(\pi kz) \quad (26.7)$$

$$h(x, y, z) = \frac{1}{c_p} \cos(\pi kx) \cos(\pi ky) \cos(\pi kz) + T_{\text{ref}} \quad (26.8)$$

with  $k = 1/L$  where  $L$  is the edge-length of the cube.

## 26.2. MESH DEFINITION

Four meshes are used in this problem. The geometry is a unit cube,  $[-0.05, 0.05]^3$ . The cube is uniformly meshed with element resolutions of  $40^3$ ,  $80^3$ ,  $160^3$ , and  $320^3$ . An additional test with “THex” meshes of roughly similar element counts was also performed.

The meshes consist of 3D hexahedral elements.

## 26.3. MATERIAL SPECIFICATIONS

The enthalpy formulation results in a density ratio of  $4/3$ , a viscosity of  $1.25 \times 10^{-3}$ , and a Prandtl number of  $0.8$ . The specific heat was set to  $c_p = 10^{-2}$ ,  $P_{\text{ref}} = 10^2$ ,  $R = 10$ , and  $\overline{MW} = 30$ .

The mixture fraction formulation uses a density ratio  $10/1$ , a viscosity of  $10^{-3}$ , and a Schmidt number of  $0.8$ .

## 26.4. INITIAL CONDITIONS

The manufactured solution is applied as the initial condition.

## 26.5. BOUNDARY CONDITIONS

Inflow boundary conditions are placed along all sides of the domain, with the manufactured solution for velocity and  $h$  or  $Z$  specified.

## 26.6. SOLUTION PROCEDURE

- The pressure projection uses the fourth-order smoothing algorithm with a scaling proportional to the time step.
- The mesh refinement study is performed with a constant CFL number of 0.4.
- The linear systems are solved with an Ro residual norm scaling and a solver tolerance of  $10^{-5}$ .
- A purely central CVFEM discretization is used for all equations.
- A differential buoyancy model is assumed, with a gravity vector of  $(-5, +6, +7)$ . The reference density is unity.

# 27. K-EPSILON MANUFACTURED SOLUTION

<b>Dimension:</b>	3D
<b>Transient/Steady:</b>	steady
<b>Laminar/Turbulent:</b>	turbulent
<b>Isothermal/Thermal:</b>	isothermal
<b>Temperature/Enthalpy:</b>	N/A
<b>Uniform/Nonuniform:</b>	uniform
<b>Combustion:</b>	no
<b>Soot:</b>	no
<b>Coupled Mechanics:</b>	no
<b>Regression Test:</b>	none

This manufactured solution was derived to test the k-epsilon turbulent model equations. The manufactured solution was performed on orthogonal meshes using fuego-2.obeta and 2.ibeta development.

## 27.1. ANALYTIC OR BENCHMARK SOLUTION

Steady Manufactured Solution:

The following solution equations (1)-(4) for velocity components and pressure is a modified solution taken from Ethier and Steinman<sup>1</sup>. The solution from [1] is an exact 3-D transient solution to the Navier-Stokes equations. It has been modified to be steady for this manufactured solution test in order to test spatial accuracy. Temporal accuracy could also be tested in the future by including the temporal terms.

---

<sup>1</sup>Ethier, C.R. and Steinman, D.A., 'Exact Fully 3D Navier-Stokes Solutions for Benchmarking', Int. J. Numer. Methods Fluids, Vol. 19, pp. 369-375 (1994)

### ***velocity and pressure fields***

$$u(x, y, z) = -a[e^{ax} \sin(ay + dz) + e^{az} \cos(ax + dy)] \quad (27.1)$$

$$v(x, y, z) = -a[e^{ay} \sin(az + dx) + e^{ax} \cos(ay + dz)] \quad (27.2)$$

$$w(x, y, z) = -a[e^{az} \sin(ax + dy) + e^{ay} \cos(az + dx)] \quad (27.3)$$

where  $a = \frac{\pi}{4}$ ,  $d = \frac{\pi}{2}$ .

Two pressure fields were tested:

$$p(x, y, z) = -\frac{1}{2}(u^2 + v^2 + w^2) \quad (27.4)$$

$$p(x, y, z) = \sin(c_1 x) \sin(c_2 y) \sin(c_3 z) \quad (27.5)$$

where  $c_1 = \frac{\pi}{2L}$ ,  $c_2 = \frac{\pi}{2M}$ ,  $c_3 = \frac{\pi}{2N}$ .

### ***kinetic energy***

$$k(x, y, z) = -\frac{3}{2}C_d d^2[e^{az} \sin(ax + dy) + e^{ax} \cos(ay + dz)] + C \quad (27.6)$$

where  $C_d = 0.09$  and  $C = 2$  (added to avoid negative values of k).

### ***turbulence dissipation***

$$\varepsilon(x, y, z) = k^2 \quad (27.7)$$

Domain:  $-L \leq x \leq L, -M \leq y \leq M, -N \leq z \leq N$

where  $L = M = N = 0.5$

## **27.2. MESH DEFINITION**

The meshes consist of 3D orthogonal hexahedral elements with equal spacing.

The solution was tested on grids:  $10^3, 20^3, 40^3, 80^3$ .

## 27.3. MATERIAL SPECIFICATIONS

Constant properties.

$$\rho = 1, \mu = 0.001$$

## 27.4. INITIAL CONDITIONS

The manufactured solution is applied as the initial condition.

## 27.5. BOUNDARY CONDITIONS

All boundaries of the domain have specified velocities, kinetic energy and dissipation. These boundary values are fixed to the manufactured solution with an 'inflow' condition.

The option for 'omission of near wall turbulent k-epsilon transport equation' was invoked.

## 27.6. SOLUTION PROCEDURE

The projection methods of stabilized and fourth order smoothing with timestep scaling were tested. The first order upwind factor was set to zero, thus the theoretical order of accuracy is two for the velocities, k, epsilon, and pressure and one for the partial derivatives of pressure.

It was found that no under relaxation provided converged solutions. Cases with under relaxation factors for turbulent viscosity, dissipation, and kinetic energy with 0.75, and momentum and pressure of 0.5 were performed for comparison.

An automatic time step was used with a  $CFL = 2.0$ . All nonlinear residuals are converged to a tolerance of  $10^{-16}$ . Serial and parallel runs were made.

## 27.7. VERIFICATION EXPERIMENTS

### Case 1: Pressure field defined by equation (27.4) ( $dp/dn \neq 0$ )

For the following results, the pressure field as specified in equation (27.4) was used. Figure 27.7-1 shows the  $L_2$  error norms for all velocity components, k, epsilon and pressure. Note that for all cases the mesh

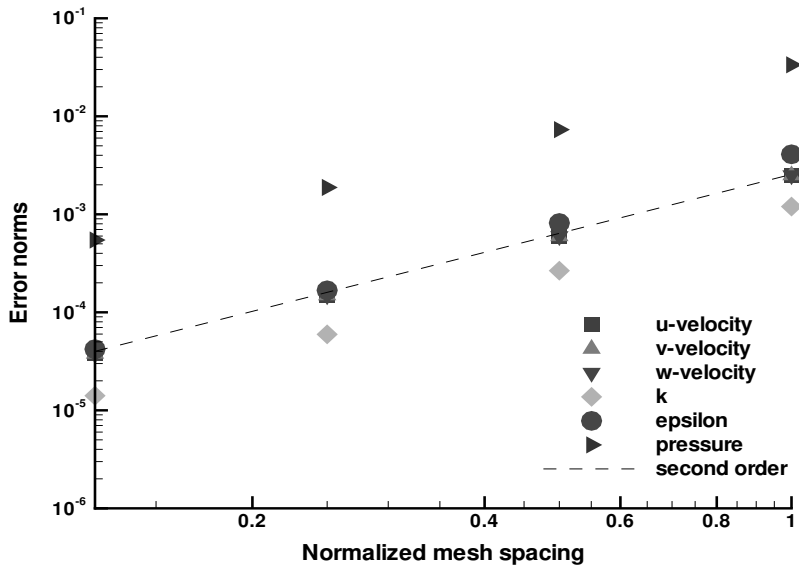


**Figure 27.7-1.. Plot of L2 error norms vs normalized mesh spacing for velocity components, k, epsilon, and pressure. Case 1.**

spacing has been normalized to the  $10^3$  mesh, which corresponds to a mesh spacing of 1. Figure 27.7-2 shows the L<sub>2</sub> error norms for the partial derivatives of pressure. Figure 27.7-3 shows the infinity error norms for all velocity components, k, epsilon and pressure. Figure 27.7-4 shows the infinity error norms for the partial derivatives of pressure.

Quantities were evaluated at interior nodal locations. Note that the pressure is expressed as  $\hat{p} = \bar{p} + \frac{2}{3}\bar{\rho}k$ , where  $\bar{p}$  is the true pressure. Thus, in order to compare pressure fields,  $\frac{2}{3}\bar{\rho}k$  was added to the analytical pressure solution during post-processing. The computed pressure field can float by some constant, thus the pressure field was normalized by setting the computed pressure equal to the maximum value of the analytical solution at the same nodal location for all meshes. The amount subtracted to make these values equivalent was then subtracted from all the other nodes. The residual norms dropped by twelve orders of magnitude for each mesh.

The results indicate that all velocity components, k, and epsilon approach second order behavior for the L<sub>2</sub> and infinity error norms. The pressure field is approaching second order behavior for the L<sub>2</sub> norms but not for the infinity norms. Second order accuracy is expected for all variables except for the partial derivatives of pressure, which should show first order behavior. The results indicate that first order behavior is not achieved for both measures of error for the partial derivatives of pressure. Finer grid sets were tested to determine if resolution was a factor, but results still did not provide the expected order of accuracy. All of the other projection method options in version 2.0beta were tested and the results did not display the expected order of accuracy.

To investigate why the partial derivatives of pressure were not displaying the expected order of accuracy

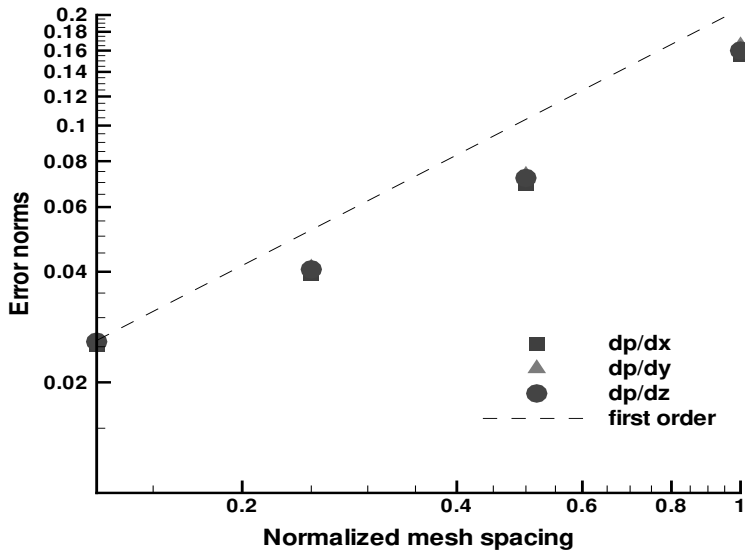


**Figure 27.7-2.. Plot of L2 error norms vs normalized mesh spacing for partial derivatives of pressure. Case 1.**

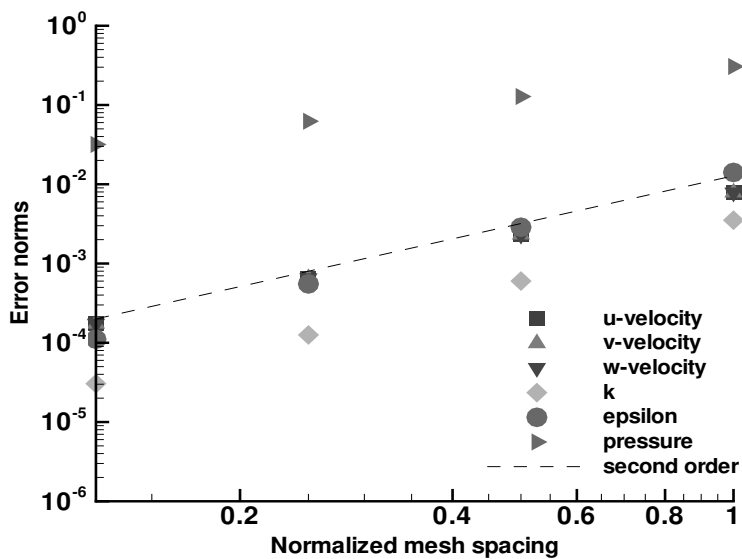


**Figure 27.7-3.. Plot of infinity error norms vs normalized mesh spacing for velocity components, k, epsilon, and pressure. Case 1.**

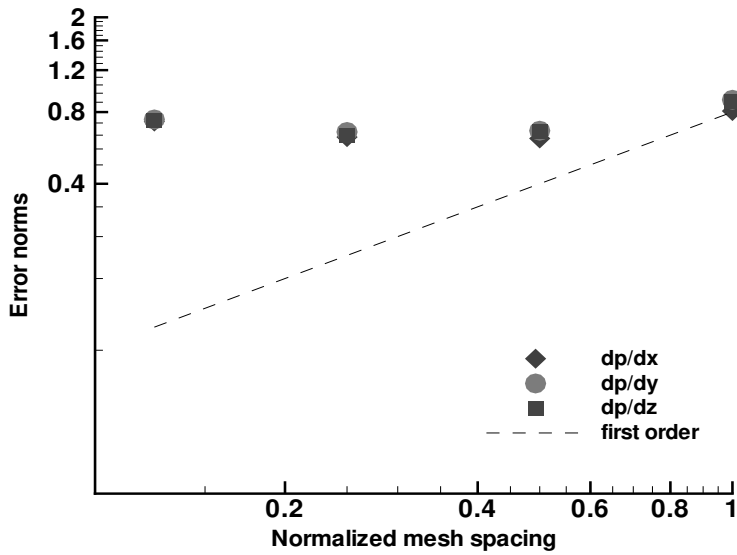


**Figure 27.7-4.. Plot of infinity error norms vs normalized mesh spacing for partial derivatives of pressure. Case 1.**

a 2D steady manufactured solution case was tested. The motivation of testing this case is it provides a simpler problem since the turbulent mechanics model is not invoked and it is faster running. The manufactured solution is a modification of an exact unsteady solution first proposed by G.I. Taylor. The manufactured solution for the velocity and pressure field is the following.

#### *velocity and pressure fields*

$$u(x, y) = -\cos(\pi x) \sin(\pi y) \quad (27.8)$$

$$v(x, y) = \sin(\pi x) \cos(\pi y) \quad (27.9)$$

$$p(x, y) = -0.25(\cos(2\pi x) + \cos(2\pi y)) \quad (27.10)$$

This solution was tested on grids  $25^2$ ,  $50^2$ ,  $100^2$ ,  $200^2$  on a domain of  $-0.05 < x < 0.5$ ,  $-0.05 < y < 0.05$ . The values used for density and viscosity are 1.0 and .01 respectively. Table 27.7-1 shows the results for the L<sub>2</sub> and infinity norms for velocities, pressure, and partial derivatives of pressure.

The results indicate that the velocities and pressure are not approaching the expected second order accuracy, and the partial derivatives of pressure are not approaching the expected first order accuracy for either the L<sub>2</sub> or the infinity error norms. This behavior could be due to the pressure solution having non-zero values for its normal partial derivatives at the boundaries. The formation of the Poisson equation used in the projection scheme has an implicit assumption of a zero value for the normal partial derivatives of pressure. Thus, a pressure solution which has a zero condition for its normal partial derivatives was then tested. This was achieved by using the pressure solution defined by equation (10),

**Table 27.7-1.. Order of accuracy for pressure solution defined by equation (10) where  $dp/dn \neq 0$  at the boundaries**

variable	order of accuracy					
	L <sub>2</sub> norm			infinity norm		
	decreasing $\Delta x \Rightarrow$					
u	1.89	1.86	1.84	1.87	1.62	1.64
v	1.89	1.86	1.84	1.87	1.62	1.64
p	1.62	1.51	1.44	1.13	1.07	1.04
dpdx	1.02	0.95	0.89	0.66	0.62	0.58
dpdy	1.02	0.95	0.89	0.66	0.62	0.58

**Table 27.7-2.. Order of accuracy for pressure solution defined by equation (13) where  $dp/dn = 0$  at the boundaries**

variable	order of accuracy					
	L <sub>2</sub> norm			infinity norm		
	decreasing $\Delta x \Rightarrow$					
u	1.59	1.81	1.91	1.56	1.82	1.92
v	1.59	1.80	1.91	1.57	1.82	1.92
p	2.48	2.43	2.34	1.94	1.98	2.00
dpdx	1.50	1.51	1.50	0.985	0.996	0.999
dpdy	1.50	0.50	1.50	0.983	0.996	0.999

but with the wave length modified to have  $dp/dn = 0$  at the boundaries. The modified velocity and pressure fields are the following.

*velocity and pressure fields,  $dp/dn=0$*

$$u(x, y) = -\cos(A\pi x) \sin(A\pi y) \quad (27.11)$$

$$v(x, y) = \sin(A\pi x) \cos(A\pi y) \quad (27.12)$$

$$p(x, y) = -0.25(\cos(2A\pi x) + \cos(2A\pi y)) \quad (27.13)$$

where  $A = 20$ . A domain of  $-0.05 < x < 0.05$ ,  $-0.05 < y < 0.05$  with grids  $25^2$ ,  $50^2$ ,  $100^2$ ,  $200^2$  and material specification of  $\rho = 1.0$  and  $\mu = 0.01$  was used. Table 27.7-2 shows the results for the L<sub>2</sub> and infinity norms for velocities, pressure, and partial derivatives of pressure.

The results indicate that the velocities and pressure are approaching or equaling second order accuracy, and the partial derivatives of pressure are approaching or equaling first order accuracy. Thus, it would appear that a pressure field with  $dp/dn = 0$  provides the correct boundary condition to result in the expected order of accuracy. With knowledge of this result, a manufactured solution for the k-epsilon equations with a modified pressure field was tested.

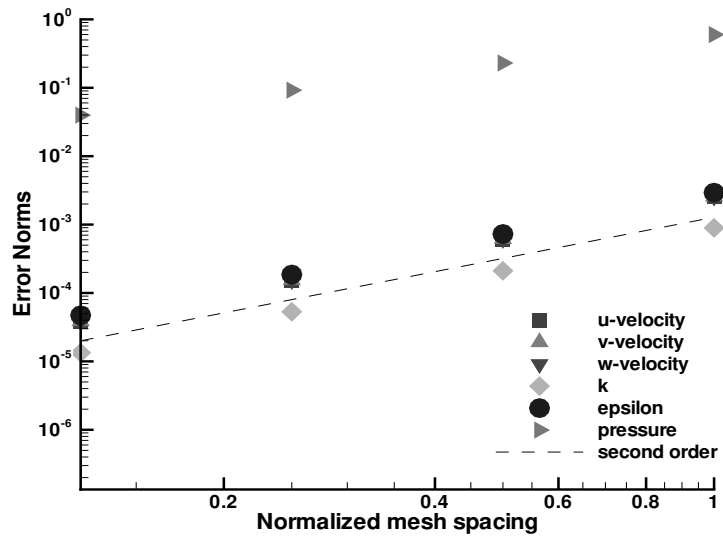


**Figure 27.7-5.. Plot of L2 error norms vs normalized mesh spacing for velocity components, k, epsilon, and pressure. Case 2. Projection method = stabilized.**

#### Case 2: Pressure field defined by equation (27.5) ( $dp/dn=0$ )

For the following results, the pressure field as specified in equation (27.5) was used. These results were obtained using version 2.1 beta instead of version 2.0 beta. It was found that the results using 2.0 versus 2.1 beta were equivalent for the projection method of stabilized. Figure 27.7-5 shows the L<sub>2</sub> error norms for all velocity components, k, epsilon and pressure. Figure 27.7-6 shows the L<sub>2</sub> error norms for the partial derivatives of pressure. Figure 27.7-7 shows the infinity error norms for all velocity components, k, epsilon and pressure. Figure 27.7-8 shows the infinity error norms for the partial derivatives of pressure.

The results indicate that the velocities, k, and epsilon error norms are of second order. The pressure field is showing a slight deviation from second order. The partial derivatives of pressure are not quite first order, but is showing much better convergence than the results from case 1 ( $dp/dn \neq 0$ ). These results were obtained using the project method of 'stabilized' with  $CFL = 2$  and no relaxation. The performance of the projection method of 'fourth order smoothing with timestep scaling' was also tested with  $CFL = 2$  and no relaxation. Figure 27.7-9 shows the L<sub>2</sub> error norms for all velocity components, k, epsilon and pressure. Figure 27.7-10 shows the L<sub>2</sub> error norms for the partial derivatives of pressure. Figure 27.7-11 shows the infinity error norms for all velocity components, k, epsilon and pressure. Figure 27.7-12 shows the infinity error norms for the partial derivatives of pressure.

The results indicate that the velocities, k, and epsilon are exceeding the expected order of accuracy for the L<sub>2</sub> and infinity norms. The pressure field is approaching second order for the L<sub>2</sub> and infinity norms,

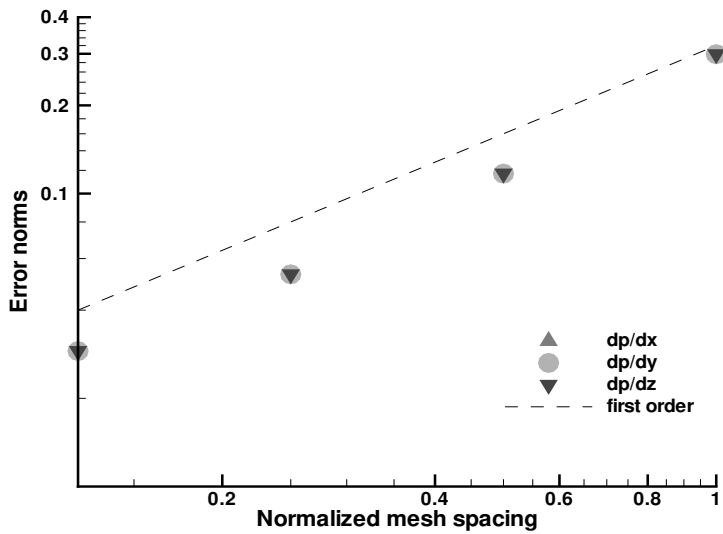


**Figure 27.7-6.. Plot of L2 error norms vs normalized mesh spacing for partial derivatives of pressure. Case 2. Projection method = stabilized.**

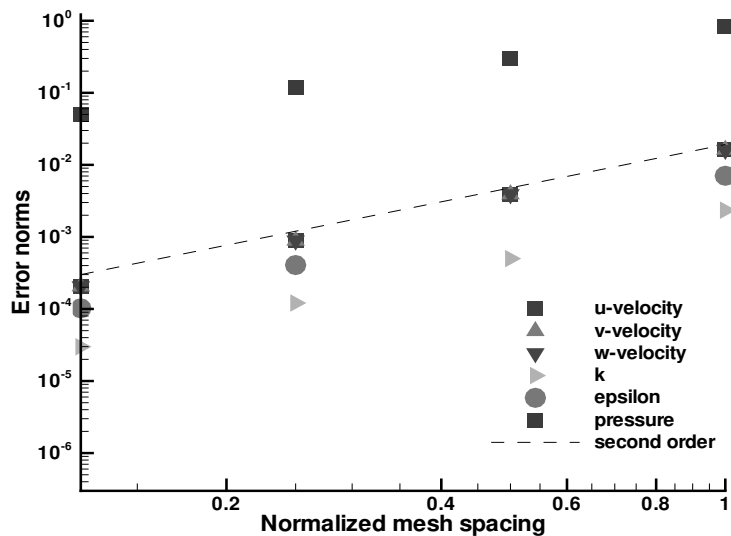


**Figure 27.7-7.. Plot of infinity error norms vs normalized mesh spacing for velocity components, k, epsilon, and pressure. Case 2. Projection method = stabilized.**

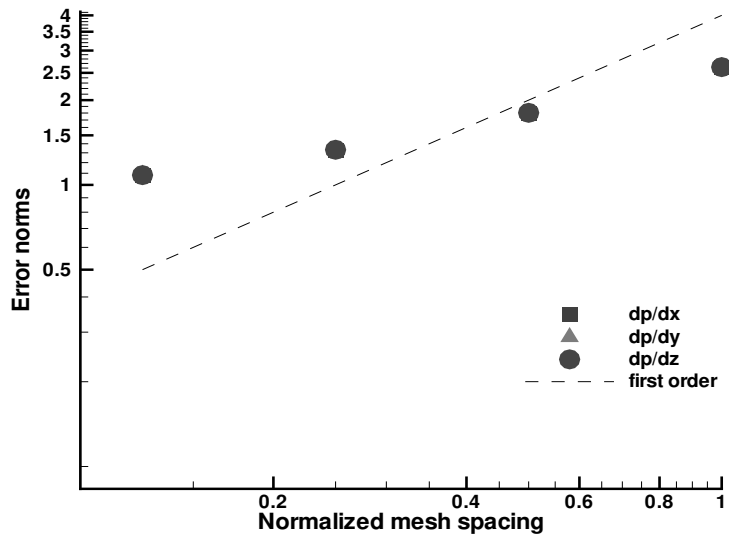


**Figure 27.7-8.. Plot of infinity error norms vs normalized mesh spacing for partial derivatives of pressure. Case 2. Projection method = stabilized.**

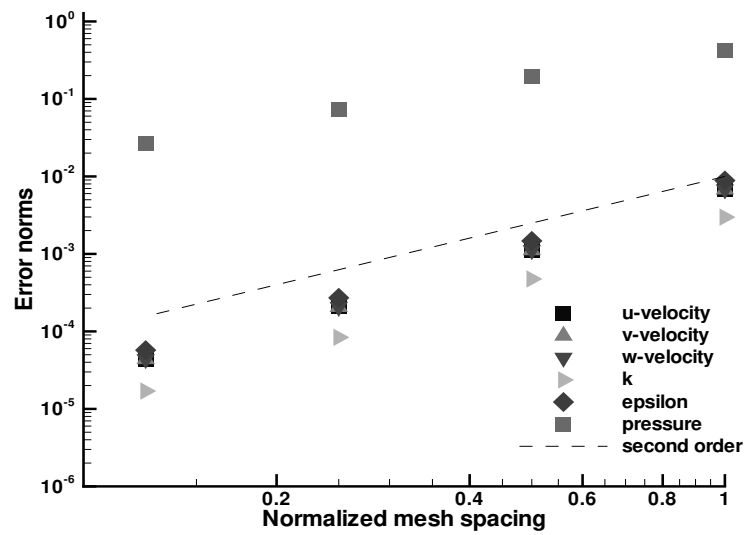


**Figure 27.7-9.. Plot of L2 error norms vs normalized mesh spacing for velocity components, k, epsilon, and pressure. Case 2. Projection method = fourth order smoothing with timestep scaling.**

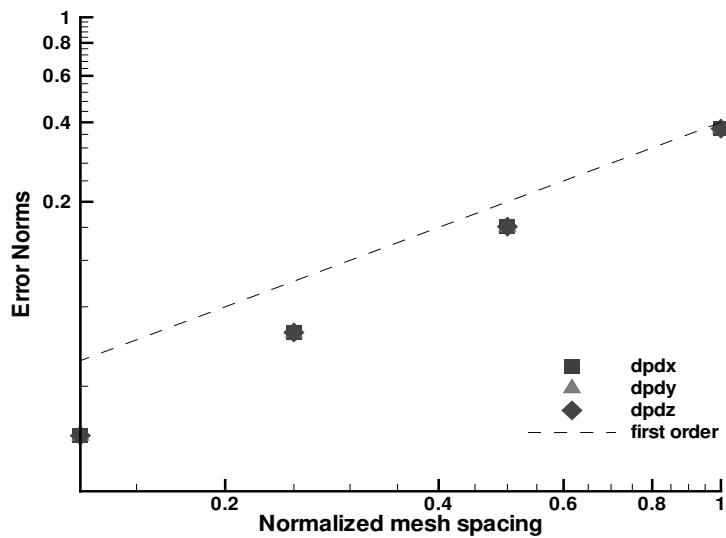


**Figure 27.7-10.. Plot of L2 error norms vs normalized mesh spacing for partial derivatives of pressure. Case 2. Projection method = fourth order smoothing with timestep scaling.**

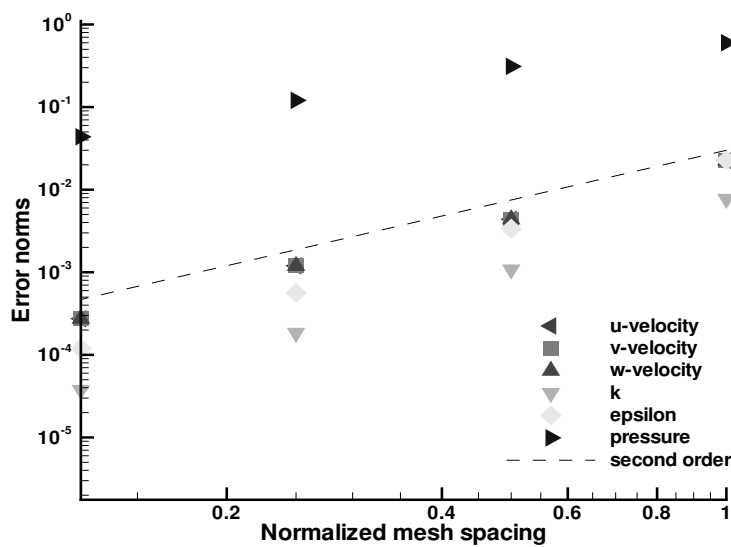


**Figure 27.7-11.. Plot of infinity error norms vs normalized mesh spacing for velocity components, k, epsilon, and pressure. Case 2. Projection method = fourth order smoothing with timestep scaling.**

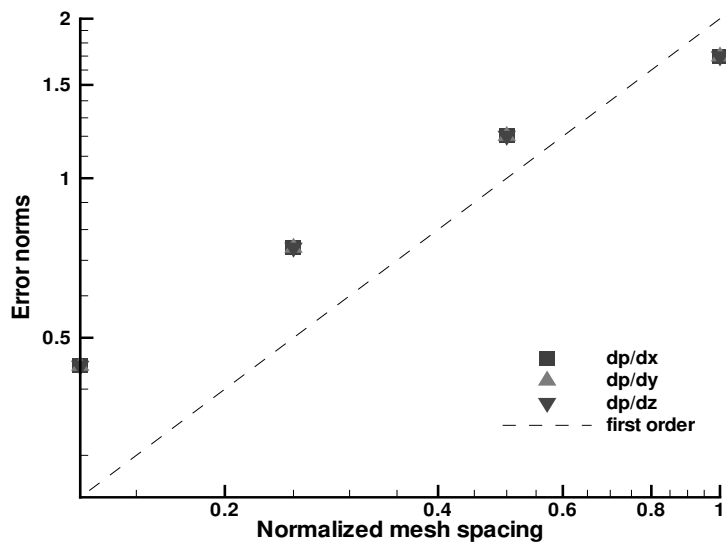


**Figure 27.7-12.. Plot of infinity error norms vs normalized mesh spacing for partial derivatives of pressure. Case 2. Projection method = fourth order smoothing with timestep scaling.**

and the partials derivatives of pressure exceed first order for the L<sub>2</sub> norms and approach first order for the infinity norms. Thus, the projection method option of 'fourth order smoothing with timestep scaling' provides better results than the 'stabilized' method, and provides the expected order of accuracy. The 'stabilized' method also took longer to converge with execution times that were about 5-6 times greater than the 'fourth order' method.

# 28. CONJUGATE HEAT TRANSFER MANUFACTURED SOLUTION

<b>Dimension:</b>	3D
<b>Transient/Steady:</b>	steady
<b>Laminar/Turbulent:</b>	n/a
<b>Isothermal/Thermal:</b>	thermal
<b>Temperature/Enthalpy:</b>	N/A
<b>Uniform/Nonuniform:</b>	uniform
<b>Combustion:</b>	no
<b>Soot:</b>	no
<b>Coupled Mechanics:</b>	yes
<b>Regression Test:</b>	none

Manufactured solutions of a form similar to that in Chapter 25 are used to test steady conjugate heat transfer coupling.

The steady manufactured solutions are run on regular, orthogonal hex meshes and on tet meshes.

This series of test is run with `fuego-2.1Development`.

## 28.1. ANALYTIC OR BENCHMARK SOLUTION

Three different steady state solutions are used:

$$T_1(x, y, z) = ax + by + cz + d \quad (28.1)$$

$$T_2(x, y, z) = \cos(a\pi x) \sin(b\pi y) \sin(c\pi z) + d \quad (28.2)$$

$$T_3(x, y, z) = \sin(a\pi x) \sin(b\pi y) \sin(c\pi z) + d \quad (28.3)$$

where, for all equations,  $a = 3$ ,  $b = c = 2$ . For solution 1,  $d = 100$ ; for solutions 2 and 3,  $d = 2$ .

The source terms corresponding to these solutions are

$$S_1(x, y, z) = 0 \quad (28.4)$$

$$S_2(x, y, z) = ((a\pi)^2 + (b\pi)^2 + (c\pi)^2) (\cos(a\pi x) \sin(b\pi y) \sin(c\pi z)) \quad (28.5)$$

$$S_3(x, y, z) = ((a\pi)^2 + (b\pi)^2 + (c\pi)^2) (\sin(a\pi x) \sin(b\pi y) \sin(c\pi z)) \quad (28.6)$$

These solutions and source terms are defined on the cubic domain  $-0.5 \leq x, y, z \leq 0.5$ . This domain is divided into two regions by an interface defined by the  $x = 0$  plane, with continuity of temperature and flux across the interface (for the continuous problem).

Although there is no fluid flow in either half of the domain, the two regions represent the fluid and solid regions in a conjugate heat transfer simulation. The part of the domain defined by  $-0.5 \leq x < 0$  will therefore be referred to in the following sections as the “fluid”, and the part with  $0 < x \leq 0.5$  will be referred to as the “solid”.

## 28.2. MESH DEFINITION

Three different families of meshes are used:

- **Mesh 1:** Both the fluid and solid regions are discretized with a regular orthogonal hexahedral mesh, such that all elements are cubes with side  $h$ . Four levels of mesh refinement are tested:  $h = 0.1, 0.05, 0.025$ , and  $0.0125$ . The total numbers of nodes in these meshes are  $N = 1452, 9702, 70, 602$ ; and  $538, 002$ , respectively. Note that the number of nodes for each mesh is not a perfect cube, since the nodes on the  $x = 0$  interface are represented in both regions’ meshes.
- **Mesh 2:** Both the fluid and solid regions are discretized with an unstructured tetrahedral mesh. The discretization of the interface is not the same on the two regions, so that there is not a node-to-node match between the two. Meshes are created by beginning with a coarse tetrahedral mesh and refining uniformly. Four levels of mesh refinement are tested; the total numbers of nodes in these meshes are  $N = 1919, 13, 372, 99, 526$ ; and  $767, 306$ .
- **Mesh 3:** Both the fluid and solid regions are discretized with an unstructured tetrahedral mesh. The discretization of the interface is the same on the two regions, so that there is a node-to-node match between the two. Meshes are created by beginning with a coarse tetrahedral mesh and refining uniformly. Four levels of mesh refinement are tested; the total numbers of nodes in these meshes are  $N = 1922, 13, 397, 99, 728$ ; and  $768, 926$ .

## 28.3. MATERIAL SPECIFICATIONS

Constant properties are used throughout the domain, equal in both regions:

$$\rho = 1.0 \tag{28.7}$$

$$\kappa = 1.0 \tag{28.8}$$

$$c_p = 1.0 \tag{28.9}$$

All properties are in cgs units.

## 28.4. INITIAL CONDITIONS

The manufactured solution is applied as the initial condition in both domains.

## 28.5. BOUNDARY CONDITIONS

The temperatures are fixed to the manufactured solution on all domain walls ( $x = \pm 0.5$ ,  $y = \pm 0.5$ , and  $z = \pm 0.5$ ). At the fluid-solid interface,  $x = 0$ , Fuego enforces loose temperature coupling: at each time step, the temperature of the solid at the interface is transferred (with interpolation, if necessary) to the fluid nodes and applied as a fixed temperature boundary condition. A heat transfer coefficient and reference temperature are computed from the resulting fluid solution and transferred to the solid region, where they are used in a convective heat transfer boundary condition.

## 28.6. SOLUTION PROCEDURE

All results presented use Fuego for both the fluid and solid regions. In the fluid region, all flow velocities are zero. A Fuego conduction-only region is used to represent the solid.

A fixed time step of  $\Delta t = 0.1\text{s}$  is used. All nonlinear residuals are converged to a tolerance of  $10^{-16}$ .

## 28.7. VERIFICATION EXPERIMENTS

### 28.7.1. MMS1: Linear temperature field

Because the linear temperature field solution of equation (28.1) lies within the function space of the linear finite elements used in Fuego, an ideal formulation should give numerical solutions that match the exact solution to within machine precision, even for coarse meshes. The error norms in the fluid region (computed at the nodes) for the three different meshes, using the coarsest mesh for each mesh family, are given in Table 28.7-1.

**Table 28.7-1.. Error norms in fluid region for manufactured solution  $T_1(x, y, z)$ . Meshes used are the coarsest meshes in each mesh family.**

Mesh	$\ e\ _{L_2}$	$\ e\ _{L_1}$	$\ e\ _{L_\infty}$
Mesh 1	$2.11 \times 10^{-15}$	$5.63 \times 10^{-15}$	$2.84 \times 10^{-14}$
Mesh 2	$3.85 \times 10^{-4}$	$1.04 \times 10^{-4}$	$4.97 \times 10^{-3}$
Mesh 3	$3.25 \times 10^{-15}$	$6.23 \times 10^{-16}$	$2.84 \times 10^{-14}$

Machine-level error is achieved on meshes 1 and 3, which both have conforming surface discretizations at the interface, but not on mesh 2, which does not conform at the interface. It is clear from these results that the error in for this linear solution is wholly due to interpolation at the interface. It should be recalled that even though the temperature field is linear for this case, and therefore the heat flux is constant, the individual components of the convective heat transfer that are passed between regions (convection coefficient and reference temperature) may not be linear fields, and therefore are subject to interpolation errors.

### 28.7.2. MMS2 and MMS3: Trigonometric function solutions

The convergence plot for solution  $T_2(x, y, z)$  on Mesh 1 is shown in Figure 28.7-1. The convergence is only first order. One source of error for the conjugate heat transfer coupling can be seen by comparing with Figure 28.7-2, showing second order convergence for solution  $T_3(x, y, z)$ . The important difference between these two solutions is that solution  $T_2$  has a nonzero source term at the  $x = 0$  interface, while the source term for  $T_3$  goes to zero at the interface. A similar difference in convergence rates can be seen in a 1-D version of this verification study (not shown). The poor convergence rate for  $T_2$  is apparent from examination of the equations solved at the interface nodes; it is caused by the neglect of the control volume at the interface when a Dirichlet boundary condition is applied. The source term in a layer of volume with thickness proportional to the element size  $h$  is therefore unaccounted for at these surface nodes.

The convergence plots for solution  $T_3(x, y, z)$  on Mesh 2 and Mesh 3 are shown in Figures 28.7-3 and 28.7-4. For these meshes the convergence is between first and second order; the rate is close to 1.5 for the  $L_1$  and  $L_2$  errors, and slightly worse for the  $L_\infty$  error. The reasons for the deterioration of convergence rate when using a tetrahedral mesh are unclear, and will be the subject of further study.

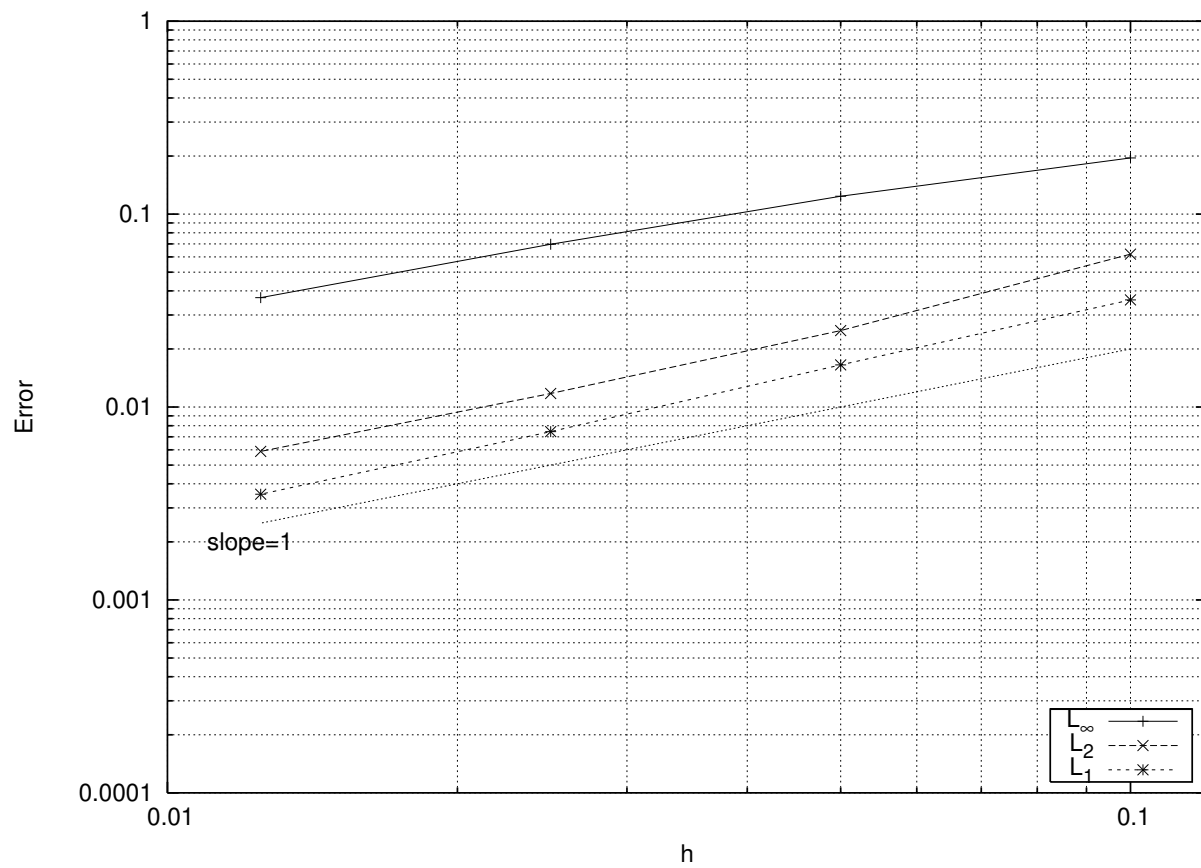


**Figure 28.7-1.. Plot of error vs. mesh spacing for solution  $T_2(x, y, z)$  solved on Mesh 1.**

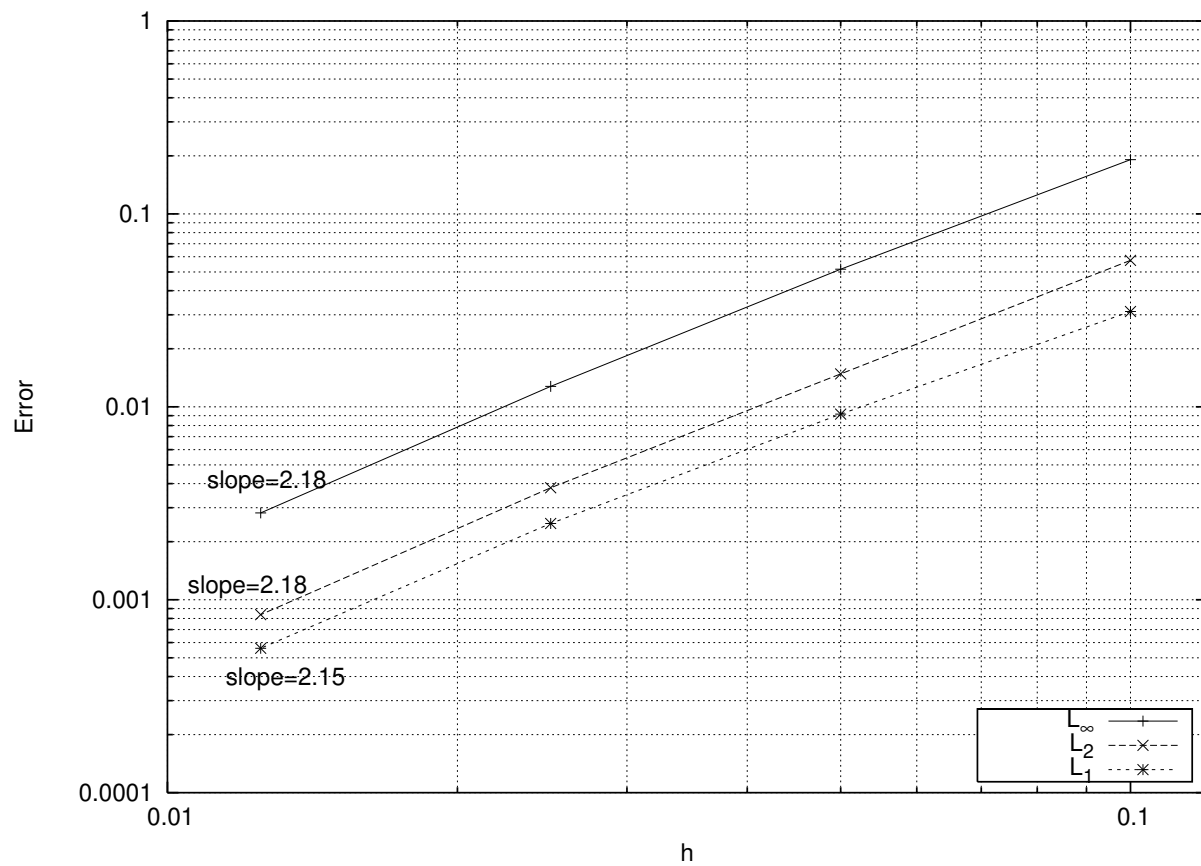


Figure 28.7-2..

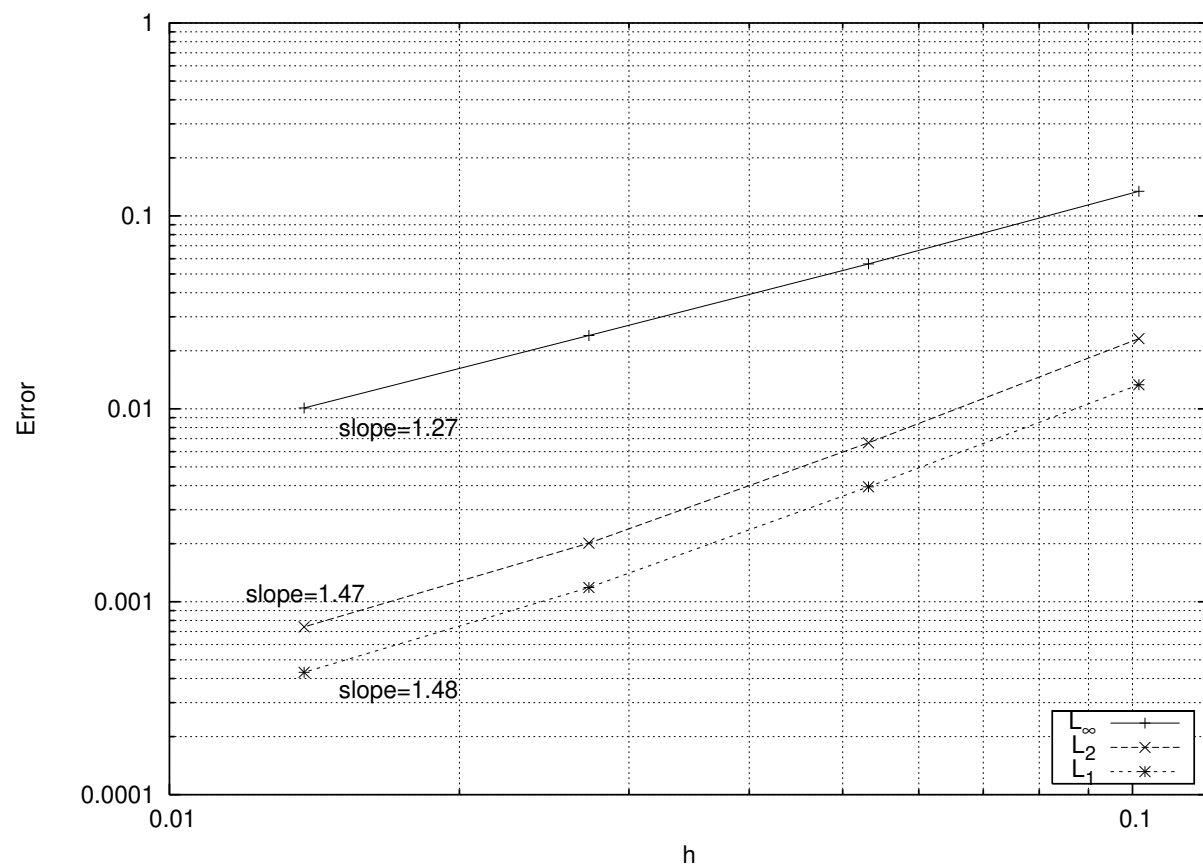


Figure 28.7-3..

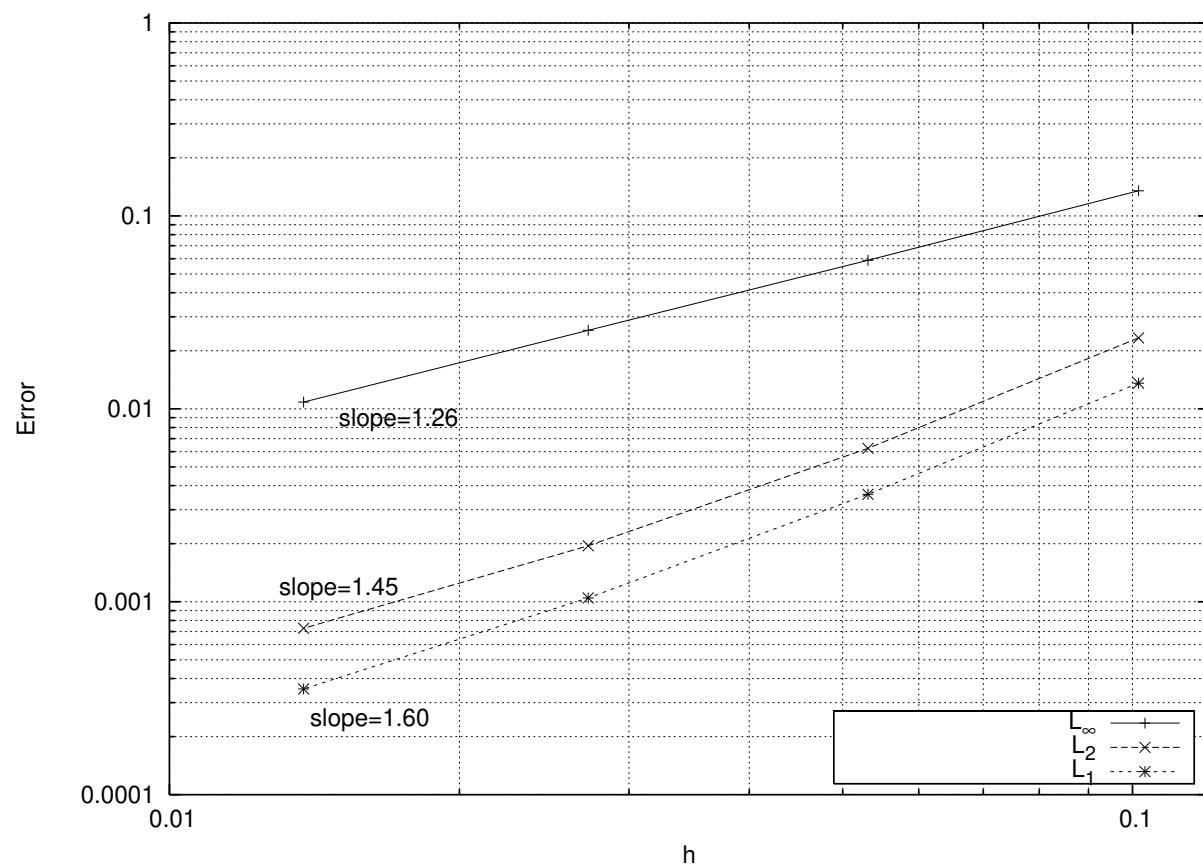


Figure 28.7-4..

# 29. POROUS MEDIA

<b>Dimension:</b>	3D
<b>Transient/Steady:</b>	steady
<b>Laminar/Turbulent:</b>	laminar
<b>Isothermal/Thermal:</b>	isothermal
<b>Temperature/Enthalpy:</b>	N/A
<b>Uniform/Nonuniform:</b>	uniform
<b>Combustion:</b>	no
<b>Soot:</b>	no
<b>Coupled Mechanics:</b>	no
<b>Regression Test:</b>	fuego/puvw_duct_2

This problem is used to verify the implementation of the porous media flow capability.

## 29.1. MATERIAL SPECIFICATIONS

The material properties in Fuego are a fluid with a density of 1E-3 kg/m<sup>3</sup> and a viscosity of 1E-4 kg/m s.

## 29.2. INITIAL CONDITIONS

The initial conditions used in Fuego were a  $x$ ,  $y$ , and  $z$  components of velocity of 0 m/s, 0 m/s, 30 cm/s respectively. The channel was aligned with the flow in the  $z$  direction and the initial velocity is the analytical average velocity through the duct.

## 29.3. BOUNDARY CONDITIONS

The boundary conditions used in Fuego were a fixed inflow and outflow pressure of  $2*1.1322e5$  and 0.0 dynes/cm<sup>2</sup> respectively. No slip walls were used for the channel wall.

## 29.4. ANALYTIC OR BENCHMARK SOLUTION

Darcy's law describes steady, creeping flow through a stationary porous medium as

EQN

where  $q$  is the specific discharge rate (volume flow rate per unit of total cross-sectional area; note where  $u_z$  is the fluid velocity component in the  $z$  direction) and  $k$  is the permeability of the medium. This expression can be derived from the fluid momentum equation,

$$\frac{\partial}{\partial t} \epsilon \rho u_i + \frac{\partial}{\partial x_j} \epsilon \rho u_j u_i = \frac{\partial}{\partial x_i} p + \frac{\partial}{\partial x_j} \tau_{ij} + \rho g_i + \beta(u_i^s - u_i) \quad (29.1)$$

by neglecting the transient, inertial, stress, body force, and turbulent dispersion force terms. The  $z$ -component of momentum then becomes

EQN

For a porous medium where there is a significant solid volume fraction, is given by,

EQN

For creeping flow through a stationary porous medium with significant solid volume fraction, the second term in the above equation is negligible compared with the first term. Substituting the reduced expression for  $\tau_{ij}$  into equation (5.2) and rearranging gives (5.3)

Comparing with equation (5.1) we see that an expression for  $k$  is

(5.4)

It is noted that the Kozeny-Carman equation given in Bear (1972) for the permeability of a porous medium of constant diameter spheres is

(5.5)

The test problem proposed to solve in Fuego is three-dimensional, steady, creeping flow through a stationary bed of spheres packed in a cubic arrangement (the least compact arrangement). Let the spheres have diameter (0.01 cm); the porosity is . Equation (5.4) then gives a permeability . Assume a 2D channel geometry with channel height of 100 particle diameters or 1 cm and channel length of 10 cm. Let the channel surfaces be slip surfaces. Assuming a Reynolds number of unity the specific discharge rate is

(5.6)

for air at atmospheric pressure and 300 K. Solving equation (5.1) for the pressure drop gives  $1.1322 \times 10^5$  dynes/cm<sup>2</sup> over a 10 cm length of porous medium. Apply this pressure drop to the channel and solve the flow problem. The resulting air velocity should be close to 33.5 cm/s.

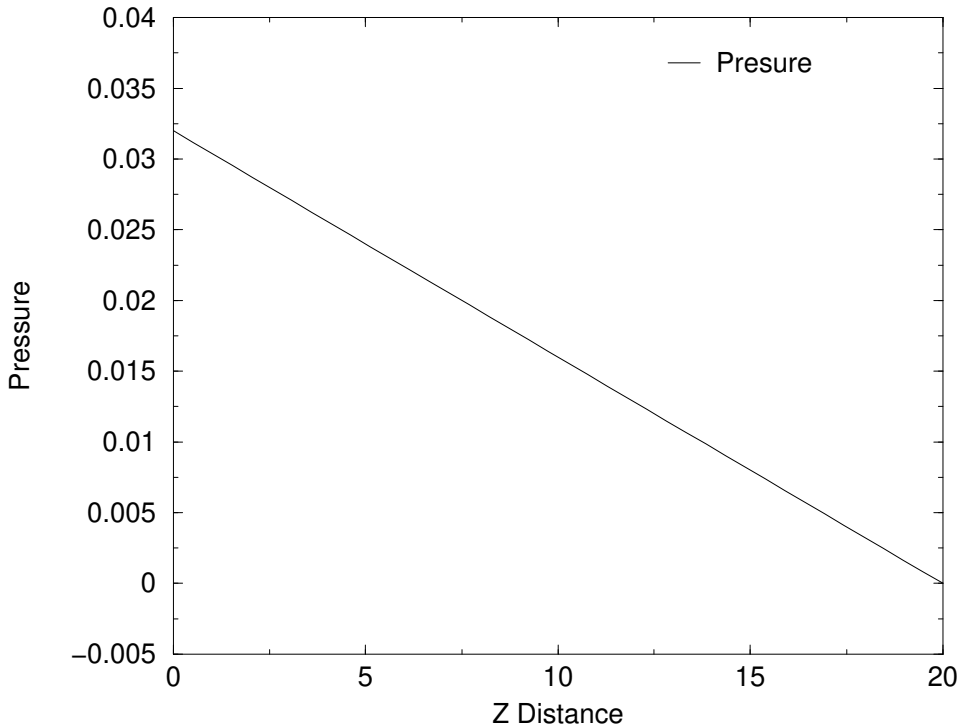


**Figure 29.4-1.. Centerline pressure in duct showing linear change.**

## 29.5. MESH DEFINITION

Three different meshes were used for the Fuego calculations. The three different mesh sizes for the  $x$ ,  $y$ , and  $z$ , directions are  $20 \times 40 \times 40$ ,  $40 \times 80 \times 80$ , and  $80 \times 160 \times 160$ . The meshes consist of 3D hexahedral elements. The arbitrary revolution simulation was performed on the  $20 \times 40 \times 40$  mesh.

## 29.6. SOLUTION PROCEDURE

Options selected in the Fuego run were: **CFL LIMIT** = 0.1, **TIME STEP CHANGE FACTOR** = 1.25, **TRANSIENT STEP TYPE** IS automatic, **UPWIND METHOD** IS MUSCL, one nonlinear iteration per time step. For  $u$ ,  $v$ ,  $w$ , **SOLUTION METHOD** IS bicgstab, **PRECONDITIONING METHOD** IS jacobi, **RESIDUAL NORM TOLERANCE** = 1.0e-6. For continuity **SOLUTION METHOD** IS gmres, **PRECONDITIONING METHOD** IS jacobi, **RESIDUAL NORM TOLERANCE** = 1.0e-8.

This page intentionally left blank.

# BIBLIOGRAPHY

- [1] Ghia, U., K. N. Ghia, and C. T. Shinn. "High-Re Solutions for Incompressible Flow Using the Navier-Stokes Equations and a Multigrid Method". *Journal of Computational Physics*, **48**(3):387–411, 1982.
- [2] Bird, R. B., W. E. Stewart and E. N. Lightfoot. *Transport Phenomena*. John Wiley and Sons, 1960.
- [3] Blottner, F. G. and A. R. Lopez. "Benchmark Example for a Multi-Component Gas Mixture Flow (Turbulent, Multi-Component Gas Mixture Section Revised)". Sandia National Laboratories internal memo, Albuquerque, NM, August 2001.
- [4] Yih, C.-S. *Fluid Mechanics*. West River Press, Ann Arbor, Michigan, 1977.
- [5] Yih, C.-S. "Laminar Free Convection Due to a Line Source of Heat". *Transactions of the American Geophysics Union*, **33**:669–672, 1952.
- [6] Yih, C.-S. "Free Convection Due to Buoyancy Sources". In *Symposium on the Use of Models in Geophysical Fluid Mechanics*, pages 117–133. 1956.
- [7] Brand, R. S., and F. J. Lahey. "The Heated Laminar Jet". *Journal of Fluid Mechanics*, **29**:305–315, 1967.
- [8] Berker, R. "Mouvement d'un fluide visqueux incompressible". In *Handbuch der Physik, Volume 8, Part 2*. Springer Verlag, Berlin, 1963.
- [9] Shah, R. K. and M. S. Bhatti. "Assessment of Test Techniques and Correlation for Single-Phase Heat Exchangers". In *6th NATO Advanced Study Institute on Thermal-Hydraulics and Fundamentals of Two-Phase-Flow Heat Exchangers, Portugal*. July 1987.
- [10] Özışık, M. N., R. M. Cotta, and W. S. Kim. "Heat Transfer in Turbulent Forced Convection Between Parallel-Plates". *Canadian Journal of Chemical Engineering*, **67**:771–776, 1989.
- [11] Kader, B. A. "Temperature and Concentration Profiles in Fully Turbulent Boundary Layers". *Int. J. Heat Mass Transfer*, **24**:1541–1544, 1981.
- [12] Marriott, P. G. "Heat Transfer in the Entrance Region of a Parallel Wall Passage". Master's thesis, Univ. Manchester, 1969.
- [13] Hatton, A. P., and N. H. Woolley. "Heat Transfer in Two-Dimensional Turbulent Confined Flows". *Heat and Fluid Flow*, **3**:13–21, 1973.
- [14] Stephenson, P. L. "A Theoretical Study of Heat Transfer in Two-Dimensional Turbulent Flow in a Circular Pipe and between Parallel and Diverging Plates". *Int. J. Heat Mass Transfer*, **19**:413–423, 1976.

[15] Launder, B. E. "On the Computation of Convective Heat Transfer in Complex Turbulent Flows". Journal of Heat Transfer, **110**:1112–1128, 1988.

[16] IM Aksit and JB Moss. A hybrid scalar model for sooting turbulent flames. Combustion and flame, **145**(1):231–244, 2006.

[17] Kin M Leung, Rune P Lindstedt, and WP Jones. A simplified reaction mechanism for soot formation in nonpremixed flames. Combustion and flame, **87**(3):289–305, 1991.

[18] Kee, R. J., F. M. Rupley, and J. A. Miller. "CHEMKIN-II: A Fortran Chemical Kinetics Package for the Analysis of Gas-Phase Chemical Kinetics". Technical Report SAND89-8009B, Sandia National Laboratories, Livermore, 1991.

[19] Kee, R. J., G. Dixon-Lewis, J. Warnatz, M. E. Coltrin, and J. A. Miller. "A Fortran Computer Code Package for the Evaluation of Gas-Phase Multicomponent Transport Properties". Technical Report SAND86-8246, Sandia National Laboratories, Livermore, 1991.

[20] Kee, R. J., F. M. Rupley, and J. A. Miller. "The Chemkin Thermodynamic Data Base". Technical Report SAND87-8215B, Sandia National Laboratories, Livermore, 1992.

[21] Burns, S. P., J. R. Howell, and D. E. Klein. "Application of the Finite Element Method to the Solution of Combined Natural Convection-Radiation in a Horizontal Cylindrical Annulus". In Lewis, R. W. and P. Durbetaki, editor, Numerical Methods in Thermal Problems, Volume IX. Pineridge Press Limited, Swansea, U.K., 1995.

[22] Morales, J. C. and A. Campo. "Radiative Effects on Natural Convection of Gases Confined in Horizontal, Isothermal Annuli". ASME Developments in Radiative Heat Transfer, **29**:659–671, 1992.

[23] Domino, S. P., and W. G. Houf. "SIERRA/Fuego Participating Media Radiation (PMR) Simulation". Sandia National Laboratories internal memo, Albuquerque, NM, Jan 2000.

[24] Salari, K. and P. Knupp. "Code Verification by the Method of Manufactured Solutions". Technical Report SAND2000-1444, Sandia National Laboratories, Albuquerque, NM, June 2000.

[25] Abdel-Rakman, A. A., W. Chakroun, and S. F. Al-Fahed. "LDA Measurements in The Turbulent Round Jet". Mecahnics Reasearch Communications, **24**:277–288, 1997.

[26] White, F. M. Viscous Fluid Flow. McGraw-Hill, Inc., 2nd ed., 1991.

[27] Schlichting, H. Boundary Layer Theory. McGraw-Hill, Inc., 7th ed., 1979.

[28] White, F. M. Viscous Fluid Flow. McGraw-Hill, Inc., 1st ed., 1974.

[29] Clift, R., J. R. Grace, and M. E. Weber. Bubbles, Drops, and Particles. Academic Press, Inc., 1978.

[30] Batchelor, G. K. An Introduction to Fluid Dynamics. Cambridge University Press, 1967.

[31] Mills, A. F. Heat Transfer. Richard D. Irwin, Inc., 1992.

# DISTRIBUTION

## Email—Internal

Name	Org.	Sandia Email Address
Technical Library	01911	sanddocs@sandia.gov

This page intentionally left blank.

This page intentionally left blank.



**Sandia  
National  
Laboratories**

Sandia National Laboratories is a multimission laboratory managed and operated by National Technology & Engineering Solutions of Sandia LLC, a wholly owned subsidiary of Honeywell International Inc., for the U.S. Department of Energy's National Nuclear Security Administration under contract DE-NA0003525.